Design of a permanent magnet synchronous machine for hybrid electric vehicles with twin electric machines and a range extender

An, Jeongki

(2020)

DOI (TUprints): https://doi.org/10.25534/tuprints-00011826

Publikationstyp: Ph.D. Thesis

Fachbereich: 18 Department of Electrical Engineering and Information Technology

Quelle des Originals: https://tuprints.ulb.tu-darmstadt.de/11826

Design of a permanent magnet synchronous machine for hybrid electric vehicles with twin electric machines and a range extender

Dem Fachbereich Elektrotechnik und Informationstechnik
der Technischen Universität Darmstadt
zur Erlangung des akademischen Grades eines
Doktor-Ingenieurs (Dr.-Ing.)
genehmigte Dissertation

von

M.Sc. Jeongki An

geboren am 04.11.1983
in Busan, Südkorea

Referent:	Prof. Dr.-Ing. habil. Dr. h.c. Andreas Binder
Korreferent:	Prof. Dr. phil. Dr. techn. habil. Harald Neudorfer
Tag der Einreichung:	17. 09. 2019
Tag der mündlichen Prüfung:	15. 04. 2020

D17
Darmstadt 2019

An, Jeongki: Design of a permanent magnet synchronous machine for hybrid electric vehicles with twin electric machines and a range extender
Darmstadt, Technische Universität Darmstadt,
Jahr der Veröffentlichung der Dissertation auf TUprints: 2020
URN: urn:nbn:de:tuda-tuprints-118268
URI: https://tuprints.ulb.tu-darmstadt.de/id/eprint/11826
Tag der mündlichen Prüfung: 15.04.2020

Vorwort

Die vorliegende Arbeit ist während meiner Tätigkeit als wissenschaftlicher Mitarbeiter und Doktorand am Institut für Elektrische Energiewandlung der Technische Universität Darmstadt entstanden.

Für mich war die Erstellung dieser Arbeit eine Herausforderung und persönlich bereichernde Erfahrung zugleich. Den zahlreichen Personen, die mich in vielfältiger Art und Weise unterstützt haben, die mich während der Promotionszeit begleitet und mir Rückhalt gegeben haben, möchte ich an dieser Stelle ganz herzlich danken.

Vor allem möchte ich mich bei meinem Doktorvater Prof. Dr.-Ing. habil. Dr. h.c. Andreas Binder für seine hervorragende Unterstützung und sein persönliches Engagement bei der Betreuung dieser Arbeit bedanken. Durch seine konstruktiven Anmerkungen und Hinweise hat er entscheidend zum Gelingen meiner Arbeit beigetragen. Ebenfalls herzlich bedanken möchte ich mich bei Herrn Prof. Dr. phil. Dr. techn. habil. Harald Neudorfer für die freundliche Übernahme des Koreferats dieser Dissertation.

Danken möchte ich der Forschungsvereinigung Antriebstechnik (FVA) und dem Deutsches Zentrum für Luft- und Raumfahrt (DLR) für die finanzielle Unterstützung während meiner Zeit als Wissenschaftlicher Mitarbeiter. Ich bedanke mich bei meinen DE-REX-Projekt Kollegen, Ruben König, Andreas Viehmann und Sebastian Fischer, mit denen ich zusammen gearbeitet und von denen ich viel gelernt habe. An Herrn Arno Huber von der Firma *THIEN eDrives* GmbH, Lustenau, Österreich, geht ebenfalls mein herzlicher Dank für die Unterstützung bei der Konstruktion der Prototypenmaschine.

Weiterhin möchte ich mich besonders bei allen technischen Mitarbeitern am Institut für Elektrische Energiewandlung bedanken. Im Einzelnen bei Anette Gallinat für die Unterstützung bei technischen Zeichnungen, bei Annette Siler für die Buchhaltung meines DE-REX-Projekts, bei Markus Lohnes für die Unterstützung bei der Konstruktion und der Fertigung der Prototypenmaschine, bei Andreas Fehringer für die Unterstützung bei der Fertigung der weitere Elektromotoren für die DE-REX-Antriebsstränge, bei Klaus Gütlich für die Unterstützung bei allen elektrischen Installationen für den Prüfstand und die DE-REX-Antriebsstränge.

Ich möchte mich außerdem bei allen Mitdoktoranden und Kollegen für das besonders angenehme Arbeitsklima und die vielen fachlichen Diskussionen bedanken: Gabriel Bergmann, Stefan Dewenter, Bogdan Funieru, Oliver Magdun, Fabian Mink, Mehran Mirzaei, Kersten Reis, Jinou Wang, Björn Deusinger, Daniel Dietz, Nicolas Erd, Yves

Gemeinder, Marcel Lehr, Xing Li, Gael Messager, Sascha Neusüs, Martin Weicker. Mit ihnen war ich sehr glücklich über nicht nur die vielen interessanten fachlichen Gespräche, sondern auch die stets freundschaftliche Gemeinschaft.

Ebenso möchte ich mich bei allen engagierten Studenten, Ajaya Sharma, Miquel Tost Candel und Yuan Zhang bedanken, die mich durch ihre Masterarbeit bei meiner Dissertation unterstützt haben.

Ein herzliches Dankeschön möchte ich an meine Frau So Yeon Lee richten, die mich während meiner Doktorarbeit bedingungslos unterstützt hat. Sie hat es geschafft, mir auch in stressigen Zeiten den Rücken frei zu halten, sodass ich mich vollständig auf meine Dissertation konzentrieren konnte.

Zu guter Letzt möchte ich mich bei meiner Familie bedanken: Bei meinen Eltern Seongchun An und Sunsoon Jung, sowie meiner Schwester, Jeongeun An. Meinen Eltern danke ich von Herzen, dass sie mir diese Ausbildung ermöglicht und mich auf meinem bisherigen Lebensweg vorbehaltlos unterstützt, gefördert und gefordert haben, wodurch sie mir die Basis für meine persönliche und berufliche Entwicklung ermöglichten. Durch ihren steten Rückhalt, ihren Zuspruch und ihre Liebe haben sie im wesentlichen Maße zum Gelingen der Arbeit beigetragen. Mein ganz besonderer Dank gilt meiner Frau So Yeon Lee, deren Unterstützung, Verständnis und Geduld in den letzten Jahren schier grenzenlos war, die mich immer wieder ermutigt hat, weiter zu machen und die mir auch in stressigen Zeiten den Rücken freigehalten hat. Dir, liebe Soy, und unserem Kind Jimin Hannah, widme ich diese Arbeit. Vielen Dank für alles.

Jeongki An
im Mai 2020

Motivation

With volatility of oil prices and the carbon emission reduction in line with the United Nations Framework Convention on Climate Change (UNFCCC), electric vehicles are emerging as feasible solutions for CO_2 emission reduction. However, electric vehicles still have many difficulties to replace conventional fossil fuel vehicles. Due to lower energy density of lithium-ion battery compared to fossil fuels and its technical limitation, electric vehicles have relative short mileages and long recharging time of batteries. Additionally, because of high battery costs, electric vehicles are not currently competitive in the market. In order to overcome these drawbacks, auto companies (amongst others) are trying to use plug-in hybrid systems and range extender drive systems. The market share of the hybrid-electric vehicle with these technologies is clearly increasing year by year. Although they are not ideal solutions for electric vehicles with zero emission, these transitional solutions will be a major thrust to achieve Germany's carbon emission reduction target.

The "Twin-Drive-Transmission with a range extender (DE-REX)" is a novel powertrain concept for electric and hybrid vehicles. The powertrain consists of two electric machines, two-speed sub-transmission and an internal combustion engine for a range extender. Thus, it is suitable for both pure electric and hybrid driving to increase driving range and reduce carbon emissions. The main aim of this work is to design a permanent magnet synchronous machine with high power density for hybrid vehicles with the DE-REX powertrain. Furthermore, construction and measurement results of a prototype machine are presented in this thesis. At the end, possible downsizing methods of a slightly over-dimensioned electric machine will be discussed.

Motivation

Angesichts der Volatilität der Ölpreise und der Reduzierung der CO_2-Emissionen im Einklang mit der United Nations Framework Convention on Climate Change (UNFCCC) erweisen sich Elektrofahrzeuge als praktikable Lösungen für CO_2-armes Fahren. Elektrofahrzeuge haben jedoch immer noch viele Schwierigkeiten, herkömmliche Fahrzeuge mit fossilen Brennstoffen zu ersetzen. Aufgrund der relativ geringen Energiedichte der Lithium-Ionen-Batterie gegenüber fossilen Brennstoffen und ihrer technischen Grenze haben Elektrofahrzeuge eine relativ kurze Reichweite und eine lange Ladezeit der Batterien. Darüber hinaus sind Elektrofahrzeuge aufgrund der hohen Batteriekosten auf dem Markt zurzeit nicht wettbewerbsfähig. Um diese Nachteile zu überwinden, versuchen Automobilunternehmen u.a., Plug-In-Hybridsysteme und Range-Extender-Antriebe einzusetzen. Der Marktanteil der Elektrohybridfahrzeuge mit diesen Technologien steigt von Jahr zu Jahr deutlich an. Obwohl es sich dabei nicht um ideale Lösungen für emissionsfreie Elektrofahrzeuge handelt, werden diese Übergangslösungen ein wichtiger Beitrag zur Erreichung des deutschen Ziels der CO_2-Reduktion sein.

Der "Doppel-E-Antrieb mit Range Extender (DE-REX)" ist so ein innovatives Antriebskonzept für Elektro- und Hybridfahrzeuge. Der Antriebsstrang besteht aus zwei vergleichsweise kleinen elektrischen Maschinen, zwei Teilgetrieben mit jeweils zwei Gängen und einem Verbrennungsmotor für einen Range Extender. Somit ist es sowohl für rein elektrisches Fahren als auch Hybridfahren geeignet, um die Reichweite zu erhöhen und die CO_2-Emissionen zu reduzieren. Das Hauptziel dieser Arbeit ist die Auslegung einer permanenterregten Synchronmaschine mit hoher Leistungsdichte für Hybridfahrzeuge mit dem DE-REX-Antriebsstrang. Weiterhin werden in dieser Arbeit die Konstruktion und Messergebnisse eines Maschinenprototyps vorgestellt. Am Ende werden mögliche Downsizing-Methoden dieser etwas überdimensionierten elektrischen Maschine diskutiert.

Abstract

In this work, design processes of an electric machine with a high power to weight and volume ratios via an intensified water jacket cooling for the DE-REX powertrain are presented. For a high-power density, a 6-pole interior permanent magnet synchronous machine with a continuous power of 24 kW and a short-term power of 48 kW (30 s, overload) at rated speed of 4167 min^{-1} was designed. The electric machine rotates up to a maximum speed of 10000 min^{-1} with field weakening control to achieve the demanded maximum speed of 180 km/h at hybrid driving mode. A prototype electric machine and four further electric machines for the DE-REX powertrain (two for the powertrain test bench and two for the prototype vehicle) were constructed and tested in the *Institute of Electrical Energy Conversion* at TU Darmstadt. Based on the measurement results, the electromagnetic design of the machines was validated and the analytically and numerically calculated losses were verified. In addition, measured efficiency maps of the prototype machine with the corresponding inverter were created over the entire torque-speed range. The functionality test of the DE-REX powertrain was performed at the individual electric machine test bench with two driving cycles, the NEDC and the WLTC. The effectiveness of the chosen cooling system was verified by temperature measurements. The measured temperatures showed that the machine has certain thermal reserve for the used Thermal Class H. Thus, the machine could produce more power to avoid high thermal reserve and to increase thermal utilization. Also, it is possible to downsize the machine to avoid big thermal reserve. In this work, two possible downsizing methods are presented; increasing electromagnetic and thermal utilization by reducing active volume of electric machine and using hair wave winding which has higher slot fill factor. The redesigned machine with round wire lap winding reduced an active volume by 23 %. Using a hairpin lap winding, the redesigned machine had an active volume reduction of 32 %, compared to the prototype machine.

Kurzfassung

In dieser Arbeit werden die Konstruktionsprozesse einer elektrischen Maschine mit einem hohen Leistung-Masse-Verhältnis und hohen Leistung-Volumen-Verhältnis über eine intensivierte Wassermantelkühlung für den DE-REX-Antriebsstrang vorgestellt. Für eine hohe Leistungsdichte wurde eine 6-polige innenliegende permanentmagnetische Synchronmaschine mit einer Dauerleistung von 24 kW und einer maximalen Kurzzeitleistung von 48 kW (30 s, Überlast) bei der Nenndrehzahl von 4167 min^{-1} ausgelegt. Die elektrische Maschine dreht bis zu einer Höchstdrehzahl von 10000 min^{-1} mit Feldschwächungssteuerung, um die geforderte Fahrzeug-Höchstgeschwindigkeit von 180 km/h im Hybridbetrieb zu erreichen. Am Institut für Elektrische Energiewandlung der TU Darmstadt wurden ein Prototyp einer Elektromaschine und vier weitere Elektromaschinen für den DE-REX-Antriebsstrang (zwei für den X-in-the-Loop-Prüfstand und zwei für das Prototyp-Fahrzeug) gebaut und getestet. Basierend auf den Messergebnissen wurde die elektromagnetische Auslegung der Maschinen validiert und die analytisch und numerisch berechneten Verluste messtechnisch verifiziert. Darüber hinaus wurden gemessene Wirkungsgradkennfelder der Prototypmaschine mit dem entsprechenden Umrichter über den gesamten Drehmoment-Drehzahlbereich erstellt. Der Funktionstest des DE-REX-Antriebsstrangs wurde auf dem einzelnen Elektromaschinenprüfstand mit zwei Fahrzyklen, dem NEFZ und dem WLTC durchgeführt. Die Wirksamkeit des gewählten Kühlsystems wurde durch Temperaturmessungen überprüft. Die gemessenen Temperaturen zeigten, dass die Maschine eine gewisse Temperaturreserve für die eingesetzte Wärmeklasse H aufweist. Somit könnte die Maschine mehr Leistung erzeugen, um thermisch mehr zu nutzen. Außerdem ist es möglich, die Maschine zu verkleinern, um große thermische Reserven zu vermeiden. In dieser Arbeit werden zwei mögliche Downsizing-Methoden vorgestellt: die Erhöhung der elektromagnetischen und thermischen Ausnutzung durch Reduzierung des aktiven Volumens der elektrischen Maschine und die Verwendung von Hairpin-Wicklung mit höherem Füllfaktor. Die neu ausgelegte Maschine mit Runddrahtwickelung reduzierte das aktive Volumen um 23 %. Durch die Verwendung von Hairpin-Wicklung wies die neu ausgelegt Maschine eine aktive Volumenreduzierung von 32 % gegenüber der Prototypmaschine auf.

Erklärungen laut Promotionsordnung

§ 8 Abs. 1 lit. c PromO

Ich versichere hiermit, dass die elektronische Version meiner Dissertation mit der schriftlichen Version übereinstimmt.

§ 8 Abs. 1 lit. d PromO

Ich versichere hiermit, dass zu einem vorherigen Zeitpunkt noch keine Promotion versucht wurde. In diesem Fall sind nähere Angaben über Zeitpunkt, Hochschule, Dissertationsthema und Ergebnis dieses Versuchs mitzuteilen.

§ 9 Abs. 1 PromO

Ich versichere hiermit, dass die vorliegende Dissertation selbstständig und nur unter Verwendung der angegebenen Quellen verfasst wurde.

§ 9 Abs. 2 PromO

Die Arbeit hat bisher noch nicht zu Prüfungszwecken gedient.

Datum und Unterschrift

Table of Content

Table of Content ii

Symbols in Formulas and Abbreviations vi

1. Introduction 13

1.1 Motivation 13

1.2 DE-REX powertrain concepts 15

1.3 Driving modes 16

1.3.1 Pure electric drive 16

1.3.2 Hybrid drive 17

1.4 Potential for electric energy saving of DE-REX powertrain 18

1.5 Vehicle parameters 21

1.6 Electric machine parameter 22

1.7 Thermal Classes and temperature limits 23

1.8 Overview of project DE-REX 24

1.9 Outline 25

2. Design of permanent magnet synchronous machine 27

2.1 Electromagnetic design of PMSM 27

2.1.1 Select machine dimensions 27

2.1.2 Stator winding design 28

2.2 Calculation of air-gap flux density 34

2.3 Torque generation and control strategies 37

2.4 Reduction of cogging torque and torque ripple 40

2.4.1 Step-skewed rotor 41

2.4.2 Fractional number of stator slots per pole and phase 45

2.4.3 Numerical calculation with FEM software 48

2.5 Sudden short-circuit current and torque 51

2.5.1 Analytical calculation of sudden short-circuit current and torque 51

2.5.2 Numerical calculation of sudden short-circuit current and torque 54

2.5.3 Calculation results of sudden short-circuit current and torque 55

2.6 Thermal design of the electric machine 59

2.6.1 Material properties for thermal analysis 60

2.6.2 Cooling system of the electric machine 61

2.6.3 Lumped parameter thermal network model 62
2.6.4 Numerical thermal model with FEM software JMAG 64
2.6.5 Temperature rise calculation 65
2.7 Mechanical design of the electric machine 69
3. Loss components and efficiency calculation 73
3.1 DC ohmic losses in stator winding 73
3.2 Additional eddy current losses in stator winding 75
3.3 Iron losses 79
3.4 Mechanical losses 83
3.4.1 Air friction losses 84
3.4.2 Bearing losses 85
3.5 Eddy current losses in magnets 86
3.6 Losses in the inverter 87
3.6.1 Conduction losses in IGBT and diode 88
3.6.2 Switching losses in IGBT and diode 89
3.7 Electromagnetic calculations for the electric machine at load operations 90
3.8 Loss distribution map and efficiency map 96
4. Construction of the electric machines and test bench for the individual measurement 99
4.1 Prototype machine 99
4.1.1 Stator of the prototype machine 99
4.1.2 Rotor of the prototype machine 102
4.2 Construction of the electric machines for the DE-REX powertrain 104
4.3 Test bench for individual measurement of the prototype machine 107
4.4 Measurement devices 110
5. Measurement of the prototype electric machine 113
5.1 Generator no-load operation 113
5.2 Generator short-circuit operation 118
5.3 Motor load operation 119
5.3.1 Load operations with industrial inverter ServoOne 121
5.3.2 Temperature rise with load operations with the industrial inverter 122
5.3.3 Load operations with DMC524 inverter 126
5.3.4 Temperature rise with load operation with the DMC524 inverter 130
5.4 Measured efficiency map of the electric machine 132

5.5 Demagnetization test at sudden short circuit after generator no-load 135
5.6 Measurement of DE-REX powertrain with driving cycles at test bench for individual measurement of electric machines 137
5.6.1 Test results with the NEDC 138
5.6.2 Test results with the WLTC 140
6. Vehicle simulation model 143
6.1 Structure of vehicle simulation model 144
6.2 Transmission for the DE-REX powertrain 145
6.3 Driving cycles module 146
6.3.1 New European Driving Cycle (NEDC) 147
6.3.2 HYbrid technology approaching efficient Zero Emission Mobility (HYZEM) highway cycle 148
6.3.3 Worldwide harmonized Light vehicles Test Cycle (WLTC) for a class 3 vehicle 149
6.4 Driving resistances module 150
6.5 Determine driving mode module 151
6.6 Driving strategy with thermal management of both electric machines 153
6.7 Simulation results with both driving strategies 155
6.7.1 Simulation results with NEDC 155
6.7.2 Simulation results with WLTC 159
6.7.3 Simulation results with HYZEM-highway driving cycle 162
7. Downsizing possibilities for the prototype machine 165
7.1 Machine downsizing by increasing thermal utilization via decreasing active volume of electric machine 166
7.1.1 Shortening of active iron length of the machine 166
7.1.2 Redesign of electric machine with increased electro-magnetic utilization and thermal utilization 168
7.2 Machine downsizing by increasing the slot fill factor with a hairpin winding 171
7.2.1 Hairpin winding 171
7.2.2 Increase of slot fill factor with hairpin winding for reduction of active mass of electric machine 172
8. Summary and conclusions 179
Appendix A. Drawings of electric machine components 183
Appendix B. Material properties 194

Appendix C. Thermal network model 196

Appendix D. Analytical calculation of short-circuit current and torque 201

Symbols in Formulas and Abbreviations

Symbols in formulas

Symbol	*Unit*	*Description*
A	A/cm	Current loading of electric machine
A_{cu}	mm^2	Cross section of conductor per turn
A_{f}	m^2	Facing surface of vehicle
A_{channel}	mm^2	Cross section of the cooling channel
A_{mot}	m^2	Machine cooling surface
A_{str}	mm^2	Cross section of a strand
A_{so}	mm^2	Slot opening area
A_{Q}	mm^2	Slot area
a	-	Parallel branches
a_{i}	-	Number of strands per turn
B	T	Flux density
B_{R}	T	Remanence
$B_{\delta,1}$	T	Air gap flux density
B_{M}	mm	Magnet segment width
b_{st}	mm	Stator tooth width
$b_{\mathrm{Q,av}}$	mm	Average slot width
B_{str}	mm	Width of equivalent square strand
C	kVA·min/m^3	Electromagnetic utilization (*Esson*'s number)
c	J/(kg·K)	Specific heat capacity
c_{f}	-	Air friction coefficient
c_{Ft}	W/kg	Eddy current loss coefficient
c_{Hy}	W/kg	Hysteresis loss coefficient
c_{w}	-	Drag coefficient
d	mm	Diameter
d_{str}	mm	Diameter of a strand
d_{E}	mm	Skin depth
d_{channel}	mm	Hydraulic diameter of the cooling channel
d_{ro}	mm	Rotor outer diameter

d_{sh}	mm	Shaft diameter
d_{si}	mm	Stator inner diameter
d_{so}	mm	Stator outer diameter
E_{on}	mJ	Turn-on energy loss per pulse (IGBT)
E_{off}	mJ	Turn-off energy loss per pulse (IGBT)
E_{rec}	mJ	Reverse recovery energy per pulse (Diode)
f	Hz	Frequency
f_{r}	-	Roll resistance coefficient
f_{sw}	kHz	Switching frequency
f_{s}	Hz	Fundamental frequency
H	kA/m	Magnetic field strength
H_{cB}	kA/m	Magnetic coercivity
h_{bridge}	mm	Height of rotor iron bridge
h_{sy}	mm	Height of stator yoke
h_{M}	mm	Magnet height
I	A	Current (RMS)
I_{sd}	A	Current in d-axis (RMS)
I_{max}	A	Maximum current (RMS)
I_{N}	A	Nominal current (RMS)
I_{sq}	A	Current in q-axis (RMS)
I_{s1}	A	Stator current (RMS)
I_{sc}	A	Stator current at short circuit (RMS)
i	-	Gear ratio
i_{d}	A	Current in d-axis
i_{q}	A	Current in q-axis
i_{s}	A	Stator current
$i_{\mathrm{s,max}}$	A	Maximum stator current
J	$\mathrm{A/mm^2}$	Current density of electric machine
J	$\mathrm{kg{\cdot}m^2}$	Moment of inertia
k_{f}	-	Slot filling factor
k_{d}	-	Distribution factor
k_{p}	-	Pitching factor
k_{R1}	-	Loss increase factor for 1st order current displacement effect
k_{R2}	-	Loss increase factor for 2nd order current displacement effect

k_{skew}	-	Skew factor
k_{V}	-	Iron loss increase factor
k_{w}	-	Winding factor
L_{d}	mH	Inductance in d-axis
l_{Fe}	mm	Iron stack length
L_{h}	mH	Main inductance
L_{q}	mH	Inductance in q-axis
$L_{\mathrm{s}\sigma}$	mH	Stator leakage inductance
l_{b}	mm	Length of the overhang winding
L_{channel}	mm	Total length of the spiral cooling jacket
L_{M}	mm	Axial length of magnet segment
M	Nm	Torque
M_{e}	Nm	Electromagnetic torque
M_{m}	Nm	Shaft torque
M_{max}	Nm	Maximum torque
M_{N}	Nm	Rated torque
M_{sc}	Nm	Sudden short-circuit torque
$\widehat{M}_{\mathrm{cog}}$	Nm	Cogging torque amplitude
m	-	Number of phases
m	-	Modulation index
m	kg	Mass
m_{act}	kg	Active mass
m_{T}	-	Number of vertically placed wires in one slot
N_{c}	-	Number of turns per coil
N_{cog}	-	Period of the cogging torque in a slot pitch rotation
N_{s}	-	Number of turns per phase
N_{step}	-	Number of step skew
n	min^{-1}	Rotating speed
n_{h}	-	Number of horizontally placed wires in one slot
n_{max}	min^{-1}	Maximum rotational speed
n_{v}	-	Number of vertically placed wires in one slot
P_{d}	W	Total losses
P_{d0}	W	No-load losses
$P_{\mathrm{d,ad}}$	W	Stray load losses

$P_{\mathrm{d,cu,AC}}$	W	Copper losses considering the effect of current displacement
$P_{\mathrm{d,cu,ad}}$	W	Additional eddy current losses
$P_{\mathrm{d,cu,DC}}$	W	DC resistive losses
$P_{\mathrm{d,cu,WO}}$	W	Copper losses in the PM machine winding overhang
$P_{\mathrm{d,cu,slot}}$	W	Copper losses in the PM machine winding in slots
$P_{\mathrm{d,inv}}$	W	Losses in inverter
$P_{\mathrm{d,PWM}}$	W	Additional motor losses due to PWM inverter supply
P_{e}	kW	Electromagnetic power
$P_{\mathrm{d,Fe,r}}$	W	Losses in rotor iron
$P_{\mathrm{d,Fe,st}}$	W	Iron losses in stator teeth
$P_{\mathrm{d,Fe,sy}}$	W	Iron losses in stator yoke
$P_{\mathrm{d,fr,air}}$	W	Air friction losses
$P_{\mathrm{d,M}}$	W	Losses in magnets
P_{max}	kW	Maximum power
P_{N}	kW	Rated output power (motor)
p	-	Number of pole pair
p_{Fe}	W/kg	Specific iron loss
p_{u}	-	Number of pole pair of a base winding
Q_{u}	-	Slot number of a base winding
Q_{s}	-	Slot number
q	-	Number of slots per pole per phase
Re	-	Reynolds number
R_{m}	MPa	Material ultimate tensile strength
$R_{\mathrm{p0.2}}$	MPa	Material yield strength
R_{s}	m Ω	Stator winding resistance per phase
r	mm	Radius
S_{N}	kVA	Rated apparent power
t	s	Time
Ta	-	*Taylor* number
U_{DC}	V	Inverter DC-link voltage
U_{channel}	mm	Circumference of the cooling channel
U_{i}	V	Induced voltage (RMS)
U_{LL}	V	Line-to-line voltage (RMS)
U_{p0}	V	Induced voltage (RMS)

$U_{\mathrm{s,max}}$	V	Maximum phase voltage (RMS, Y)
$U_{\mathrm{s,ph}}$	V	Phase voltage (RMS)
u_{s}	V	Voltage
$u_{\mathrm{s,max}}$	V	Voltage limit
$\dot{V}$	l/min	Coolant flow rate
W	m	Slot pitch
W	Ws	Energy
$\hat{w}$	%	Torque ripple
X_{d}	Ω	Reactance in d-axis
X_{q}	Ω	Reactance in q-axis
α	1/K	Temperature coefficient of resistivity
α	W/(m^2·K)	Heat transfer coefficient
α_{k}	W/(m^2·K)	Heat transfer coefficient at cooling channel surface
β^*	°	Current angle respect to q-axis
δ	mm	Mechanical air gap length
φ	rad	Phase angle
η	%	Efficiency
κ	S/m	Conductivity
κ_{M}	S/m	Magnet conductivity
$\kappa_{\mathrm{M,eff}}$	S/m	Modified magnet conductivity
λ	-	Rotational inertia constant
λ	W/(m·K)	Thermal conductivity
$\lambda_{\mathrm{coolant}}$	W/(m·K)	Thermal conductivity of coolant
μ	-	Harmonic order
$\mu_{\mathrm{M,rel}}$	-	Relative permeability of the magnet
μ_0	-	Permeability in vacuum
μ_{Fe}	-	Relative permeability of iron lamination
ν	-	Harmonic order
ν_{coolant}	m^2/s	Kinematic viscosity of coolant
ϑ	°C	Temperature
ϑ_{h}	°C	Hotspot temperature
ϑ_{amb}	°C	Ambient temperature
ρ	kg/m^3	Material mass density
σ_{Mises}	MPa	*von Mises* stress

σ_t	MPa	Tangential tensile stress
τ_p	-	Pole pitch
τ_Q	-	Slot pitch
Ω	rad/s	Rotational angular speed
ω	rad/s	Electric frequency
ω_s	rad/s	Electric frequency of the machine
Ψ_M	Vs	Magnet flux linkage

Abbreviations

AMT	Automated Manual Transmission
BLDC	Brushless DC motor
C	Coupling
CAD	Computer Aided Design
CAN	Controller Area Network
CO_2	Carbon dioxide
DE	Driving End
DE-REX	Doppel-E-Antrieb mit Range Extender
ECE15	Urban driving cycle
EM	Electric Machine
EMF	ElectroMotive Force
EU	European Union
EUDC	Extra-Urban Driving Cycle
EVID	Electric Vehicle IDentification
FEM	Finite Element Method
FOC	Field Oriented Control
HiL	Hardware-in-the-Loop
HYZEM	HYbrid technology approaching efficient Zero Emission Mobility
ICE	Internal Combustion Engine
IGBT	Insulated Gate Bipolar Transistor
IPMSM	Interior Permanent Magnet Synchronous Machine
MTPA	Maximum Torque per Ampere
MTPV	Maximum Torque per Voltage
NDE	Non-Driving End
NEDC	New European Driving Cycle

NdFeB	Neodymium-iron-boron
OP	Operating Point
PID	Proportional Integral and Derivative
PM	Permanent Magnet
PMSM	Permanent Magnet Synchronous Machine
PWM	Pulse Width Modulation
REX	Range EXtender
RMS	Root Mean Square
SOC	State of Charge
SPMSM	Surface Permanent Magnet Synchronous Machine
STM	Sub-Transmission
UDDS	Urban Dynamometer Driving Schedule
UNFCCC	The United Nations Framework Convention on Climate Change
VCU	Vehicle Control Unit
WLTC	Worldwide harmonized Light vehicles Test Cycle
WLTP	Worldwide harmonized Light vehicles Test Procedure

1. Introduction

1.1 Motivation

Since the Industrial Revolution, mankind has advanced civilization at a completely different pace than before the Industrial Revolution. In this process, large amounts of fossil fuels such as coal and oil have been consumed. This mass consumption of fossil fuels has inevitably led to the massive release of greenhouse gases such as carbon dioxide (CO_2), which is known to be the most significant factor in global warming and climate change.

Through the United Nations Framework Convention on Climate Change (UNFCCC) in 2015, countries around the world set and implemented carbon emission reduction targets. The European Union, including Germany, aims to reduce carbon emissions by at least 40 % compared to 1990 levels by 2030, and by at least 80 % by 2050 [1].

In particular, the amount of carbon dioxide produced by transport (including aviation and shipping) accounts for 27 % of the total carbon dioxide emissions produced in Europe, of which CO_2 emissions generated by road transport account for almost 72 % [2]. As a result, many investments have been made in the development of electric vehicles, which are eco-friendly, and policy supports are also increasing.

In the 2010s, due to the long-term risk of depletion of fossil fuels and the instability of oil prices, electric cars became recognized as vehicles that are economically viable in addition to being eco-friendly. And with electric charging using renewable energy, electric vehicles are expected to become environmentally sustainable and economical road transports.

Experts have said that Germany needs to supply 10 million electric vehicles, including hybrid vehicles, by 2030 to meet its climate targets in line with the UNFCCC [3]. However, the achievements so far are insufficient. The German government had aimed to have a million electric vehicles on the road by 2020, but currently only 200 000 electric vehicles are on German roads [3].

This is because electric vehicles still have significant disadvantages compared with conventional fossil fuel vehicles. Due to lithium-ion batteries, which have relatively lower energy densities than conventional fossil fuels, and technical restraints of battery systems, electric vehicles have short driving ranges and long charge times. In addition, since batteries, which are core components of electric vehicles, are expensive, electric vehicles are not competitive in price in the market compared to conventional fossil fuel vehicles.

Therefore, the technical innovation of batteries is very important for the diffusion of electric vehicles. Many companies and researchers are actively investing in researching batteries with higher energy density and faster charge rate at lower prices. However, it is unlikely that the emergence of innovative battery technologies will solve these problems of electric vehicles in the short term.

As a result, until that innovative technological leap of battery systems, auto companies are trying to overcome the shortcomings of electric vehicles in various other ways: fuel-cell vehicles, battery swap technology, plug-in hybrid vehicles and electric vehicles with a range extender [4]. These latter two technologies, in particular, have already been introduced into the automobile industry. The market share of electric vehicles with these technologies is rapidly increasing year by year. Although they are not ideal technology for electric vehicles with zero emissions, these transitional solutions will be a major force in achieving Germany's goal of running 10 million electric vehicles, including hybrid vehicles, on German roads by 2030 to keep to the UNFCCC.

Many automobile companies have already launched electric vehicles with a range extender to increase the driving range, such as the Chevrolet Volt, the BMW i3-REX and the Nissan Note e-Power range extender. This concept combines an electric powertrain, complete with an electric motor and a battery system, with a downsized internal combustion engine (ICE) and a corresponding electric generator. In this case, the ICE does not directly drive the vehicle but turns the electric generator to supply electric energy directly to the electric driving motor or to charge the battery for overcoming low battery capacity. Another method to increase driving range is using a multi-speed transmission between the electric motors and wheels. In this way, operating points of the electric machine can be shifted to higher-efficiency operation regions within the torque-speed range of the drive. Recent studies have shown that multi-speed transmissions increase the driving range and improve starting torque and maximum speed to a certain extent [5, 6, 7].

Twin electric drive, or *Doppel-E-Antrieb* in German, is an innovative powertrain concept that has a two-speed transmission and two electric machines [75]. Twin electric drive in combination with an additional ICE for a range extender, or *Doppel-E-Antrieb mit Range Extender* (DE-REX), provides both pure electric drive and hybrid drive [84]. Due to the special features of the DE-REX powertrain, such as multiple operations in electric driving mode, seamless gear shifting and high flexibility in hybrid driving mode, it offers great potential with regard to increased driving range, reduced fuel consumption and enhanced driving comfort.

1.2 DE-REX powertrain concepts

The DE-REX is an innovative powertrain concept for electric and hybrid drive. The layout and 3D CAD model of the DE-REX powertrain concept are shown in Fig. 1.1 and Fig. 1.2, respectively. Instead of a large electric machine with twice the rated power, the powertrain has two identical electric machines (EM1 and EM2) with reduced rated power. They can work as traction motors or as generators. Each electric machine is coupled with two parallel two-speed sub-transmissions (STMs) with two gear ratios (i_1 and i_2). Thus, the powertrain can produce a high starting torque of 3300 Nm with a first-gear ratio $i_1 = 15$ and a high maximum speed of $v_{\text{veh}} = 180$ km/h with a second-gear ratio $i_2 = 6$. The sub-transmissions are operated with an automated manual transmission (AMT) technology with spur gears and an electromechanical gear shifting system via dog clutches. The AMT is simple, cheap and efficient compared to other transmission technologies, such as automatic transmissions and dual clutch transmissions [84].

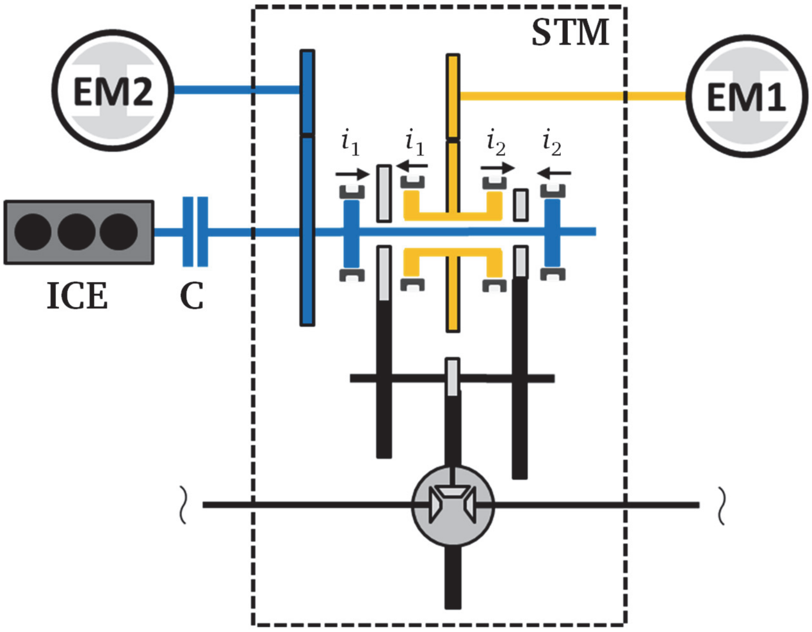

Fig. 1.1: Layout of DE-REX powertrain concept. EM: electric machine, STM: sub-transmission, ICE: internal combustion engine, C: coupling

Moreover, an additional three-cylinder turbocharged ICE with a maximum power of 65 kW is attached to the sub-transmission via a friction coupling (C). Thus, the powertrain can be operated in both parallel and series hybrid driving mode.

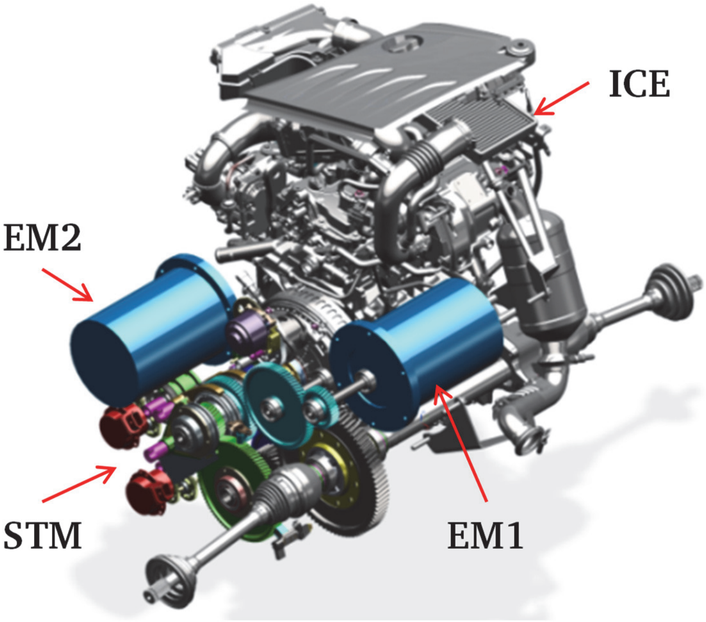

Fig. 1.2: CAD model of DE-REX powertrain. EM: electric machine, STM: sub-transmission, ICE: internal combustion engine [84]

1.3 Driving modes

1.3.1 Pure electric drive

The DE-REX powertrain uses two small identical electric machines instead of one large electric machine with double rated power. Typically, due to iron losses, a high-power electric machine has a lower efficiency than a low-power electric machine at partial loads and below rated speed. Thus, when the vehicle is driven with partial load at low speed (e.g. driving in downtown), only one electric machine is operating as a motor to propel the vehicle, while the other electric machine is switched off electrically and also mechanically by the STM, hence achieving increased powertrain efficiency. In addition, by using two-speed transmissions at each electric machine, the vehicle can be driven more efficiently by shifting the operating points to higher-efficiency regions.

In pure electric driving mode, the vehicle with the DE-REX powertrain can be driven by one electric machine only or by both electric machines simultaneously (Fig. 1.3). The gear ratio of each STM can be selected independently from the other STM. Each electric machine has two possible driving modes with two gear ratios, thus in pure electric driving mode there are eight possible driving modes in total.

During pure electric driving mode, the operating strategy in the vehicle control unit (VCU) has to decide the best combination of electric machines and their gear ratios. And in the case of pure electric driving mode with both electric machines, the necessary torque distribution between two electric machines can be determined. The best combination depends on several parameters such as driver demands, overall powertrain efficiency or thermal conditions of both electric machines. Therefore, different operating strategies were investigated in [8] and [79].

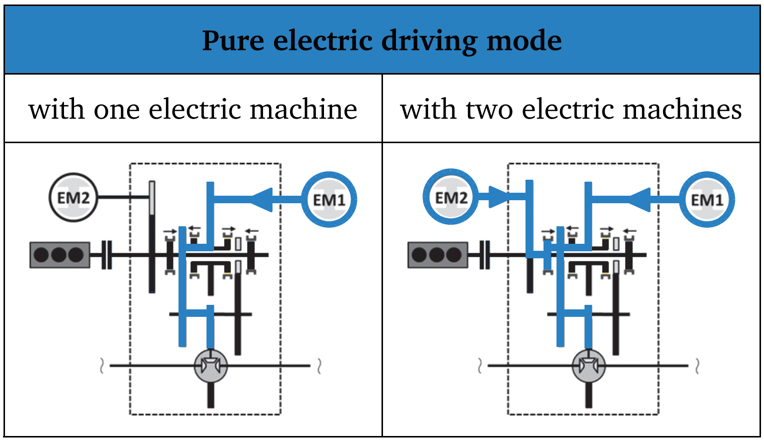

Fig. 1.3: Pure electric driving modes of DE-REX powertrain

1.3.2 Hybrid drive

When the state of charge (SOC) of the battery is low, the ICE will be coupled with the second STM via the mechanical coupling (C), either generating electric energy with the second electric machine (EM2) in series-hybrid mode or directly driving the vehicle in parallel-hybrid mode. In hybrid driving mode, the DE-REX powertrain has three superordinated driving modes: parallel-hybrid driving mode with an electric machine, parallel-hybrid driving mode with two electric machines and series-hybrid driving mode (Fig. 1.4). More specifically, 10 parallel driving modes are possible with consideration of the two gear ratios of each STM.

During parallel-hybrid driving mode, like pure electric mode, the powertrain can operate one electric machine or both electric machines with the ICE. In this driving mode, the VCU can decide to charge the battery by shifting up the ICE operating point for increasing the ICE efficiency or to discharge the battery for driving the electric machines by shifting down the ICE operating point for driving comfort. Due to lower energy losses during energy conversion in parallel-hybrid mode, when the operating strategy aims at highest powertrain efficiency, the parallel-hybrid driving modes in the DE-REX powertrain are selected most frequently by the VCU [9].

In series-hybrid driving mode, the first electric machine (EM1) drives the vehicle with a proper gear ratio. Meanwhile, the ICE drives the second electric machine (EM2) as a generator for converting the ICE power into electric power. Depending on the vehicle load and the selected driving mode with the ICE power, the generated electric power transfers directly to EM1 or charges the traction battery. Consequently, the powertrain can achieve both better driving performance and longer driving ranges.

Hybrid driving mode		
Parallel-hybrid driving with one electric machine	Parallel-hybrid driving with two electric machines	Series-hybrid driving
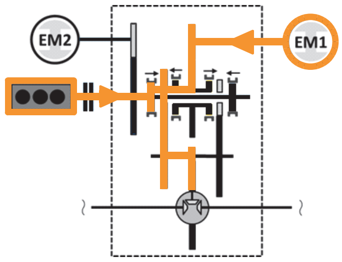	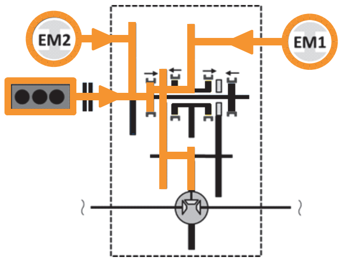	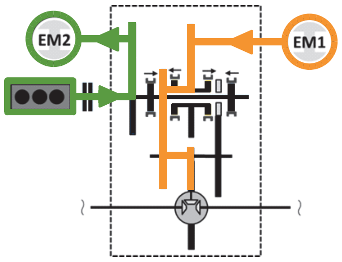

Fig. 1.4: Parallel- and series-hybrid driving modes of DE-REX powertrain

1.4 Potential for electric energy saving of DE-REX powertrain

The DE-REX powertrain shows high efficiency in both pure electric drive and hybrid drive. To clarify the energy-saving benefit of the two-speed transmission and the downsized electric machines, the electrical energy consumption of the DE-REX powertrain concept (2EMs2G) was compared to the conventional powertrain concept, which has one central electric machine and a single gear ratio (1EM1G). For the electric machine with high power, the scaled efficiency map from the electric machine with low power was applied. For estimating the electric energy consumption of each powertrain, the New European Driving Cycle (NEDC), the Urban Dynamometer Driving Schedule (UDDS) and the Worldwide harmonized Light vehicles Test Cycle (WLTC) were used. To ensure a meaningful comparison, all powertrain concepts had the same requirements for a final speed of 180 km/h, a minimum required vehicle starting torque of 2500 Nm and a maximum rotation speed of the electric machine of 10000 min^{-1}. To achieve these requirements with the conventional powertrain concept (1EM1G), the vehicle needed an electric machine with maximum power of 169 kW and a gear ratio of $i = 6.45$. It had excessively high power for the required driving power of both driving cycles. Thus, the electric machine was not used efficiently. As a result, the 1EM1G powertrain showed high energy consumption of 14.7 kWh / 100 km in the NEDC, 14.4 kWh / 100 km in the UDDS and 16.9 kWh / 100 km in the WLTC. Using a two-speed transmission with one electric machine (1EM2G), the first gear ratio $i_1 = 14.81$ was used to produce high starting torque, and the second gear ratio $i_2 = 5.93$ was used to drive the vehicle to the maximum speed of 180 km/h. Thus, the required electric power of the electric machine was reduced to 96 kW. The energy consumption was 12.7 kWh / 100 km in the NEDC, 12.0 kWh / 100 km in the UDDS and 15.0 kWh / 100 km in the WLTC, which corresponded to reductions of 14 % in the NEDC, 17 % in the UDDS and 11 % in the WLTC (Table 1.1). This is because of the shift of operating points through two gear ratios, which meant the electric machine was used more efficiently. In reality, transmission losses can be further reduced with a smaller maximum torque of the electric machine [75]. The DE-REX powertrain concept (2EMs2G) further reduces energy consumption by 2 % in the NEDC, 4 % in the UDDS and 3 % in the WLTC. This is mainly due to the downsized electric machines. This comparison of the simulation results illustrates the potential for electric energy savings to be increased with the DE-REX powertrain.

Table 1.1 Comparison of calculated*) energy consumption of electric vehicles with different powertrain concepts

Powertrain concepts	**1 electric machine with single gear ratio (1EM1G)**	**1 electric machine with two gear ratios (1EM2G)**	**2 electric machines with two gear ratios (2EMs2G)**
	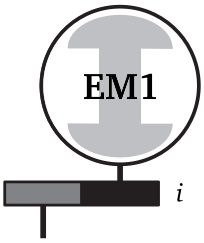	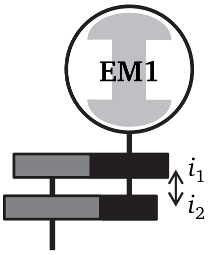	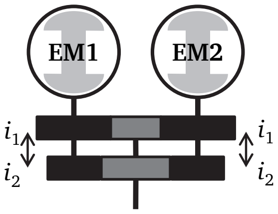
Peak power EM1	169 kW	96 kW	48 kW
Gear ratios	i = 6.45	i_1=14.81, i_2=5.93	i_1=14.81, i_2=5.93
Peak power EM2	-	-	48 kW
Gear ratios	-	-	i_1=14.81, i_2=5.93
Energy consumption in NEDC	14.7 kWh/100km	12.7 kWh/100km	12.4 kWh/100km
Energy consumption in UDDC	14.4 kWh/100km	12.0 kWh/100km	11.5 kWh/100km
Energy consumption in WLTC	16.9 kWh/100km	15.0 kWh/100km	14.5 kWh/100km

*) With vehicle parameters: total mass $m = 1780$ kg, air drag coefficient $c_\mathrm{w} = 0.26$, front area $A_\mathrm{f} = 2.423$ m^2, air density at 20 °C $\rho_\mathrm{air} = 1.2$ kg/m^3, dynamic wheel radius $r_\mathrm{dyn} = 0.308$ m, rolling resistance coefficient $f_\mathrm{r} = 0.011$, rotating mass adding factor Δm=0.1 [71]

1.5 Vehicle parameters

The DE-REX powertrain was designed for a mid-size compact vehicle. As a reference vehicle, a Mercedes-Benz B class vehicle was selected. For selecting powertrain parameters, specifications with some essential requirements for the vehicle and the powertrain were defined, and they are listed in Table 1.2. The parameters for the driving simulation based on the reference vehicle are listed in Table 1.3.

Table 1.2 Requirements for a compact vehicle with DE-REX powertrain

Property		Requirement
CO_2 emission		< 27 g/km
Pure electric driving range		> 60 km
Maximum speed in pure electric driving		> 140 km/h
Maximum speed in pure ICE driving		> 120 – 140 km/h
Maximum speed in hybrid driving		> 180 km/h
Starting torque on the wheels		> 2500 Nm
Acceleration	60 – 100 km/h	< 8.8 s
	80 – 120 km/h	< 14.5 s
	0 – 100 km/h	9.3 – 11.9 s

Table 1.3 Vehicle parameters for the driving simulation

Parameter		Value	Comment
Vehicle mass	m_{veh}	1780 kg	Kerb weight: 1510 kg, Battery weight: 200 kg, One driver weight: 70 kg
Drag coefficient	c_{w}	0.26	From Mercedes-Benz B class
Facing surface of the vehicle	A_{f}	2.432 m^2	From Mercedes-Benz B class
Dynamic radius of tyre	r_{tyre}	0.308 m	Tyre 195/65 R15

1.6 Electric machine parameter

As a drawback, the DE-REX powertrain is rather complex and takes up much space in the vehicle. All the components, an ICE, two electric machines with corresponding inverters and two parallel two-speed sub-transmissions, must be installed in the engine compartment. Thus, the size of electric machine must be compact, which means that the electric machine needs high power density. Due to lack of horizontal space in the engine compartment, each electric machine must be shorter than 250 mm. Additionally, both inverters are located above the electric machines, thus the maximum outer diameter of the electric machine is limited to 175 mm. Based on the results of the optimization method from the previous projects *EVID* (Identification of optimal powertrain for electric vehicles) [10] and *Doppel-e-Antrieb* [75] by the Institute of Electrical Energy Conversion (EW) and the Institute for Mechatronic Systems in Mechanical Engineering (IMS) at Technische Universität Darmstadt, the boundary conditions of the electric machine were specified with the requirements of the DE-REX powertrain (Table 1.2). For steady-state operations, the rated power per each electric machine should be $P_{\mathrm{N}} = 24\,\mathrm{kW}$, which corresponds to a rated torque of $M_{\mathrm{N}} = 55\,\mathrm{Nm}$ and a rated speed of $n_{\mathrm{N}} = 4167\,\mathrm{min}^{-1}$. The maximum power of $P_{\max} = 48\,\mathrm{kW}$ was definded by a 100 % overload capacity ($M_{\max} = 110\,\mathrm{Nm}$) at rated speed with a short-term operation (S2 – 30 s). In order to meet the required maximum speed of $v_{\mathrm{veh,max}} = 180\ \mathrm{km/h}$, the maximum rotation speed of the electric machine was set to $n_{\max} = 10000\,\mathrm{min}^{-1}$. Based on these requirements, three operating points (OPs) were defined in Table 1.4 and Fig. 1.5.

Table 1.4 Required operating points (OPs) for the electric machine

	OP1	**OP2**	**OP3**
Operating mode	Overload condition S2 – 30 s	Rated operation S2 – 30 min	Field weakening range S2 – 30 s
Power	48 kW	24 kW	48 kW
Torque	110 Nm	55 Nm	45.8 Nm
Rotation speed	$4167\ \mathrm{min}^{-1}$	$4167\ \mathrm{min}^{-1}$	$10000\ \mathrm{min}^{-1}$

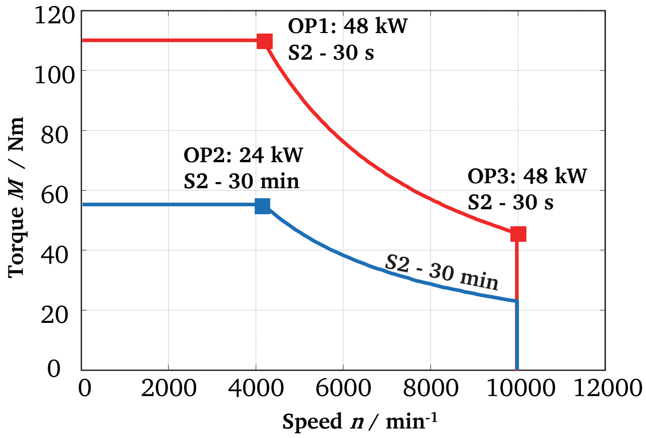

Fig. 1.5: Torque-speed characteristic curve of the electric machine with the required operating points

1.7 Thermal Classes and temperature limits

Losses in electric machines produce heat and increase temperature in winding and insulation. According to *Arrhenius*' law, the chemical degradation process of insulation materials accelerates exponentially with temperature [11]. Since the temperature of insulation materials is the predominant factor for the ageing of the insulation system, the different Thermal Classes for electrical insulation system with corresponding temperature limits are defined in IEC 60085 [12]. In addition, permissible operating temperature limits of electric machines are defined in IEC 60034 [13], for industrial machines, and in IEC 60349 [14], for traction machines (Table 1.5). One of the major differences of IEC 60034 for industrial machines to IEC 60349 for traction machine is the limits of temperature rise corresponding to the maximum temperature limit.

Table 1.5 Limits of temperature rise of AC stationary windings of synchronous machines in both standards IEC 60034 and IEC 60349 [13, 14]

Standards	**Thermal Class of insulation system**			
	130 (B)	**155 (F)**	**180 (H)**	**200**
IEC 60034-1¹⁾	80 K	105 K	125 K	-
IEC 60349-2	130 K	155 K	180 K	200 K

¹⁾: AC windings of machine having outputs above 600 W (or VA) except AC windings which are self-cooled without a fan (IC 40) and/or with encapsulated windings

According to the standard IEC 60034, the temperature limit of the Thermal Class H is $\vartheta_{\max} = 40\ ^\circ\mathrm{C} + 125\ \mathrm{K} + 15\ \mathrm{K} = 180\ ^\circ\mathrm{C}$ with the ambient temperature of 40 °C and the additional hot spot temperature rise of 15 K. With regard to the standard IEC 60349, however, the maximum permissible temperature rise is 180 K. With the ambient temperature of 40 °C, the winding can operate up to 220 °C. Additionally, for totally encapsulated machine, the temperature rise limit increases 10 K, so the temperature limit of the Thermal Class H with IEC 60349 is $\vartheta_{\max} = 40\ ^\circ\mathrm{C} + 180\ \mathrm{K} + 10\ \mathrm{K} = 230\ ^\circ\mathrm{C}$. The reason of high maximum temperature limit in IEC 60349 is the shorter expected life-span of the electric machine for road vehicles. For industrial electric machine, the life-span of ca. 20000 h is expected, however, the electric machine for road vehicle has expected life-span of 4000 – 5000 h.

The electric machines for the powertrain DE-REX are directly exposed to the heat from an ICE in the engine compartment, and thus higher ambient temperature will be expected. Additionally, for the compact design of the powertrain DE-REX, the electric machines are mounted next to the ICE, thus the vibration from the ICE could affect ageing of the insulation system. Therefore, in spite of higher temperature limit from IEC 60349, the standard IEC 60034 is adopted in this thesis for electric machine design.

1.8 Overview of project DE-REX

From the beginning of year 2015 to the middle of year 2018, the cooperative project DE-REX, which was supported by the German Federal Ministry for Economic Affairs and Energy, *Bundesministerium für Wirtschaft und Energie* in German, was conducted with the consortium partners. They consisted of *Institute of Electrical Energy Conversion*, *Institute for Mechatronic Systems in Mechanical Engineering*, *Institute for Internal Combustion Engines and Powertrain Systems* (all of them TU Darmstadt), *Daimler*, *MAGNA-GETRAG* and *AKKA*. During the project, the electric machines and the transmission system were designed and two complete DE-REX powertrain prototypes were constructed. One prototype is running on an X-in-the-Loop-test bench (Fig. 1.6) and the other one was integrated into a demonstrator vehicle (Fig. 1.7). The performance of the DE-REX powertrain had been tested and evaluated.

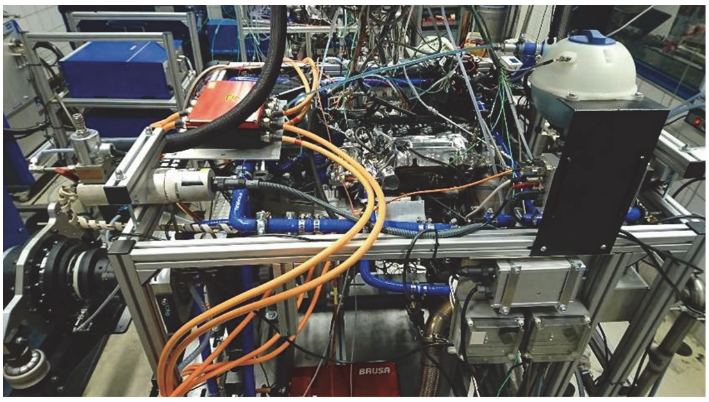

Fig. 1.6: DE-REX powertrain at the X-in-the-Loop test bench

Fig. 1.7: DE-REX powertrain in the demonstrator vehicle (Mercedes Benz B-class)

1.9 Outline

This thesis is focused on design and evaluation of an IPMSM for the DE-REX powertrain. In Chapter 1, the DE-REX powertrain concept and its benefits are introduced. For the DE-REX powertrain, an IPMSM with an embedded V-shaped magnet arrangement was designed. The main design step and control strategies for the electric machine are addressed in Chapter 2. Chapter 3 presents all losses in the electric machine: ohmic losses, eddy current losses in the stator winding, iron losses, mechanical losses, additional eddy current losses in magnets, and losses in the inverter. With these losses, the efficiency maps of the electric machine and of the electric system are introduced in the same chapter. In Chapter 4, all steps to construct a prototype electric machine and four further electric machines for the DE-REX powertrain are described. Additionally, the test bench for the individual measurement of the prototype machine is presented. In Chapter 5, all measurement results are presented. To validate the electromagnetic design of the prototype machine, the generator no-load and short-circuit tests are performed and discussed in the same chapter. Vehicle driving simulation models are introduced in Chapter 6 to investigate functionalities and energy flow of the DE-REX powertrain. In addition, a new operation strategy is introduced to achieve further energy saving and to avoid unwanted thermal derating of electric machines in the same chapter. Given the large thermal reserve of the prototype electric machine, two possible methods for downsizing the electric machine are presented in Chapter 7. And two downsized electric machine designs are presented and the calculation results of them are compared with the prototype electric machine. The results of this thesis are summarized and concluded in Chapter 8.

2. Design of permanent magnet synchronous machine

In this chapter, the design of the permanent magnet synchronous machine is discussed.

2.1 Electromagnetic design of PMSM

2.1.1 Select machine dimensions

The stator inner diameter of the machine d_{si} and the active iron stack length of the machine l_{Fe} were determined via *Esson*'s number C, which is calculated (2.1)

$$C = \frac{m \cdot U_{\mathrm{i}} \cdot I_{\mathrm{s,1}}}{d_{\mathrm{si}}^2 \cdot l_{\mathrm{Fe}} \cdot (f/p)}, \tag{2.1}$$

with the number of stator phases m, the induced stator RMS voltage U_{i} per phase due to the rotating fundamental magnetic field and the sine wave stator RMS current $I_{\mathrm{s,1}}$ [15]. Due to the limited space in the engine compartment of the hybrid vehicle, a high-speed machine with high electromagnetic utilization was designed. For a given number of turns per phase N_{s} in the stator winding, the induced voltage per frequency $U_{\mathrm{i}}/f \sim N_{\mathrm{s}} \cdot B_{\delta,1}$ is limited by the magnetic air-gap flux density amplitude $B_{\delta,1}$ to avoid excessive iron saturation on the stator teeth and yoke. Hence, for a given geometry, a high electromagnetic utilization means a high current per phase $I_{\mathrm{s,1}}$. As a first step, considering only the ohmic losses in the stator winding, the thermal utilization of the machine is proportional to the product of the current loading A and the current density per conductor turn in the winding J. Hence, for a high-power density and thus a high electromagnetic utilization, a high thermal utilization $A \cdot J$ is also needed, which requires a strong cooling system. To meet that need, the electric machine was given a water-jacket cooling system with a helical cooling duct. In addition, the winding overhangs were cast in an epoxy-based resin to improve the heat flow from the winding overhang to the water jacket housing. This reduced the temperature in the winding overhangs, which are the hotspots in closed electric machines. Based on this design, an *Esson*'s number of ca. 5 $\mathrm{kVA} \cdot \mathrm{min/m^3}$, which is rather high for such a small machine, and a thermal utilization corresponding to $A \cdot J = 5000\ (\mathrm{A/cm}) \cdot (\mathrm{A/mm^2})$ were chosen [16]. From an empirical knowledge, the ratio between the active iron stack length and the inner diameter of the stator, called slimness $\lambda = l_{\mathrm{Fe}}/d_{\mathrm{si}}$, was set to 1.5 for a 6-pole machine. With it, the inner diameter of the stator and the iron stack length were selected, with $d_{\mathrm{si}} = 92.8$ mm and $l_{\mathrm{Fe}} = 140$ mm.

2.1.2 Stator winding design

For the design of the stator winding, generally there are two winding method options: a tooth coil winding method and a distribution winding method. For a shorter machine length, or to minimize ohmic losses with a shorter winding overhang length and high fill factor, the tooth coil winding method is suitable. However, it causes harmonics of relatively high amplitude in the air-gap flux. As the rotation speed of the field wave harmonics differs from the rotor rotational speed, these harmonics induce voltages in the conductive parts of the rotor (e.g. the rotor iron stack and magnets) and produce eddy currents, which cause undesirable additional losses and heat in the rotor. To minimize these additional losses in the rotor, a two-layer short-pitched distribution winding was inserted in the stator.

The number of slots per pole and phase q_{s} is expressed as (2.2), with the number of stator slots Q_{s}, the number of pole pairs p and the number of phases m. In order to produce an air-gap field from the stator current in an ideal sinus shape as much as possible, the machine needs a high number of stator slots per pole and phase q_{s} [15]. However, if the electric machine has a number of slots per pole and phase higher than 2 with the given inner diameter of the stator $d_{\mathrm{si}} = 92.8$ mm from Chapter 3.1.1, the structure of the stator teeth and slots is too narrow to hold the copper winding and this can cause problems with the mechanical stability of the machine. Thus, the number of slots per pole and phase for an air-gap field without sub-harmonics selected as $q_{\mathrm{s}} = 3/2$ or $q_{\mathrm{s}} = 2$. The parameters needed to design the stator winding are presented in Table 2.1.

$$q_{\mathrm{s}} = \frac{Q_{\mathrm{s}}}{2p \cdot m} = \frac{q_{\mathrm{nu}}}{q_{\mathrm{de}}} \tag{2.2}$$

Table 2.1 Parameters for stator winding design for double-layer winding

Denominator of the q_s	q_{de}	odd	even
Number of slots of a base winding	Q_{u}	$2m \cdot q_{\mathrm{nu}}$	$m \cdot q_{\mathrm{nu}}$
Number of pole pairs of a base winding	p_{u}	q_{de}	$\frac{q_{\mathrm{de}}}{2}$
Number of slots per phase that excite north pole field at a given time	q_1	q_{nu}	$\frac{q_{\mathrm{nu}}+1}{2}$
Number of slots per phase that excite south pole field at a given time	q_2	q_{nu}	$\frac{q_{\mathrm{nu}}-1}{2}$
Harmonic orders ($g = \pm 1, \pm 2, \pm 3, \ldots$)	ν	$\frac{1+2m \cdot g}{q_{\mathrm{de}}}$	$2 \cdot \frac{1+m \cdot g}{q_{\mathrm{de}}}$

2.1.2.1 Integer slot winding $q_s = 2$

With the number of slots per pole and phase $q_s = 2$, the electric machine has $Q_s = 36$ stator slots and a slot pitch of $\tau_Q = 8.1$ mm. The machine has a constant tooth width of $b_{st} = 4.6$ mm to avoid high saturation at the stator tooth. Fig. 2.1 shows the back EMF voltage phasor diagram and the *Tingley* schema for the three-phase winding machine with $q_s = 2$ with the electrical angle between the voltage phasors in adjacent slots $\alpha_Q = (360° \cdot p_u)/Q_u = 30°$. The number on each phasor indicates the number of each slot,

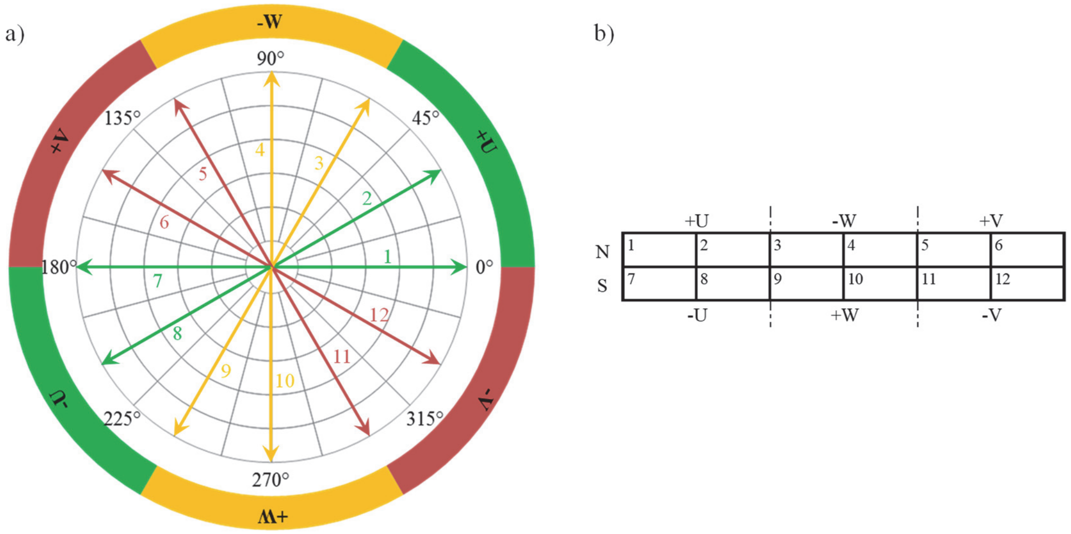

Fig. 2.1: a) Back EMF voltage phasor diagram and b) *Tingley* schema for one pole pair with $q_s = 2, \alpha_Q = 30°$. The number on the voltage phasor is each stator's slot number. Colour: U-phase (green), V-phase (red), W-phase (yellow)

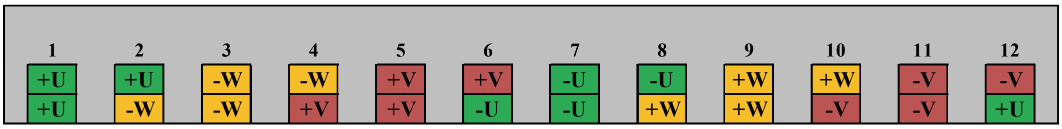

1	2	3	4	5	6	7	8	9	10	11	12
+U	+U	-W	-W	+V	+V	-U	-U	+W	+W	-V	-V
+U	-W	-W	+V	+V	-U	-U	+W	+W	-V	-V	+U

Fig. 2.2: Winding scheme in the stator slots for one pole pair with $q_{\mathrm{s}} = 2$, $W/\tau_{\mathrm{p}} = 5/6$. Colour: U-phase (green), V-phase (red), W-phase (yellow)

and the winding scheme for this phasor diagram is shown in Fig. 2.2 (upper layer). Using short-pitched winding $W/\tau_{\mathrm{p}} = 5/6$, the amplitudes of the 5th and 7th harmonics are minimized.

2.1.2.2 Fractional slot winding $q_{\mathrm{s}} = 3/2$

When the number of slots per pole and phase q_{s} is a fractional number, this winding is called a fractional slot winding. The fractional slot winding has some advantages; mainly there are more opportunities to choose the number of slots and the short pitching. In addition, unlike the integral slot winding, the fractional slot winding has a fractional number of slots per pole $Q_{\mathrm{s}}/(2p) = m \cdot q_{\mathrm{s}}$ which is not periodic with the stator pole pitch. Hence the amplitude of the cogging torque can be much smaller. It is thus possible to achieve low cogging torque with a fractional slot winding even without skewing of the slots [15]. As previously mentioned, a fractional slot winding also has disadvantages, which come from a larger number of field harmonics and usually also higher amplitudes of the harmonics. This point is discussed in the next chapter (Fig. 2.5).

When the electric machine has the number of slots per pole and phase $q_{\mathrm{s}} = 3/2$, the number of stator slots is $Q_{\mathrm{s}} = 27$. The machine has fewer slots than with $q_{\mathrm{s}} = 2$ for the same stator inner diameter, thus it has a greater slot pitch of $\tau_Q = 10.8$ mm and a bigger constant tooth width of $b_{\mathrm{st}} = 6.2$ mm. For the base winding period, the $q_{\mathrm{s}} = 3/2$ winding has $Q_{\mathrm{u}} = 9$ slots for $p_{\mathrm{u}} = 1$ pole pair, which means that there are no field subharmonics. The back EMF voltage phasor diagram and the *Tingley* schema for the machine with $q_{\mathrm{s}} = 3/2$ are presented in Fig. 2.3 with the electrical angle between the voltage phasors in adjacent slots $\alpha_{\mathrm{Q}} = (360° \cdot p_{\mathrm{u}})/Q_{\mathrm{u}} = 40°$. Fig. 2.4 shows the winding scheme in the stator slots of a basic winding period. The winding is short-pitched with the coil width of $W = 4$ and the pole pitch of $\tau_{\mathrm{p}} = Q_{\mathrm{u}}/(2p_{\mathrm{u}})$.

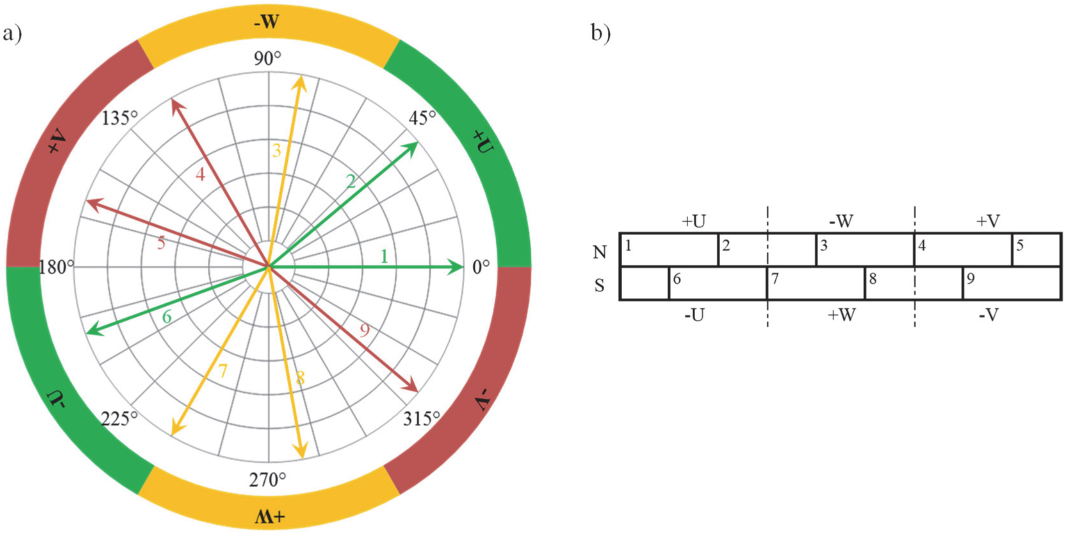

Fig. 2.3: a) Back EMF voltage phasor diagram and b) *Tingley* schema for one pole pair with $q_\text{s} = 3/2\,, \alpha_\text{Q} = 40°$. The number on the voltage phasor is each stator's slot number. Colour: U-phase (green), V-phase (red), W-phase (yellow)

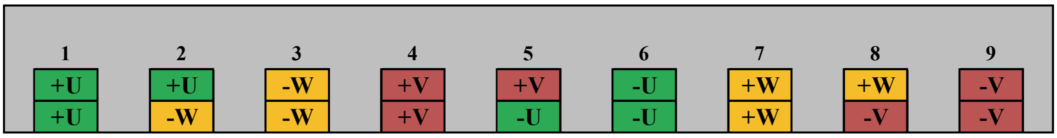

1	2	3	4	5	6	7	8	9
+U	+U	-W	+V	+V	-U	+W	+W	-V
+U	-W	-W	+V	-U	-U	+W	-V	-V

Fig. 2.4: Winding scheme in the stator slots for one pole pair with $q_\text{s} = 3/2$, $W/\tau_\text{p} = 4/4.5$. Colour: U-phase (green), V-phase (red), W-phase (yellow)

2.1.2.3 Winding factor [15]

The winding factor $k_{\text{w},\nu}$ can be calculated either with the ratio of the geometric sum of back EMF voltage phasors to the sum of their absolute values or with general equations of the ν^th harmonic winding factor, which is the product of the pitching factor $k_{\text{p},\nu}$ and the distribution factor $k_{\text{d},\nu}$ as in (2.3). The pitching factor of ν^th harmonic is calculated with the short-pitched coil span W and the pole pitch τ_p in (2.4).

$$k_{\text{w},\nu} = k_{\text{p},\nu} \cdot k_{\text{d},\nu} \tag{2.3}$$

$$k_{\mathrm{p},\nu} = \sin\left(\nu \cdot \frac{W}{\tau_{\mathrm{p}}} \cdot \frac{\pi}{2}\right) \tag{2.4}$$

For the distribution factor calculation, a parameter Y is defined as $Y = (g_{\min} \cdot Q_{\mathrm{u}} + 1)/p_{\mathrm{u}}$ with an auxiliary integer variable $g_{\min}$, which is the smallest integer to make Y an integer. These formulas are suitable for both symmetrical integral slot windings and fractional slot windings. The integral slot winding is a special type of the fractional slot winding $q_{\mathrm{de}} = 1$. Thus, the distribution factor for the integral slot winding can be simplified with (2.5) ($q_1 = q_2 = Q_{\mathrm{u}}/(2m)$, if Q_{u} is an even number and $q_1 = q_2 + 1 = (Q_{\mathrm{u}} + m)/(2m)$, if Q_{u} is an odd number).

$$\begin{aligned} k_{\mathrm{d},\nu} &= \frac{\sin(\nu \cdot \alpha_{\mathrm{Q}} \cdot Y \cdot q_1/2) - \cos(\nu \cdot p_{\mathrm{u}} \cdot \pi \cdot Y) \cdot \sin(\nu \cdot \alpha_{\mathrm{Q}} \cdot Y \cdot q_2/2)}{(q_1 + q_2) \cdot \sin(\nu \cdot \alpha_{\mathrm{Q}} \cdot Y/2)} \\ &= \frac{\sin\left(\frac{\nu\pi}{2m}\right)}{q_{\mathrm{s}} \cdot \sin\left(\frac{\nu\pi}{2m \cdot q_{\mathrm{s}}}\right)} \quad (\text{if } q_{\mathrm{s}} \text{ is integer}) \end{aligned} \tag{2.5}$$

The amplitudes of the field harmonics are proportional to $k_{\mathrm{w},\nu}/\nu$, which means that higher-order harmonics have lower amplitude. Calculated winding factors, relative field amplitudes of air-gap flux density in the radial direction, and the spectrum of the field harmonics amplitudes for the integral slot winding $q_{\mathrm{s}} = 2$ with short pitching of $W/\tau_{\mathrm{p}} = 5/6$ and the fractional slot winding $q_{\mathrm{s}} = 3/2$ with short pitching of $W/\tau_{\mathrm{p}} = 4/4.5$ are shown in Table 2.2 and Fig. 2.5.

The short pitching of the winding is mainly used to reduce low-order harmonics $\nu = -5, \nu = 7$, because the amplitude of high-order harmonic components is reduced by a factor $1/\nu$. As mentioned above, in the case of the integral slot winding, the 5th and 7th harmonics are strongly reduced by the short pitching of $W/\tau_{\mathrm{p}} = 5/6$. In the case of the fractional slot winding, because of the asymmetry of the air-gap field distribution to the abscissa, also harmonics with even ordinal numbers occur and are shown in Fig. 2.5 b). In addition, the longest wave length of the air-gap field waves for the fractional slot winding $q_{\mathrm{s}} = 3/2$ is the same as with $q_{\mathrm{s}} = 2$, occurring at $\nu = 1$. Thus, there occur no sub-harmonics in Fig. 2.5 b). For the further design, the $q_{\mathrm{s}} = 2$ was chosen.

Table 2.2 Calculated pitching factors $k_{\mathrm{p},\nu}$, distribution factors $k_{\mathrm{d},\nu}$, winding factors $k_{\mathrm{w},\nu}$ and relative harmonic field amplitudes of radial component of air-gap flux density for the integer slot winding $q_\mathrm{s} = 2$ with short pitching of $W/\tau_\mathrm{p} = 5/6$ and fractional slot winding $q_\mathrm{s} = 3/2$ with short pitching of $W/\tau_\mathrm{p} = 4/4.5$ (assuming infinite permeability of stator iron $\mu_\mathrm{Fe} = \infty$, without considering of stator slot opening)

Integral slot winding $q_\mathrm{s} = 2$, short pitching of $W/\tau_\mathrm{p} = 5/6$					Fractional slot winding $q_\mathrm{s} = 3/2$, short pitching of $W/\tau_\mathrm{p} = 4/4.5$				
$\boldsymbol{\nu}$	$\boldsymbol{k_{\mathrm{p},\nu}}$	$\boldsymbol{k_{\mathrm{d},\nu}}$	$\boldsymbol{k_{\mathrm{w},\nu}}$	$\left\lvert\frac{\boldsymbol{B_{\delta,\nu}}}{\boldsymbol{B_{\delta,1}}}\right\rvert$	$\boldsymbol{\nu}$	$\boldsymbol{k_{\mathrm{p},\nu}}$	$\boldsymbol{k_{\mathrm{d},\nu}}$	$\boldsymbol{k_{\mathrm{w},\nu}}$	$\left\lvert\frac{\boldsymbol{B_{\delta,\nu}}}{\boldsymbol{B_{\delta,1}}}\right\rvert$
1	0.966	0.966	0.933	100 %	1	0.985	-0.960	-0.945	100 %
5	0.259	0.259	0.067	1.4 %	2	0.342	0.177	0.061	3.2 %
7	0.259	-0.259	-0.067	1.0 %	4	-0.643	-0.218	0.140	3.7 %
11	0.966	-0.966	-0.933	9.1 %	5	0.643	-0.218	-0.140	3.0 %
13	-0.966	-0.966	0.933	7.7 %	7	-0.342	0.177	-0.061	0.9 %
17	-0.259	-0.259	0.067	0.4 %	8	-0.985	-0.960	0.945	12.5%
19	-0.259	0.259	-0.067	0.4 %	10	0.985	-0.960	-0.945	10.0%
23	-0.966	0.966	-0.933	4.3 %	11	0.342	0.177	0.061	0.6 %
25	0.966	0.966	0.933	4.0 %	13	-0.643	-0.218	0.140	1.1 %
29	0.259	0.259	0.067	0.2 %	14	0.643	-0.218	-0.140	1.1 %
31	0.259	-0.259	-0.067	0.2 %	16	-0.342	0.177	-0.061	0.4 %

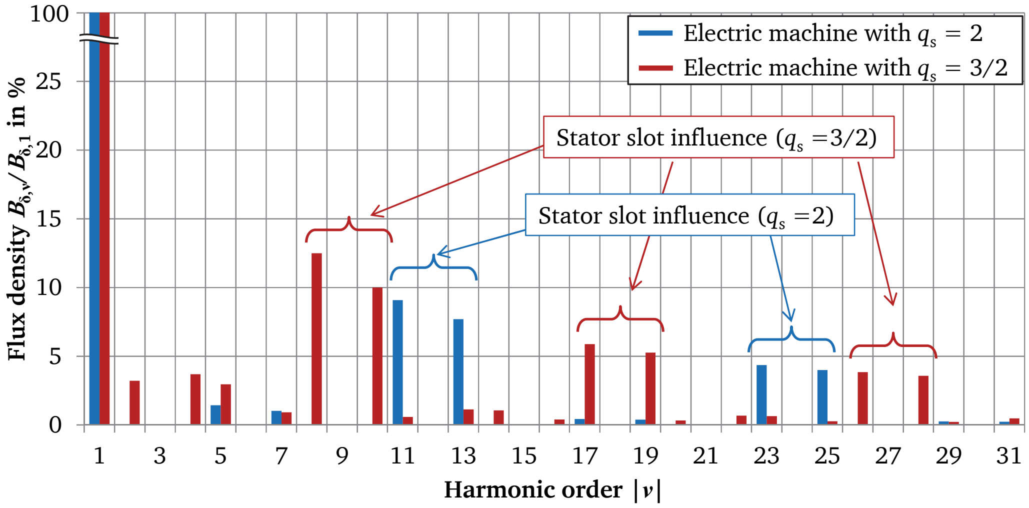

Fig. 2.5: Calculated relative field amplitudes spectrum of radial components of air-gap flux density a) for the integer slot winding $q_s = 2$ with short pitching of $W/\tau_p = 5/6$ (blue) and b) for the fractional slot winding $q_s = 3/2$ with short pitching of $W/\tau_p = 4/4.5$ (red) (assuming infinite permeability of stator iron $\mu_{Fe} = \infty$, without considering of stator slot opening)

2.2 Calculation of air-gap flux density

For a surface permanent magnet synchronous machine (SPMSM), the amplitude of the fundamental component of the rotor radial air-gap flux density $B_{\delta,1}$ (excited by the rotor magnets) can be analytically predicted, without considering the iron saturation, as (2.6) and (2.7), with a pole coverage ratio α_p, a relative permeability of the magnet $\mu_{M,rel}$, an air-gap width δ, a magnet height h_M, and a remanence of the magnet B_R, assuming rare-earth PM with a linear $B_M(H_M)-$curve in the second and the forth quadrants of the B_M-H_M-plane [15].

$$B_{\delta,1} = \frac{4}{\pi} \cdot B_p \cdot \sin\left(\alpha_p \cdot \frac{\pi}{2}\right) \tag{2.6}$$

$$B_p = \frac{B_R}{1 + \mu_{M,rel} \cdot \delta / h_M} \tag{2.7}$$

Unlike for the SPMSM, the amplitude of the fundamental component of the radial air-gap flux density of an interior permanent magnet synchronous machine (IPMSM) with buried V-shaped magnets is hard to predict by analytical calculation, due to the complexity of the rotor shape and of the leakage flux distribution in the rotor iron bridges. Therefore, the air-gap flux density can be calculated either with an equivalent magnetic circuit or with a Finite Element Method (FEM) calculation.

To calculate the air-gap flux density via an equivalent magnetic circuit, a constant flux source of a permanent magnet Φ_M and the magnetic reluctances R_m for the magnet $R_\mathrm{m,M}$, air gap $R_{\mathrm{m},\delta}$, rotor iron bridge $R_\mathrm{m,Fe,B}$ and stator teeth $R_\mathrm{m,Fe,st}$ were applied in Fig. 2.6 b). Since the heights of the stator yoke $h_\mathrm{s,yoke}$ and rotor yoke $h_\mathrm{r,yoke}$ have high enough values, the magnetic reluctance of the stator yoke $R_\mathrm{m,Fe,sy}$ and rotor yoke $R_\mathrm{m,Fe,ry}$ have negligible values. In addition, the magnetic reluctances of the ferromagnetic material are varied in their saturation level because of the nonlinearity of material permeability. Thus, an iteration process was used to calculate more accurate magnetic reluctances of the stator teeth $R_\mathrm{m,Fe,st}$ and of the rotor iron bridge $R_\mathrm{m,Fe,B}$ with an iron sheet of type M270-35A. At a magnet temperature of $\vartheta_\mathrm{M} = 100\ ^\circ\mathrm{C}$, high-energy neodymium-iron-boron (NdFeB) permanent magnets of type VACODYM 863 TP (see Appendix B) have a remanence of $B_{\mathrm{R},100^\circ\mathrm{C}} = 1.14\ \mathrm{T}$ and a coercive field strength of

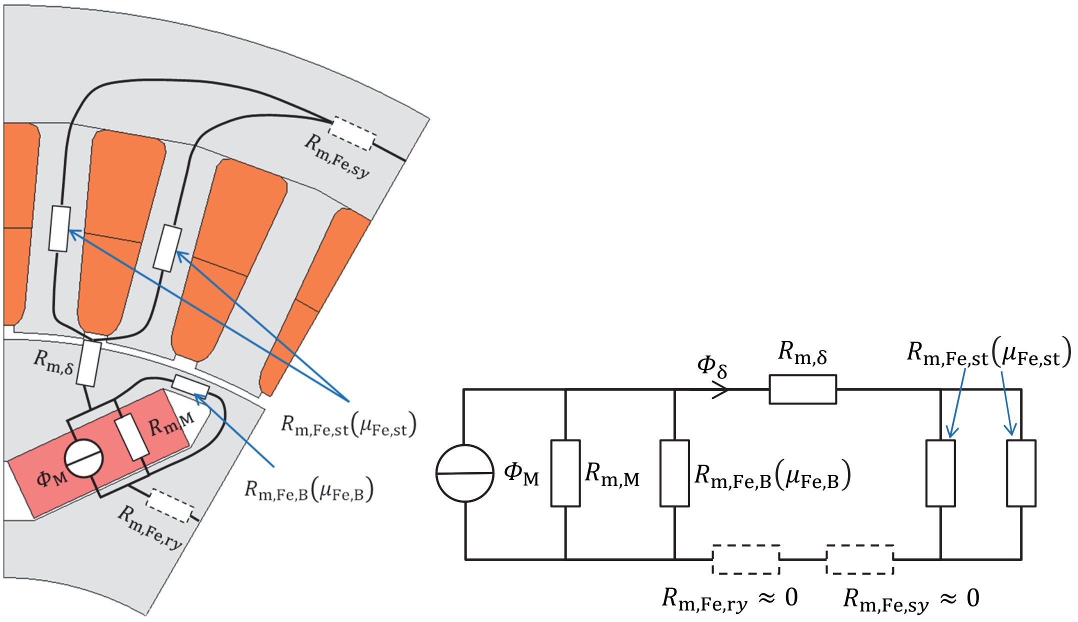

a) b)

Fig. 2.6: a) The magnetic flux path on the interior permanent magnet synchronous machine with $2p = 6$, $q_\mathrm{s} = 2$, and b) the equivalent magnetic circuit of the electric machine

$H_{\mathrm{cB},100^\circ\mathrm{C}} = 848\ \mathrm{kA/m}$. With these values, the analytically calculated rotor-excited radial air-gap flux density fundamental with the equivalent magnetic circuit is $B_{\delta,1} = 0.740\ \mathrm{T}$.

Using FEM simulation software JMAG, the radial component of the air-gap flux density was also calculated and is shown in Fig. 2.7. One stator slot opening was aligned with the rotor pole axis. The waveform shows the influence of the stator slotting on the radial component of the air-gap flux density. The dashed line represents the *Fourier* fundamental component of the air-gap flux density distribution. The amplitude of the fundamental component is $B_{\delta,1} = 0.768$ T, and it fits well to the analytically obtained value.

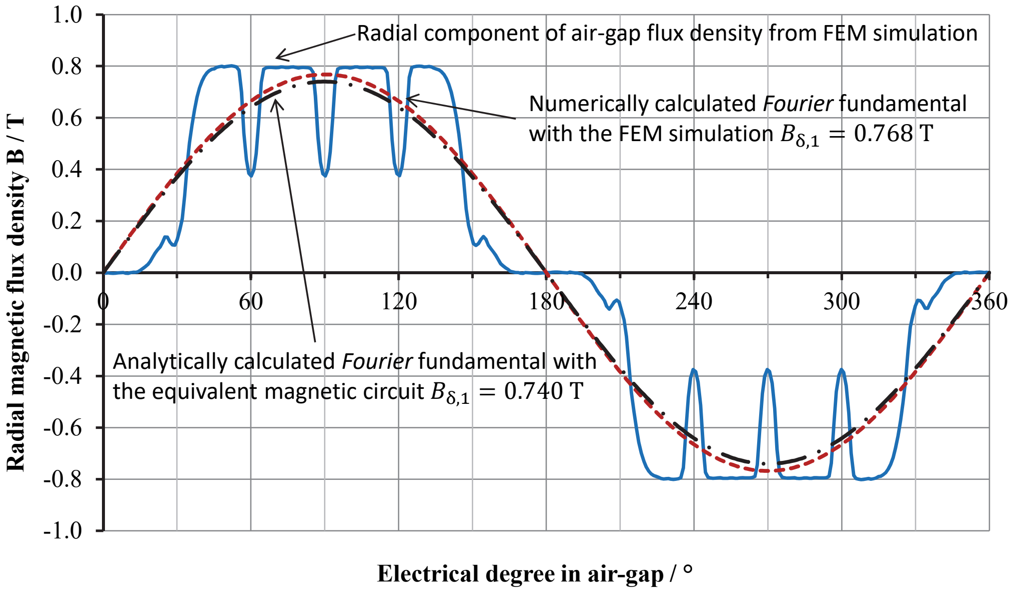

Fig. 2.7: Analytically and numerically calculated radial component of air-gap flux density per pole pair, and corresponding *Fourier* fundamental of the interior permanent magnet synchronous machine with $2p = 6$, $q_s = 2$

2.3 Torque generation and control strategies

The Field Oriented Control (FOC) of the inverter control software is based on projections which transform a three-phase sine wave current system with RMS value per phase I_{s1} into two electrically 90°-shifted sine wave components:

$$\hat{I}_{\mathrm{sd}} = \sqrt{2} \cdot I_{\mathrm{sd}} = \sqrt{2} \cdot I_{\mathrm{s1}} \cdot \sin \beta^* \tag{2.8}$$

$$\hat{I}_{\mathrm{sq}} = \sqrt{2} \cdot I_{\mathrm{sq}} = \sqrt{2} \cdot I_{\mathrm{s1}} \cdot \cos \beta^* \tag{2.9}$$

with the stator RMS current I_{s1} and current phase-shift angle β^* with respect to the induced back EMF stator phase voltage $U_{\mathrm{i}} = U_{\mathrm{p0}}$ at no-load.

The d-axis stator current component I_{sd} magnetizes the synchronously moving rotor along the rotor pole axis. Hence, the corresponding stator self-inductance L_{d} is determined mainly by the flux path across the permanent magnets, which have a high magnetic reluctance due to the low permeability of the magnet ($\mu_{\mathrm{M,rel}} \approx 1$), yielding a small value of L_{d}.

The q-axis stator current component I_{sq} magnetizes the rotor mainly along the rotor inter-pole axis, where no magnets but ferromagnetic rotor iron is placed, which causes less magnetic reluctance. Hence, the corresponding stator self-inductance L_{q} is larger. This means that, due to the special rotor design of the IPMSM with the buried V-shaped magnet, the stator self-inductance in the q-axis L_{q} is by about 2 to 3 times bigger than the d-axis inductance L_{d}, depending on the load condition, which defines the degree of iron saturation ($L_{\mathrm{d}} < L_{\mathrm{q}}$). Hence, according to the basic torque equation (2.10), for the average electromagnetic torque in air gap M_{e} [15], with the help of a negative d-component current $I_{\mathrm{sd}} < 0$ (hence a negative β^*), the machine can generate an additional reluctance torque.

$$\begin{aligned} M_{\mathrm{e}} &= \underbrace{\frac{m}{2} \cdot p \cdot \Psi_{\mathrm{M}} \cdot \hat{I}_{\mathrm{sq}}}_{\text{field torque}} + \underbrace{\frac{m}{2} \cdot p \cdot \left(L_{\mathrm{d}} - L_{\mathrm{q}}\right) \cdot \hat{I}_{\mathrm{sd}} \cdot \hat{I}_{\mathrm{sq}}}_{\text{reluctance torque}} \\ &= m \cdot p \cdot \left(\frac{\Psi_{\mathrm{M}}}{\sqrt{2}} \cdot I_{\mathrm{sq}} + \left(L_{\mathrm{d}} - L_{\mathrm{q}}\right) \cdot I_{\mathrm{sd}} \cdot I_{\mathrm{sq}}\right) \\ &= m \cdot p \cdot \left(\Psi_{\mathrm{M}} \cdot I_{\mathrm{s1}} \cdot \cos \beta^* / \sqrt{2} + \left(L_{\mathrm{d}} - L_{\mathrm{q}}\right) \cdot I_{\mathrm{s1}}^2 \cdot \sin(2\beta^*)/2\right) \end{aligned} \tag{2.10}$$

As seen in (2.10), the produced electromagnetic torque in the air gap is a function of the stator winding flux linkage per phase of the rotor permanent magnets Ψ_{M}; the stator d- and q-axis winding self-inductances L_d and L_q, respectively; the stator current per phase I_s; and the current phase shift angle β^*. Typically, the first three parameters do not change dramatically, thus these parameters are considered as constant values. For producing a given torque value, there are infinite combinations of the stator current I_s1 and current phase shift angle β^*. Hence, using proper current values I_s1 and current phase shift angle β^*, the required torque can be achieved with a minimized current; thus, the machine has minimum ohmic losses, which are usually the dominant losses in the electric machine. This operation is called maximum torque per ampere (MTPA) control. To determine the necessary current I_s1 and its angle β^*, the constant torque loci in the d- and q- current plane for the electric machine were calculated for the machine with $q_\mathrm{s} = 2$ and with $q_\mathrm{s} = 3/2$ (Fig. 2.9). The black concave curves show the constant torque loci. All the current combinations (I_s1, β^*) on a constant torque locus produce the same electromagnetic torque. The red line shows the trajectory of the minimum current combinations via MTPA control.

$$U_\mathrm{d} = R_\mathrm{s} \cdot I_\mathrm{d} - \omega_\mathrm{s} \cdot L_\mathrm{q} \cdot I_\mathrm{q} \tag{2.11}$$

$$U_\mathrm{q} = R_\mathrm{s} \cdot I_\mathrm{q} + \omega_\mathrm{s} \cdot \left(L_\mathrm{d} \cdot I_\mathrm{d} + \Psi_\mathrm{M}/\sqrt{2}\right) \tag{2.12}$$

$$U_\mathrm{s} = \sqrt{U_\mathrm{d}^2 + U_\mathrm{q}^2} \leq U_\mathrm{s,lim} \tag{2.13}$$

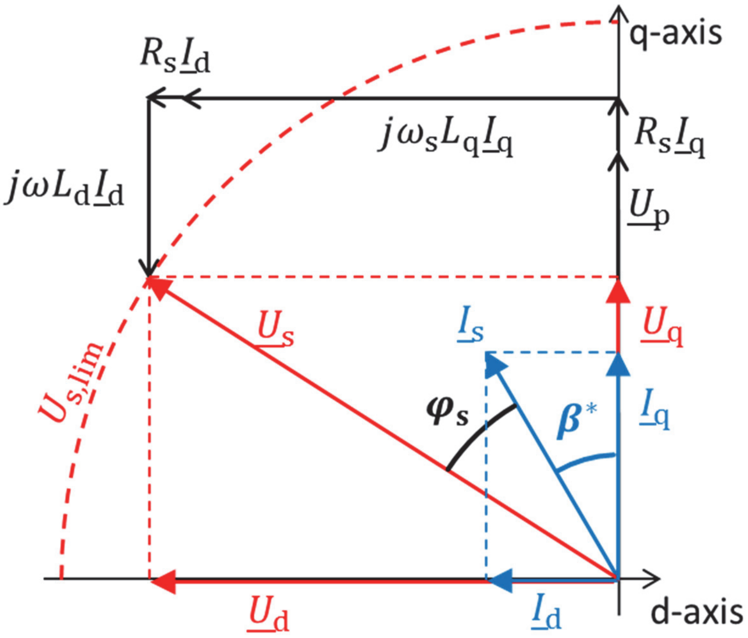

Fig. 2.8: Phasor diagram of the IPMSM

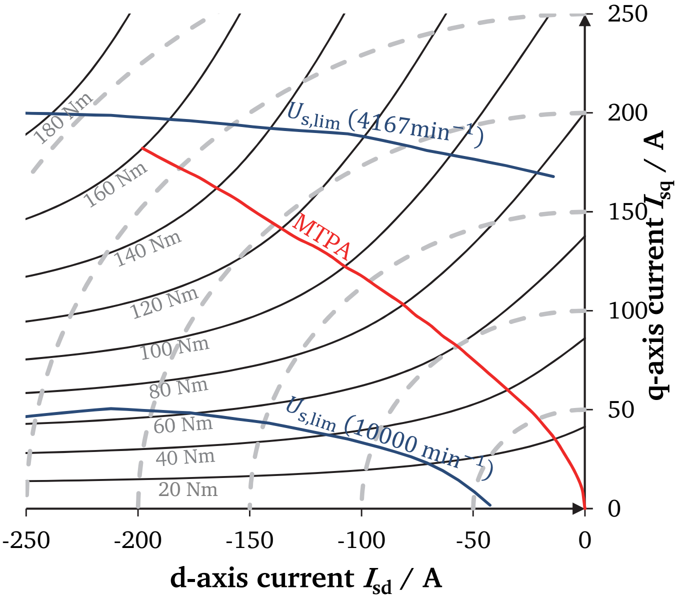

Fig. 2.9: Calculated constant torque loci of the IPMSM with $q_s = 2$ in d- and q-axis current components plane. black curves: constant torque curves, red line: MTPA line, blue line with $U_{s,lim}$: voltage limit curve at rated speed 4167 min^{-1} and at maximum speed 10000 min^{-1}

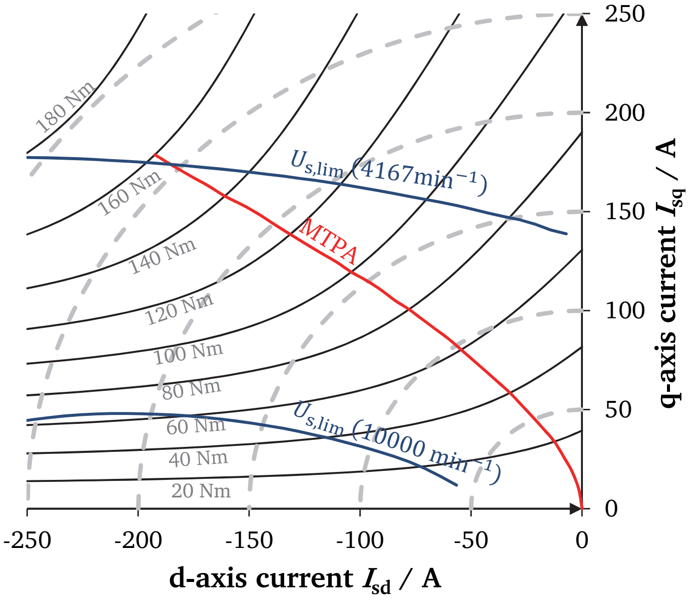

Fig. 2.10: Calculated constant torque loci of the IPMSM with $q_s = 3/2$ in d- and q-axis current components plane. black curves: constant torque curves, red line: MTPA line, blue line with $U_{s,lim}$: voltage limit curve at rated speed 4167 min^{-1} and at maximum speed 10000 min^{-1}

For the field weakening region, the controller must regulate the terminal voltage U_{s}, which is limited to stay under the maximum allowed inverter voltage $U_{\mathrm{s,lim}}$. The curved blue line presents the maximum allowed voltage curve at a given rotation speed. As long as the current phasor locates inside of this blue curve, the electric machine generates torque without exceeding the voltage limit $U_{\mathrm{s,lim}}$. The voltage limit curve can be calculated with the general voltage equations (2.11)−(2.13) (Fig. 2.8). With increasing rotation speed, the voltage limit curve shrinks. Therefore, in the field weakening region, the MTPA control does not fit to find the optimal currents. The optimal current here is determined not by the MTPA, but by the voltage limit curve, the so-called maximum torque per voltage (MTPV) control.

2.4 Reduction of cogging torque and torque ripple

Based on the magnetic pull force due to *Maxwell* stress, the interaction between the magnetic field of the permanent magnets in the rotor and the stator slots causes an oscillating torque with moving rotor. In electric and hybrid vehicles, this undesired torque reduces the life span of the powertrain components, increases mechanical vibrations (and, consequently, the acoustic noise level), and reduces driving comfort. During the design process of an electric machine, it is important to minimize this oscillating torque. The cogging torque is one of the main reasons for this torque oscillation. It exists even at no-load, when there is no stator current ($I_{\mathrm{s}} = 0$ A). The combination of the number of stator slots Q_{s} and the pole count $2p$ determines the period of the cogging torque time-function N_{cog}, corresponding to a slot pitch shifting τ_{Q} [17].

$$N_{\mathrm{cog}} = \frac{2p}{\mathrm{GCD}(Q_{\mathrm{s}}, 2p)} \tag{2.14}$$

And the corresponding mechanical angular period of the cogging torque is calculated with (2.15).

$$\alpha_{\mathrm{cog}} = \frac{360°}{N_{\mathrm{cog}} \cdot Q_{\mathrm{s}}} \tag{2.15}$$

This period of the cogging torque N_{cog} shows a rough correspondence to the cogging torque amplitude. When the value of N_{cog} is small, it means that the magnetic pull forces between the permanent magnet and the stator tooth tip occur at different stator slots the same relative rotor position with same direction of pull. Consequently, the superimposed pull forces of all other tooth tips build up a high cogging torque amplitude. Hence, the big number N_{cog} of the period of the cogging torque means that the magnetic pull force on one stator tooth tip does not synchronize well with other tooth tips, thus, it yields a low-amplitude cogging torque. Therefore, a proper selection of the number of stator slots Q_{s} and the pole count $2p$ can reduce the cogging torque amplitude. Table 2.3 presents the period of the cogging torque in a slot pitch rotation for both electric machines from 2.1.2. The electric machine with a fractional number of stator slots per pole and phase has a greater N_{cog}, thus, it will show less cogging torque.

The torque ripple under load can be further reduced by control technique, such as harmonic current injection [18]. The reduction of cogging torque may be done by skewing the rotor and using a fractional number of stator slots per pole and phase as shown in the following.

Table 2.3 Cogging torque parameters for the electric machine with an integer number of stator slots per pole and phase $q_{\mathrm{s}} = 2$ and with a fractional number of stator slots per pole and phase $q_{\mathrm{s}} = 3/2$

Number of stator slots per pole and phase	q_{s}	2	3/2
Pole count	$2p$	6	6
Number of stator slots	Q_{s}	36	27
Greatest common divisor of Q_{s} and $2p$	$\mathrm{GCD}(Q_{\mathrm{s}}, 2p)$	6	3
Number of periods of cogging torque in a slot pitch rotation	N_{cog}	1	2
Mechanical angular period of cogging torque	α_{cog}	10°	6.67°

2.4.1 Step-skewed rotor

Skewing of stator slots or rotor magnets is an effective method to reduce the cogging torque and also the torque ripple at load. Electromagnetically, skewing of stator slots and skewing of rotor magnets works equally well. However, skewing of stator slots has some disadvantages: a decrease in slot fill factor, an increase in winding length and added difficulty in automating wire winding. On the other hand, the continuous skewing of the magnet on the rotor is often not easy to build, such as in an IPMSM. In this case, the rotor is subdivided into N_{step} sections in the axial direction with section length of $\Delta l_{\mathrm{Fe}} = l_{\mathrm{Fe}}/N_{\mathrm{step}}$. These rotor sections skew to each other by a mechanical step-skewed angle of $\Delta\alpha_{\mathrm{skew}} = \alpha_{\mathrm{skew}}/N_{\mathrm{step}}$, called staggering.

Skewing the electric machine reduces not only cogging torque and torque ripple under load, but reduces also the harmonics in the back EMF induced voltage, especially the slot harmonics. Certainly, it also reduces the amplitude of the fundamental component of the back EMF induced voltage slightly. The skewing factor is calculated by (2.16) for a continuously skewed machine, where α_{skew} in mechanical degrees.

$$k_{\mathrm{skew},\mathrm{v}} = \frac{\sin\left(\frac{\nu \cdot \alpha_{\mathrm{skew}} \cdot p}{2}\right)}{\frac{\nu \cdot \alpha_{\mathrm{skew}} \cdot p}{2}} \tag{2.16}$$

In the case of a step-skewed machine, each rotor section induces the stator voltage with a different phase. The phase-shift of the induced voltage between contiguous sections is the electrical step-skewed angle of $\alpha_{\mathrm{skew}} \cdot p/N_{\mathrm{step}}$ in electrical degrees. Thus, the sum of all induced voltages is smaller than in the un-skewed machine by the step-skewing factor (2.17).

$$k_{\mathrm{skew},\nu} = \frac{\sin\left(\frac{\nu \cdot \alpha_{\mathrm{skew}} \cdot p}{2}\right)}{N_{\mathrm{step}} \cdot \sin\left(\frac{\nu \cdot \alpha_{\mathrm{skew}} \cdot p}{2 \cdot N_{\mathrm{step}}}\right)} \tag{2.17}$$

For complete elimination of the cogging torque, the skewing angle α_{skew} has to be a multiple of the mechanical angular period of the cogging torque $\alpha_{\mathrm{skew}} = k \cdot \alpha_{\mathrm{cog}}$ (k: integer). Generally, the constant k is selected as unity to minimize the reduction of the fundamental component of the induced voltage.

For the prototype, an electric machine with an integer $q_{\mathrm{s}} = 2$ was designed with a skewing angle of $\alpha_{\mathrm{skew}} = k \cdot 360°/(N_{\mathrm{cog}} \cdot Q_{\mathrm{s}}) = 1 \cdot 360°/(1 \cdot 36) = 10°$ and an axial skew by $N_{\mathrm{step}} = 5$ discrete steps with the mechanical step-skewed angle of $\Delta\alpha_{\mathrm{skew}} = \alpha_{\mathrm{skew}}/N_{\mathrm{step}} = 10°/5 = 2°$. In order to consider this step-skewed rotor in 2D-FEM, the five simulations were done with different rotor initial angles -4°, -2°, 0°, +2°, and +4°. After that all five simulation results were added and averaged. To clarify the effect of the rotor skewing, both with 2D-FEM (JMAG software) calculated back EMF induced stator voltage wave forms (with and without skewing) at rated speed $n_{\mathrm{N}} = 4167\ \mathrm{min}^{-1}$

are shown in Fig. 2.11. With the step-skewed rotor, there are fewer harmonic components in the induced voltage; in particular, the slot harmonic 11th and 13th components were reduced.

With the same stator current I_{s1} and the current phase shift angle β^*, the electric machine with the step-skewed rotor produces less average electromagnetic torque than the machine with an un-skewed rotor. As an example, there is an electric machine with a 5-step-skewed rotor. Even though the same stator current I_s and current angle β^* are applied in the machine, each rotor segment faces a different current angle due to the discrete step-skewed angle of $\Delta\alpha_{\text{skew}}$ (2.18, 2.19). Fig. 2.12 shows the corresponding current phasors, which are oriented to the q-axis of the middle rotor segment.

$$I_{\text{sq},n} = I_{s1} \cdot \cos(\beta^* + n \cdot \Delta\alpha_{\text{skew}} \cdot p) \tag{2.18}$$

$$\begin{gathered} I_{\text{sd},n} = I_{s1} \cdot \sin(\beta^* + n \cdot \Delta\alpha_{\text{skew}} \cdot p) \\ n = -2, -1, 0, 1, 2 \end{gathered} \tag{2.19}$$

Due to the different current shift angles β^* of the current vectors with respect to the induced voltage, each rotor segment produces a different electromagnetic torque $M_{\text{e},n}$. The sum of the electromagnetic torque components of all n rotor segments is calculated as (2.20), with $\Psi'_{\text{M}} = \Psi_{\text{M}}/n = \Psi_{\text{M}}/5$.

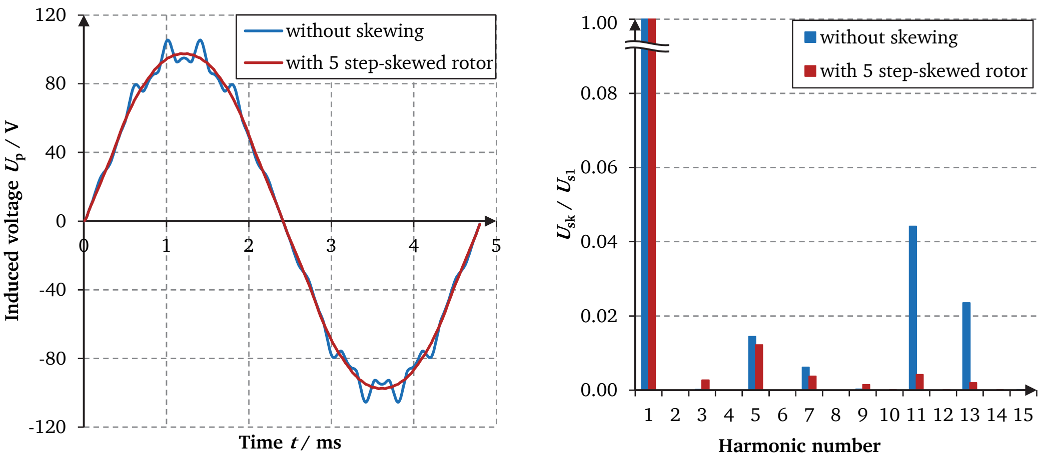

a) b)

Fig. 2.11: Calculated no-load induced phase voltage at rated speed $n_{\text{N}} = 4167 \text{ min}^{-1}$ with 2D-FEM (JMAG software) a) Back EMF induced stator voltage wave forms (blue: without rotor skewing, red: with 5-step-skewed rotor) and b) *Fourier* voltage spectrum

$$\begin{aligned} M_\mathrm{e} &= M_{\mathrm{e},-2} + M_{\mathrm{e},-1} + M_{\mathrm{e},0} + M_{\mathrm{e},+1} + M_{\mathrm{e},+2} \\ &= m \cdot p \cdot \left[\Psi'_\mathrm{M}/\sqrt{2} \cdot \left(I_{\mathrm{sq},-2} + I_{\mathrm{sq},-1} + I_{\mathrm{sq},0} + I_{\mathrm{sq},+1} + I_{\mathrm{sq},+2}\right)\right. \\ &\qquad + \left(L_{\mathrm{d},-2} - L_{\mathrm{q},-2}\right) \cdot I_{\mathrm{sd},-2} \cdot I_{\mathrm{sq},-2} + \left(L_{\mathrm{d},-1} - L_{\mathrm{q},-1}\right) \cdot I_{\mathrm{sd},-1} \cdot I_{\mathrm{sq},-1} \\ &\qquad + \left(L_{\mathrm{d},0} - L_{\mathrm{q},0}\right) \cdot I_{\mathrm{sd},0} \cdot I_{\mathrm{sq},0} + \left(L_{\mathrm{d},+1} - L_{\mathrm{q},+1}\right) \cdot I_{\mathrm{sd},+1} \cdot I_{\mathrm{sq},+1} \\ &\qquad \left. + \left(L_{\mathrm{d},+2} - L_{\mathrm{q},+2}\right) \cdot I_{\mathrm{sd},+2} \cdot I_{\mathrm{sq},+2}\right] \end{aligned} \tag{2.20}$$

Generally, the self-inductances in the d-axis L_d and q-axis L_q, depending on the current amplitude and the current shift angle, are similar ($L_\mathrm{d} \approx L_{\mathrm{d},n}$, $L_\mathrm{q} \approx L_{\mathrm{q},n}$). Thus, the torque equation (2.20) is simplified to (2.21).

$$\begin{gathered} M_\mathrm{e} = m \cdot p \cdot \left(k_\mathrm{sk1} \cdot \frac{\Psi_\mathrm{M}}{\sqrt{2}} \cdot I_\mathrm{sq} + k_\mathrm{sk2} \cdot \left(L_\mathrm{d} - L_\mathrm{q}\right) \cdot I_\mathrm{sd} \cdot I_\mathrm{sq}\right) \\ \text{with } k_\mathrm{sk1} = \frac{\sin\left(\frac{\alpha_\mathrm{skew} \cdot p}{2}\right)}{N_\mathrm{step} \cdot \sin\left(\frac{\alpha_\mathrm{skew} \cdot p}{2 \cdot N_\mathrm{step}}\right)} \text{ and } k_\mathrm{sk2} = \frac{\sin(\alpha_\mathrm{skew} \cdot p)}{N_\mathrm{step} \cdot \sin\left(\frac{\alpha_\mathrm{skew} \cdot p}{N_\mathrm{step}}\right)} \end{gathered} \tag{2.21}$$

For the prototype machine with $p = 3, \alpha_\mathrm{skew} = 10°$ and $N_\mathrm{step} = 5$, the machine has skew factors of $k_\mathrm{sk1} = 0.9891$ and $k_\mathrm{sk2} = 0.9567$.

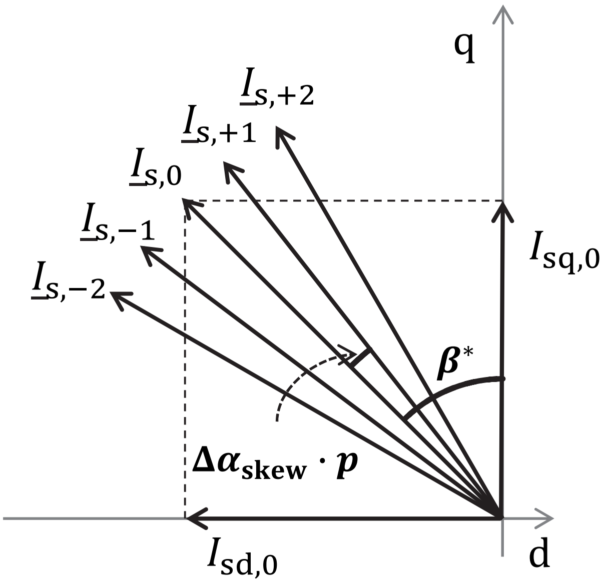

Fig. 2.12: Current phasors for each rotor segment of 5-step-skewed rotor with negative I_d-component

2.4.2 Fractional number of stator slots per pole and phase

With a fractional number of stator slots per pole and phase, cogging torque and torque ripple of the electric machine can also be minimized. First, the physical meaning of this method will be discussed, and then this method will be approached with mathematical calculations.

When an electric machine has a fractional number of stator slots per pole and phase, the stator teeth and the magnets are not fully aligned with each other. Each magnet of the electric machine sees a fractional number of slots, which means that a magnet pole faces a different integer number of slots than its neighbouring magnet poles. In the case of the electric machine with $q_\mathrm{s} = 3/2$, as seen in Fig. 2.13, the north pole, between 0 and 180 electrical degrees, faces five stator slots, whereas the south pole, between 180 and 360 electrical degrees, faces only four stator slots. Due to this difference in the number of slots facing each pole, or misalignment between the stator teeth and rotor magnets, the cogging torque contributions from adjacent magnet poles are out of phase with each other. Thus, the overall cogging torque and torque ripple are lower than they would be if these individual contributions were in phase.

Now the possibility of minimizing the cogging torque and torque ripple by adopting a fractional number of slots per phase and pole will be discussed mathematically. For

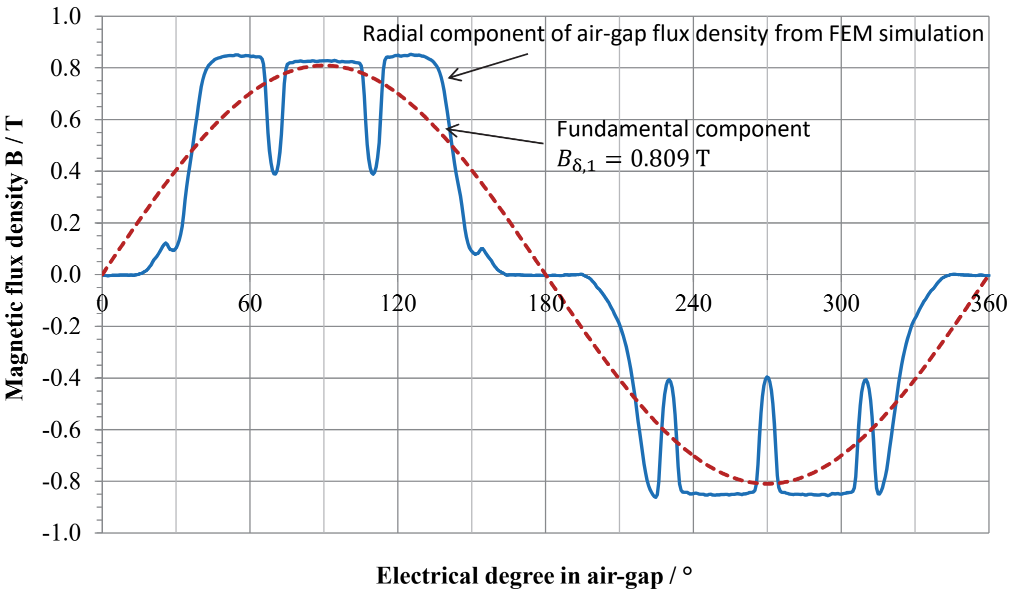

Fig. 2.13: 2D-FEM numerically calculated radial component of air-gap flux density per pole pair, and corresponding *Fourier* fundamental of the interior permanent magnet synchronous machine with a fractional number of stator slots per pole and phase $q_\mathrm{s} = 3/2$ and pole count $2p = 6$

determining the harmonic components of cogging torque at no-load, the electromagnetic torque in the air gap is calculated using the general equation (2.22), with the radial flux density distribution in the air gap $B_\mathrm{n} = B$, the current loading distribution A, the mechanical circumferential displacement along the air gap x, and the mechanical rotational displacement along the air gap γ_m.

$$\begin{aligned} M_\mathrm{e} &= \frac{d_\mathrm{si}}{2} \cdot l_\mathrm{Fe} \cdot \int_0^{2p \cdot \tau_\mathrm{p}} B(x,t) \cdot A(x,t) \cdot dx \\ &= \left(\frac{d_\mathrm{si}}{2}\right)^2 \cdot l_\mathrm{Fe} \cdot \int_0^{2\pi} B(\gamma_\mathrm{m},t) \cdot A(\gamma_\mathrm{m},t) \cdot d\gamma_\mathrm{m} \end{aligned} \tag{2.22}$$

As explained in [15], the electromagnetic torque is calculated with an integration of the tangential component of the *Maxwell* stress tensor in the air gap $f_\mathrm{t} = B_\mathrm{n} \cdot H_\mathrm{t}$. In (2.22), the tangential component of the magnetic field strength in the air gap H_t is replaced by current loading A. At no-load condition, the current loading distribution A can be replaced by the equivalent current loading component from the fluctuation of the magnetic flux density in the air gap due to the slot openings. To consider this equivalent current loading, the magnetic field from the rotor magnet, without considering the slot opening effect, is calculated with (2.23). Due to the slot opening, the radial magnetic flux density distribution in the air gap is distorted. This slot opening effect on the magnetic field in the air gap is considered in (2.24) with integer numbers of l of a slotting permeance function, described with a FOURIER-series with harmonic components λ_l and the average value k_c of CARTER's coefficient. Due to the small amplitudes with higher harmonic order μ of the rotor field harmonics, only the fundamental component of the rotor magnetic field $\hat{B}_1$ is considered in (2.24) to calculate the equivalent current loading.

$$B_\mathrm{r}(\gamma_\mathrm{m},t) = \sum_{\mu=1,3,5,\ldots}^{\infty} \hat{B}_\mu \cdot \cos\big(\mu \cdot p \cdot (\gamma_\mathrm{m} - \Omega_\mathrm{m} \cdot t)\big) \tag{2.23}$$

$$\begin{aligned} B_\delta(\gamma_\mathrm{m},t) &= B_\mathrm{r}(\gamma_\mathrm{m},t) \cdot \left(\frac{1}{k_\mathrm{c}} + \sum_{l=1}^{\infty} \lambda_l \cdot \cos(l \cdot Q_\mathrm{s} \cdot \gamma_\mathrm{m})\right) \\ &\cong \hat{B}_1 \cdot \cos\big(p \cdot (\gamma_\mathrm{m} - \Omega_\mathrm{m} \cdot t)\big) \cdot \left(\frac{1}{k_\mathrm{c}} + \sum_{l=1}^{\infty} \lambda_l \cdot \cos(l \cdot Q_\mathrm{s} \cdot \gamma_\mathrm{m})\right) \end{aligned} \tag{2.24}$$

Using the trigonometric identities, the fluctuation share of the magnetic flux density due to the slot opening is simplified in (2.25).

$$B_{\sim}(\gamma_{\mathrm{m}},t)=\frac{\hat{B}_1}{2}\cdot\sum_{l=1}^{\infty}\lambda_l\cdot\begin{Bmatrix}\cos\big((p+Q_{\mathrm{s}}\cdot l)\cdot\gamma_{\mathrm{m}}-p\cdot\Omega_{\mathrm{m}}\cdot t\big)\\+\cos\big((p-Q_{\mathrm{s}}\cdot l)\cdot\gamma_{\mathrm{m}}-p\cdot\Omega_{\mathrm{m}}\cdot t\big)\end{Bmatrix}\tag{2.25}$$

By taking the derivative of $B_{\sim}$ with respect to the mechanical displacement of γ_{m}, the equivalent current loading is calculated by (2.26).

$$\begin{aligned}A(\gamma_{\mathrm{m}},t)=-\frac{\delta\cdot\hat{B}_1}{2\mu_0}\cdot\frac{2}{d_{\mathrm{si}}}&\\\cdot\sum_{l=1}^{\infty}\lambda_l\cdot&\begin{Bmatrix}(p+Q_{\mathrm{s}}\cdot l)\cdot\sin\big((p+Q_{\mathrm{s}}\cdot l)\cdot\gamma_{\mathrm{m}}-p\cdot\Omega_{\mathrm{m}}\cdot t\big)\\+(p-Q_{\mathrm{s}}\cdot l)\cdot\sin\big((p-Q_{\mathrm{s}}\cdot l)\cdot\gamma_{\mathrm{m}}-p\cdot\Omega_{\mathrm{m}}\cdot t\big)\end{Bmatrix}\end{aligned}\tag{2.26}$$

Substituting the equivalent current loading $A(\gamma_{\mathrm{m}},t)$ from (2.26) and the magnetic field from the rotor without considering the slot opening effect $B_{\mathrm{r}}(\gamma_{\mathrm{m}},t)$ into the general torque equation (2.22), the amplitude of the cogging torque components $M_{\mathrm{cog},l,\mu}$ is proportional to the fundamental component of the rotor magnetic field $\hat{B}_1$, the permeance parameter λ_{l}, and the amplitude of the magnetic field harmonic component $\hat{B}_{\mu}$, excited by the rotor magnets.

$$\begin{aligned}M_{\mathrm{cog},l,\mu}=\left(\tfrac{d_{\mathrm{si}}}{2}\right)^2 l_{\mathrm{Fe}}&\\\cdot\int_0^{2\pi}\hat{A}_l\sin\big((p\pm Q_{\mathrm{s}}\cdot l)\gamma_{\mathrm{m}}-p\Omega_{\mathrm{m}}t\big)&\cdot\hat{B}_{\mu}\cos\big(\mu p(\gamma_{\mathrm{m}}-\Omega_{\mathrm{m}}t)\big)\,d\gamma_{\mathrm{m}}\end{aligned}\tag{2.27}$$

In addition, the pole count of both waves of the current loading $(p\pm Q_{\mathrm{s}}\cdot l)$ and the rotor magnetic field $(\mu\cdot p)$ must be the same to generate a non-vanishing cogging torque (2.28). Otherwise, the integration of the sine term will be zero and will not contribute to generating the cogging torque.

$$\mu=1\pm\frac{Q_{\mathrm{s}}}{p}\cdot l=1\pm2\cdot m\cdot q_{\mathrm{s}}\cdot l\tag{2.28}$$

The rotor magnetic field curve B_{r} is an abscissa-symmetric function, and so it has only odd harmonics ordinal number μ. Table 2.4 shows the harmonic orders of the rotor magnetic field, which produce the cogging torque, with the smallest possible number of l, for electric machines with an integer number of stator slots per pole and phase $q_{\mathrm{s}}=2$

and for those with a fractional number of stator slots per pole and phase $q_\mathrm{s} = 3/2$. Clearly, the electric machine with $q_\mathrm{s} = 3/2$ has higher rotor harmonic orders than the machine with $q_\mathrm{s} = 2$. The amplitude of the rotor harmonic $\hat{B}_\mu$ decreases with an increase of the harmonic order, $\hat{B}_\mu \sim 1/\mu$. Therefore, a fractional number of slots per pole and phase of the electric machine produces a lower cogging torque amplitude.

Table 2.4 First harmonic orders of the rotor magnetic field which are producing the cogging torque for an electric machine with $q_\mathrm{s} = 2$ and with $q_\mathrm{s} = 3/2$

Number of stator slots per pole and phase q_s	2	3/2
Pole count $2p$	6	6
Number of stator slots Q_s	36	27
Minimum integer number l	1	2
Harmonic orders of the rotor magnetic field μ	11, 13	17, 19

2.4.3 Numerical calculation with FEM software

In the following, the torque ripple at no-load (cogging torque) and at the rated operation of the electric machines with previous methods from 2.4.1 and 2.4.2 were numerically simulated with FEM software JMAG. To compare the simulation results with the electric machine without any cogging torque reduction method, some design parameters were kept constant for all electric machines, such as the slot opening width b_so, the rotor geometry and the materials of the machine. The numerical simulations for one electrical period ($t = 4.8$ ms at $n_\mathrm{N} = 4167/\mathrm{min}$) were run, and the calculated cogging torques and the torque ripple at the rated torque are shown in Fig. 2.14 and Fig. 2.15, respectively.

Without any cogging torque reduction method, the electric machine produces a high cogging torque amplitude $\hat{M}_\mathrm{cog} = 1.77$ Nm, which is 3.2 % of the rated torque $M_\mathrm{N} = 55$ Nm. As seen in Fig. 2.14 b), the cogging torque repeats at one period per one slot pitch ($N_\mathrm{cog} = 1$), which was calculated analytically with (2.11). With a step-skewed rotor, the amplitude of the cogging torque was virtually eliminated (99.4 % reduction), thus it is hard to see in the figure. Additionally, a step-skewed rotor reduced the torque fluctuation of the electric machine at rated load condition by 82.3 % (Fig. 2.15). These

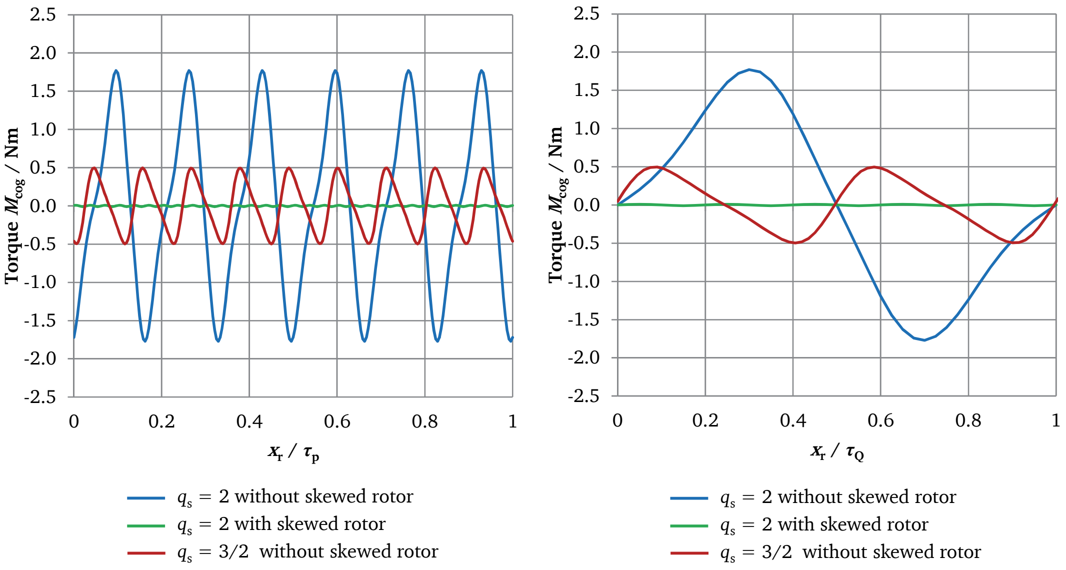

a) half electric period τ_p

b) one slot pitch τ_Q

Fig. 2.14: 2D-FEM numerically calculated cogging torque waves for the electric machines with $q_s = 2$ (with and without skewed rotor) and with $q_s = 3/2$ without skewed rotor during a) half electrical period τ_p and b) a slot pitch τ_Q

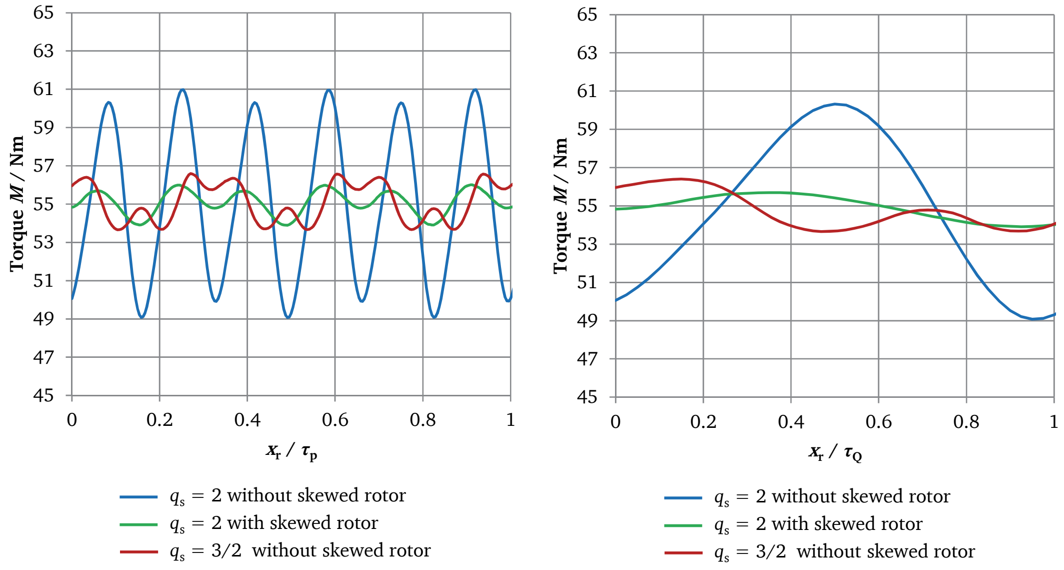

a) half electric period $2\tau_\mathrm{p}$

b) one slot pitch τ_Q

Fig. 2.15: 2D-FEM numerically calculated torque ripple for the electric machines with $q_s = 2$ (with and without skewed rotor) and with $q_s = 3/2$ without skewed rotor during a) half electrical period τ_p and b) a slot pitch τ_Q at $M_\mathrm{av} = 55$ Nm

simulated results show that step-skewing of the rotor diminishes the torque ripple effectively. The electric machine with a step-skewed rotor, of course, needs 1.8 % more stator current to produce the same electromagnetic torque at rated load, due to the skew-

ing factor (2.21). It also produces more heat in the stator winding by ohmic losses; consequently, step-skewing will reduce efficiency to some degree.
Using a fractional number of stator slots per pole and phase $q_\mathrm{s} = 3/2$ caused a 72.0 % reduction of the calculated cogging torque amplitude $\widehat{M}_\mathrm{cog} = 0.50$ Nm compared to the un-skewed electric machine (Fig. 2.14 a). In addition, the cogging torque wave has two periods ($N_\mathrm{cog} = 2$) per one slot pitch rotor rotation, which means that the cogging torque occurs more frequently (Fig. 2.14 b). This supports the argument from the beginning of this chapter that a higher period number N_cog of the cogging torque in a stator slot pitch rotation yields a lower amplitude cogging torque. In addition, the step-skewed electric machine produced 75.4 % less torque ripple at the rated load compared with the un-skewed machine (Fig. 2.15). This shows that using a fractional number of stator slots per pole and phase is an efficient method to reduce torque fluctuation in an electric machine. Table 2.5 shows a summary of the numerically simulated results of the electric machines.

Table 2.5 2D-FEM numerically calculated cogging torque at no-load and torque ripple at the rated OP2 for the electric machine with $q_\mathrm{s} = 2$ with and without skewed rotor and with $q_\mathrm{s} = 3/2$ without skewed rotor at $M_\mathrm{N} = M_\mathrm{av} = 55$ Nm (M_max / M_min: maximum / minimum value at the torque curve)

Number of stator slots Q_s	36	36	27
Number of stator slots per pole and phase q_s	2	2	3/2
Skewed rotor	no skew	5-step	no skew
Amplitude of the cogging torque at no-load $\widehat{M}_\mathrm{cog}$	1.77 Nm	0.01 Nm	0.50 Nm
Cogging torque ratio with rated load $\widehat{M}_\mathrm{cog}/M_\mathrm{N}$	3.22 %	0.02 %	0.90 %
Stator current at OP2	92.1 A (reference)	93.8 A (+1.8 %)	89.5 A (-2.8 %)
Torque ripple at OP2 ($M_\mathrm{max} - M_\mathrm{min}$)	11.9 Nm	2.1 Nm	2.9 Nm
$\widehat{w} = (M_\mathrm{max} - M_\mathrm{min})/(2 \cdot M_\mathrm{av})$	10.83 %	1.92 %	2.66 %
Torque at constant current $I_\mathrm{s} = 95$ A	56.9 Nm (reference)	55.8 Nm (-1.9 %)	58.7 Nm (+3.2 %)

2.5 Sudden short-circuit current and torque

In major fault conditions, such as a sudden short-circuit (either line-to-line or three-phase short-circuit) the electric machine produces high sudden short-circuit current, which is dependent on the switching instant relative to the stator voltage zero-crossing. The sudden short-circuit current produces a large magnetic counter-field in the permanent magnets. Permanent magnets are vulnerable to losing their magnetization in a strong opposing magnetic field, especially at high magnet temperature. Therefore, a high sudden short-circuit current causes a drastically increased risk for the demagnetization of the magnets. Once demagnetization has taken place in the permanent magnets, it reduces the back EMF stator induced voltage, due to the reduction of the magnetic flux linkage, and consequently the electromagnetic torque is reduced. In addition, the sudden short circuit may cause severe mechanical stresses on stator windings and winding overhangs, due to overheating and high forces. During the sudden short circuit, the rotor also suffers a large transient alternating electromagnetic torque, which can damage the coupling or the machine shaft. Therefore, sudden short-circuit tests and, in advance of these, appropriate calculations are necessary.

2.5.1 Analytical calculation of sudden short-circuit current and torque

To estimate the sudden short-circuit current and the transient torque via an analytic calculation, the dynamic equations of the PMSM are used [19]. For the simple analytic calculation, the following assumptions are made and only the symmetrical short-circuit case (short circuit on all three phase output terminals) is considered.

- Constant rotor permanent magnet flux linkage with stator winding Ψ_{M}
- No difference between sub-transient, transient and synchronous inductances: $L''_{\mathrm{d}} = L'_{\mathrm{d}} = L_{\mathrm{d}}$ and $L''_{\mathrm{q}} = L'_{\mathrm{q}} = L_{\mathrm{q}}$ (no damper cage, no rotor field winding)
- Constant rotational speed (Ω_{m} = constant) of the electric machine

In the electrically conductive parts of the rotor, such as the permanent magnets and the rotor iron sheets, transient induced eddy currents may occur, but this influence is small due to the axial and radial segmented magnets and laminated 0.5 mm rotor iron sheets [20]. Therefore, the flux linkage of the permanent magnets is assumed to remain constant during the transient state (Ψ_M = constant), and the sub-transient inductances are the same as the synchronous inductances ($L''_\mathrm{d} = L_\mathrm{d}$, $L''_\mathrm{q} = L_\mathrm{q}$). In addition, the PMSM does not have field windings in the rotor, thus the transient d-axis inductances are equal to the synchronous inductances ($L'_\mathrm{d} = L_\mathrm{d}$). The set of dynamic equations of the PMSM contain as a mechanical equation *Newton*'s second law of motion. Due to this mechanical equation, the set of dynamic equations of the PMSM is non-linear. As the electrical time constants are shorter than the mechanical time constant, the changing of the rotational speed of the electric machine, during the sudden short-circuit, may be ignored. With a constant rotational speed, the non-linear dynamic equations are changed to linear equations by omitting the mechanical equation. The sudden short-circuit current in phase U is given as [77]

$$\begin{aligned} i_\mathrm{U}(t) = &-\left(i_\mathrm{pd}\cdot\cos(\omega_\mathrm{s}t+\gamma_0)-i_\mathrm{pq}\cdot\sin(\omega_\mathrm{s}t+\gamma_0)\right)\\ &+\tfrac{1}{2}e^{-a\cdot t}\cdot\left[\left(K_\mathrm{d}+M_\mathrm{q}\right)\cdot\cos\left((\omega_\mathrm{s}+b)t+\gamma_0\right)+\left(K_\mathrm{d}-M_\mathrm{q}\right)\cdot\cos\left((\omega_\mathrm{s}-b)t+\gamma_0\right)\right.\\ &\left.-\left(K_\mathrm{q}-M_\mathrm{d}\right)\cdot\sin\left((\omega_\mathrm{s}+b)t+\gamma_0\right)-\left(K_\mathrm{q}+M_\mathrm{d}\right)\cdot\sin\left((\omega_\mathrm{s}-b)t+\gamma_0\right)\right] \end{aligned} \tag{2.29}$$

with the coefficients

$$i_\mathrm{pd} = \frac{\omega_\mathrm{s}^2 L_\mathrm{q}\Psi_\mathrm{M}}{L_\mathrm{d}L_\mathrm{q}(a^2+b^2)}, \tag{2.30}$$

$$i_\mathrm{pq} = \frac{\omega_\mathrm{s} R_\mathrm{s}\Psi_\mathrm{M}}{L_\mathrm{d}L_\mathrm{q}(a^2+b^2)} = i_\mathrm{pd}\cdot\frac{1}{\omega_\mathrm{s}\cdot\tau_\mathrm{q}}, \tag{2.31}$$

$$K_\mathrm{d} = i_\mathrm{d0}+i_\mathrm{pd}, \tag{2.32}$$

$$M_\mathrm{d} = -\left(i_\mathrm{d0}-i_\mathrm{pd}\right)\cdot\frac{a}{b}+\frac{R_\mathrm{s}L_\mathrm{d}i_\mathrm{d0}+\omega_\mathrm{s}L_\mathrm{q}^2 i_\mathrm{q0}}{L_\mathrm{d}L_\mathrm{q}b}, \tag{2.33}$$

$$K_\mathrm{q} = i_\mathrm{q0}+i_\mathrm{pq}, \tag{2.34}$$

$$M_\mathrm{q} = -\left(i_\mathrm{q0}-i_\mathrm{pq}\right)\cdot\frac{a}{b}+\frac{-\omega_\mathrm{s}L_\mathrm{d}^2 i_\mathrm{d0}+R_\mathrm{s}L_\mathrm{q}i_\mathrm{q0}-L_\mathrm{d}\omega_\mathrm{s}\Psi_\mathrm{M}}{L_\mathrm{d}L_\mathrm{q}b}, \tag{2.35}$$

$$a = \frac{1}{2}\cdot\left(\frac{1}{\tau_\mathrm{d}}+\frac{1}{\tau_\mathrm{q}}\right), \tag{2.36}$$

$$b = \frac{1}{2}\cdot\sqrt{4\omega_\mathrm{s}^2-\left(\frac{1}{\tau_\mathrm{d}}-\frac{1}{\tau_\mathrm{q}}\right)^2}, \tag{2.37}$$

the electric no-load time constants in the d- and q-axis $\tau_\mathrm{d} = L_\mathrm{d}/R_\mathrm{s}$, $\tau_\mathrm{q} = L_\mathrm{q}/R_\mathrm{s}$, and the initial condition of $i_\mathrm{d}(0) = i_\mathrm{d0}$, $i_\mathrm{q}(0) = i_\mathrm{q0}$, when the sudden short-circuit occurs.

At high rotational speed, due to $\omega_s \gg 1/\tau_\mathrm{d}, 1/\tau_\mathrm{q}$, equation (2.29) can be simplified with $b \approx \omega_\mathrm{s}$ as

$$
\begin{aligned}
i_{\mathrm{U}}(t) \cong & -\sqrt{i_{\mathrm{pd}}^2 + i_{\mathrm{pq}}^2} \cdot \cos(\omega_{\mathrm{s}} t + \gamma_0 + \beta_1) \\
& + \frac{1}{2} e^{-\frac{t}{\tau_{\mathrm{a}}}} \cdot \left[\sqrt{\left(K_{\mathrm{d}} + M_{\mathrm{q}}\right)^2 + \left(K_{\mathrm{q}} - M_{\mathrm{d}}\right)^2} \cdot \cos(2\omega_{\mathrm{s}} t + \gamma_0 + \beta_2) \right. \\
& \left. + \sqrt{\left(K_{\mathrm{d}} - M_{\mathrm{q}}\right)^2 + \left(K_{\mathrm{q}} + M_{\mathrm{d}}\right)^2} \cdot \cos(\gamma_0 + \beta_3) \right],
\end{aligned}
\tag{2.38}
$$

with the stator armature time constant of

$$\tau_{\mathrm{a}} = \frac{1}{a} = \frac{\tau_{\mathrm{d}} \tau_{\mathrm{q}}}{2(\tau_{\mathrm{d}} + \tau_{\mathrm{q}})}, \tag{2.39}$$

$$\beta_1 = \arctan\left(\frac{1}{\omega_{\mathrm{s}} \cdot \tau_{\mathrm{q}}}\right), \tag{2.40}$$

$$\beta_2 = \arctan\left(\frac{K_{\mathrm{q}} - M_{\mathrm{d}}}{K_{\mathrm{d}} + M_{\mathrm{q}}}\right), \tag{2.41}$$

$$\text{and } \beta_3 = \arctan\left(\frac{K_{\mathrm{q}} + M_{\mathrm{d}}}{K_{\mathrm{d}} - M_{\mathrm{q}}}\right). \tag{2.42}$$

The sudden short-circuit current has an AC component with the stator angular frequency ω_{s}, which is the steady-state short-circuit current. There are also a transient AC component with double stator angular frequency $2\omega_{\mathrm{s}}$ and a transient DC component. Both components decay with the stator armature time constant τ_{a}. In addition, the amplitude of the DC short-circuit current component is determined by the switching instant of an angle γ_0, which means that the short-circuit current has a maximum DC current offset when the angle $\gamma_0 + \beta_3$ is 0. The detailed derivation process of (2.29) can be found in Appendix D.

The electromagnetic short-circuit torque can be calculated with (2.43), which is derived with (2.29). It has a constant value due to I^2R-losses and a big alternating component with roughly ω_{s} (for $\tau_{\mathrm{d}} = \tau_{\mathrm{q}}$, hence for $L_{\mathrm{d}} = L_{\mathrm{q}}$)and if $L_{\mathrm{d}} \neq L_{\mathrm{q}}$ also with roughly $2\omega_{\mathrm{s}}$.

$$
\begin{aligned}
m_{\mathrm{e}}(t) &= \frac{m}{2} \cdot p \cdot \left(\Psi_{\mathrm{M}} \cdot i_{\mathrm{q}}(t) + \left(L_{\mathrm{d}} - L_{\mathrm{q}}\right) \cdot i_{\mathrm{d}}(t) \cdot i_{\mathrm{q}}(t)\right) \\
&= \frac{m}{2} \cdot p \cdot \left[-\frac{i_{\mathrm{pd}}}{\omega_{\mathrm{s}} \cdot \tau_{\mathrm{q}}} \left(\Psi_{\mathrm{M}} - \left(L_{\mathrm{d}} - L_{\mathrm{q}}\right) \cdot i_{\mathrm{pd}}\right) + e^{-\frac{t}{\tau_{\mathrm{a}}}} \cdot A_1 \cdot \cos(bt - \alpha_1) \right. \\
&\quad \left. + \frac{1}{2} \cdot \left(L_{\mathrm{d}} - L_{\mathrm{q}}\right) \cdot e^{-\frac{2t}{\tau_{\mathrm{a}}}} \cdot \left(\left(K_{\mathrm{d}} K_{\mathrm{q}} + M_{\mathrm{d}} M_{\mathrm{q}}\right) + A_2 \cdot \cos(2bt - \alpha_2)\right) \right],
\end{aligned}
\tag{2.43}
$$

with the coefficients

$$A_1 = \sqrt{\left(K_{\mathrm{q}} \Psi_{\mathrm{M}} - \left(L_{\mathrm{d}} - L_{\mathrm{q}}\right)\left(K_{\mathrm{q}} i_{\mathrm{pd}} + K_{\mathrm{d}} i_{\mathrm{pq}}\right)\right)^2 + \left(M_{\mathrm{q}} \Psi_{\mathrm{M}} - \left(L_{\mathrm{d}} - L_{\mathrm{q}}\right)\left(M_{\mathrm{q}} i_{\mathrm{pd}} + M_{\mathrm{d}} i_{\mathrm{pq}}\right)\right)^2}, \tag{2.44}$$

$$A_2 = \sqrt{\left(K_\mathrm{d}K_\mathrm{q} - M_\mathrm{d}M_\mathrm{q}\right)^2 + \left(K_\mathrm{d}M_\mathrm{q} + M_\mathrm{d}K_\mathrm{q}\right)^2}, \tag{2.45}$$

$$\alpha_1 = \arctan\left(\frac{M_\mathrm{q}\Psi_\mathrm{M} - (L_\mathrm{d} - L_\mathrm{q})\cdot(M_\mathrm{q}i_\mathrm{pd} + M_\mathrm{d}i_\mathrm{pq})}{K_\mathrm{q}\Psi_\mathrm{M} - (L_\mathrm{d} - L_\mathrm{q})\cdot(K_\mathrm{q}i_\mathrm{pd} + K_\mathrm{d}i_\mathrm{pq})}\right), \tag{2.46}$$

$$\alpha_2 = \arctan\left(\frac{K_\mathrm{d}M_\mathrm{q} + M_\mathrm{d}K_\mathrm{q}}{K_\mathrm{d}K_\mathrm{q} - M_\mathrm{d}M_\mathrm{q}}\right). \tag{2.47}$$

The sudden short-circuit torque is caused by all three phase currents, not by only one phase current. That is why the amplitude of the short-circuit torque does not depend on the switching instant γ_0 [15].

2.5.2 Numerical calculation of sudden short-circuit current and torque

In the previous section, the sudden short-circuit current and torque were analytically calculated with assumed constant d- and q-axis inductances L_d, L_q and the stator magnetic flux linkage from the rotor permanent magnets Ψ_M. In reality, however, the inductances vary with the degree of saturation of the iron stacks, and the stator magnetic flux linkage also may be reduced by transient induced eddy currents in the rotor magnets. Thus, to consider the influence of the iron saturation and eddy current reaction fields on the rotor magnets, 2D non-linear time-step numerical calculations were done with the help of the FEM software JMAG. With this software, the sudden short-circuit current, short-circuit torque, and magnetic flux distribution were simulated for constant rotor speed in a time-step solution with a step-wise rotating rotor. To minimize the

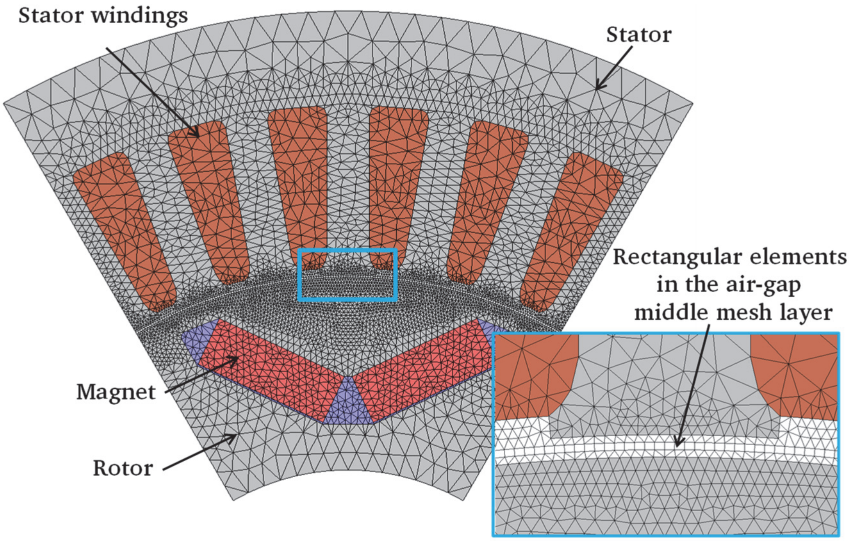

Fig. 2.16: 2D finite element model (FEM software JMAG) and the air-gap mesh for the IPMSM with $q_\mathrm{s} = 2$ and 5 step-skewed rotor

computing error of the numerical calculation, the air-gap mesh of the electric machine model was modelled as three layers with regular, nearly equal-sized mesh elements with a good aspect ratio. The upper mesh layer was fixed to the stator and did not rotate. The lower mesh layer rotated with the rotor. The middle layer mesh was reconfigurated for each step-wise rotor motion. The electromagnetic torque on the rotor was calculated with the middle mesh layer by the method of *Maxwell*'s stress tensor. When the rotor rotates, this middle mesh layer is regenerated automatically for each position of rotor movement. To reduce the influence of air-gap mesh distortion for calculating the electromagnetic torque, 1080 rectangular finite elements along the circumference of the air gap were used instead of triangular elements (Fig. 2.16). Using a time step of $\Delta t = 0.0133\,\mathrm{ms}$ and having the rotor rotate by the width of one element $\Delta\gamma = 0.33°$ (mechanical degree), the elements in the middle mesh layer were kept rectangular during the regeneration of the mesh at each time step. The rotor with 5 step skewing was used to calculate sudden short-circuit currents and torque.

2.5.3 Calculation results of sudden short-circuit current and torque

2.5.3.1 Sudden short circuit at generator no-load condition

At generator no-load operation, the electric machine is driven externally at constant speed with open stator winding terminals. Thus, the initial stator current is zero, $i_{\mathrm{d0}} = 0\,\mathrm{A}$ and $i_{\mathrm{q0}} = 0\,\mathrm{A}$. To consider the worst case for biggest current amplitude in phase U, a three-phase symmetrical short circuit was switched at voltage zero crossing in phase U ($\gamma_0 = 0$). Fig. 2.17 shows the comparisons between the results of the analytical and the numerical calculations.

Except for a small deviation shortly after the fault occurs, both results fit well with each other. The difference seen at the first current peak comes from the high iron saturation due to the high short-circuit current amplitude, which is considered by the numerical calculation with FEM software. The numerically calculated torque shows stator slotting influence, even though 5 step-skewed rotor was used for sudden short-circuit simulation at the numerical calculation. This means the skewed rotor could not compensate the torque ripple at short circuit.

Fig. 2.18 shows the magnetic flux distribution at the first peak of the stator current in phase U ($t = 2.4\,\mathrm{ms}$). Significantly high iron saturation is noticeable in the stator teeth

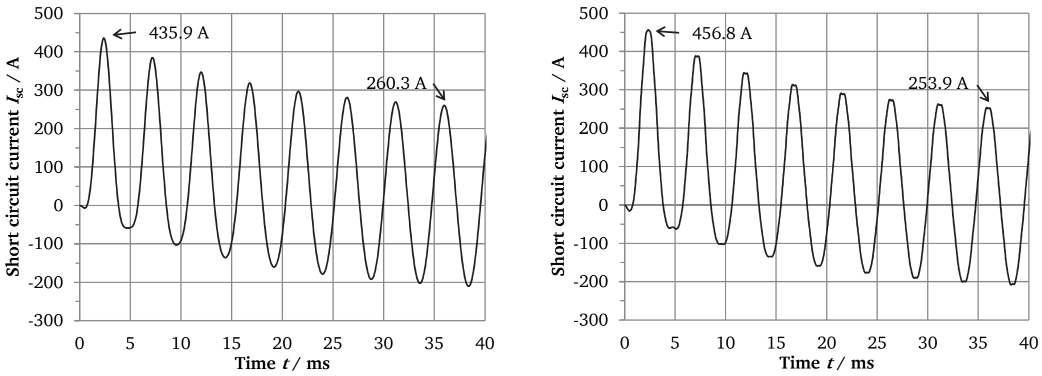

a) Sudden short-circuit current (analytical calculation)

b) Sudden short-circuit current (numerical calculation)

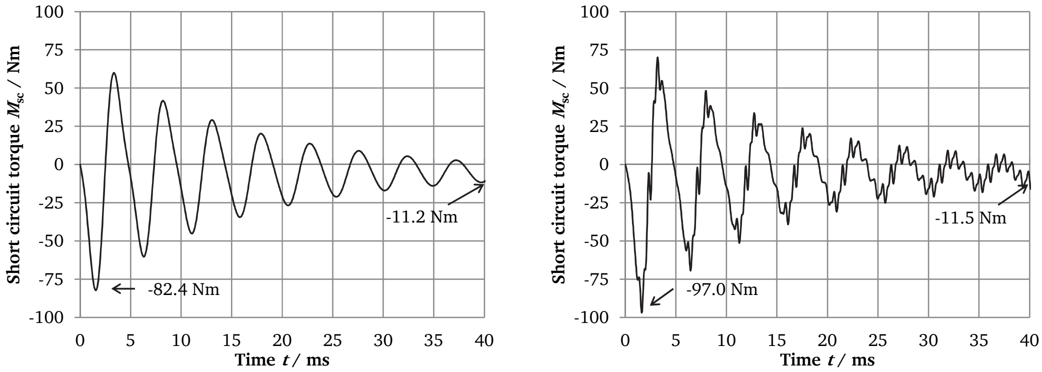

c) Sudden short-circuit torque (analytical calculation)

d) Sudden short-circuit torque (numerical calculation)

Fig. 2.17: Comparison between analytical calculation results and numerical calculation results of the sudden short-circuit current of phase U and of the short-circuit torque at short circuit after generator no-load condition, with low saturated constant inductances (for analytical calculation) $L_\mathrm{d} = 298\ \mu\mathrm{H}$ and $L_\mathrm{q} = 830\ \mu\mathrm{H}$ at a magnet temperature of 100 °C for the IPMSM with $q_\mathrm{s} = 2$ and 5 step skewed rotor

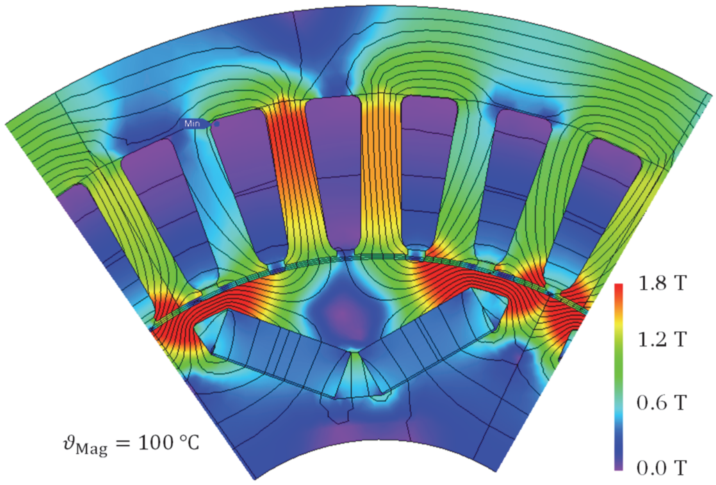

Fig. 2.18: Numerically calculated magnetic flux distribution at 2.4 ms after the short circuit at generator no-load condition, maximum current in phase U

and around the rotor iron bridges, which causes the deviation between the analytical and numerical calculations that is seen at the first current peak.

2.5.3.2 Sudden short circuit at rated load

For the numerical calculation of sudden short-circuit at load operation of the electric machine, a three-phase sine-wave current was impressed into the three-phase stator winding of the FEM simulation model. To verify the results of the analytical calculations of the sudden short-circuit current and torque with respect to the initial motor conditions, a three-phase short circuit was initiated at rated operation of the electric machine $P_\mathrm{N} = 24\ \mathrm{kW}$, $M_\mathrm{N} = 55\ \mathrm{Nm}$. For the rated load operation, the electric machine needs the fundamental stator phase current of $I_{\mathrm{s},1} = 99\ \mathrm{A}$ with the current phase shift angle of $\beta^* = -32.5°$, leading to the initial current components of $i_{\mathrm{d}0} = -75.2\ \mathrm{A}$ and $i_{\mathrm{q}0} = 118\ \mathrm{A}$. This current and current phase shift angle were impressed in the stator winding to produce rated torque.

Fig. 2.19 shows the comparison between analytical and numerical calculations of the sudden short-circuit current and torque at motor rated load condition. Once again, the analytically calculated current has an 8.9 % lower first current peak, as the high iron saturation of the electric machine is not considered analytically (Fig. 2.20). Note, that sudden short circuit at load yields a significantly higher transient current and torque peaks, when compared to sudden short circuit at no-load operation. Compared with the first current peak of sudden short-circuit current at no-load condition, the highest

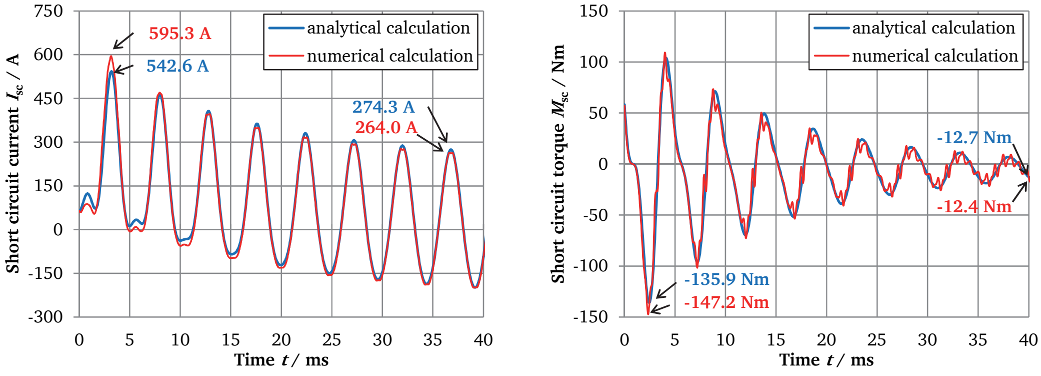

a) Sudden short-circuit current b) Sudden short-circuit torque

Fig. 2.19: Comparison between analytical calculation results (blue) and numerical calculation results (red)of the sudden short-circuit current of phase U and of the short-circuit torque at motor rated load condition, with low saturated constant inductances (for analytical calculation) $L_\mathrm{d} = 298\ \mu\mathrm{H}$ and $L_\mathrm{q} = 830\ \mu\mathrm{H}$ at a magnet temperature of 100 °C for the IPMSM with $q_\mathrm{s} = 2$ and 5 step skewed rotor

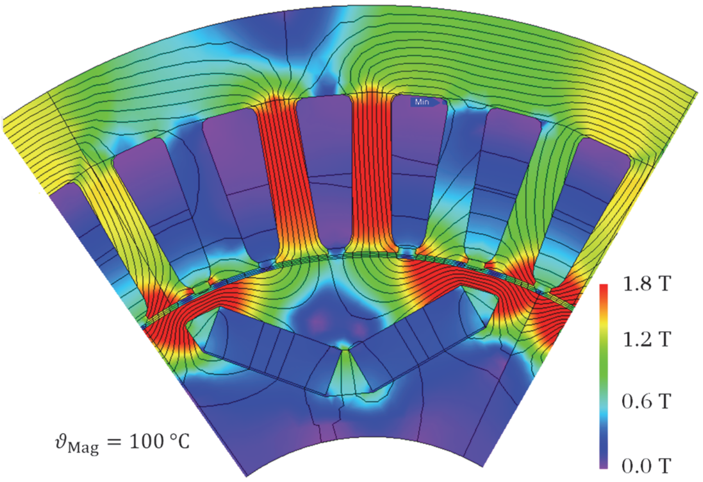

Fig. 2.20: Numerically calculated magnetic flux distribution at 3.2 ms after the short circuit at the rated load operation, maximum current in phase U

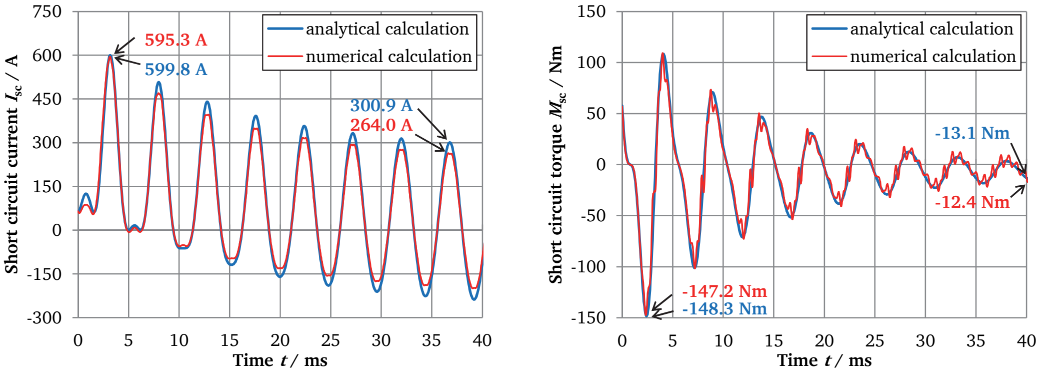

a) Sudden short-circuit current

b) Sudden short-circuit torque

Fig. 2.21: Comparison between analytical calculation results (blue) and numerical calculation results (red)of the sudden short-circuit current of phase U and of the short-circuit torque at motor rated load condition, with high saturated constant inductances (for analytical calculation) $L_{\mathrm{d}} = 261\ \mu\mathrm{H}$ and $L_{\mathrm{q}} = 777\ \mu\mathrm{H}$ at a magnet temperature of 100 °C for the IPMSM with $q_{\mathrm{s}} = 2$ and 5 step skewed rotor

current peak is increased by 30.3 % (595 A instead 457 A) and the torque peak is increased by 51.8 % (147 Nm instead of 97 Nm).

In order to check the influence of the iron saturation on the sudden short-circuit current, the analytical calculation was repeated with the calculated highly saturated smaller inductances $L_{\mathrm{d}} = 261\ \mu\mathrm{H}$ and $L_{\mathrm{q}} = 777\ \mu\mathrm{H}$ at the rated motor operation of the electric machine (Fig. 2.21). As a result, the two calculations fit well at the first current peak, at which time the electric machine is highly saturated. However, after the first peak of the sudden short-circuit current, some discrepancies appear between the current calculations. This difference comes from different inductances L_{d}, $L_{\mathrm{q}}$with differing degrees of magnetic saturation. In order to estimate more accurately the sudden short-circuit current by analytical calculation, the iron saturation-dependent inductances $L_\mathrm{d}(i_\mathrm{d}, i_\mathrm{q})$ and $L_\mathrm{q}(i_\mathrm{d}, i_\mathrm{q})$ are needed, which does not allow an analytical solution due to the non-linearity of the dynamic differential equation. The sudden short-circuit current and torque after no-load condition will be compared with the measured results in Chapter 5.5.

2.6 Thermal design of the electric machine

The purpose of the thermal behaviour analysis of an electric machine is to estimate temperature rises in various parts of the machine, especially thermally sensitive parts such as stator winding insulations and rotor permanent magnets. With the maximum allowed temperature rise in the electric machine, the continuous rated power and the short-term maximum power can be determined. When the winding temperature exceeds the maximum permissible temperature of the corresponding Thermal Class according to IEC 60034-1 for industrial motor purpose, insulation failure does not occur immediately, but the insulation life-span declines rapidly. As a rule of thumb, also the so-called *Montsinger*'s law, a temperature 10 K in excess of the maximum allowed temperature halves the life-span of the insulation [11]. Thus, high thermal load on the winding can cause an electric short circuit. As the application of the motor is for traction purpose, the standard IEC 60349-2 applies, which allows higher winding temperature for the same Thermal Class of insulation due to the much shorter total operation time of such a motor during its service life. In addition, large losses in the magnet and rotor laminations increase the magnet temperature. Due to the negative thermal coefficient of the magnet remanence, an increased magnet temperature reduces the magnetic flux linkage in the air gap, which corresponds to a reduction in the power of the electric machine. Furthermore, an elevated magnet temperature increases the risk of irreversible demagnetization of the magnet under strong stator field. Thus, heat transfer in the rotor must be considered carefully to avoid these problems. To ensure thermal stability, a thermal analysis of the electric machine is necessary during the motor design process.

There are several methods to predict the temperature rise in an electric machine. Here, a lumped parameter thermal network model and finite element analysis are discussed.

2.6.1 Material properties for thermal analysis

For the thermal analysis, typical values of the thermal properties of the material in the electric machine were used (Table 2.6). Given the insulation between the iron laminations, the iron sheet was considered as an anisotropic material which has better thermal conductivity in radial direction than in axial direction. Except for the iron laminations, all other materials were considered as isotropic materials, which have the same thermal conductivity in all directions. To increase heat transfer in the stator slots, after winding of the stator coils, the stator windings were impregnated with resin. To fill voids in the insulation resin, a vacuum pressure impregnation process was also carried out to ensure void-free insulation. For the stator windings, the impregnating resin *Dobeckan MF 8005* from company *Elantas Europe* GmbH was used. However, the exact thermal properties of this epoxide resin were not available. Thus, the average thermal conductivity of two other epoxide resins, one of which has high thermal conductivity $\lambda_{\mathrm{resin}} = 1\ \mathrm{W/(m \cdot K)}$ and the other low thermal conductivity $\lambda_{\mathrm{resin}} = 0.35\ \mathrm{W/(m \cdot K)}$, was used for the slot filling, yielding an average value $\lambda_{\mathrm{resin}} = 0.675\ \mathrm{W/(m \cdot K)}$.

Table 2.6 Material properties for thermal analysis

Material	**Thermal conductivity λ**		**Specific heat capacity c**	**Mass density ρ**
	$\mathrm{W/(m \cdot K)}$		**$\mathrm{W \cdot s/(kg \cdot K)}$**	**$\mathrm{kg/m^3}$**
Copper	400		380	8960
Aluminium alloy 7075 [70]	160		862	2800
Iron lamination	25 (radial)	1 (axial)	485	7850
Magnet	10		450	7680
Insulation paper [69]	0.14		1200	0.95
Epoxy based resin for winding impregnation	0.675		1400	1600
Epoxy based resin for casting winding overhang (EPIKOTE) [65]	1		1400	1950

2.6.2 Cooling system of the electric machine

Due to the high-power density of the electric machine for the DE-REX powertrain, a water jacket cooling method was designed to cool the machine effectively (Fig. 2.22). The spiral cooling channel with a height of 4 mm and a width of 13 mm was designed as helical cooling channel with 8 turns around the stator lamination stack to increase the contact surface in the cooling channel. The cooling effect of the system is also highly dependent on the thermal properties of the coolant medium. Higher specific heat capacity c and lower kinematic viscosity ν of the coolant increase the cooling capacity. Water is a good and common coolant, with a high specific heat c and low kinematic viscosity ν. However, water is not a suitable coolant for automotive applications due to its high freezing point at 0 °C. To allow operation at temperatures below 0 °C, a water and glycol mixture (50 % / 50 %) was used for cooling the electric machine. This mixture has a freezing point below −40 °C. Thus, under conditions above −40 °C, the freezing of the coolant should not occur. This mixture does, however, have a lower specific heat capacity c and a higher kinematic viscosity ν than water. Therefore, the cooling system with the water and glycol mixture has less cooling capacity than with pure water only. The properties of both coolants at a coolant temperature of 60 °C and at a coolant pressure of 1 bar are presented in Table 2.7.

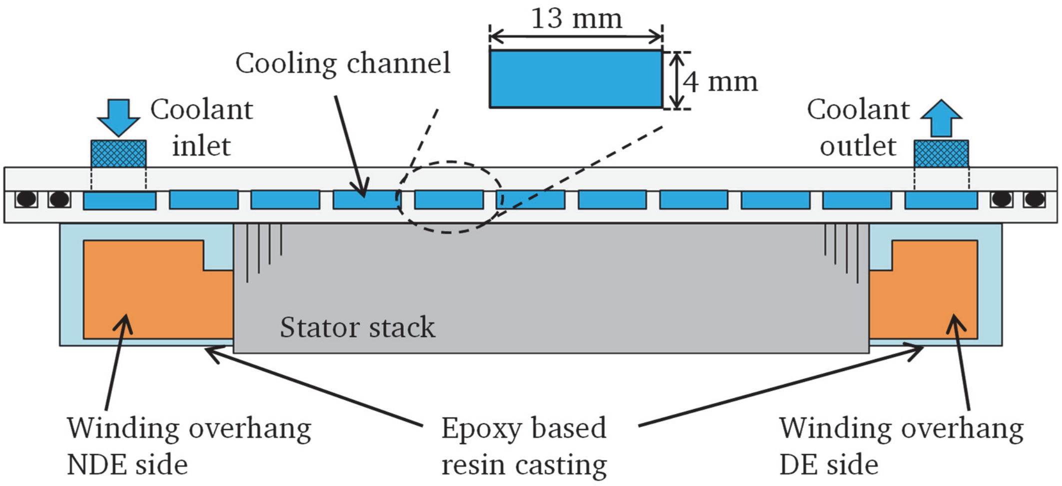

Fig. 2.22: Arrangement of the spiral cooling channels for liquid cooling jacket of the electric machine

The heat transfer coefficient $\alpha_{\mathrm{channel}}$ at the cooling channel surface is calculated with [21]

$$\alpha_{\mathrm{channel}} = 0.024 \cdot (c_{\mathrm{coolant}} \cdot \rho_{\mathrm{coolant}})^{0.3} \cdot \frac{\lambda_{\mathrm{coolant}}^{0.7}}{d_{\mathrm{channel}}^{0.2} \cdot \nu_{\mathrm{coolant}}^{0.5}} \cdot v_{\mathrm{coolant}}^{0.8}, \tag{2.48}$$

with the specific heat capacity of the coolant c_{coolant} in $\mathrm{W \cdot s/(kg \cdot K)}$, the mass density of the coolant ρ_{coolant} in $\mathrm{kg/m^3}$, the heat conductivity of the coolant $\lambda_{\mathrm{coolant}}$ in $\mathrm{W/(m \cdot K)}$, the hydraulic diameter of the cooling channel $d_{\mathrm{channel}} = 4 \cdot A_{\mathrm{channel}}/U_{\mathrm{channel}}$ in m (where the cross section area is A_{channel} and the wetted perimeter is U_{channel}), the kinematic viscosity of the coolant ν_{coolant} in $\mathrm{m^2/s}$, and the average velocity of the coolant in the cooling channel v_{coolant} in m/s. With the coolant volume rate of $\dot{V}_{\mathrm{coolant}} = 6\ \mathrm{l/min}$ based on the velocity of the coolant $v_{\mathrm{coolant}} = 1.92\ \mathrm{m/s}$, the heat transfer coefficient of the coolant with water and glycol mixture is $\alpha_{\mathrm{channel}} = 4425\ \mathrm{W/(m^2 \cdot K)}$. As mentioned, this value is by more than 60 % lower than the heat transfer coefficient of water as a coolant $\alpha_{\mathrm{water,channel}} = 11637\ \mathrm{W/(m^2 \cdot K)}$.

Table 2.7 Thermal properties of both coolants at a coolant temperature of 60 °C and a pressure of 1 bar [66]

Coolant properties		**Water/glycol: 50 % / 50 %**	**Water**
Specific heat capacity c	$\mathrm{W \cdot s/(kg \cdot K)}$	3410	4183
Mass density ρ	$\mathrm{kg/m^3}$	1057	983.2
Thermal conductivity λ	$\mathrm{W/(m \cdot K)}$	0.394	0.6508
Kinematic viscosity ν	$\mathrm{m^2/s}$	$1.5 \cdot 10^{-6}$	$0.474 \cdot 10^{-6}$

2.6.3 Lumped parameter thermal network model

The lumped parameter thermal model is an analytical method to estimate the temperature rise in the electric machine. The model is also known as a thermal equivalent circuit, which is similar to an electrical circuit with lumped resistive-capacitive parameters. A thermal equivalent circuit consists of thermal resistances, heat sources, and thermal capacitances which are represented in an electrical circuit by electrical resistances, current sources, and capacitors. Heat flow or heat current corresponds to electrical current,

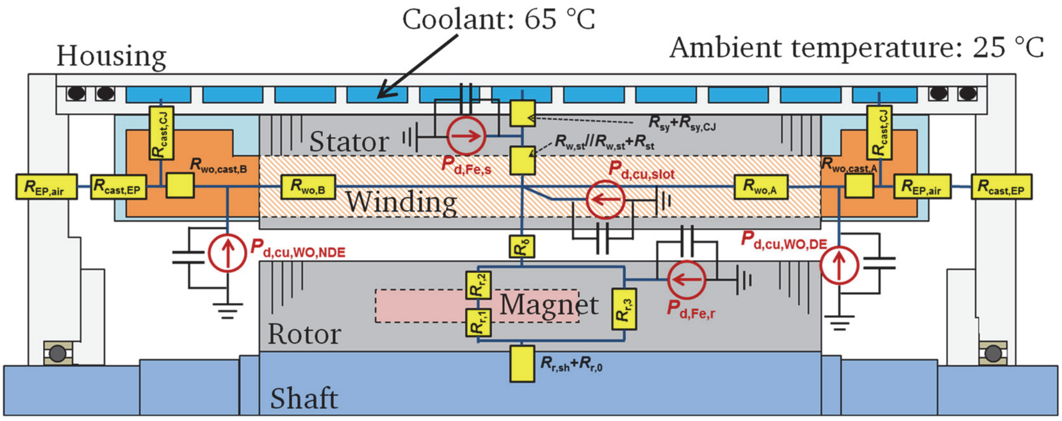

Fig. 2.23: Thermal network model of the electric machine with heat sources, heat capacitors and thermal resistances (see Appendix C)

and temperature differences in a machine component correspond to voltage drops. For the thermal analysis, the electric machine components were divided into a number of lumped components which had thermal capacitors and heat sources. They were connected to each other via thermal resistances.

Fig. 2.23 shows a simplified thermal network model of the electric machine for the DE-REX powertrain. The detailed thermal network model is discussed in Appendix C. The thermal resistances are represented by yellow rectangles. The heat sources, which represent losses in the electric machine, are indicated by the red circles with arrows at the corresponding position of the machine. Since the ohmic losses in the stator winding do not occur locally at a single node, the heat source of the stator winding is split into three separate heat sources: the ohmic losses in the stator slot $P_{\mathrm{d,cu,slot}}$, in the winding overhang Non-Driving End (NDE) side $P_{\mathrm{d,cu,WO,NDE}}$, and in the winding overhang Driving End (DE) side $P_{\mathrm{d,cu,WO,DE}}$. Since the winding overhang at the NDE side has a neutral point connection of the three-phase stator winding, where correspondingly additional heat is produced, the temperature rise in the winding overhang on the NDE side can be crucial. Thus, separate temperature rises in the two winding overhangs were considered. Furthermore, the thermal network model considers the iron losses in the stator lamination $P_{\mathrm{d,Fe,s}}$ and the rotor lamination $P_{\mathrm{d,Fe,r}}$ as well as the air friction losses in the air gap $P_{\mathrm{d,fr,air}}$. The thermal capacitors of heat storage are located parallel to the heat sources. The rotation of the rotor leads to air turbulence in the air gap and increases the equivalent thermal conductivity in the air gap $\lambda_{\delta,\mathrm{eq}}$ [22]. This enhances the heat transfer from the stator to the rotor and vice versa. Since the stator winding usually has a significantly higher temperature than the rotor, the rotor is cooled with an equivalent heat transfer coefficient $\alpha_{\mathrm{shaft}} = 14.1\ \mathrm{W/(m^2 \cdot K)}$ via the rotor shaft and through both bearings to the both end shields [16]. The coolant inlet temperature and the ambient temperature are selected based on the maximum permissible coolant outlet temperature at the used DMC524 inverter of company *BRUSA* of $\vartheta_{\mathrm{coolant}} = 65\ ^\circ\mathrm{C}$ and $\vartheta_{\mathrm{amb}} = 25\ ^\circ\mathrm{C}$ as inverter and motor are cooled in series with the same coolant flow, resulting with the lower temperature at the more sensitive power electronics of the inverter. Due to the increase of the stator winding resistance with rising winding temperature (3.3), the ohmic losses in the stator winding continuously increase with increasing winding temperature, which requires a simultaneous calculation of the temperature and loss distribution. The thermal analysis with the thermal network model was carried out with the program MATLAB Simulink with time steps of one second up to the corresponding end times (= intended operating times, OP2: 30 min, OP1 and OP3: 30 s). The time step is much shorter than the lowest thermal time constant and is therefore sufficiently small.

2.6.4 Numerical thermal model with FEM software JMAG

Based on the calculated ohmic losses in the stator winding and the calculated iron losses in the stator and the rotor lamination, the thermal behaviour of the electric machine was investigated with help of the FEM software JMAG. Due to the need to calculate the temperature rise in the winding overhangs and due to the mixed radial-axial direction of heat flow in the machine, a 2D FEM thermal model was not suitable. Thus, a 3D FEM thermal model of the electric machine was built for calculating the temperature rise at each operating point. However, for 3D FEM calculation, a high-performance computer and long simulation time are required. Thus, to simplify the 3D model, all electrical conductors per slot were combined into a single slot conductor with an equivalent trapezoidal form, indicated as yellow components in the cross section in Fig. 2.24. In addition, the insulation paper and resin for winding impregnation in the stator slot were considered as a homogenous slot filling material around the copper conductor, indicated as green components in the cross section in Fig. 2.24. For this, an equivalent thermal conductivity of the slot filling material was calculated as

$$\lambda_{\mathrm{sf,eq}} = \frac{h_{\mathrm{resin}} + h_{\mathrm{paper}}}{\frac{h_{\mathrm{resin}}}{\lambda_{\mathrm{resin}}} + \frac{h_{\mathrm{paper}}}{\lambda_{\mathrm{paper}}}} = \frac{\lambda_{\mathrm{resin}} \cdot \lambda_{\mathrm{paper}} \cdot (h_{\mathrm{resin}} + h_{\mathrm{paper}})}{\lambda_{\mathrm{paper}} \cdot h_{\mathrm{resin}} + \lambda_{\mathrm{resin}} \cdot h_{\mathrm{paper}}}, \tag{2.49}$$

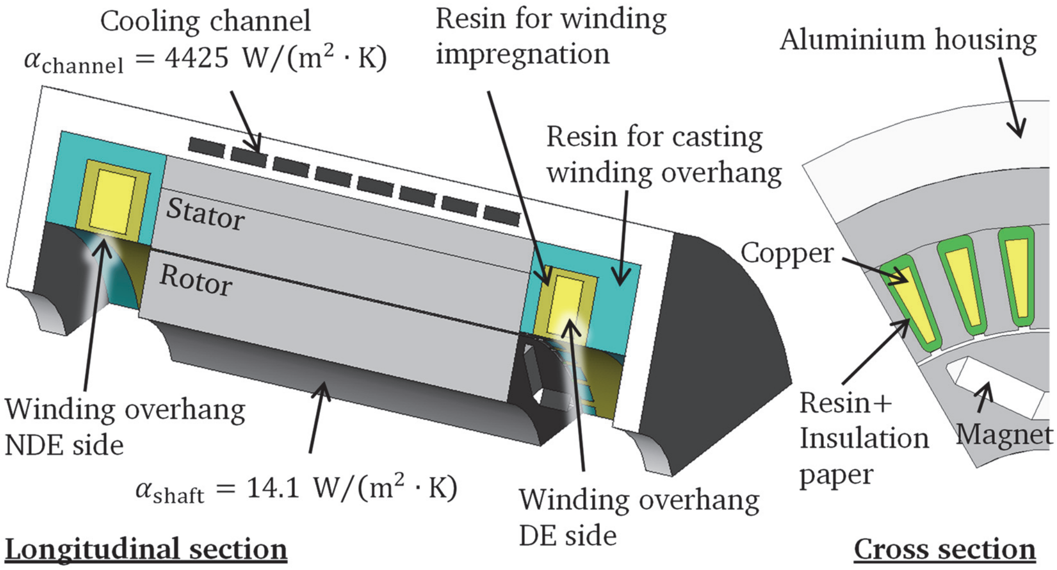

Fig. 2.24: Longitudinal and cross sections of the 3D thermal FEM model with omitted motor shaft (Program package JMAG)

where h_{resin} and λ_{resin} are the thickness and thermal conductivity of the simplified winding impregnation in the stator slot, respectively, and h_{paper} and λ_{paper} are the thickness and thermal conductivity of the insulation paper, respectively. With the thickness of the simplified winding impregnation in the stator $h_{\text{resin}} = 0.85$ mm and the insulation paper $h_{\text{paper}} = 0.25$ mm, the equivalent thermal conductivity of the slot filling material is $\lambda_{\text{sf,eq}} = 0.3597\ \text{W}/(\text{m} \cdot \text{K})$.

Given the symmetry per pole of the electric machine and the consequent symmetrical temperature distribution, it was sufficient to perform the FEM thermal calculation with one magnet pole and with the corresponding six stator slots and the associated housing and rotor segments. For the cooling effect on the housing surface with respect to adjacent non-moving air, an estimated heat transfer coefficient of $\alpha_{\text{air}} = 15\ \text{W}/(\text{m}^2 \cdot \text{K})$, which consists of natural convection and low heat radiation at a temperature difference of 60…80 K, was applied in the 3D FEM model.

2.6.5 Temperature rise calculation

Fig. 2.25 shows the comparison between analytically and numerically calculated temperature rise of the electric machine during 30 minutes at rated motor operation OP2. The calculation results show good agreement on the temperature rise at the stator windings. The analytical result gives a magnet temperature that is about 5 K lower than that

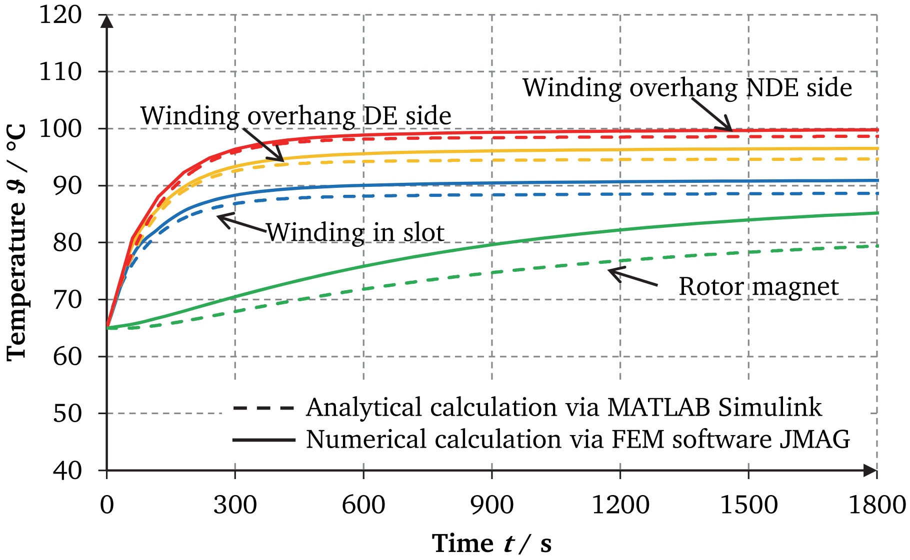

Fig. 2.25: Calculated temperature rises at rated motor load (OP2) with the average coolant temperature 65 °C and the initial temperature 65 °C: Temperature rise after 30 min at the winding overhang NDE side (red) $\Delta\vartheta_{\mathrm{WO,NDE}} = 33.6$ K (analytical), 34.8 K (numerical); at the winding overhang DE side (yellow) $\Delta\vartheta_{\mathrm{WO,DE}} = 29.7$ K (analytical), 31.5 K (numerical); at the winding in the stator slot (blue) $\Delta\vartheta_{\mathrm{slot}} = 23.6$ K (analytical), 25.9 K (numerical); and at the rotor magnet (green) $\Delta\vartheta_{\mathrm{M}} = 14.4$ K (analytical), 20.2 K (numerical)

shown by the numerical calculation after 30 min rated operation. This difference comes from the simplified geometry of the rotor magnet and of the rotor stack for the equivalent thermal network model, caused by the corresponding limited number of nodes for the rotor model. However, the calculation results of the thermal equivalent model show sufficient accuracy to predict the temperature rise during the driving cycle. Thus, this thermal network model was applied in the driving simulation model. The temperature in the winding overhang is higher than the temperature at the winding in the slot and the temperature of the stator iron sheets. The highest temperature occurs in the winding overhang on the NDE side with $\vartheta_{\mathrm{WO,NDE}} = 98.6$ °C (analytical), 99.8 °C (numerical). These temperatures are 4.0 K (analytical) and 3.3 K (numerical) higher than those in the winding overhang on the DE side, due to the losses in the neutral point connection on the NDE side. The temperature in the insulation is approximately as high as the temperature in the copper winding. Thus, the insulation has 80 K temperature reserve before reaching the maximum permissible temperature for its thermal class of stator windings (Thermal Class H) according to IEC 60034-1. As the motor is used for traction purpose, an even higher admissible temperature increase of 180 K is available due to IEC 60349-2. The temperature in the magnet is $\vartheta_{\mathrm{M}} = 79.4$ °C (analytical), 85.2 °C

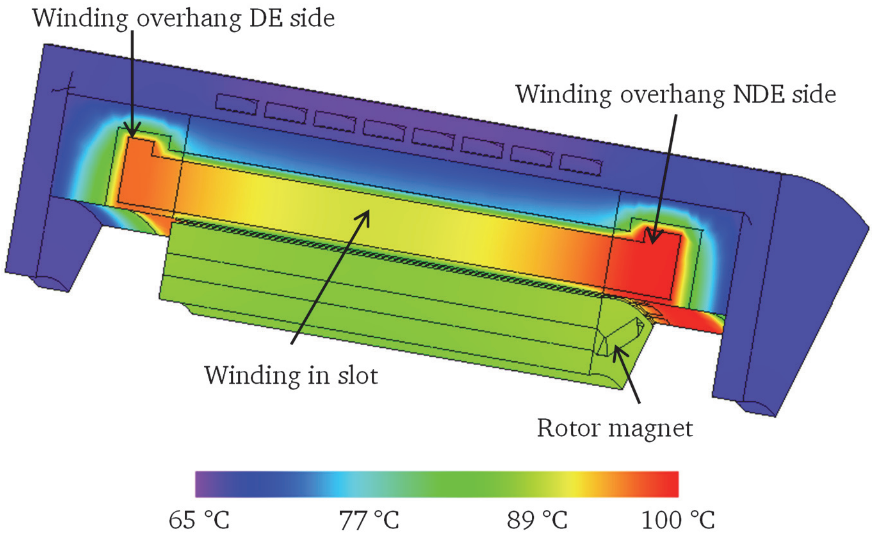

Fig. 2.26: Calculated temperature distribution at steady state at rated motor load (OP2) by numerical calculation with the average coolant temperature 65 °C: Steady-state temperature rise at the winding overhang NDE side $\vartheta_{\mathrm{WO,NDE}} = 100.0$ °C, at the winding overhang DE side $\vartheta_{\mathrm{WO,DE}} = 96.7$ °C , at the winding in the stator slot (blue) $\vartheta_{\mathrm{slot}} = 91.1$ °C, and at the rotor magnet (green) $\vartheta_{\mathrm{M}} = 87.7$ °C

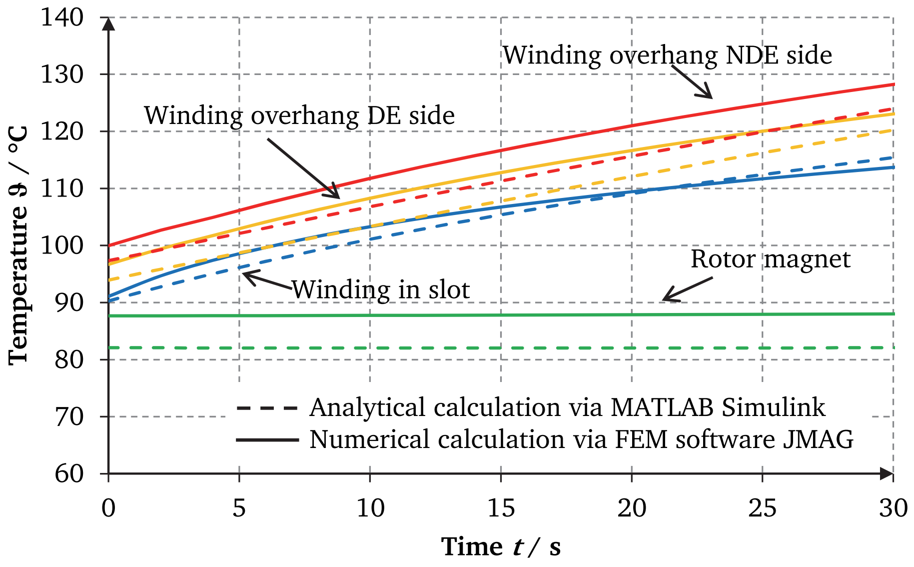

Fig. 2.27: Calculated temperature rises at motor overload (OP1) with the average coolant temperature 65 °C and the initial temperatures set to the steady-state temperature after rated motor load OP2: Temperature rise after 30 s of overload OP1 at the winding overhang NDE side (red) $\Delta\vartheta_{\mathrm{WO,NDE}} = 26.7$ K (analytical), 28.3 K (numerical); at the winding overhang DE side (yellow) $\Delta\vartheta_{\mathrm{WO,DE}} = 26.3$ K (analytical), 26.4 K (numerical); at the winding in the stator slot (blue) $\Delta\vartheta_{\mathrm{slot}} = 25.1$ K (analytical), 22.6 K (numerical); and at the rotor magnet (green) $\Delta\vartheta_{\mathrm{M}} = 0.0$ K (analytical), 0.4 K (numerical)

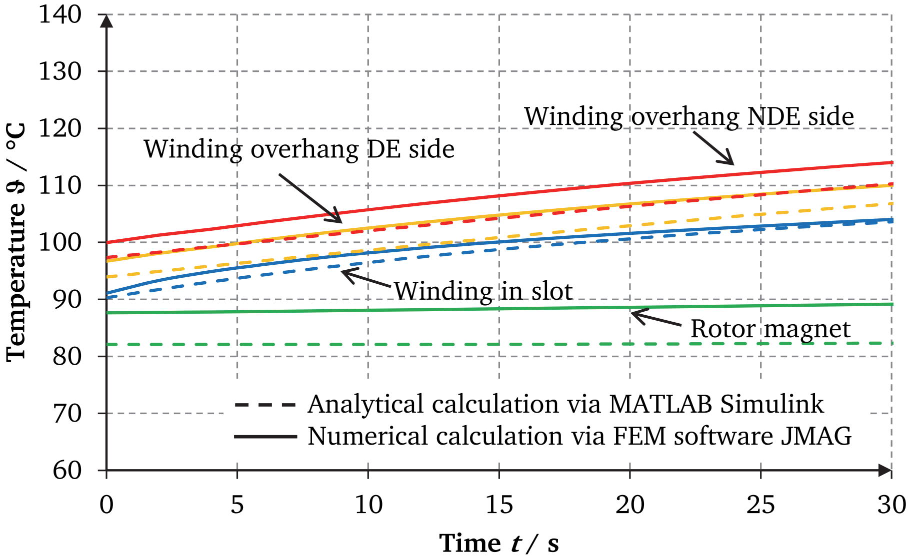

Fig. 2.28: Calculated temperature rises at motor overload (OP3) with the average coolant temperature 65 °C and the initial temperatures set to the steady-state temperature after rated motor load OP2: Temperature rise after 30 s of overload OP3 at the winding overhang NDE side (red) $\Delta\vartheta_{\mathrm{WO,NDE}} = 13.0$ K (analytical), 14.1 K (numerical); at the winding overhang DE side (yellow) $\Delta\vartheta_{\mathrm{WO,DE}} = 12.9$ K (analytical), 13.3 K (numerical); at the winding in the stator slot (blue) $\Delta\vartheta_{\mathrm{slot}} = 13.3$ K (analytical), 12.9 K (numerical); and at the rotor magnet (green) $\Delta\vartheta_{\mathrm{M}} = 0.3$ K (analytical), 1.5 K (numerical)

(numerical) after 30 minutes rated operation. Due to the long thermal time constant in the magnet, the magnet temperature did not reach its final temperature during these 30 min. Fig. 2.26 shows the temperature distribution at the thermally steady state of the electric machine at rated motor operation. A static temperature analysis showed the final magnet temperature would be about $\vartheta_{\mathrm{M},\infty} = 82.1$ °C (analytical), 87.7 °C (numerical), which is well below the 170 °C maximum operating temperature for the VACODYM 863 TP magnet.

The temperature rises for OP1 and OP3 were calculated with the shorter operating time of 30 s. The initial temperatures of the electric machine components were derived from the steady-state temperatures of the rated operation OP2. The simulated temperature rises for OP1 and OP3 are shown in Fig. 2.27 and Fig. 2.28, respectively. Due to the short operating duration 30 s, which is much lower than the thermal time constants, the temperature rises almost linear. The maximum temperature does not exceed the maximum permissible temperature of Thermal Class H materials (180 °C, IEC 60034-1) and the limit 230 °C according to IEC 60349-2. Thus, the electric machine can be operated at even higher overload, or a cheaper insulation material with a lower maximum permissible temperature, such as Thermal Class F with $\vartheta_{\max} = 155$ °C, can be used for mass production. The magnet temperatures show negligible small increases due to the low rotor losses and the short overload operating time.

2.7 Mechanical design of the electric machine

Due to the buried magnets in its rotor, an IPMSM does not require any carbon- or glass-fibre bandage to fix the magnets. They are fixed by the rotor lamination itself. In addition, with the buried magnet configuration, a smaller air-gap distance can be realized to reduce the magnet mass. As seen in Fig. 2.16, this electric machine does not have a middle iron bridge between two magnets in one pole. Thus, both side iron bridges per pole must withstand the centrifugal force of the magnets and of the rotor iron segment above the magnets. Therefore, it is indispensable to verify the mechanical stability of the rotor iron at high rotation speed and overspeed test. Accurate analytical calculation of mechanical stress on this complex rotor configuration is complicated. It can, however, be estimated by using an equivalent ring arrangement, as shown in Fig. 2.29. To calculate the tangential tensile stress placed on the side iron bridges by the centrifugal

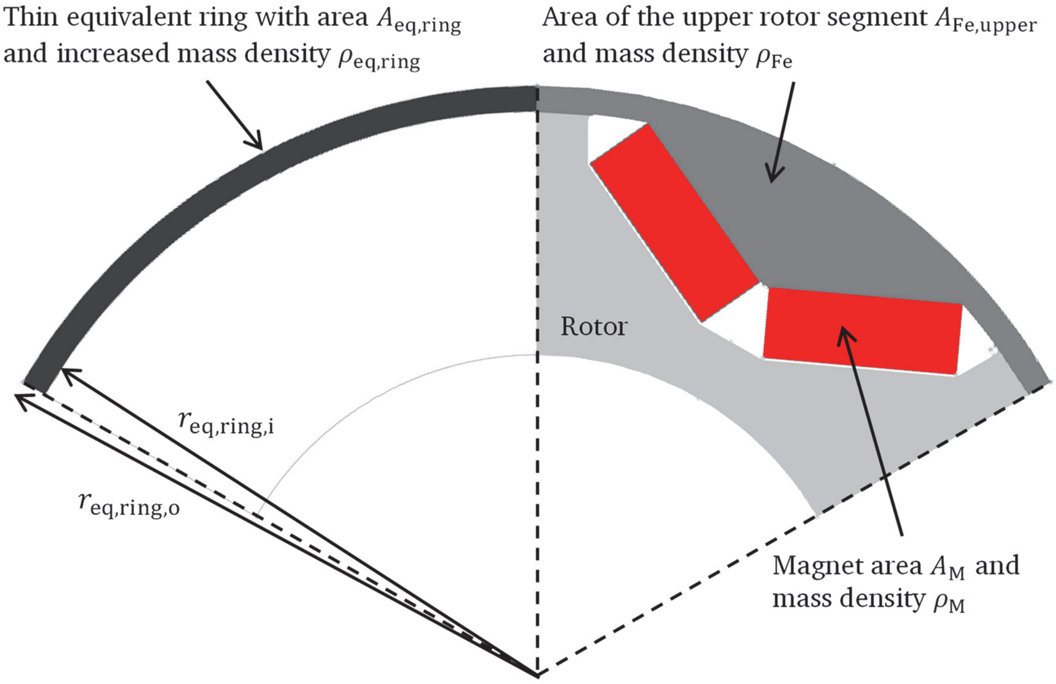

Fig. 2.29: Equivalent ring section with equivalent mass density as a replacement arrangement of the rotor buried magnets and rotor lamination segment above the magnets

force, a thin equivalent ring area $A_{\mathrm{eq,ring}}$ with an increased mass density $\rho_{\mathrm{eq,ring}}$ was used [23].

The thickness of the equivalent ring was defined by the height of the side iron bridge of the rotor $h_{\mathrm{bridge}} = 2\,\mathrm{mm}$. The tangential tensile stress in the equivalent ring $\sigma_{\mathrm{t,eq,ring}}$ with the corresponding equivalent mass density is calculated as follows:

$$\sigma_{\mathrm{t,eq,ring}} = r_{\mathrm{eq,ring,av}}^{2} \cdot (2\pi \cdot n)^{2} \cdot \rho_{\mathrm{eq,ring}}, \tag{2.50}$$

$$\rho_{\mathrm{eq,ring}} = \frac{(\rho_{\mathrm{Fe}} \cdot A_{\mathrm{Fe,upper}} + \rho_{\mathrm{M}} \cdot A_{\mathrm{M}})}{A_{\mathrm{eq,ring}}}, \tag{2.51}$$

with the average radius of the equivalent ring $r_{\mathrm{eq,ring,av}} = \left(r_{\mathrm{eq,ring,i}} + r_{\mathrm{eq,ring,o}}\right)/2$ in m, the rotational speed n in 1/s, the mass density of the rotor iron lamination ρ_{Fe} and the magnet ρ_{M} in kg/m^3, and the area of the upper rotor segment $A_{\mathrm{Fe,upper}}$ and the magnets A_{M} in m^2.

According to IEC 60349-2, the rotor iron must withstand 2 min of over-speed, which is 120 % of the maximum speed ($n_{\mathrm{max}} = 10000\,\mathrm{min}^{-1}$), thus the over-speed is 12000 min^{-1}. Since the mechanical stress is concentrated on the edges of the magnet pocket, a stress concentration factor of 2 was considered, i.e. $\sigma_{\mathrm{t,max}} = 2 \cdot \sigma_{\mathrm{t,eq,ring}}$. Furthermore, it has to be considered that the metal gives way by repeatedly applied loads much earlier than its steady-state yield strength point, which is determined by tensile testing. This phenomenon, the so-called fatigue of the metal, can be quantified with the stress-cycle (S-N) curve, also known as a *Wöhler* curve. In the case of the prototype machine, therefore, a safety factor of 2 was assumed. It reduces the maximum permissible tensile stress by half ($\sigma_{\mathrm{t,max}} < R_{\mathrm{m}}/2$). The analytical calculation shows that the maximum tangential

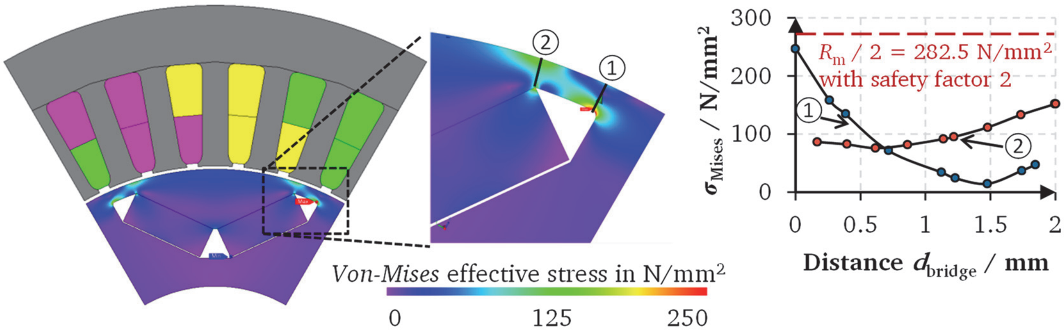

Fig. 2.30: Calculated *Von-Mises* effective stress distribution in the rotor iron bridge at over-speed 12000 min^{-1}

stress in the rotor iron bridge is $\sigma_{\mathrm{t,max}} = 206.7\ \mathrm{N/mm^2}$, which is below one half of the maximum permissible tensile strength of the iron lamination M270-35A, $R_{\mathrm{m}}/2 = 282.5\ \mathrm{N/mm^2}$. In the analytical calculation, only the centrifugal force was considered for the mechanical stress calculation.

The magnetic pulling force between the magnets and the iron sheets in the magnet pockets, which is proportional to the square of the magnetic flux density, was neglected in the analytical calculation of the mechanical stress on the rotor iron bridge. On the other hand, the magnetic pull was considered in the mechanical 2D FEM simulation. The numerically calculated pull on each magnet is 387.1 kN/m^2. This shows good agreement with the analytically calculated magnetic pull (387.2 kN/m^2). The mechanical stress on the rotor iron lamination was numerically calculated with FEM software JMAG. Fig. 2.30 shows the results of the numerical calculation of *von-Mises* effective stress in the rotor. The maximum *von-Mises* effective stress σ_{Mises} in the rotor iron bridge is 245 N/mm^2, but it is only in a limited area on the inside of the rotor iron bridge due to the stress concentration effect. Thus, the rotor iron bridge has enough height to withstand the centrifugal force at high rotation speed.

3. Loss components and efficiency calculation

For the efficiency calculation of the electric machine, the calculation of the ohmic losses $P_{\mathrm{d,cu,DC}}$ and eddy current losses in the stator winding $P_{\mathrm{d,cu,AC}}$, the iron losses $P_{\mathrm{d,Fe}}$ as the sum of hysteresis losses $P_{\mathrm{d,Fe,hy}}$ and the classical eddy current losses $P_{\mathrm{d,Fe,ed}}$ in the stator and rotor iron laminations, the air friction losses on the rotor surface $P_{\mathrm{d,fr,air}}$, the bearing losses $P_{\mathrm{d,fr,bearing}}$, the additional eddy current losses in the magnets $P_{\mathrm{d,M}}$, and the switching and conduction losses in the inverter$P_{\mathrm{d,inv}}$ are presented in this chapter.

3.1 DC ohmic losses in stator winding

Typically, ohmic losses are the dominant losses of the electric machine at low and medium speed. The ohmic losses produce heat by conducting the current in the stator copper winding and cause a temperature increase in the stator winding and in the electric machine. Thus, during the design process, it is important to consider that the produced heat must be dissipated properly in order to avoid undesired heat damage of the insulation. The ohmic losses are proportional to the resistance of the stator winding R_{s} and proportional to the square of the RMS stator current I_{s}^2. The DC winding resistance at ambient air temperature of 20 °C is calculated with (3.1), with the number of turns per phase N_{s}, the axial iron stack length l_{Fe}, the average length of the winding overhang l_{b}, the electric conductivity of copper $\kappa_{\mathrm{cu,20°C}} = 57\,\mathrm{MS/m}$ at 20°C, the number of parallel branches a per phase, the number of parallel strands a_{i} per branch and the cross-section area of each strand A_{str}.

$$R_{\mathrm{DC,20°C}} = \frac{2 \cdot N_{\mathrm{s}}(l_{\mathrm{Fe}} + l_{\mathrm{b}})}{\kappa_{\mathrm{cu,20°C}} \cdot a \cdot a_{\mathrm{i}} \cdot A_{\mathrm{str}}} \tag{3.1}$$

The average winding overhang length of the electric machine with a distributed winding with round wires can be calculated approximately with (3.23.2) with the average coil span in m [24].

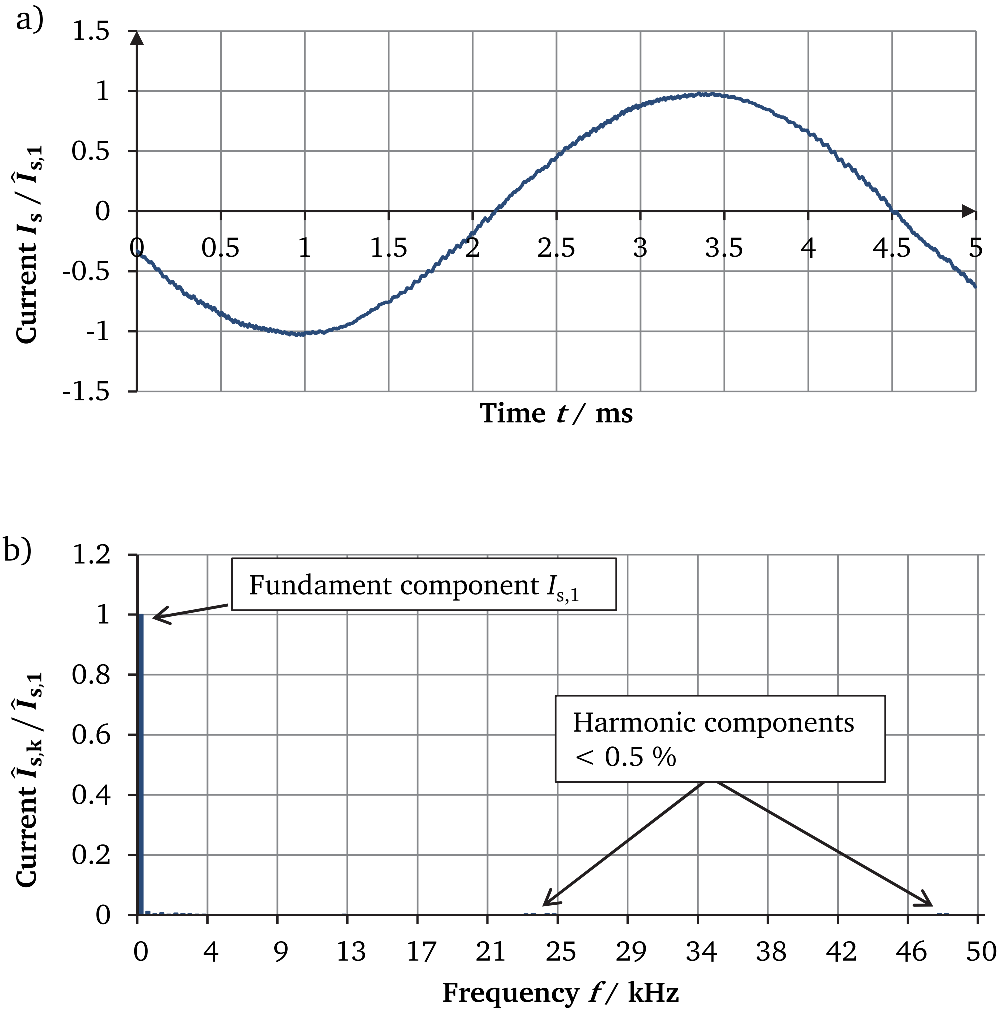

Fig. 3.1: Measured rated phase current (U-phase): a) Current waveform in per unit value, b) *FOURIER* amplitude spectrum of the measured phase current in per unit value with the amplitude of the fundamental component $\hat{I}_{s,1} = 140$ A, rated speed of $n = 4167\ \text{min}^{-1}$, the rated frequency of $f_s = 208.35$ Hz and the switching frequency of $f_{sw} = 24$ kHz

$$l_b = 1.2 \cdot W + 0.05, \quad [l_b] = \text{m}, [W] = \text{m} \tag{3.2}$$

With the average winding overhang length of $l_b = 98.6$ mm, the calculated stator phase resistance is $R_{s,20°C} = 19.58\ \text{m}\Omega$. This shows a satisfying agreement with the measured average stator resistance per phase of $R_{s,20°C} = 20.13\ \text{m}\Omega$ as (3.2) is only a rough estimate. For calculating the ohmic losses of the electric machine, the measured resistance value was used.

The stator resistance varies with the temperature of the stator winding ϑ_{cu}. The copper has a positive temperature coefficient of resistivity $\alpha_{cu} = 1/255$ at 20 °C. The resistivity of the copper rises with increasing temperature $\rho_{\mathrm{cu}}(\vartheta_{\mathrm{cu}}) = \rho_{\mathrm{cu,20°C}} \cdot \left(1 + \alpha_{\mathrm{cu}}(\vartheta_{\mathrm{cu}} - 20)\right)$, and the winding resistance at the winding temperature of ϑ_{cu} is calculated by (3.3).

$$R_{\mathrm{DC}}(\vartheta_{\mathrm{cu}}) = R_{\mathrm{DC,20°C}} \cdot \left(1 + \frac{\vartheta_{\mathrm{cu}} - 20}{235 + 20}\right),\ [\vartheta_{\mathrm{cu}}] = °\mathrm{C} \tag{3.3}$$

For the winding resistance calculation, the average winding temperature $\vartheta_{\mathrm{cu,av}}$ should be used. This value was approximated by the measured winding temperature in the stator slot in the axial centre of the iron stack and by both winding overhangs' average temperature, from (5.5).

Fig. 3.1 shows the measured stator phase current waveform at rated load OP2 and its *FOURIER* amplitude spectrum. Due to the high switching frequency of $f_{\mathrm{sw}} = 24\,\mathrm{kHz}$ and the big stator inductance, the measured current shows near sinusoidal shape. The measured amplitudes of the higher-order current harmonics around the switching frequency and its multiples are less than 0.5 % of the amplitude of the fundamental component. Thus, the current ripple from the Pulse-Width Modulation (PWM) voltage signal has been neglected for further loss calculation, due to its small values. The DC ohmic losses in the stator winding are calculated with (3.4) with the number of phases m_{s}.

$$P_{\mathrm{d,cu,DC}} = m_{\mathrm{s}} \cdot R_{\mathrm{DC}}(\vartheta_{\mathrm{cu}}) \cdot I_{\mathrm{s,1}}^2 \tag{3.4}$$

3.2 Additional eddy current losses in stator winding

In order to reduce the skin effect inside the copper conductor caused by the AC high frequency slot leakage flux, the conductors of the prototype machine were separated into four parallel strands per each turn ($2 \times \emptyset 0.67\,\mathrm{mm}$ and $2 \times \emptyset 0.8\,\mathrm{mm}$), and those strands were connected in parallel $a_{\mathrm{i}} = 4$. Due to the high frequency, causing eddy currents, the current density in each strand might not be evenly distributed over the cross-section of the strand. Further, due to the untwisted strands, the current in the four parallel strands might not be evenly distributed. This unequally distributed current among the parallel strands, which is the so-called first-order current displacement effect, and the non-uniform current density in each strand, which is the so-called second-order current displacement effect, cause additional ohmic losses in the stator winding. These additional losses, according to [25], are estimated analytically with the increased resistance factor for the first-order current displacement effect k_{R1}, and for the second-order current displacement effect $\bar{k}_{\mathrm{R2}}$. The equations (3.5) – (3.9) are used in the analytical calculation of the additional ohmic losses from the first-order current displacement on the electric machine with a two-layer winding. For simplification of the calculation, the round strands with diameter d_{str} are replaced by a square conductor, which has the same cross section area, with the conductor height of $b_{\mathrm{str}} = \sqrt{\pi} \cdot d_{\mathrm{str}}/2$.

$$P_{\mathrm{d,cu,ad1}} = m_{\mathrm{s}} \cdot R_{\mathrm{DC}}(\vartheta_{\mathrm{cu}}) \cdot I_{\mathrm{s,1}}^2 \cdot (k_{\mathrm{R1}} - 1), \tag{3.5}$$

with

$$k_{\mathrm{R1}} = \varphi(\xi_1) + \frac{m_{\mathrm{v}}^2 - 1}{4} \cdot \psi(\xi_1), \tag{3.6}$$

$$\varphi(\xi_1) = \xi_1 \cdot \frac{\sinh(2\xi_1) + \sin(2\xi_1)}{\cosh(2\xi_1) - \cos(2\xi_1)}, \tag{3.7}$$

$$\psi(\xi_1) = 2\xi_1 \cdot \frac{\sinh(\xi_1) - \sin(\xi_1)}{\cosh(\xi_1) + \cos(\xi_1)}, \tag{3.8}$$

$$\xi_1 = n_{\mathrm{v}} \cdot b_{\mathrm{str}} \cdot \sqrt{\pi \cdot \mu_0 \cdot f_{\mathrm{s}} \cdot \kappa_{\mathrm{cu}}(\vartheta_{\mathrm{cu}}) \cdot \frac{l_{\mathrm{Fe}}}{l_{\mathrm{Fe}} + l_{\mathrm{b}}} \cdot \frac{n_{\mathrm{h}} \cdot b_{\mathrm{str}}}{b_{\mathrm{Q,av}}}}, \tag{3.9}$$

where $\xi_1$is the ‘reduced conductor height’ for the first-order current displacement effect, n_{v} is the number of stacked strands per turn in a vertical position, $n_{\mathrm{h}}$is the number of strands side by side, $b_{\mathrm{Q,av}}$ is the average slot width and m_{v} is the number of conductor layers in vertical slot position.

The increased resistance factor for the first-order current displacement effect k_{R1} varies with the strands’ arrangement in the slot. When the 4 strands are vertically aligned, huge current displacement occurs due to the big total height per turn, the so-called ‘worst case’ (Fig. 3.2 a). When the 4 strands lie horizontally in the slot, the current displacement effect is minimized, the so-called ‘best case’ (Fig. 3.2 b). For estimating the increased resistance factor for the first-order current displacement, the average value of both cases was used.

The additional ohmic losses from the second-order current displacement are calculated according to [25] with (3.10) – (3.17). Due to the different stray fluxes in the conductors in the stator slot and the conductors in the winding overhang, the resistance increasing factor $\bar{k}_{\mathrm{R2}}$ is used (3.12). Typically, the stray magnetic flux in the winding overhang of electric machine with a rating < 100 kW is negligibly small, thus the resistance increasing factor for the winding overhang is $k_{\mathrm{R2,wo}} = 1$ [25]. In addition, due to the short-pitched winding $W < \tau_{\mathrm{p}}$ of the stator, two different phase currents may flow in the upper and lower layer per stator slot (e.g., +U and –W phase in the slot number 2 in Fig. 2.2). This phase shift between two phase currents excites less slot stray flux than would a slot with two same-phase currents in upper and lower layer (e.g., +U and +U phase in the slot number 1 in Fig. 2.2). Thus, this effect is considered with equations (3.12) – (3.14), where $Q_{\mathrm{a}} = 18$ is the total number of stator slots with two same-phase currents, $Q_{\mathrm{b}} = 18$ is the total number of stator slots with two different-phase currents, k_{R2a} is the resistance correction factor for the slot with the same-phase currents, and k_{R2b} is the resistance correction factor for the slot with two different-phase currents with the current phase shift $\Delta\varphi$ between the phase current in upper and lower layer $\Delta\varphi = \frac{\pi}{3}$.

$$P_{\mathrm{d,cu,ad2}} = m_{\mathrm{s}} \cdot R_{\mathrm{DC}}(\vartheta_{\mathrm{cu}}) \cdot I_{\mathrm{s,1}}^2 \cdot \left(\bar{k}_{\mathrm{R2}} - 1\right), \tag{3.10}$$

with

$$\bar{k}_{\mathrm{R2}} = \frac{k_{\mathrm{R2}} \cdot l_{\mathrm{Fe}} + k_{\mathrm{R2,wo}} \cdot l_{\mathrm{b}}}{l_{\mathrm{Fe}} + l_{\mathrm{b}}} = \frac{k_{\mathrm{R2}} \cdot l_{\mathrm{Fe}} + l_{\mathrm{b}}}{l_{\mathrm{Fe}} + l_{\mathrm{b}}}, \tag{3.11}$$

$$k_{\mathrm{R2}} = \frac{k_{\mathrm{R2a}} \cdot Q_{\mathrm{a}} + k_{\mathrm{R2b}} \cdot Q_{\mathrm{b}}}{Q_{\mathrm{a}} + Q_{\mathrm{b}}}, \tag{3.12}$$

$$k_{\mathrm{R2a}} = \varphi(\xi_2) + \frac{m_{\mathrm{T}}^2 - 1}{3} \cdot \psi(\xi_2), \tag{3.13}$$

$$k_{\mathrm{R2b}} = \varphi(\xi_2) + \left(\frac{5m_{\mathrm{T}}^2 - 8}{24} + \frac{m_{\mathrm{T}}^2}{8}\cos(\Delta\varphi)\right) \cdot \psi(\xi_2), \tag{3.14}$$

$$\varphi(\xi_2) = \xi_2 \cdot \frac{\sinh(2\xi_2) + \sin(2\xi_2)}{\cosh(2\xi_2) - \cos(2\xi_2)}, \tag{3.15}$$

$$\psi(\xi_2) = 2\xi_2 \cdot \frac{\sinh(\xi_2) - \sin(\xi_2)}{\cosh(\xi_2) + \cos(\xi_2)}, \tag{3.16}$$

$$\xi_2 = b_{\mathrm{str}} \cdot \sqrt{\pi \cdot \mu_0 \cdot f_{\mathrm{s}} \cdot \kappa_{\mathrm{cu}}(\vartheta_{\mathrm{cu}}) \cdot \frac{n_{\mathrm{h}} \cdot b_{\mathrm{str}}}{b_{\mathrm{Q,av}}}}. \tag{3.17}$$

The calculated ohmic losses with the resistance correction factors (k_{R1} and $\bar{k}_{\mathrm{R2}}$) at the three operation points OP1…OP3 are presented in Table 3.1. The ohmic losses in the stator winding are increased by 1.0 % at rated speed of 4167 min^{-1} ($f_{\mathrm{s}} = 208.35$ Hz) and by 5.5 % at maximum speed of 10000 min^{-1} ($f_{\mathrm{s}} = 500$ Hz), compared to the corresponding DC ohmic losses $P_{\mathrm{d,cu,DC}}$.

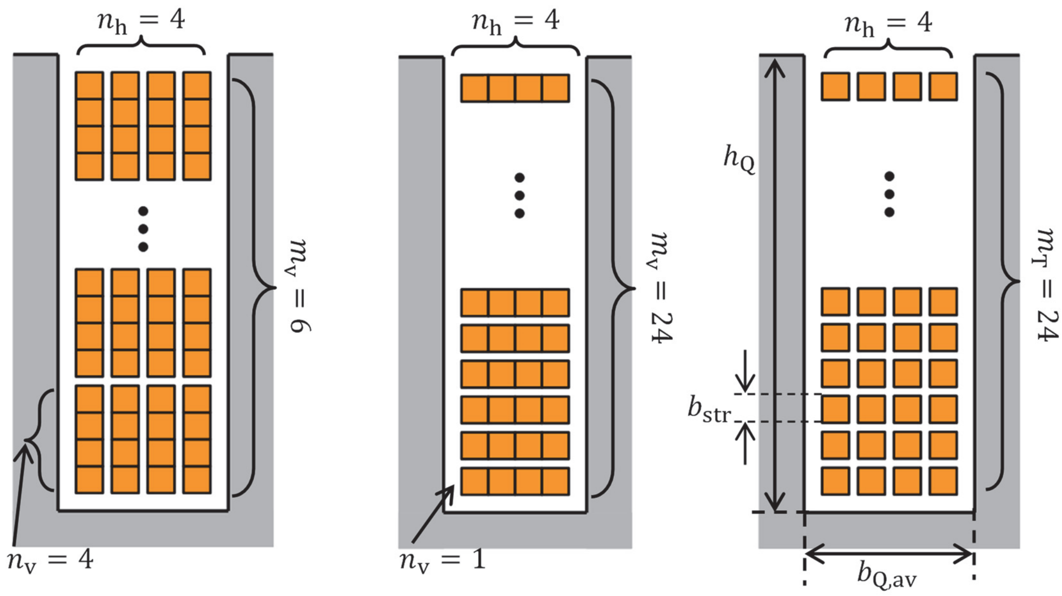

a) b) c)

Fig. 3.2: Arrangement of strands in the stator slot for the additional ohmic losses calculation of a) first-order current displacement effect for the worst case, b) first-order current displacement effect for the best case, and c) second-order current displacement effect

Table 3.1 Calculated ohmic losses in the stator winding at load condition OP1…OP3 with $\vartheta_{cu} = 100$ °C and $R_s(100°C) = 26.4$ mΩ

	OP1	**OP2**	**OP3**
Speed n / min^{-1}	4167	4167	10000
Current $I_{s,1}$ / A	184.0	95.3	138.4
k_{R1} / -	1.0087	1.0087	1.0499
$\bar{k}_{R2}$ / -	1.0017	1.0017	1.0096
$P_{d,cu,DC}$ / W	2686.9	719.8	1519.2
$P_{d,cu,ad1}$ / W	23.3	6.2	75.8
$P_{d,cu,ad2}$ / W	4.5	1.2	14.5
$P_{d,cu,AC}$ / W	2714.7	727.3	1609.5

3.3 Iron losses

At AC conditions, iron losses arise in the stator and the rotor laminations. These iron losses increase, as the frequency and flux density increase. According to *H. Jordan* in [26], the iron losses can be separated into static hysteresis losses and dynamic eddy current losses. The hysteresis losses are proportional to the frequency f and the eddy current losses increase with the square of the frequency f^2. Both loss components increase proportionally with the square of the amplitude of the magnetic flux density B^2 (3.18). The unit of the loss coefficients of p_{Fe}, c_{Hy}, and c_{Ft} is W/kg.

$$p_{\mathrm{Fe}} = \left(c_{\mathrm{Hy}} \cdot \frac{f}{f_0} + c_{\mathrm{Ft}} \cdot \left(\frac{f}{f_0}\right)^2\right) \cdot \left(\frac{B}{B_0}\right)^2 \tag{3.18}$$

Typically, for automobile applications the powertrain is equipped with a high-speed electric machine to increase power density. Thus, thin iron laminations are used to reduce iron losses in the electric machine. For the prototype electric machine of the DE-REX powertrain, the iron sheet type M270-35A with a lamination thickness of 0.35 mm was used, which is guaranteed by the sheet manufacturer to have losses of less than 2.7 W/kg at the frequency of 50 Hz and the magnetic flux density of 1.5 T [27]. For the iron loss calculation, the loss coefficients c_{Hy} and c_{Ft} can be estimated either by means of a system of linear equations or by the method of least squares with a certain frequency range [28]. For example, by means of a system of linear equations, with the iron loss density of 2.47 W/kg and 5.92 W/kg at a flux density of 1.5 T and frequencies of 50 Hz and 100 Hz, respectively (from the core loss data in Appendix B), the estimated loss coefficients are c_{Hy} = 1.98 W/kg and c_{Ft} = 0.49 W/kg, with the base frequency f_0 = 50 Hz and the base magnetic flux density B_0 = 1.5 T. With these obtained loss coefficients and the amplitude of the magnetic flux density in the iron sheets, the iron losses can be calculated either analytically or numerically by post-processing of FEM software data. This method, however, may cause large errors of the iron loss, when the operating frequency range differs strongly from the value range 50…100 Hz [29]. Thus, selecting the correct frequency range for the loss coefficient calculation is necessary. To minimize the estimation errors within the given frequency range, the iron losses can be estimated by entering the complete set of measured core loss data of the material for each available measured frequency (50, 100, 200, 400, 1000, and 2500 Hz for M270-35A iron sheet in Appendix B) from the electrical steel company into the FEM software. Via FEM software JMAG, the iron losses for the prototype machine can be determined by post-processing with the complete measured set of core loss data. During the magnetic field analysis process, the software calculates the variation of the magnetic flux density per each finite element for an electrical period of the magnetic stator and rotor fields. After the simulation, the variation of the magnetic flux density is decomposed into several frequency orders k by *Fourier* series expansion of the flux-density variation with time in post-processing by the software JMAG. Using the iron loss calculation method with the core loss table, the iron losses are calculated with (3.19) [30]

$$P_{\mathrm{d,Fe}} = \sum_{i=1}^{n_{\mathrm{el}}} \left\{ \sum_{k=1}^{N} a(B_k) \cdot f_k + b(B_k, f_k) \cdot f_k^2 \right\} \cdot V_i \cdot \rho_{\mathrm{Fe}} \,, \tag{3.19}$$

where B_k is magnetic flux density *Fourier* amplitude in T at the frequency order k, f_k is frequency in Hz at the frequency order k, $a(B_k)$ is the hysteresis loss coefficient at the magnetic flux density B_k, $b(B_k, f_k)$ is the eddy current loss coefficient at the magnetic flux density B_k and the frequency f_k, V_i is volume of each iron finite element in m^3, ρ_{Fe}

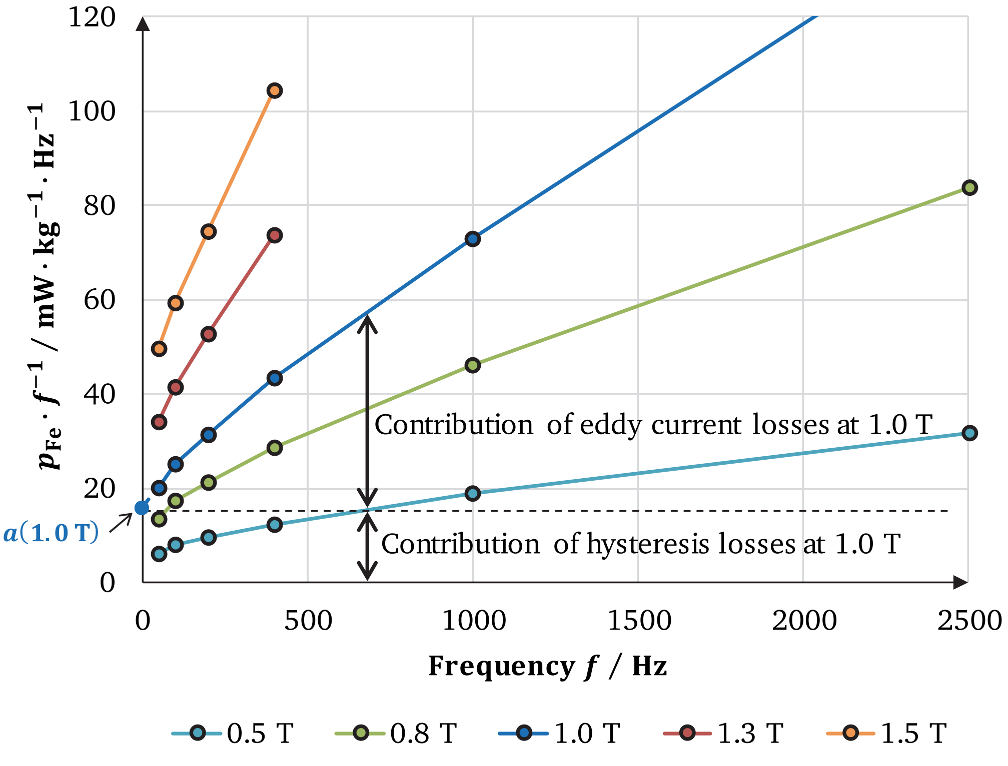

Fig. 3.3: Identifying the loss coefficients $a(B)$ and $b(B,f)$ of the M270-35A iron sheet via measured losses values for the iron losses calculation in the FEM software JMAG

is the mass density of the iron lamination, n_{el} is number of finite elements, and N is the maximum frequency order $k_{\max} = N$.

In order to determine the loss coefficients $a(B_k)$ and $b(B_k, f_k)$ by the frequency separation method, the iron losses density p_{Fe} at a certain magnetic flux density B is written as the following dependence on the frequency f.

$$p_{\mathrm{Fe}} = a(B) \cdot f + b(B, f) \cdot f^2 \tag{3.20}$$

By dividing both sides by frequency f, the iron loss density equation is

$$\frac{p_{\mathrm{Fe}}}{f} = a(B) + b(B, f) \cdot f. \tag{3.21}$$

Fig. 3.3 shows the core loss density graph of the M270-35A iron sheet as calculated by equation (3.21). The loss coefficient $a(B)$ at flux density B can be found at the intersection between the loss density curve and the y-axis, and the gradient of the loss density curve is the loss coefficient $b(B, f)$. Since the gradient of the loss density curve varies slightly with the frequency, the frequency dependence is also considered in the loss coefficient $b(B, f)$. With the frequency separation method, the core loss data of these values, which are not included in the core loss table, can be interpolated [30].

During the manufacturing process of the iron lamination of the prototype machine, the contour of the lamination is affected by laser cutting, which causes a local reduction of the magnetic permeability and an increase of hysteresis losses near the contour. In addition, the sharp edges at the contour due to cutting can damage the insulation of the adjacent lamination sheets and thus may cause additional eddy current losses. Thus a 50 % iron loss increase ($k_{\mathrm{v}} = 1.5$) was considered by estimation and experience from literature for the calculation of iron losses in comparison to the sheet manufacturer data. The iron losses were numerically calculated for no-load generator operation $P_{\mathrm{d,Fe0}}$. These losses are caused by the rotating magnetic field from the rotor permanent magnet in the stator iron stack. Thus, the magnet temperature, due to the depending remanence, is an essential factor in determining these iron losses. Fig. 3.4 shows the calculated iron losses at no-load for two magnet temperatures of $\vartheta_{\mathrm{M}} = 35$ °C, the steady-state temperature at no-load with n_{N}, and $\vartheta_{\mathrm{M}} = 100$ °C, the steady state temperature at rated load OP2. Due to the negative thermal coefficient of magnet remanence and correspondingly less remanence at higher temperature, the no-load iron losses with $\vartheta_{\mathrm{M}} = 100$ °C show approximately 20 % lower values than at $\vartheta_{\mathrm{M}} = 35$ °C.

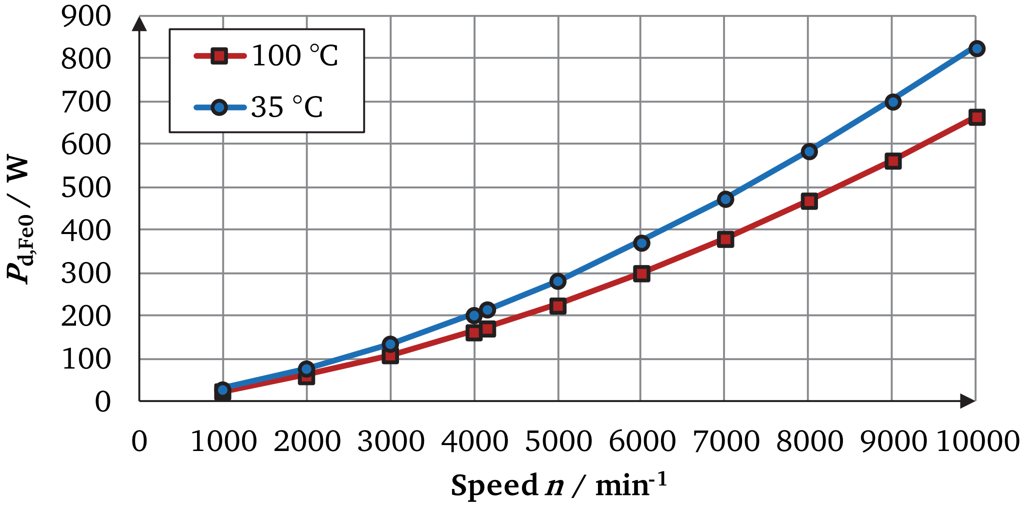

Fig. 3.4: Calculated iron losses at no-load $P_{\mathrm{d,Fe0}}$ with different magnet temperatures of $\vartheta_{\mathrm{M}} = 100$ °C and $\vartheta_{\mathrm{M}} = 35$ °C via FEM software JMAG with the loss increase factor $k_{\mathrm{v}} = 1.5$

At load operation, the AC stator winding field adds to the rotor field and increases the iron losses $P_{\mathrm{d,Fe}} > P_{\mathrm{d,Fe0}}$. The numerically calculated iron losses for each load OP are presented in Table 3.2. All FEM simulations at load operation were simulated with sinusoidal current feeding in the three-phase windings. As mentioned previously, the very small current ripple of the stator winding from the PWM voltage signal was not considered for the iron losses calculation.

At rated speed of $n_{\mathrm{N}} = 4167\ \mathrm{min}^{-1}$, even though the stator teeth have 30 % less iron mass than the stator yoke, the iron losses in the stator teeth $P_{\mathrm{d,Fe,st}}$ have a value similar to that for the stator yoke $P_{\mathrm{d,Fe,sy}}$ because of higher magnetic flux density in the narrow stator teeth. At the maximum speed of $n_{\max} = 10000\ \mathrm{min}^{-1}$, the iron losses in the stator teeth are 170 % greater than those in the stator yoke due to the high frequency and high magnetic flux density, caused by the big stator field which is needed to reduce the rotor field to keep the stator voltage limit.

The permanent magnet magnetic field is constant in the rotor. However, the air-gap field fluctuates due to the rather big stator slot openings in comparison to the small air-gap distance. This oscillating field, which has a slot frequency of $Q_{\mathrm{s}} \cdot n$ and its multiples, causes iron losses in the rotor $P_{\mathrm{d,Fe,r}}$. Thus, at no-load with the maximum speed, the rotor produces 4.9 times the iron loss produced at rated speed. In addition, the stator field harmonics at load operation increase the iron losses in the rotor. Comparing rotor iron losses at OP2 and OP1 for the same rotation speed, the rotor iron losses at OP1 are

49 % higher than those at OP2 due to the higher stator field harmonics from the higher operating current. The rotor iron losses at OP3 are about 5 times higher than those at OP2 due to the high rotation speed and hence high AC frequency of the local iron flux density.

Table 3.2 Calculated iron losses in the prototype machine at each load condition with the magnet temperature of $\vartheta_\mathrm{M} = 100$ °C and the iron loss increase factor of $k_\mathrm{v} = 1.5$ ($P_\mathrm{d,Fe,st}$: iron losses in stator teeth, $P_\mathrm{d,Fe,sy}$: iron losses in stator yoke, $P_\mathrm{d,Fe,r}$: iron losses in the rotor, and $P_\mathrm{d,Fe} = P_\mathrm{d,Fe,st} + P_\mathrm{d,Fe,sy} + P_\mathrm{d,Fe,r}$: total iron losses in the electric machine)

	No-load		**OP1**	**OP2**	**OP3**
Speed n / min^{-1}	4167	10000	4167	4167	10000
Stator frequency f_s / Hz	208.35	500	208.35	208.35	500
$P_\mathrm{d,Fe,st}$ / W	88.9	336.9	214.1	168.4	747.1
$P_\mathrm{d,Fe,sy}$ / W	77.0	285.6	203.9	159.7	276.1
$P_\mathrm{d,Fe,r}$ / W	8.9	43.7	39.5	26.5	132.1
$P_\mathrm{d,Fe}$ / W	174.8	666.2	457.6	354.6	1155.3

Note: The small eddy current losses $P_\mathrm{d,M}$ in the rotor magnets are treated in section 3.5.

3.4 Mechanical losses

Mechanical friction losses are attributed to the additional torque needed to overcome the drag associated with the rotating rotor. In this section, the air friction losses in the air gap and the bearing friction losses are discussed. Total mechanical friction losses can be calculated with equation (3.22).

$$P_\mathrm{d,fr} = P_\mathrm{d,fr,air} + P_\mathrm{d,fr,bearing} \tag{3.22}$$

3.4.1 Air friction losses

When the electric machine is rotating, the air resistance in the air gap drags the rotor. This drag force $F_{\mathrm{fr,air}}$ depends on the air's properties, on the rotor geometry and on the rotational speed of the rotor. The drag force can be calculated as

$$F_{\mathrm{fr,air}} = \frac{1}{2} \cdot \rho_{\mathrm{air}}(\vartheta_{\mathrm{air}}) \cdot c_{\mathrm{f}} \cdot v_{\mathrm{r}}^2 \cdot A_{\mathrm{airgap}}, \tag{3.23}$$

where $\rho_{\mathrm{air}}(\vartheta_{\mathrm{air}})$ is the air mass density in kg/m^3 at an air temperature of ϑ_{air}; c_{f} is the drag coefficient, which is a dimensionless number; v_{r} is the surface speed of the rotor in m/s; and A_{airgap} is the rotor surface area on the air gap side in m^2. The drag coefficient, or air friction coefficient, c_{f} can be empirically determined on the basis of measurements. Here, the air friction coefficients from *M. Mack* in [31] were used. The empirically determined air friction coefficients in an annulus formed between two concentric rotating cylinders are suitable for the air friction loss calculation of the rotating rotor cylinder with a small air gap. The air friction coefficient varies with the flow regime in the air gap. In order to determine the flow regime in the air gap, the *Reynolds* number is used. The *Reynolds* number is the ratio of the inertial force to the viscous force of the fluid. It can be calculated with n as the rotational speed in 1/s, r_{ro} as the outer radius of the rotor in m, and $\nu_{\mathrm{air}}(\vartheta_{\mathrm{air}})$ as the kinematic viscosity of air at the air temperature ϑ_{air} in m^2/s, using (3.24).

$$Re = \frac{2\pi \cdot n \cdot r_{\mathrm{ro}}^2}{\nu_{\mathrm{air}}(\vartheta_{\mathrm{air}})} \tag{3.24}$$

At low *Reynolds* number Re, the air flow in the air gap will be laminar. As the *Reynolds* number increases, the air flow regime will be changed to turbulent. In order to determine the air friction coefficient in an annulus formed between two concentric cylinders, the ratio between the air-gap distance and the rotor radius δ/r_{ro} should also be considered by introducing the *Taylor* number, which is a dimensionless number. The *Taylor* number indicates the relative effects of inertial forces and viscosity on the rotating rotor surface. The *Taylor* number is defined as (3.25).

$$Ta = \frac{2\pi \cdot n \cdot r_{\mathrm{ro}} \cdot \delta}{\nu_{\mathrm{air}}(\vartheta_{\mathrm{air}})} \cdot \sqrt{\frac{\delta}{r_{\mathrm{ro}}}} \tag{3.25}$$

For calculating the kinematic viscosity and the mass density of air, an air temperature of $\vartheta_{\mathrm{air}} = 100\ {}^\circ\mathrm{C}$ was used, which corresponds to $\nu_{\mathrm{air}} = 23.06 \cdot 10^{-6}\ \mathrm{m^2/s}$ and $\rho_{\mathrm{air}} = 0.946\ \mathrm{kg/m^3}$. The air friction coefficients c_{f}, depending on the air flow regime in the air gap, are listed in (3.26).

$$\begin{aligned} c_{\mathrm{f}} &\cong \frac{8}{Re} && (Re < 170) \\ &\cong \frac{1.8}{Re} \cdot \left(\frac{\delta}{r_{\mathrm{ro}}}\right)^{-0.25} \cdot \frac{r_{\mathrm{si}}^2}{r_{\mathrm{si}}^2 - r_{\mathrm{ro}}^2} && (Re > 170 \text{ and } Ta < 41.3) \\ &\cong 7 \cdot 10^{-3} && (Re > 170 \text{ and } Ta > 41.3) \end{aligned} \tag{3.26}$$

Only the air friction losses in the air gap were calculated, while the air friction losses at other parts of the rotor surface are negligible due to the bigger mechanical clearances. The air friction losses are determined as (3.27).

$$P_{\mathrm{d,fr,air}} = F_{\mathrm{fr,air}} \cdot (2\pi \cdot n) \cdot r_{\mathrm{ro}} = \frac{1}{2} \rho_{\mathrm{air}}(\vartheta_{\mathrm{air}}) \cdot c_{\mathrm{f}} \cdot (2\pi \cdot n)^3 \cdot r_{\mathrm{ro}}^3 \cdot A_{\mathrm{airgap}} \tag{3.27}$$

The calculated air friction losses for the prototype machine are $P_{\mathrm{d,fr,air}} = 1.1\ \mathrm{W}$ at rated speed 4167 min^{-1} and $P_{\mathrm{d,fr,air}} = 14.7\ \mathrm{W}$ at maximum speed 10000 min^{-1}. Compared to other losses, such as the ohmic losses or the iron losses, they are very small, due to the small rotor size.

3.4.2 Bearing losses

The lubrication and the friction between the inner and outer ring of the ball bearing drag the rotor and build a friction torque on the shaft. To estimate the friction torque in the bearings, a simple equation was used. The friction torque on the bearings depends on the load force in axial and radial direction F_{a} and F_{r} on the bearing, the type of bearing and the lubricant properties of the bearing. The bearing friction losses can be estimated via the frictional torque (3.28) [24]

$$M_{\mathrm{fr,bearing}} = 0.5 \cdot \mu_{\mathrm{bearing}} \cdot F \cdot d_{\mathrm{bearing}}, \tag{3.28}$$

where μ_{bearing} is the friction coefficient of the bearing and $F = \sqrt{F_{\text{a}}^2 + F_{\text{r}}^2}$ is the total bearing load, with the load force in axial direction F_{a}, the load force in radial direction F_{r}, and d_{bearing} as the average diameter of the bearing. The typical value of the friction coefficient of the grease-lubricated ball bearing ranges from 0.0010 to 0.0050 [24]. Here, an estimated bearing friction coefficient of $\mu_{\text{bearing}} = 0.0050$ is used, due to the special ball bearings (type: SKF 61806) for high-speed operation. The axial load force on the bearing is neglected here $F_{\text{a}} \approx 0$. With the rotor mass of 9.1 kg, the calculated friction torque is $M_{\text{fr,bearing}} = 6.69 \cdot 10^{-3}$ Nm. For both side bearings, the bearing friction losses at the rotation speed of the rotor n in 1/s is calculated with (3.29)

$$P_{\text{d,fr,bearing}} = 2 \cdot M_{\text{fr,bearing}} \cdot (2\pi \cdot n) \cdot k_{\text{bearing}} \tag{3.29}$$

With a safety factor $k_{\text{bearing}} = 2$ for additional load force by the unbalanced magnetic pull, the calculated bearing losses at rated speed $n_{\text{N}} = 4167\ \text{min}^{-1}$ and the maximum speed $n_{\text{max}} = 10000\ \text{min}^{-1}$ are 5.8 W and 14.0 W, respectively. Like the air friction losses, the friction losses in the bearings are negligibly small.

3.5 Eddy current losses in magnets

Due to the stator slot openings, the rotor magnetic field in the air gap is modulated, and the additional field space harmonic with a slot frequency of $f_{\text{Q}} = n \cdot Q_{\text{s}}$ is produced in the air gap. These harmonic components rotate asynchronously with the rotor speed; thus, they produce additional eddy current losses in the magnets $P_{\text{d,M}}$.

Many researchers have published analytical calculation methods to estimate eddy current losses in a magnet for surface-mounted magnets of an electric machine [32, 33, 34, 35, 36, 37]. The eddy current losses in a buried V-shaped magnet, however, are hard to calculate analytically, because they are shielded by the rotor iron bridges on top of the magnets. Thus, the 2D FEM software JMAG was used in a time-step solution with moving rotor mesh to calculate the eddy current losses in the electric machine's buried V-shaped separated magnets. To consider the 3D end effects of the axial segmentation of the magnets in a 2D FEM model, the *Russell-Norsworthy* end coefficient $\kappa_{\text{M,eq}}$ was used (3.30) [38], with the conductivity of NdFeB-magnets $\kappa_{\text{M}} = 754072$ S/m, the width b_{M} and the length l_{M} of the magnet segment.

$$\kappa_{\mathrm{M,eq}} = \kappa_{\mathrm{M}} \cdot \left(1 - \frac{2}{\pi} \cdot \frac{b_{\mathrm{M}}}{l_{\mathrm{M}}} \cdot \tanh\left(\frac{\pi}{2} \cdot \frac{l_{\mathrm{M}}}{b_{\mathrm{M}}}\right)\right) \tag{3.30}$$

The calculated eddy current losses in the magnets P_{M} of the machine at each operating point are presented in Table 3.3. In order to reduce the additional eddy current losses, the magnets were segmented in circumferential and axial directions. In addition, due to the buried V-shaped magnet, the rotor iron bridge and iron segments above these magnets shield these magnets from the harmonic components of the air-gap magnetic flux density with their rather small pole pitch. Therefore, the calculated eddy current losses show negligibly small values and may be ignored. In the same way, the additional eddy current losses in the magnets due to the magnetic air gap field of the stator current ripple due to the PWM inverter operation were ignored.

Table 3.3 Calculated eddy current losses in the magnets at each load condition with the magnet temperature of $\vartheta_{\mathrm{M}} = 100$ °C

	OP1	**OP2**	**OP3**
Speed n / min^{-1}	4167	4167	10000
Stator frequency f_{s} / Hz	208.35	208.35	500
Slot frequency $n \cdot Q_{\mathrm{s}}$ / Hz	2500	2500	6000
Simulation step Δt / μs	1.33	1.33	5.56
$P_{\mathrm{d,M}}$ / W	0.7	0.2	1.5

3.6 Losses in the inverter

A 3-phase power electronics inverter with a B6 switch with a digital controller was used and allows the production of various 3-phase AC-voltages at various frequencies with different amplitude to drive the electric machine under different load conditions. To convert direct current into alternating current, the DC link voltage is chopped up into discrete parts by the switching components of the inverter (IGBTs) with the anti-parallel freewheeling diodes. During the switching of the power electronics on and off, switching losses in the inverter switching components are incurred. Losses in the power modules of the inverter can be divided into conducting losses in an Insulated Gate Bipolar Transistor (IGBT) $P_{\mathrm{Q,cond}}$ and in an anti-parallel freewheeling diode $P_{\mathrm{D,cond}}$ and the above noted switching losses in the IGBT $P_{\mathrm{Q,sw}}$ and the diode $P_{\mathrm{D,sw}}$. Thus, total losses in the power electronics of the inverter with 6 IGBTs and 6 diodes are calculated with (3.31).

$$P_{\mathrm{d,inv}} = 6 \cdot \left(P_{\mathrm{Q,sw}} + P_{\mathrm{Q,cond}} + P_{\mathrm{D,sw}} + P_{\mathrm{D,cond}}\right) \tag{3.31}$$

The power losses for controlling of the inverter are neglected here. To increase the DC link voltage utilization by 15 %, space vector modulation (SVM) was considered instead of sinusoidal PWM (SPWM). According to *Ph. Perruchoud* in [39], the total power losses in power electronics can be analytically estimated with a phase current $\hat{I}_{\mathrm{s1}}$, a phase angle φ and a modulation index m. Here the current ripple in the AC stator current is neglected, which means that the motor side stator current per phase is sinusoidal.

3.6.1 Conduction losses in IGBT and diode

The conduction losses can be divided into losses from the constant voltage drop in the electronic component, which is proportional to average current $\bar{I}$, and resistive losses in the resistive element, which are proportional to the square of the RMS current $|I|^2_{\mathrm{RMS}}$. The conduction losses in the power electronics are calculated as [39],

$$P_{\mathrm{Q,cond}} = \bar{I}_{\mathrm{Q}} \cdot U_{\mathrm{Q}} + \left|I_{\mathrm{Q}}\right|^2_{\mathrm{RMS}} \cdot R_{\mathrm{Q}}, \tag{3.32}$$

$$P_{\mathrm{D,cond}} = \bar{I}_{\mathrm{D}} \cdot U_{\mathrm{D}} + |I_{\mathrm{D}}|^2_{\mathrm{RMS}} \cdot R_{\mathrm{D}}, \tag{3.33}$$

with the average current:

$$\bar{I}_{\mathrm{Q}} = \hat{I}_{\mathrm{s1}} \cdot \left(\frac{1}{2\pi} + \frac{m}{8} \cdot \cos\varphi\right) \text{ (for the IGBT)}, \tag{3.34}$$

$$\bar{I}_{\mathrm{D}} = \hat{I}_{\mathrm{s1}} \cdot \left(\frac{1}{2\pi} - \frac{m}{8} \cdot \cos\varphi\right) \text{ (for the diode)}, \tag{3.35}$$

and the square of the RMS current:

$$\left|I_{\mathrm{Q}}\right|^2_{\mathrm{RMS}} = \hat{I}^2_{\mathrm{s1}} \cdot \left(\frac{1}{8} + m \cdot \frac{30\cos\varphi - \cos 3\varphi}{90 \cdot \pi}\right) \text{ (for the IGBT)}, \tag{3.36}$$

$$|I_{\mathrm{D}}|^2_{\mathrm{RMS}} = \hat{I}^2_{\mathrm{s1}} \cdot \left(\frac{1}{8} - m \cdot \frac{30\cos\varphi - \cos 3\varphi}{90 \cdot \pi}\right) \text{ (for the diode)}. \tag{3.37}$$

3.6.2 Switching losses in IGBT and diode

During the turning on and turning off of the power electronics switch, energy loss E_{on} and E_{off}, respectively, occurs due to the overlapped current and voltage waves. Thus, the switching losses in the power electronics of the inverter depend on the switching frequency f_{sw}, the dynamic properties of the power module (IGBT and diode) and the stator current.

$$P_{\mathrm{Q,sw}} = \frac{f_{\mathrm{sw}} \cdot (E_{\mathrm{on}} + E_{\mathrm{off}})}{\pi} \cdot \frac{\hat{I}_{\mathrm{s1}}}{\sqrt{2} \cdot I_{\mathrm{CN}}} \tag{3.38}$$

$$P_{\mathrm{D,sw}} = \frac{f_{\mathrm{sw}} \cdot E_{\mathrm{rec}}}{\pi} \cdot \frac{\hat{I}_{\mathrm{s1}}}{\sqrt{2} \cdot I_{\mathrm{FN}}} \tag{3.39}$$

With the characteristics of the IGBT module FF300R06KE3 in Table 3.4, the total power losses in the machine at the rated operation OP2 are 585.6 W, which corresponds to an inverter efficiency of 97.8 %.

Table 3.4 Characteristic values of the IGBT and diode in the IGBT module FF300R06KE3 from company *Infineon* [67]

IGBT		**Diode**	
DC collector current I_{CN}	300 A	DC forward current I_{FN}	300 A
IGBT voltage drop U_{Q}	0.80 V	Diode voltage drop U_{D}	0.80 V
IGBT dynamic resistance R_{Q}	2.67 mΩ	Diode dynamic resistance R_{Q}	1.83 mΩ
Turn-on energy loss per pulse E_{on}	3.10 mJ	Reverse recovery energy per pulse E_{rec}	6.20 mJ
Turn-off energy loss per pulse E_{off}	12.0 mJ		

3.7 Electromagnetic calculations for the electric machine at load operations

In this section, the design of the electric machine for the DE-REX powertrain is presented. For the DE-REX powertrain, an interior permanent magnet synchronous machine (IPMSM) with embedded rotor magnets in a V-shape arrangement was designed. The electric machine design with an integer number of slots per pole and phase $q_\mathrm{s} = 2$ was used (Chapter 2.1.2.1). The stator iron stack with 36 semi-closed slots with constant tooth width has a two-layer, 5/6-short-pitched winding inserted to reduce the deviations of the air-gap flux density radial component distribution along the rotor circumference from the ideal sine wave shape for low additional rotor losses (Fig. 3.5 a). To avoid permanent demagnetization of the magnet at high magnet temperatures of up to 170 °C, high-energy neodymium-iron-boron (NdFeB) permanent magnets of type VACODYM 863 TP were used, which have a remanence of $B_{\mathrm{R,100\,°C}} = 1.14\ \mathrm{T}$ at the magnet temperature $\vartheta_\mathrm{M} = 100\ \mathrm{°C}$ and a coercive field strength of $H_{\mathrm{cB,100\,°C}} = 848\ \mathrm{kA/m}$. In order to withstand centrifugal forces at the demanded over-speed of 120 % of the maximum speed, or 12000 min^{-1} according to IEC 60034-1, the height of the side bridges h_bridge above the buried magnets must be big enough (Fig. 3.5 b). At the same time, it should not be too big so as to avoid a large magnetic rotor flux leakage through these iron bridges. Furthermore, a large magnetic reluctance difference between rotor pole and inter-pole axis (called d- and q-axis) is needed to produce an additional electromagnetic reluctance torque at a given stator current. To minimize the no-load cogging torque and the torque ripple at load, a staggered rotor with five axial rotor segments was used, resulting in a skew of the magnets by one stator slot pitch each of which has a skew angle $\alpha_\mathrm{skew} = 2\,°\ (\mathrm{mech.})$. As a result, the calculated air-gap torque ripple is reduced to about 9 % of the average value at rated operation OP2. Each rotor magnet (Fig. 3.5 b) is divided into two segments in circumferential direction and into five segments in axial direction (corresponding to the staggering) to suppress eddy current losses in the conductive magnets, caused by stator magnet field space and time harmonics. For the stator and rotor lamination, a rather thin electromagnetic sheet of 0.35 mm thickness, type SURA M270-35A, was used to reduce iron losses, especially at high speed. The main data related to the machine is presented in Table 3.5, and the geometry of the machine is shown in Fig. 3.5.

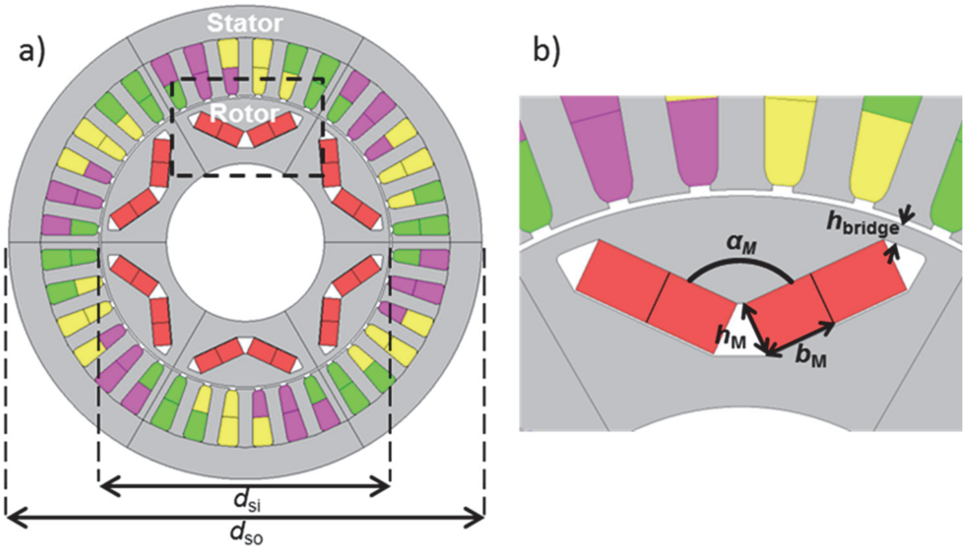

Fig. 3.5: Geometry of the prototype IPMSM: a) Axial cross section as Finite Element Method (FEM) model, b) enlarged rotor magnet arrangement with two segments per magnet. The angle α_{M} was determined numerically for a given stator current to get a maximum average electromagnetic torque. The FEM program JMAG was used.

In fact, at motor load operation the electric machine is supplied by the pulse-width modulated (PWM) three-phase output voltage system of the feeding voltage source inverter. The *Fourier* fundamental of this PWM voltage pattern has the phase voltage amplitude $\hat{U}_{s,1}$ and the fundamental frequency f_{s}. The corresponding phase current is smoothed by the machine self-inductance and the rather high switching frequency of the inverter $f_{\mathrm{sw}} = 24\,\mathrm{kHz}$. The amplitude of the current ripple is limited and is therefore rather small. Hence for the simplicity of calculation, a three-phase sine wave current supply of frequency f_{s} with RMS value $I_{\mathrm{s},1}$ is impressed in the 2D FEM into the three stator winding phases U, V, W, having a certain phase shift β^{*} with respect to the induced stator phase voltage U_{p0} at no-load. The electromagnetic simulations were done with the FEM software JMAG.

In calculating the efficiency of the electric machine η_{mot}, the ohmic losses and additional eddy current losses in the stator winding $P_{\mathrm{d,cu,AC}}$, the iron losses $P_{\mathrm{d,Fe}}$ as the sum of hysteresis losses and eddy current losses in the stator and the rotor iron stack, the air friction losses and the bearing losses $P_{\mathrm{d,fr}}$, and the additional eddy current losses in the magnet $P_{\mathrm{d,M}}$ were considered. For calculation of the ohmic losses, the temperature of the stator winding was selected at $\vartheta_{\mathrm{cu}} = 100\,^{\circ}\mathrm{C}$ as a typical average temperature during a duty cycle. The additional losses due to current displacement in the stator winding conductors, caused by the eddy currents from the AC magnetic slot leakage flux, were for simplicity calculated analytically, as described in Chapter 3.2, and were considered in the stator winding ohmic losses $P_{\mathrm{d,cu,AC}}$. The iron losses in the stator and the rotor laminations were determined by post-processing with the FEM software JMAG, with time harmonics also accounted for via a *Fourier* analysis. Due to the laser cutting and lamination stacking in the iron stacks' manufacturing process, a 50 % iron loss increase ($k_{\mathrm{v}} = 1.5$) beyond the lamination manufacturer's data was considered in calculating the iron losses. Since the buried segmented magnets are shielded by the rotor iron bridges, the additional losses due to eddy currents in the magnets, caused by small space harmonics of the (nearly sinusoidally distributed) air-gap flux density, are negligibly small. In the same way, the additional eddy current losses in the magnets due to the stator current ripple, caused by the PWM inverter operation, were ignored because the high switching frequency $f_{\mathrm{sw}} = 24\,\mathrm{kHz}$ resulted in a very small current ripple of below 0.5 % (Fig. 3.1). The calculated losses of the machine at each operating point are presented in Table 3.6.

The electromagnetic power in the air gap P_δ is given by (3.40), with the air-gap torque M_δ and the rotation speed n.

$$P_\delta = 2\pi \cdot n \cdot M_\delta \tag{3.40}$$

The mechanical torque at the shaft M_{m} can be derived from the mechanical power P_{m}, which is determined by subtracting all dissipated losses in the rotor (the friction losses $P_{\mathrm{d,fr}}$, the iron losses in the rotor $P_{\mathrm{d,Fe,r}}$, and the eddy current losses in the magnet $P_{\mathrm{d,M}}$) from the air-gap power P_δ.

$$M_{\mathrm{m}} = \frac{P_{\mathrm{m}}}{2\pi \cdot n} = \frac{P_\delta - P_{\mathrm{d,fr}} - P_{\mathrm{d,Fe,r}} - P_{\mathrm{d,M}}}{2\pi \cdot n} \tag{3.41}$$

The electrical input power of the electric machine P_{el} is the sum of all losses P_{d} and the mechanical output power P_{m}.

$$P_{\mathrm{el}} = P_{\mathrm{m}} + P_{\mathrm{d}} = P_{\mathrm{m}} + P_{\mathrm{d,cu,AC}} + P_{\mathrm{d,Fe}} + P_{\mathrm{d,fr}} + P_{\mathrm{d,M}} \tag{3.42}$$

The efficiency of the electric machine and the power factor of the fundamental components were determined by (3.43) and (3.44), respectively.

$$\eta_{\mathrm{mot}} = \frac{P_{\mathrm{m}}}{P_{\mathrm{el}}} = \frac{P_{\delta} - P_{\mathrm{d,fr}} - P_{\mathrm{d,Fe,r}} - P_{\mathrm{d,M}}}{P_{\delta} + P_{\mathrm{d,cu,AC}} + P_{\mathrm{d,Fe,s}}} \tag{3.43}$$

$$\cos\varphi = \frac{P_{\mathrm{el}}}{3 \cdot U_{\mathrm{s1}} \cdot I_{\mathrm{s1}}} \tag{3.44}$$

With consideration of the inverter losses from Chapter 3.6, the inverter efficiency and the electrical system (motor + inverter) efficiency were calculated by (3.45) and (3.46), respectively.

$$\eta_{\mathrm{inv}} = \frac{P_{\mathrm{el}}}{P_{\mathrm{el}} + P_{\mathrm{d,inv}}} \tag{3.45}$$

$$\eta_{\mathrm{sys}} = \frac{P_{\mathrm{m}}}{P_{\mathrm{el}} + P_{\mathrm{d,inv}}} \tag{3.46}$$

The losses in the motor cable between the motor and the inverter were neglected.

Table 3.5 Design parameters of the PMSM with $q_s = 2$

Machine parameter	**Symbol/unit**	**Value**
Rated power	P_N / kW	24
Rated speed	n_N / min^{-1}	4167
Maximum power	P_{max} / kW	48
Maximum speed	n_{max} / min^{-1}	10000
Number of stator slots	Q_s / -	36
Number of poles	$2p$ / -	6
Number of slots per pole and phase	q_s / -	2
Number of winding turns per phase	N_s / -	24
Number of winding turns per coil	N_c / -	12
Number of parallel branches per phase	a / -	6
Copper wire strands diameter	d_{str} / mm	2 × Ø 0.67 2 × Ø 0.80
Short-pitching	W/τ_p / -	5/6
Slot fill factor	k_f / -	0.45
Outer diameter of stator iron stack	d_{so} / mm	150
Inner diameter of stator iron stack	d_{si} / mm	92.8
Air-gap width	δ / mm	0.6
Axial iron length of stator iron stack	l_{Fe} / mm	140
Width of stator teeth	b_{st} / mm	4.6
Height of stator yoke	h_{sy} / mm	10.3
Height of a rotor iron bridge	h_{bridge} / mm	2
Height of a magnet segment	h_M / mm	5.5
Width of a magnet segment	b_M / mm	7.5
Axial length of a magnet segment	l_M / mm	28
Magnet V-angle	α_M / °	130
Active mass	m_{act} / kg	16.0

Table 3.6 Calculated load parameters, total losses, and efficiency at each OP

Parameter	**Symbol/Unit**	**OP1**	**OP2**	**OP3**
Speed	n / min^{-1}	4167	4167	10000
Mechanical torque	M_m / Nm	110.5	55.8	46.5
Air-gap torque	M_δ / Nm	110.6	55.8	46.7
Fundamental phase voltage (RMS)	U_s1 / V	109.6	95.9	122.8
Stator fundamental frequency	f_s / Hz	208.35	208.35	500
Fundamental phase current (RMS)	I_s1 / A	184.0	95.3	138.4
Current angle	β / °	-43.1	-34.8	-72.3
Phase current of d-axis component	I_d / A	-125.8	-54.4	-131.8
Phase current of q-axis component	I_q / A	134.3	78.2	42.1
Fundamental power factor (cap. / ind.: capacitive / inductive load)	$\cos\varphi$ / -	0.8576 (cap.)	0.9258 (cap.)	0.9977 (ind.)
Stator winding self-inductance of d-axis per phase	L_d / μH	253	251	288
Stator winding self-inductance of q-axis per phase	L_q / μH	579	770	834
AC ohmic losses	$P_\mathrm{d,cu,AC}$ / W	2714.7	727.3	1609.5
Iron losses	$P_\mathrm{d,Fe}$ / W	457.6	354.6	1155.3
Friction losses	$P_\mathrm{d,fr}$ / W	6.9	6.9	28.7
Eddy current losses in magnets	$P_\mathrm{d,M}$ / W	0.7	0.2	1.5
Total motor losses	P_d / W	3179.8	1088.9	2795.1
Mechanical power	P_m / W	48227.9	24328.1	48719.2
Electrical power	P_el / W	51407.7	25417.0	51514.3
Motor efficiency	η_mot / %	93.81	95.72	94.57
Inverter losses	$P_\mathrm{d,inv}$ / W	1259.4	585.6	903.2
Electrical system (motor + inverter) efficiency	η_sys / %	91.57	93.56	92.94

3.8 Loss distribution map and efficiency map

Fig. 3.6 shows the loss distributions across the torque-speed map of the electric machine. As mentioned above, the ohmic losses $P_{\mathrm{d,cu,DC}}$ are increased with the mechanical torque corresponding to the stator current. Also, in the field weakening area, the additional negative d-component current produces more ohmic losses (upper-left in Fig. 3.6). As the rotation speed is increased, the skin effect in the stator winding is enlarged. Thus, the additional eddy current losses in the windings $P_{\mathrm{d,cu,ad1,2}}$ rise with the current and the frequency (upper-right in Fig. 3.6). The iron losses distributions of stator and rotor show that iron losses increase with rotation speed, corresponding to the fundamental frequency, and with the current, corresponding to the additional stator current field (centre in Fig. 3.6). As mentioned in the Chapter 3.4, the mechanical friction losses $P_{\mathrm{d,fr}}$ are affected only by the rotation speed (bottom-left in Fig. 3.6). The inverter loss distribution across the torque and speed map $P_{\mathrm{d,inv}}$ shows a tendency similar to the ohmic losses. It is highly dependent on the stator current (bottom-right in Fig. 3.6).

Considering the losses detailed above, the efficiency map of the electric machine over torque and speed was calculated (Fig. 3.7). For the efficiency calculation, the constant winding temperature of $\vartheta_{\mathrm{cu}} = 100\ ^{\circ}\mathrm{C}$ and the magnet temperature of $\vartheta_{\mathrm{M}} = 100\ ^{\circ}\mathrm{C}$ were used. At high torque and low speed, the electric machine has lower efficiency, due to high ohmic losses. The electric machine achieves maximum efficiency of 96.3 % at 6000 min^{-1} and 45 Nm. At higher rotation speed, the efficiency decreases because of high iron losses. Incorporating the switching and conduction losses from the inverter into the efficiency map produces an efficiency map of the entire electrical system, which includes the electric machine and the inverter and is shown in Fig. 3.8. The power losses for the inverter controlling is not considered here.

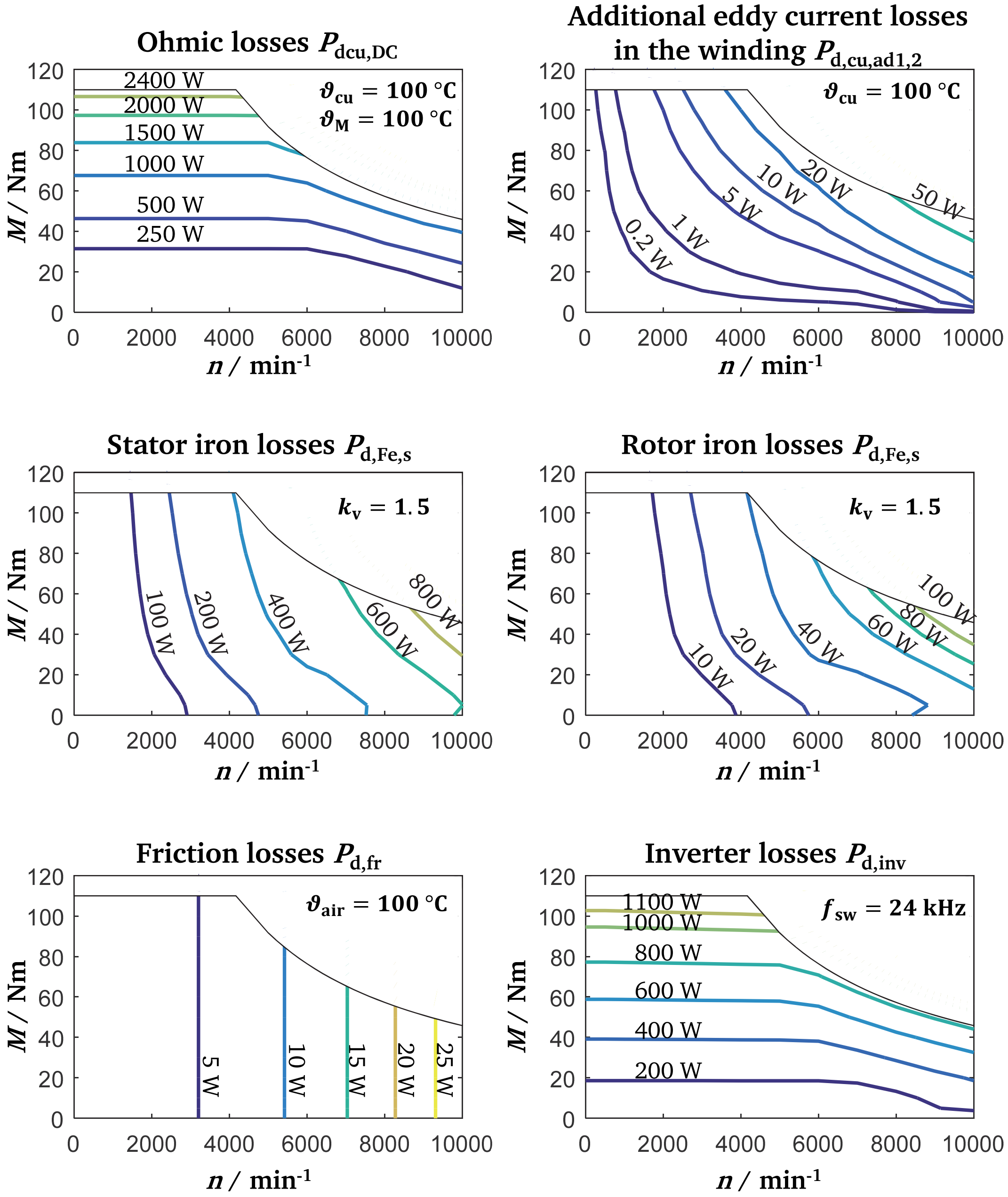

Ohmic losses $P_{\mathrm{dcu,DC}}$

Additional eddy current losses in the winding $P_{\mathrm{d,cu,ad1,2}}$

Stator iron losses $P_{\mathrm{d,Fe,s}}$

Rotor iron losses $P_{\mathrm{d,Fe,s}}$

Friction losses $P_{\mathrm{d,fr}}$

Inverter losses $P_{\mathrm{d,inv}}$

Fig. 3.6: Calculated losses distribution across the torque-speed map. Upper-left: DC ohmic losses with the winding temperature $\vartheta_{\mathrm{cu}} = 100$ °C and the magnet temperature $\vartheta_{\mathrm{M}} = 100$ °C, upper-right: additional eddy current losses in the stator winding, centre-left: stator iron losses with the loss increase factor $k_{\mathrm{v}} = 1.5$, centre-right: rotor iron losses with the loss increase factor $k_{\mathrm{v}} = 1.5$, bottom-left: total friction losses with the air temperature $\vartheta_{\mathrm{air}} = 100$ °C, bottom-right: switching and conduction losses in inverter with the switching frequency $f_{\mathrm{sw}} = 24$ kHz

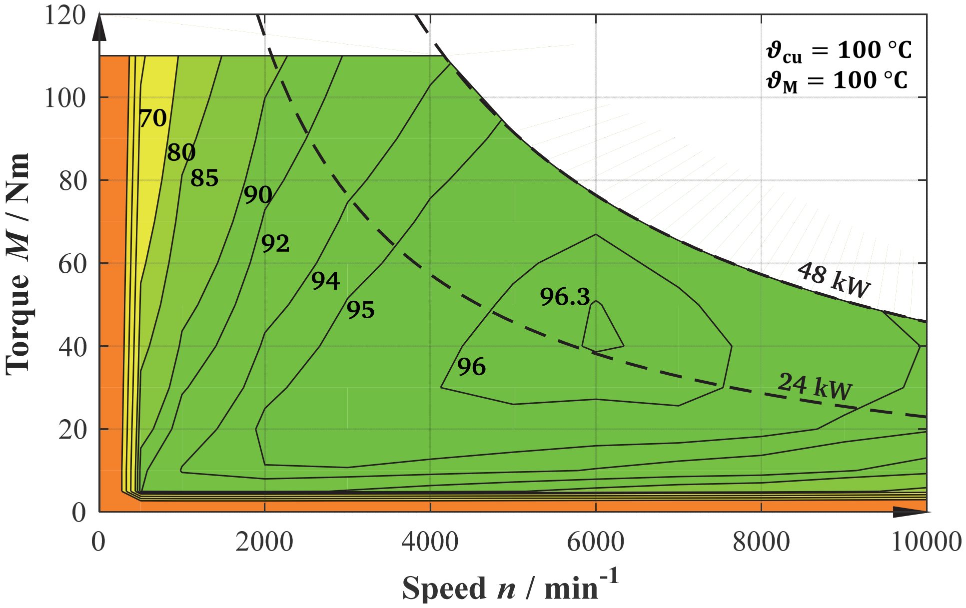

Fig. 3.7: Calculated efficiency map of the electric machine with the average stator winding temperature ϑ_{cu} = 100 °C and the rotor magnet temperature ϑ_{M} = 100 °C

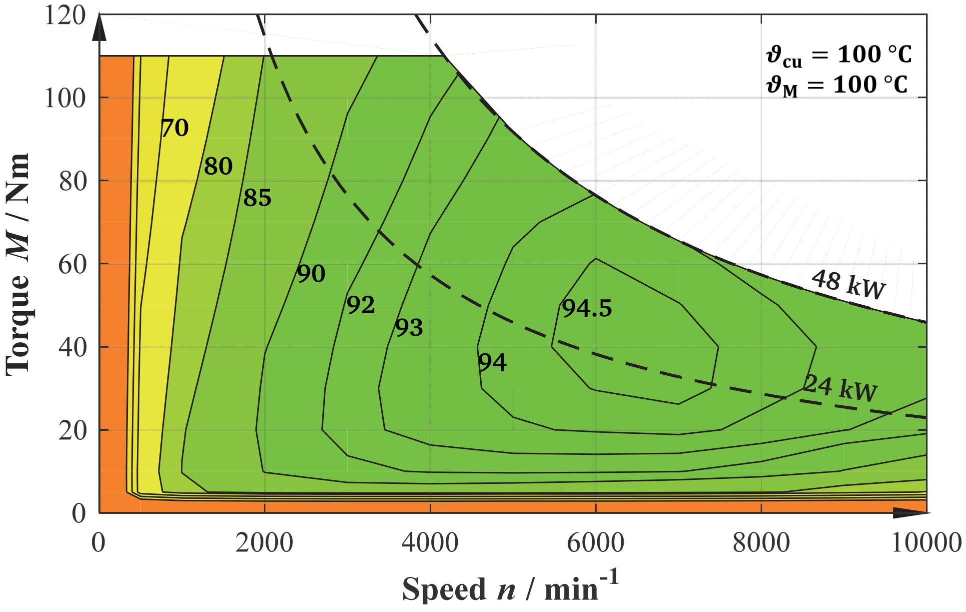

Fig. 3.8: Calculated total efficiency map of the electric machine and the inverter with the average stator winding temperature ϑ_{cu} = 100 °C and the rotor magnet temperature ϑ_{M} = 100 °C

4. Construction of the electric machines and test bench for the individual measurement

4.1 Prototype machine

Before producing four permanent magnet synchronous machines for the DE-REX powertrain (two for the powertrain test bench and two for the prototype vehicle), a prototype electric machine with the number of slots per pole and phase $q_\mathrm{s} = 2$ was built to verify the electromagnetic, thermal and mechanical design of the machine which are presented in Chapter 2.

4.1.1 Stator of the prototype machine

Fig. 4.1 shows the prototype stator, before assembling with the aluminium housing by shrink fitting. For the prototype stator, iron sheet of type M270-35A with a thickness of 0.35 mm was used to reduce the iron losses at high stator frequency. The laser-cut iron sheets were stacked and coated with a varnish, that bonded the sheets, when heated (*Backlack*). Using this bonding method, the iron sheets were not damaged and did not lose their electromagnetic properties, as they would have with the use of other conventional bonding techniques, such as riveting, clamping or welding. In addition, the iron sheets are almost round in form, except for a small outside groove for orienting the sheets. Thus, there is no unexpected local magnetic flux density increase in the stator yoke. A three-phase two-layer winding with a short pitching of $W/\tau_\mathrm{p} = 5/6$ was wound into the stator slots. Each coil turn contains four parallel copper wire strands (two strands with 0.67 mm diameter and two strands with 0.8 mm diameter) to maximize the slot fill factor. Based on the slot opening area $A_\mathrm{so} = 1.2\,\mathrm{mm}^2$ and the slot cross-section area $A_\mathrm{Q} = 90.03\,\mathrm{mm}^2$, the slot fill factor reached $k_\mathrm{f} = 0.45$. The terminals of the three-phase windings and the neutral point were placed on the NDE side. Thus, the winding overhang on the NDE side has a larger volume than the winding overhang on the DE side. Therefore, the hotspot is located in the winding overhang on the NDE side. For measuring the phase voltage, the neutral point of the star connection was placed in

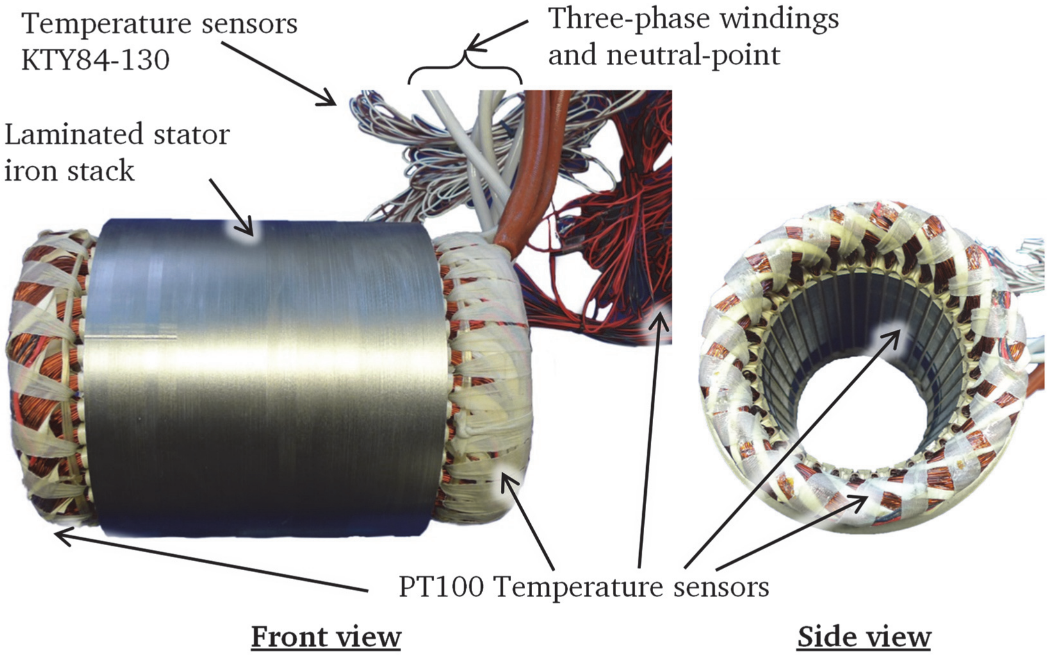

Fig. 4.1: Stator iron stack with round wire three phase motor winding, a star-point and temperature sensors, after the impregnation of the stator winding

the motor terminal of the prototype machine. For the winding temperature measurement, three PT100 temperature sensors for each stator winding phase were installed in the stator (one in the middle of the stator slot in axial direction, one in the winding overhang on the NDE side and one in the winding overhang on the DE side). In total, nine PT100 temperature sensors were mounted in the stator, although only three temperature sensors in one stator phase were measured, with the other temperature sensors used as backups. In addition, for thermal protection of the drive, two semi-conductor KTY 84-130 temperature sensors were mounted in the stator winding overhang and connected to the power converters for monitoring the winding temperature. After the winding was completed, the stator winding was impregnated with resin to improve the structural integrity of the windings, to increase the overall dielectric strength, to reduce winding vibrational noise and to improve the heat transfer from the stator winding to the stator iron stack. In order to fill the gaps between the conductors and insulation in the slot and overhang, to achieve void-free insulation, the stator was processed using vacuum pressure impregnation.

The left side of Fig. 4.2 shows the prototype stator before casting of both winding overhangs with the epoxy-based resin (EPIKOTE). The active part of the stator was inserted in the cooling jacket through a shrink-fitting technique to prevent the stator’s slipping from the cooling jacket. The cooling jacket is made of high-strength aluminium alloy

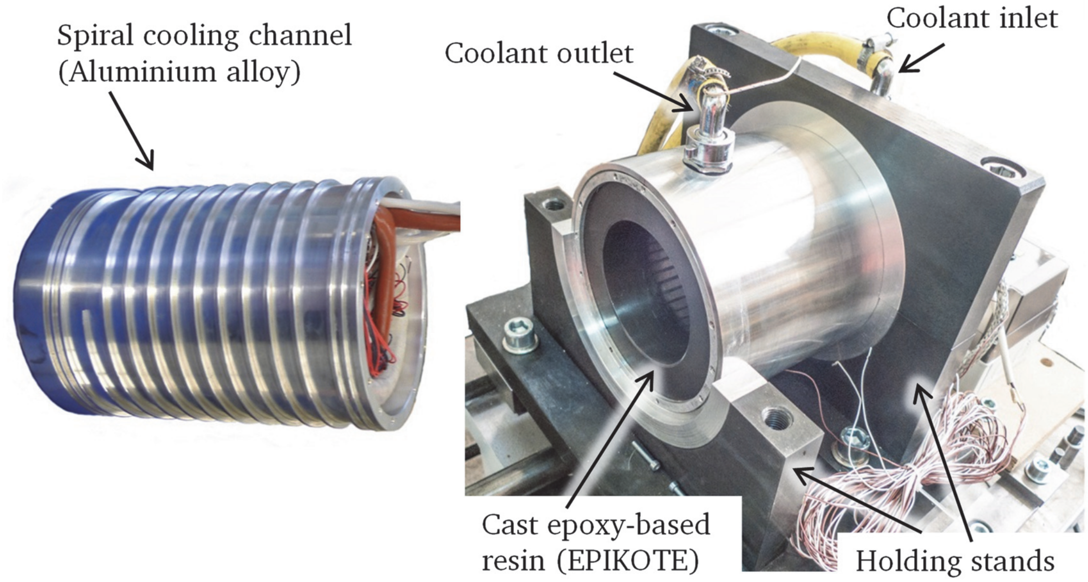

Aluminium housing with helical cooling channel

Stator with the cast epoxy-based resin around the winding overhangs and aluminium housing

Fig. 4.2: Left: Stator iron stack inside of the aluminium cooling jacket with helical cooling channel, Right: The cast epoxy-based resin around the stator winding overhangs within aluminium housing on the test bench

and has a helical cooling channel with a rectangular cross section for carrying the coolant. The electric machine was made for automotive applications, thus a glycol and water mixture (50 % / 50 %), which has a freezing point below −40 °C, was used for the coolant to prevent freezing above −40 °C. The heat generated by the losses in the electric machine is transferred to the coolant. Due to the bigger volume of winding overhang on the NDE side of the electric machine, this side produces more heat. Hence, the cold coolant flows into the coolant inlet on the NDE side and leaves the coolant outlet on the DE side. The coolant inlet and outlet are connected to a closed cooling circuit, which is driven by a Star ST 20/11 cooling pump from company *WILO*. The water pump has three adjustable power stages (75 W, 115 W, and 165 W). With the water pump power at 115 W, the required coolant flow rate of $\dot{V}_{\mathrm{coolant}} = 6\ \mathrm{l/min}$ could be achieved. Both winding overhangs were cast in epoxy-based resin of type EPIKOTE (Thermal Class H), which has a thermal conductivity of $\lambda_{\mathrm{cast}} = 1.0\ \mathrm{W/(m \cdot K)}$ (right side of Fig. 4.2). This value is much higher than the thermal conductivity value of air ($\lambda_{\mathrm{air,100°C}} = 0.0316\ \mathrm{W/(m \cdot K)}$). Thus, the casting of the winding overhang makes it easy to guide the heat flow from the winding overhang to the stator cooling jacket.

4.1.2 Rotor of the prototype machine

As discussed in Chapter 2, a 5-step-skewed ('staggered') rotor was used to minimize cogging torque at no-load and torque ripple at load. For this, the rotor iron stack was segmented into 5 sections, which had a length of $l_{\mathrm{r,seg}} = 28\,\mathrm{mm}$ each. The left side of Fig. 4.3 shows one section of the rotor iron stack. It has six V-shaped magnet pockets and one feather key to connect the rotor iron stack and the rotor shaft. When the rotor shaft has only one keyway for the feather key, each rotor segment must have a different form of the feather key to achieve a 5-step-skewed rotor. Obviously, this increases manufacture cost. Due to the six-fold rotational symmetry of the rotor, the rotor shaft had five different keyways (right side of Fig. 4.3). These keyways were staggered mechanically at -124°, -62°, 0°, 62° and 124° with regard to the alignment of the centre rotor iron package (the third rotor section). To show the magnet arrangement with these keyways in the rotor, a section view of a 3D model of the 5-step-skewed rotor is given in the right side of Fig. 4.4. Each magnet was staggered mechanically by 2° and electrically a shift of 6° with respect to the magnets in the neighbouring rotor section.

The left side of Fig. 4.4 presents the rotor assembly process after installing the first rotor iron stack section onto the rotor shaft. In order to reduce the eddy current losses in the magnets, each magnet pole was segmented in circumferential direction (with 4 permanent magnets per magnet pocket) and also in axial direction (5 permanent magnets due to the 5-step-skewed rotor). Thus, a total of 120 PM blocks was inserted in the rotor. Each permanent magnet block was coated with VACCOAT 20011 with an average thickness of approximately 15 μm to prevent chemical corrosion and to insulate against

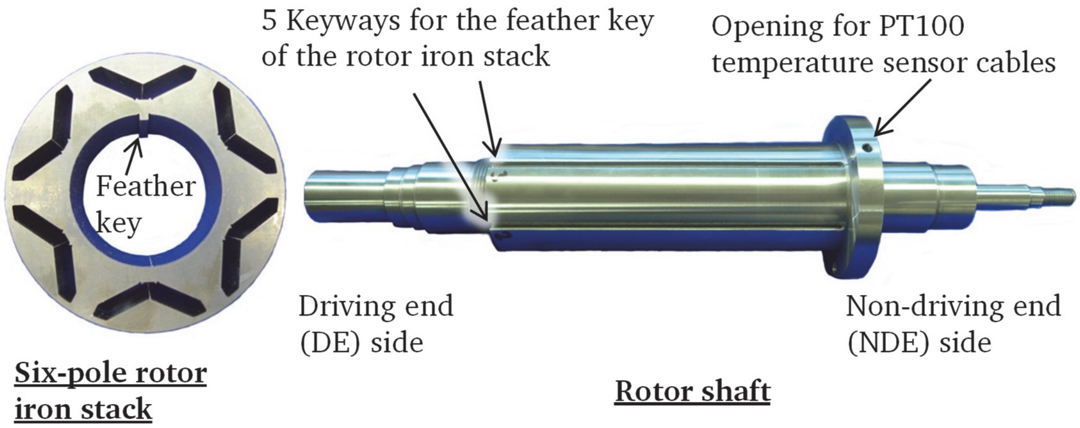

Fig. 4.3: Left: One rotor section with six-pole V-shaped magnet pockets with a feather key, Right: Rotor shaft of the prototype electric machine

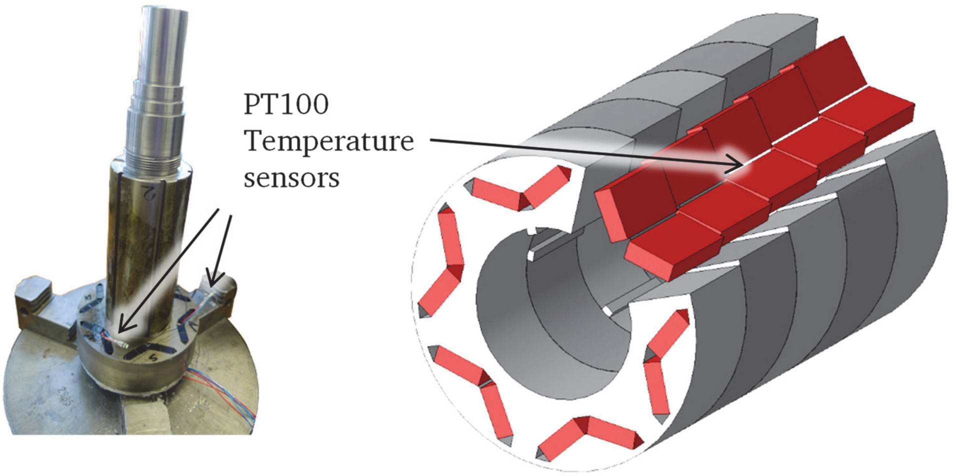

Assembly of rotor shaft and rotor iron stack

3D sectional view of 5-step skewed rotor of the prototype motor

Fig. 4.4: Left: Shrink fit of a rotor iron stack on the rotor shaft with three magnet temperature sensors (PT100), Right: Sectional view of 3D model of 5-step-skewed rotor of the prototype motor

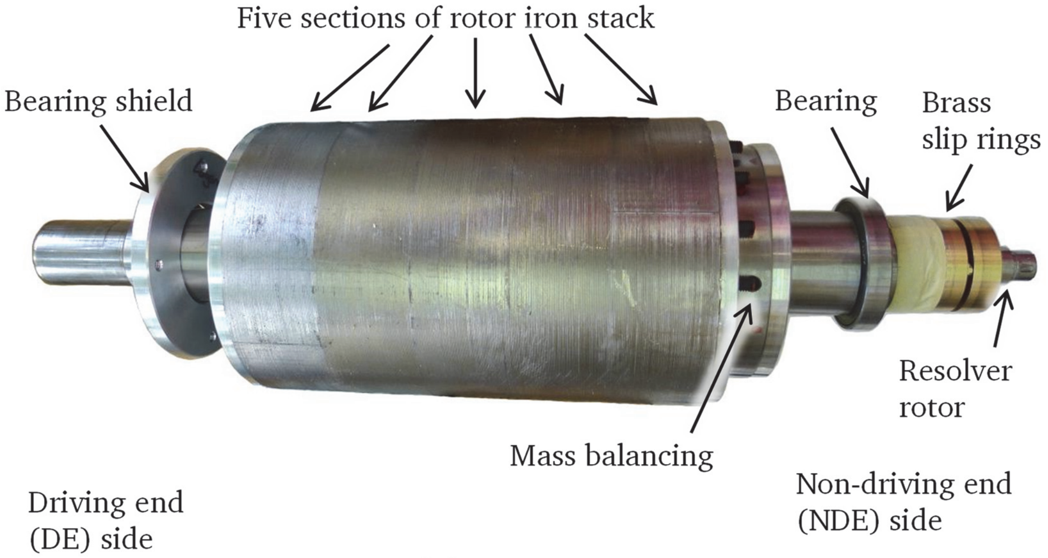

Rotor of the prototype motor

Fig. 4.5: Completed rotor of the prototype motor after balancing

the neighbouring magnets and the rotor lamination. After the magnets were inserted into the magnet pockets, the magnet pockets were filled with epoxy-based resin to fix the magnets. To measure the temperature rise in the magnets, three PT100 temperature sensors were installed in the centre of the magnet pocket in the middle of the axial motor length (one active and two as backups, left side of Fig. 4.4). The sensor cables of the active temperature sensor were passed through the hole in the rotor shaft and connected to the brass slip rings on the rotor shaft at the NDE side (Fig. 4.5). The magnet temperature was measured via slip-ring carbon brushes, which were fixed on the housing. For measurement of the rotor position, a pan cake shape six-pole resolver SinglSyn TS2224N1113E102 from company *Tamagawa* was mounted. It has a thickness of only 16 mm and an outer diameter of 25 mm [40]. Due to the thinness of this built-in resolver, it required only little mounting space, making it possible to minimize the machine volume. After the installation of all rotor parts was completed, the rotor over-speed test for 2 min at $n = 12000\ \mathrm{min}^{-1}$ (according to IEC 60349-2) and the fine mass balancing were done by company *Carl Schenck* AG in Darmstadt, Germany.

4.2 Construction of the electric machines for the DE-REX powertrain

The stator of the electric machines for the DE-REX powertrain had a manufacturing process identical to that of the prototype machine. The only differences between the two stator types were the machine housings, which include the housing inside (water cooling jacket), the housing outside, the output direction of the power cables (radial direction to the terminal box), and the terminal box with high-voltage sockets. Due to the limited width of the engine compartment of the prototype vehicle, the total axial length of the electric machine was reduced from the 315 mm of the prototype machine to 252 mm. For this restricted axial length of the electric machine, the resolver was integrated into the end plate at the NDE side (bottom-left of Fig. 4.8). In addition, the three-phase power cables, the resolver signal cables and the temperature sensor cables exited in radial direction to the terminal box to reduce the axial length of the machine. The left side of Fig. 4.6 shows two openings for the cables on the inner housing with a helical cooling channel. The right side of Fig. 4.6 shows the stator before the casting of the winding overhangs. As with the prototype machine, both winding overhangs of the electric machine were cast in epoxy-based resin of type EPIKOTE (Thermal Class H).

For the connection between the transmission and the electric machine, the spline coupling was designed according to DIN 5480 with the module $m = 1$. The rotor of the electric machine had internal splines (hub) with 15 teeth (Fig. 4.7). For rotor material, a case-hardened steel, 20MnCr5, which is same material used for the shaft of the transmission, was used. After the central axial hole at the rotor was drilled and the internal

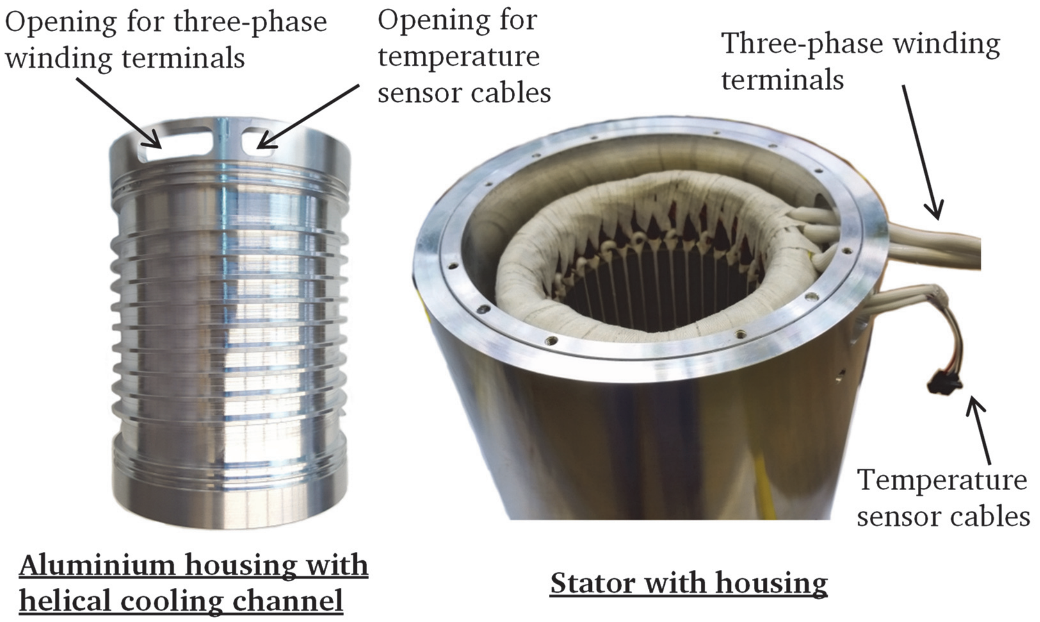

Fig. 4.6: Left: Stator inner housing with helical cooling channel, Right: Stator with inner and outer housing

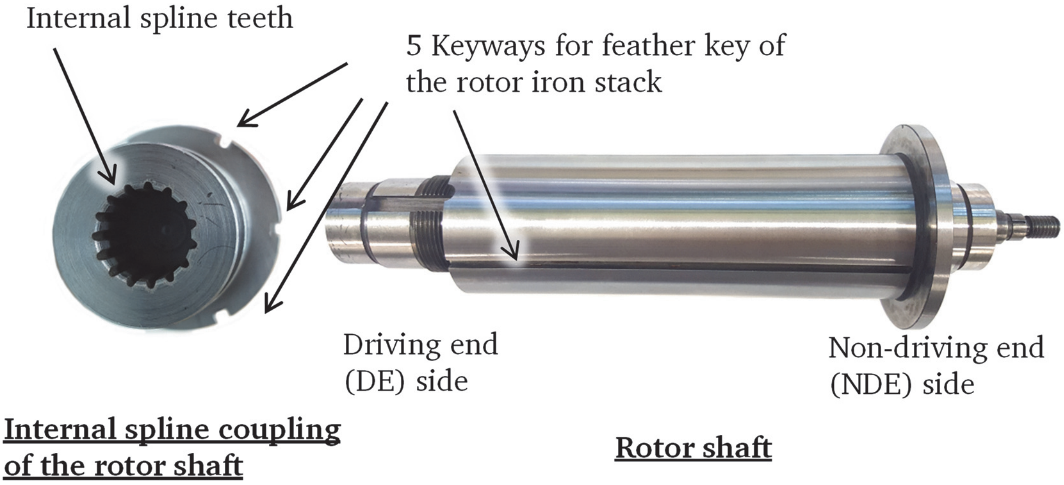

Fig. 4.7: Left: Internal spline coupling of the rotor shaft to the transmission of the DE-REX powertrain, Right: Rotor shaft of the electric machine

spline was cut in the rotor shaft, the inner surface of the internal spline teeth was case-hardened again to increase the strength of the material. The thermal stability of the magnets under load had been validated with the prototype machine, thus the magnet temperature of the electric machine for the DE-REX powertrain was not measured again. The remainder of the manufacturing process was identical to that used for the rotor of the prototype machine.

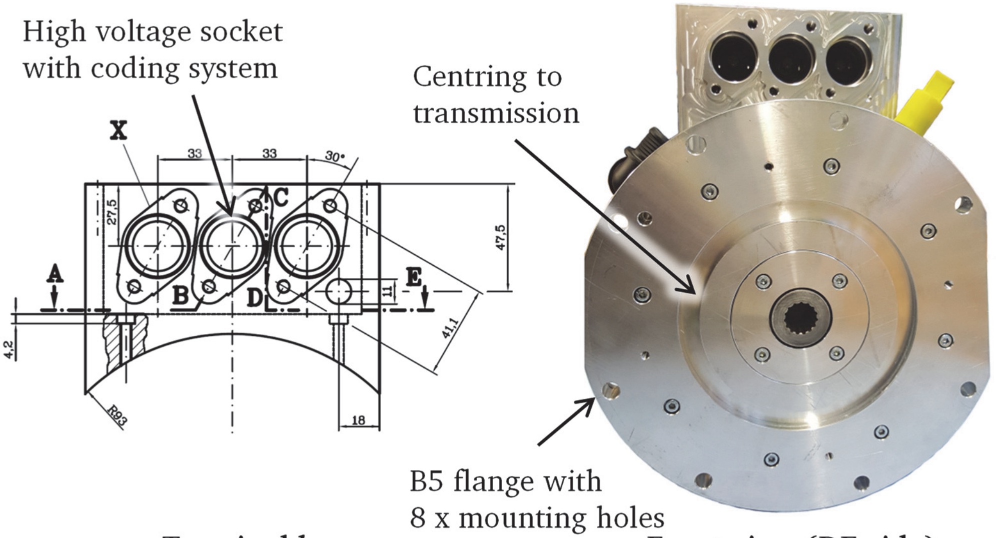

Terminal box **Front view (DE side)**

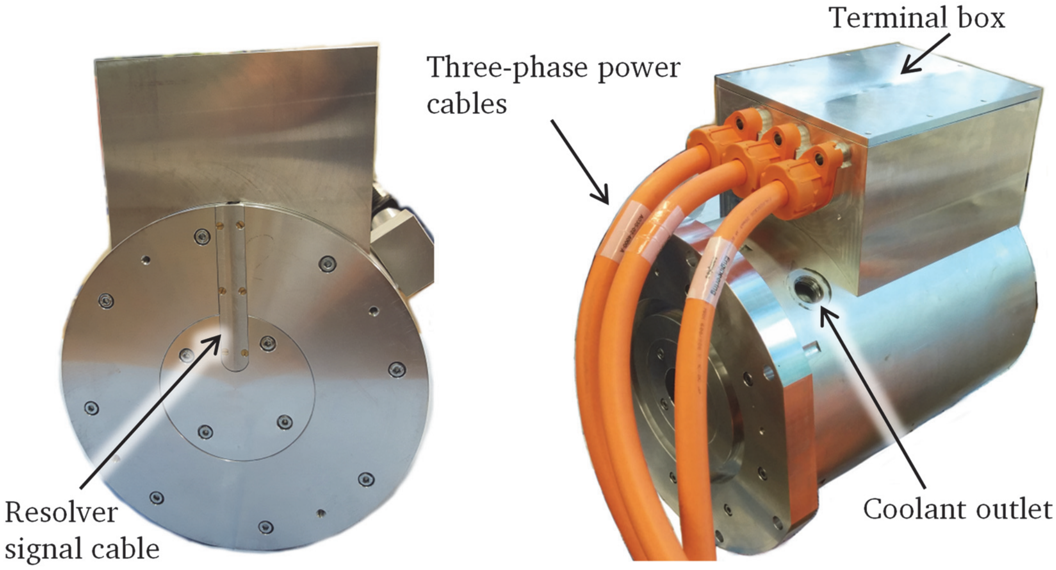

Back view (NDE side) **Machine with power cables**

Fig. 4.8: Completed electric machine for the DE-REX powertrain with the terminal box and three-phase power cables

For the convenience of mounting and demounting of the electric machine on the powertrain, high voltage sockets with interlocks from company *Rosenberger Hochfrequenztechnik* GmbH were used for the electric machine. The sockets were installed in the terminal box and were coded to prevent a phase reversal (top-left of Fig. 4.8). Three-phase power cables with plugs were connected to the terminal box and were fastened with two screws for each phase. The other ends of the cables were coupled to the DMC524 inverter (bottom-right of Fig. 4.8). The electric machine was fixed onto the DE-REX powertrain with a B5 flange with 8 mounting screws on the DE side. In order to align the electric machine and the transmission shaft, a centring was cut on the end plate at

DE side. To prevent damage to the electric machine from the vibration of other powertrain components and the electric machine itself, the NDE side of the electric machine was supported with an additional holder.

4.3 Test bench for individual measurement of the prototype machine

For measurement, the prototype machine was coupled to a cage induction machine from company *ELIN*, Austria, as a load machine (Fig. 4.9). It has a rated power of $P_\mathrm{N} = 270\,\mathrm{kW}$ and a rated speed of $n_\mathrm{N} = 16160\,\mathrm{min}^{-1}$, so it had sufficient power and speed range to load and drive the prototype machine (Table 4.1). The load machine was supplied by a frequency converter SIMOVERT AFE from company *Siemens* (Table 4.2). This converter has a regenerative feedback unit which can deliver electrical power back to the grid. It allows the induction machine to drive in a four-quadrant operation. For the measurements, the load machine was operated in a generator mode with a constant voltage per frequency (U/f = constant) control method. The prototype machine was operated with a torque control and different set point values for torque M, whereas the load machine was operated with a speed control with variable set point value for speed n, thus allowing a n-M-load point adjustment.

For the prototype machine, electrical power was initially fed by an industrial voltage source frequency inverter ServoOne SO 84.143 with a DC link voltage of $U_\mathrm{DC} = 565\,\mathrm{V}$ from company *LTi-Drives*. The inverter can drive the machine up to a fundamental stator frequency of 1600 Hz. The switching frequency can be modified to adjust the rated current of the inverter with air cooling. The rated current of the inverter is given with the

Table 4.1 Parameters of the induction machine from company *ELIN*

Rated power P_N	270 kW	Rated voltage U_N	460 V (D)
Rated speed n_N	16160 min^{-1}	Rated current I_N	431 A
Pole count $2p$	2 poles	Thermal class	H
Mass	450 kg	Cooling method	Water jacket cooling and water hollow shaft cooling via rotating sealings

Table 4.2 Parameters of SIMOVERT AFE frequency converter from company *Siemens*

	Input	Output
Rated fundamental frequency	50 … 60 Hz	0 … 600 Hz
Rated voltage (RMS)	380 … 460 V	0 … 460 V
Rated current (RMS)	247 A	260 A

options $I_{\mathrm{N}} = 143$ A, 143 A, 115 A, and 92 A by the switching frequencies $f_{\mathrm{sw}} = 4$ kHz, 8 kHz, 12 kHz, and 16 kHz respectively, due to the current derating of the inverter at higher switching frequency, caused by the increased switching losses.

For the later automotive application, the DC voltage of the battery was defined at $U_{\mathrm{DC}} \approx 300$ V. In addition, due to the limited space in the engine compartment of the prototype vehicle, a compact inverter was required. For this purpose, a DMC524 inverter from company *BRUSA Elektronik AG*, Sennwald, Switzerland, was used for the prototype machine and was tested on the test bench in the laboratory of the Institute of Electrical Energy Conversion at TU Darmstadt. The inverter has been specially designed for automobile applications, hence there is no grid-side rectifying unit but only a DC voltage link and a two-level inverter unit. Thus, it can operate electric AC machine either as motor or as generator and can thus drive the vehicle or save the regenerative energy to the battery during braking. Combined with an additional ICE range extender, the inverter and electric machine can extend the driving range by operating as a generator, charging the battery. The inverter has a rated current of 225 A, a maximum current of 300 A during short periods of 30 s, and a rated power of 79 kW. The inverter can drive the electric machine with a maximum fundamental frequency of up to 2 kHz. The inverter uses liquid coolant to cool the high-power density switching modules. The temperature of the power electronics in the inverter is regulated using a liquid pin cooling system, which is a patented technology from company *BRUSA*. Thus, the inverter can perform at an optimal temperature for its power electronic devices. The maximum admissible coolant temperature at the inlet is 65 °C with a flow rate of 6 l/min. Given the automobile application, the inverter must be protected from dust and the water, thus it has an IP protection category of IP 67 (IEC 60034-5). The inverter can perform both torque and speed control for the electrical machine. By parameterizing of the electric machine in the inverter control unit, the inverter can operate with a field-oriented current control and can also operate in the field weakening region of PMSM. All communication with

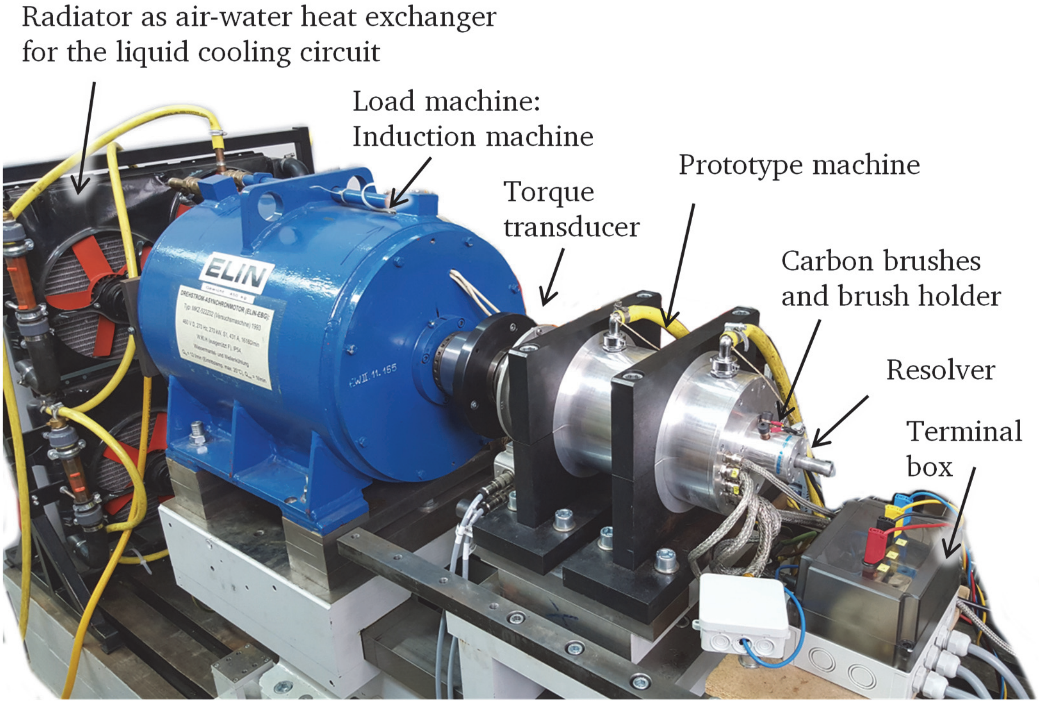

Fig. 4.9: Test bench for the prototype electric machine with: a load machine (induction machine), a prototype machine, a cooling radiator and a torque transducer

the inverter was done by a controller area network (CAN-bus), which is a standard communication protocol for the automobile industry. Further units of the DMC524 inverter type were also used for the electric machines for the DE-REX powertrain for the prototype vehicle and for the Hardware-in-the-Loop (HiL) test rig.

To validate and measure the electric machine for the DE-REX powertrain, the machine was coupled to the prototype machine via a torque transducer. For the following measurements of the four electric machines for the DE-REX powertrain for the prototype vehicle and for the HiL test rig, the prototype machine acted as load machine. Hence, both test and load machine were fed by two separate DMC524 inverters, each. The DC voltage source for both inverters was generated by a full-wave three-phase rectifier with an AC input line-to-line voltage of $U_{\mathrm{LL}} = 231\ \mathrm{V}$, which corresponds to rectified DC voltage of $U_{\mathrm{DC}} \approx 310\ \mathrm{V}$. This is close to the required battery voltage of 300 V for the later automotive application. Both the driving and loading inverter were operated at the same DC link. Thus, the test electric machine can drive as a motor or a generator, while the prototype machine operates as a generator or a motor, respectively (back-to-back connection, Fig. 4.10).

For the liquid cooling for both electric machines and both DMC524 inverters, two liquid cooling circuits were installed on the test bench for the two inverter–motor units. The power electronics in the DMC524 inverters is more sensitive to over-temperature. Thus,

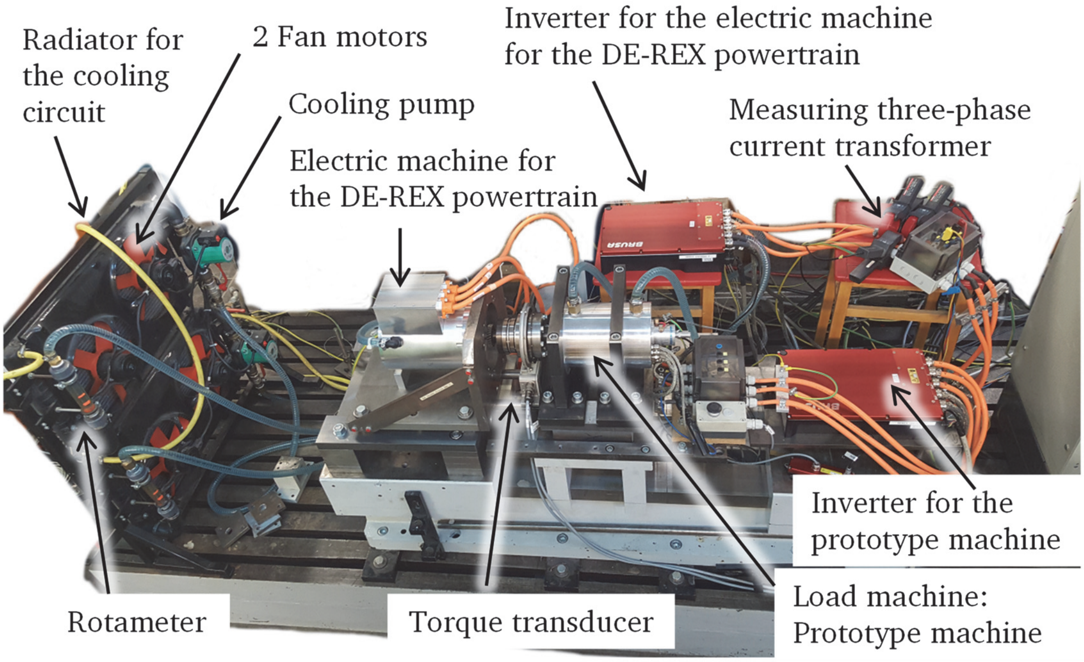

Fig. 4.10: Test bench for the individual measurement of one of the four PMSMs for the DE-REX powertrain for the prototype vehicle and for the HiL test rig with the prototype machine as a load machine and a separate feeding inverter supply for each of the two machines

the cooling system with the cold side coolant outlet was connected first to the coolant inlet of the two inverters. After cooling the inverters, the heated coolant flew to the coolant inlet of the two electric machines and through the helical cooling channel of the motor housings. The hot coolant from the outlet of the electric machine was pumped to the radiator by a Star ST 20/11 pump from company *WILO,* which was mounted at the input side of the radiator (Fig. 4.10). The radiator cooled the coolant with two fan motors for air cooling. At the output side of the radiator, a rotameter was installed in a vertical position to measure the volumetric flow rate of the coolant. The cooled coolant passed through the rotameter to the coolant inlet of the inverter, closing the cooling circuit. To satisfy the cooling system requirements of the prototype vehicle, the coolant flow rate was set to $\dot{V}_{\text{coolant}} = 6\,\text{l/min}$.

4.4 Measurement devices

For direct torque measurement, the prototype machine was coupled with the load machine via a torque transducer T10F, which has a rated torque of 200 Nm with 0.1 % measurement accuracy, from company *Hottinger Baldwin Messtechnik* (HBM) in Darmstadt, Germany. Double-disc couplings with spring packets were installed on both ends of the torque transducer rotor to accommodate a possible shaft misalignment between two machines. The torque transducer rotor transferred the measured torque signal to the stator side of the torque transducer without direct electrical contact. The measured signals were transferred to the data acquisition system MGCplus from the same company *HBM*. The measured mechanical torque and the measured rotational speed were shown on the digital display of the data acquisition system. This system transferred the data to the power analyser through 10-V analogue output signals.

The input electric power of the prototype machine at the motor terminals was measured with a high-precision power analyser Norma 5000 from company *Fluke*. The power analyser can perform precise measurement of current and voltage with 0.1 % accuracy, harmonic analysis, and fast *Fourier* transformation analysis. With the measured currents and voltages, the power analyser can calculate the electrical active power, reactive power, apparent power, and power factor [41]. The measured mechanical torque and the rotational speed signals from the torque transducer were transferred to the power analyser via analogue input. Thus, the mechanical output power and the efficiency of the electric machine could be calculated directly. The power analyser communicates with a PC through a serial communication interface. All measured data were recorded by LabVIEW software from company *National Instruments*.

Besides the aforementioned PT100 temperature sensors in the stator and the rotor, four PT100 temperature sensors were installed in the coolant inlet and outlet of the electric machine and of the DMC524 inverter to measure the coolant temperature rise. The ambient temperature was also measured. All measured temperatures were transferred to the PC by EtherCAT terminals with an EL3201 analogue input terminal from company *BECKHOFF*.

5. Measurement of the prototype electric machine

5.1 Generator no-load operation

In generator no-load operation mode, the machine is driven externally by the load machine at constant speed with an open stator winding terminal. In order to verify the calculated air-gap flux density and the proper design of the stator winding, the induced voltage U_{p0} was measured for different speeds up to 10000 min^{-1} in the no-load generator mode with the NORMA 5000 power analyser, which has an accuracy of ± 0.1 %. The rotor was warmed up previously to 100 °C to measure the induced voltage with a magnet operating temperature of $\vartheta_{\mathrm{M}} = 100$ °C. The measured induced voltage fundamentals are depicted in Fig. 5.1 over rotation speed, and they are compared to numerically calculated induced voltages. The measured induced no-load voltages are 4.86 % lower than the calculated values of the 2D FEM analysis: e.g. $U_{\mathrm{p0}} = 64.6$ V / 67.9 V, measured / calculated voltage at $n = 4167\ \mathrm{min}^{-1}$. This result comes from the flux leakage at the axial ends of the rotor magnets and the additional leakage of magnetic flux between adjacent rotor sections due to the rotor staggering, as well as the magnet insulation and rounded magnet edges, which reduce slightly the magnets' active mass. These effects were not considered in the 2D FEM calculation.

Measured induced phase voltage and induced line-to-line voltage over time using the oscilloscope (Agilent Technologies, DSO7034B) at rated speed $n = 4167\ \mathrm{min}^{-1}$ are shown in Fig. 5.2. The filtering effect of the short-pitched distributed stator 3-phase winding with $W/\tau_{\mathrm{p}} = 5/6$ (for reduction of 5th and 7th field wave harmonics) with $q =$ 2 number of slots per pole and phase and the step-skewed rotor (reducing the 11th and 13th field wave harmonics) attenuate mainly induced voltage harmonics. Hence, the voltage waveforms over time are nearly sinusoidal. The total measured harmonic distortion of the induced phase voltage is 1.36 %.

The measured no-load torque values, due to air friction, bearing friction and the no-load iron losses, and their linear interpolations at two different magnet temperatures of $\vartheta_{\mathrm{M}} =$ 35 °C and $\vartheta_{\mathrm{M}} = 100$ °C are shown in Fig. 5.3 as a function of rotation speed n. Because of the low no-load cogging torque from the stepped skewing of the rotor and the low mechanical friction of the ball bearing, the break-away torque is only about 0.2 Nm or 0.4 % of rated torque. The dependence of this value on magnet temperature is discussed in the following paragraph along with no-load losses P_{d0}.

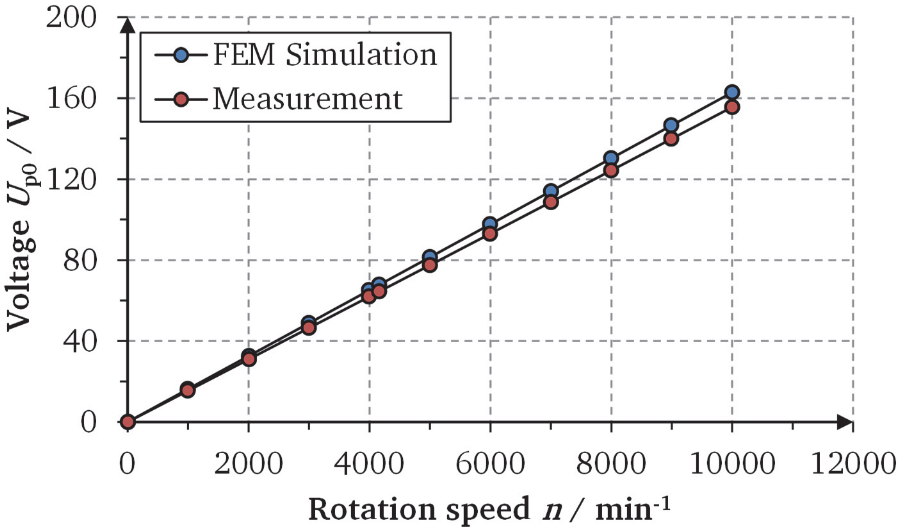

Fig. 5.1: Measured and numerically calculated no-load induced phase voltage (RMS) of the prototype electric machine up to 10000 min^{-1} with a magnet temperature of $\vartheta_{\mathrm{M}} = 100\ ^{\circ}\mathrm{C}$

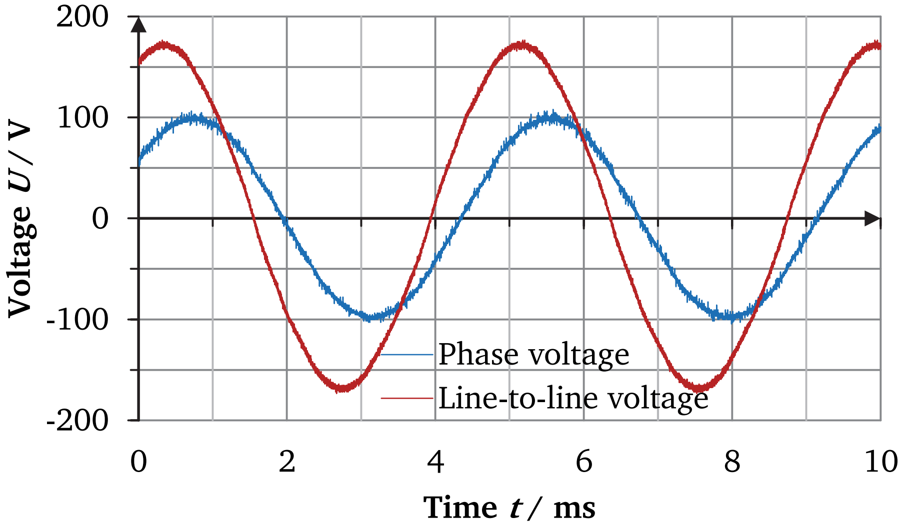

Fig. 5.2: Measured waveforms of the induced phase voltage and the induced line-to-line voltage of the prototype electric machine at 4167 min^{-1} with a magnet temperature of $\vartheta_{\mathrm{M}} = 35\ ^{\circ}\mathrm{C}$: the amplitude of the induced phase voltage fundamental is $\widehat{U}_{\mathrm{p0,ph}} = 98.7\ \mathrm{V}$, and the amplitude of the induced line-to-line voltage fundamental is $\widehat{U}_{\mathrm{p0,LL}} = 169.3\ \mathrm{V}\ \left(= \sqrt{3} \cdot 98.7\ \mathrm{V}\right)$

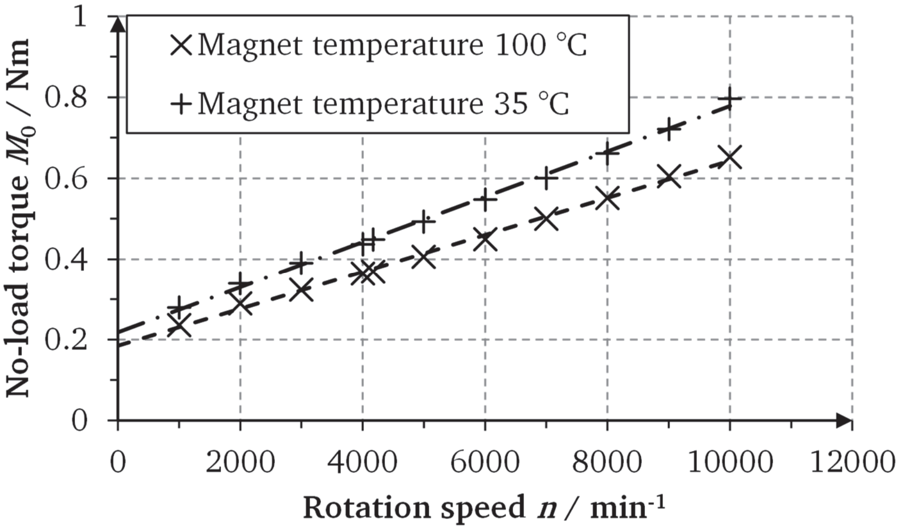

Fig. 5.3: Measured no-load torque values M_0 and their linear interpolations at no-load generator operation of the prototype machine with two different magnet temperatures of $\vartheta_\mathrm{M} = 35$ °C and 100 °C

The no-load losses $P_\mathrm{d0}$consist of friction losses $P_\mathrm{d,fr}$ and the no-load iron losses $P_\mathrm{d,Fe0}$ as the sum of no-load hysteresis and eddy current losses in the stator and in the rotor laminations, and eddy current losses in the segmented rotor magnets $P_\mathrm{d,M0}$. There are two possible methods to measure the no-load losses. The first method is measuring the generator no-load shaft torque M_0 and speed n at thermal steady state (Fig. 5.3). For this measurement, the prototype machine is coupled with a speed-controlled load machine through a torque transducer. The measured mechanical power represents the no-load losses at the given speed. In order to consider the influence of the magnet temperature on the losses, the no-load losses were measured at two different magnet temperatures of $\vartheta_\mathrm{M} = 35$ °C and $\vartheta_\mathrm{M} = 100$ °C, which correspond to the calculated steady-state temperatures of the magnets at no-load operation and rated operation (OP 2), respectively (Fig. 5.4). Since the magnet remanence flux density decreases with increasing temperature, given the negative magnet remanence temperature coefficient of -0.11 %/K, and since the iron losses are proportional to the square of the magnetic flux density ($P_\mathrm{d,Fe} \sim B^2$), the no-load losses decrease with the rise in magnet temperature. The second measurement method is the motor spin-down test. For this measurement, the prototype machine is operated alone as a motor, uncoupled from the load machine. The rotor is first warmed up to the steady-state temperature of the magnets at no-load operation $\vartheta_\mathrm{M} = 35$ °C. Then, the prototype machine is driven up by the inverter to the maximum speed of $n_\mathrm{max} = 10000\ \mathrm{min}^{-1}$. As the machine rotates at maximum speed, the driving power

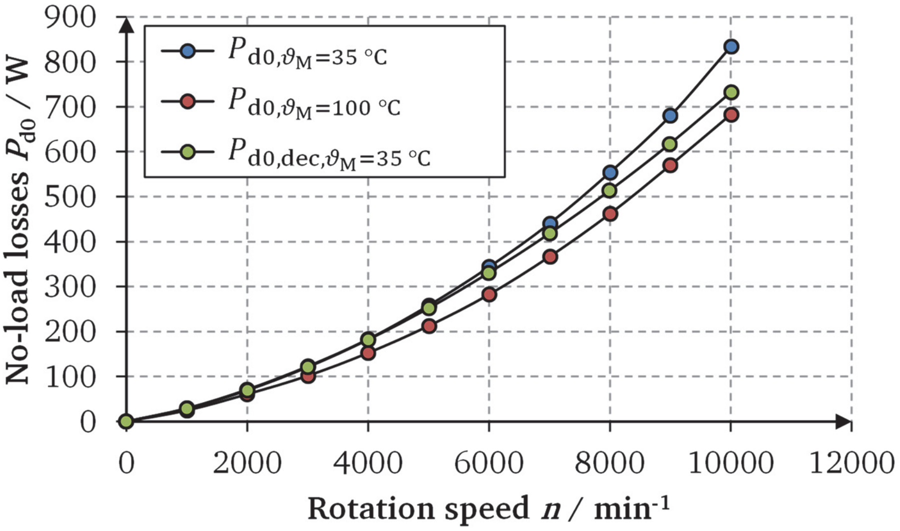

Fig. 5.4: Prototype machine: Measured no-load losses P_{d0} from a) measured no-load torque M_0 at no-load generator operation with two different magnet temperatures of $\vartheta_{\mathrm{M}} = 35$ °C and 100 °C and b) measured no-load losses from deceleration test $P_{\mathrm{d0,dec}}$ with magnet temperature of $\vartheta_{\mathrm{M}} = 35$ °C

from the inverter is switched off, the rotor decelerated, and the changing rotation speed over time is measured as the rotor decelerates (Fig. 5.5). The no-load losses are calculated using the reduction of kinetic energy W_{r} of the rotor with increasing time, using the calculated rotor moment of inertia of $J_{\mathrm{z}} = 8.27 \cdot 10^{-3}\ \mathrm{kg} \cdot \mathrm{m}^2$ in (5.1). The measured no-load losses $P_{\mathrm{d0,dec}}$ with the spin-down test are shown in Fig. 5.4. Comparison with the first method at a magnet temperature of $\vartheta_{\mathrm{M}} = 35$ °C shows good agreement, especially below 5000 min^{-1}.

$$P_{\mathrm{d0,dec}} = \frac{dW_{\mathrm{r}}}{dt} = 4\pi^2 \cdot J_z \cdot n \cdot \frac{dn}{dt} \tag{5.1}$$

$$W_{\mathrm{r}} = \frac{1}{2} \cdot J_{\mathrm{z}} \cdot (2\pi \cdot n)^2 \tag{5.2}$$

Using PT100 resistive temperature sensors, the temperature increase of the stator winding in the stator slots and in the winding overhang, and the temperature of the magnets (signal access via rotor slip rings for the sensor leads) were measured during generator no-load operation at rated speed of $n_{\mathrm{N}} = 4167\ \mathrm{min}^{-1}$, using a liquid cooling flow with a flow rate of 7 l/min (Fig. 5.6). The measured steady state temperature (and, in brackets, the temperature rise over the coolant average temperature) was 31.1 °C (1.8 K) in the stator slot, 30.9 °C (1.6 K) in the winding overhang, as the stator ohmic losses are zero,

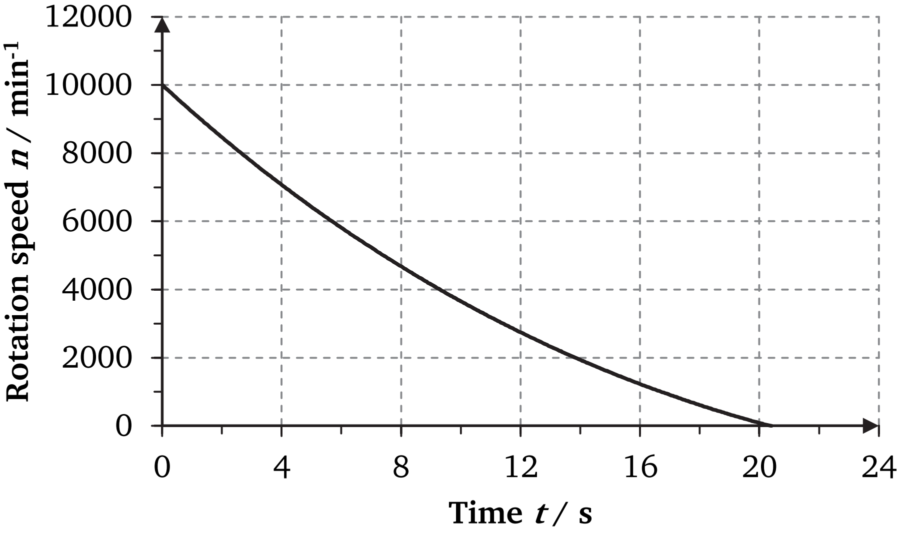

Fig. 5.5: Prototype machine: Measurement of the rotation speed over time during the deceleration of the rotor from maximum speed $n_{\mathrm{max}} = 10000\ \mathrm{min}^{-1}$ with magnet temperature of $\vartheta_{\mathrm{M}} = 35\ °\mathrm{C}$

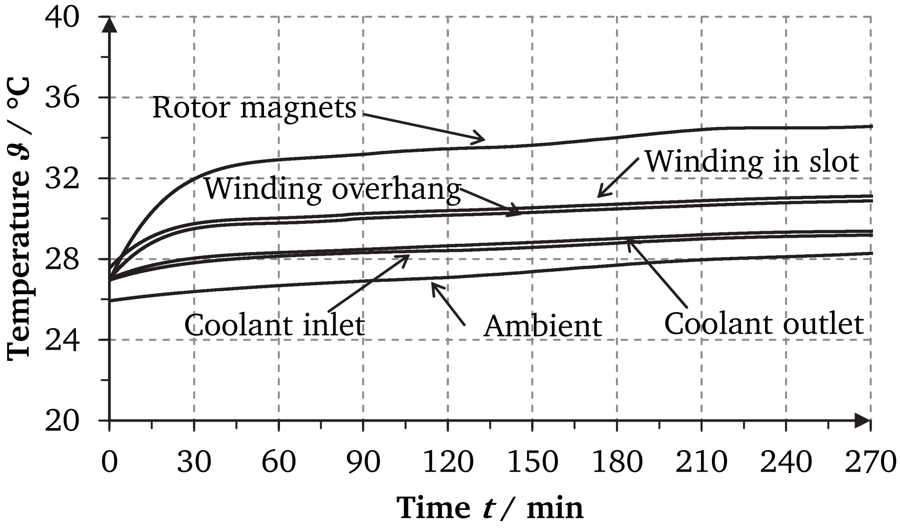

Fig. 5.6: Measured temperature rise in the prototype machine at no-load, rated speed $n_{\mathrm{N}} = 4167\ \mathrm{min}^{-1}$

and only 34.6 °C (5.3 K) in the magnets, mainly due to air friction losses. The eddy current losses $P_{\mathrm{d,M0}}$ in the magnets are according to calculation negligibly small.

5.2 Generator short-circuit operation

For the steady-state generator short-circuit test, the terminals of all three-phase stator windings were short circuited, and the prototype machine was driven by the load machine at different speed. During this measurement, the steady-state short-circuit current I_{sc} and the short-circuit torque M_{sc} were measured with the Norma 5000 power analyser and the torque transducer HBM T10F. These measured results are shown in Fig. 5.7 and Fig. 5.8 as a function of rotation speed n. To keep the temperature of the magnet and the winding constant at about $\vartheta_{\mathrm{M}} = 35\ ^\circ\mathrm{C}$ and $\vartheta_{\mathrm{cu}} = 100\ ^\circ\mathrm{C}$, the measurements were done quickly.

Due to the short-circuited stator winding terminals the phase voltage is zero, $U_{\mathrm{s}} = 0\ \mathrm{V}$. Hence the synchronous reactance X_{d} and inductance L_{d} in d-axis per stator phase are calculated with following equation from measured I_{sc}, R_{s} and U_{p0}.

$$\underline{U}_{\mathrm{s}} = 0 = \underline{U}_{\mathrm{p0}} + jX_{\mathrm{d}} \cdot \underline{I}_{\mathrm{sc}} + R_{\mathrm{s}} \cdot \underline{I}_{\mathrm{sc}} \tag{5.3}$$

$$X_{\mathrm{d}} = 2\pi f_{\mathrm{s}} \cdot L_{\mathrm{d}} = \sqrt{\left(\frac{U_{\mathrm{p0}}}{I_{\mathrm{sc}}}\right)^2 - R_{\mathrm{s}}^2} \tag{5.4}$$

For the calculation of the inductance L_{d}, the induced voltage (no-load back EMF) with the same magnet temperature $\vartheta_{\mathrm{M}} = 35\ ^\circ\mathrm{C}$ was used as the measurement of the short-circuit current. The induced voltage U_{p0} and the short-circuit current I_{sc} at rated speed

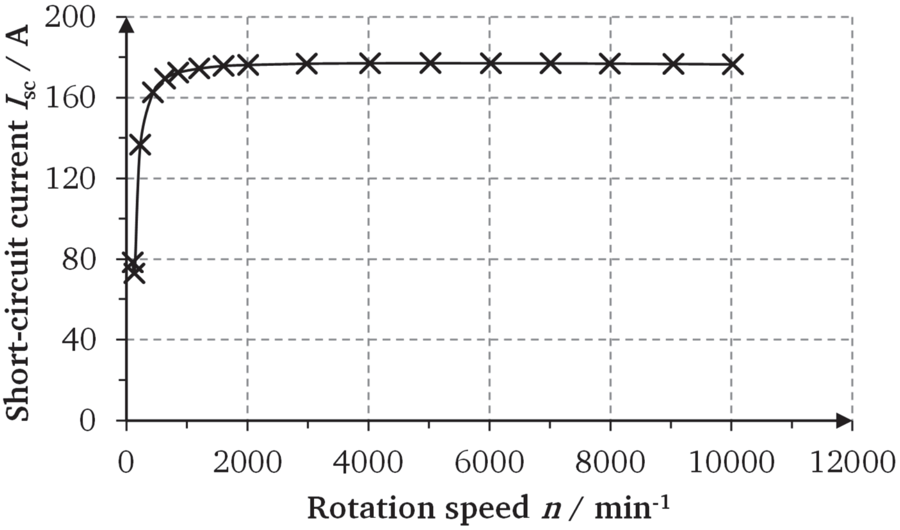

Fig. 5.7: Prototype machine: Measured steady-state short-circuit current I_{sc} (RMS) at generator no-load operation ($\vartheta_{\mathrm{M}} = 35\ ^\circ\mathrm{C}$ and $\vartheta_{\mathrm{cu}} = 100\ ^\circ\mathrm{C}$)

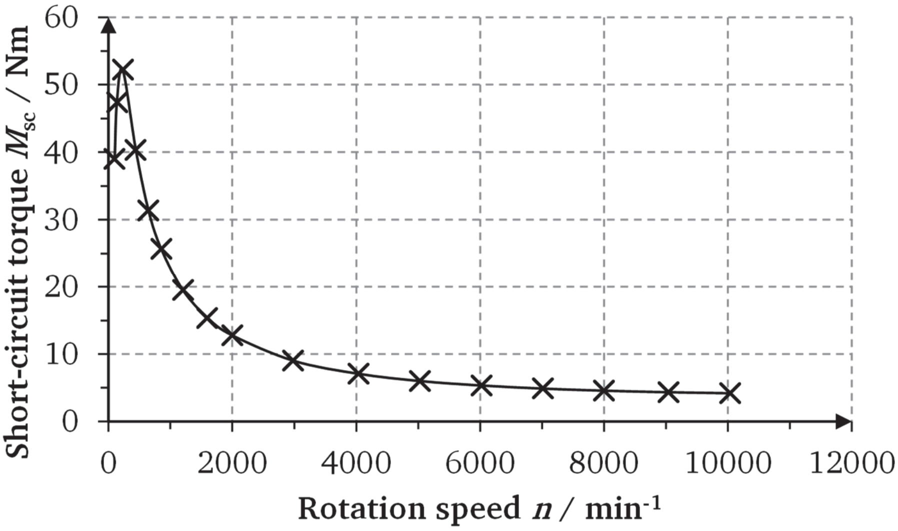

Fig. 5.8: Prototype machine: Measured short-circuit torque M_{sc} at generator no-load operation ($\vartheta_{\mathrm{M}} = 35$ °C and $\vartheta_{\mathrm{cu}} = 100$ °C)

$n_{\mathrm{N}} = 4167\ \mathrm{min}^{-1}$ with the magnet temperature of $\vartheta_{\mathrm{M}} = 35$ °C are $U_{\mathrm{p0}} = 69.1$ V and $I_{\mathrm{sc}} = 177.3$ A. Using (5.3) and (5.4) with the measured stator winding resistance at 100 °C $R_{\mathrm{s,100}} = 26.45\ \mathrm{m\Omega}$, the measured synchronous reactance and inductance in d-axis are $X_{\mathrm{d}} = 388.73\ \mathrm{m\Omega}$ and $L_{\mathrm{d}} = 296.95\ \mathrm{\mu H}$. The measured reactance has a more than 14-times bigger value than the stator winding resistance $X_{\mathrm{d}} \gg R_{\mathrm{s}}$. Therefore, the small stator winding resistance barely affects the value of the synchronous reactance at rated frequency.

5.3 Motor load operation

For load measurements, the tested prototype machine was operated via the inverter in the torque-controlled mode as a motor, and the load machine was operated as a speed-controlled generator. Due to the rotor saliency, the prototype machine was driven with an MTPA control algorithm at base speed range, but not as the field weakening range. To verify the effect of the reluctance torque of the prototype machine, the torque on the machine's rotor shaft was measured by varying the current angle β^* between 0° and $-90°$ for different stator current values I_{s} at rated speed of $n_{\mathrm{N}} = 4167\ \mathrm{min}^{-1}$ (Fig. 5.9). The measurements were performed with a magnet temperature of $\vartheta_{\mathrm{M}} = 100$ °C. Due to the difference between the inductance in the d-axis L_{d} and the inductance in the q-axis L_{q}, the measured torque increased with increasing absolute value $|\beta^*|$ of the negative current angle β^*. After it reached a maximum value, torque decreased again due to the decreasing q-current component I_{sq}. At low current levels I_s, the share of reluctance torque is smaller, as the stator flux linkage due to the rotor magnets Ψ_M is big due to the low level of load-dependent saturation. With higher stator currents, the increasing load-dependent iron saturation decreases Ψ_M, and the share of reluctance torque is increased. Since the measured no-load magnetic flux linkage Ψ_M from the generator no-load test at rated speed $n_N = 4167\ \mathrm{min}^{-1}$ was (as mentioned in Fig. 5.1) 4.9 % lower than what the FEM calculations has predicted, the prototype machine required a slightly higher stator current than predicted to produce the demanded rated torque $M_N = 55\ \mathrm{Nm}$. Due to the reluctance torque share, which is proportional to the square of the current (2.10), the required current did not increase by 4.9 %, but only by 3.8 % at the rated operating point (99.0 A / 95.4 A, measurement / simulation). Fig. 5.10 shows the measured torque curve comparison between a) the MTPA control and b) pure q-current control. Due to the saturation of the stator and the rotor iron at high current I_s, the measured torque curve with the pure q-current control shows a non-linearity at big I_s. For example, q-current control needs 38.9% more stator current (137.4 A) to generate the rated torque $M_N = 55$ Nm than MTPA control (99.0 A). Thus, it produces 93 % more ohmic losses. With MTPA control, the machine can be operated with the minimum ohmic losses, which are the major losses in the prototype machine. Thus, it can be considered that the MTPA control drives the machine with maximum motor efficiency.

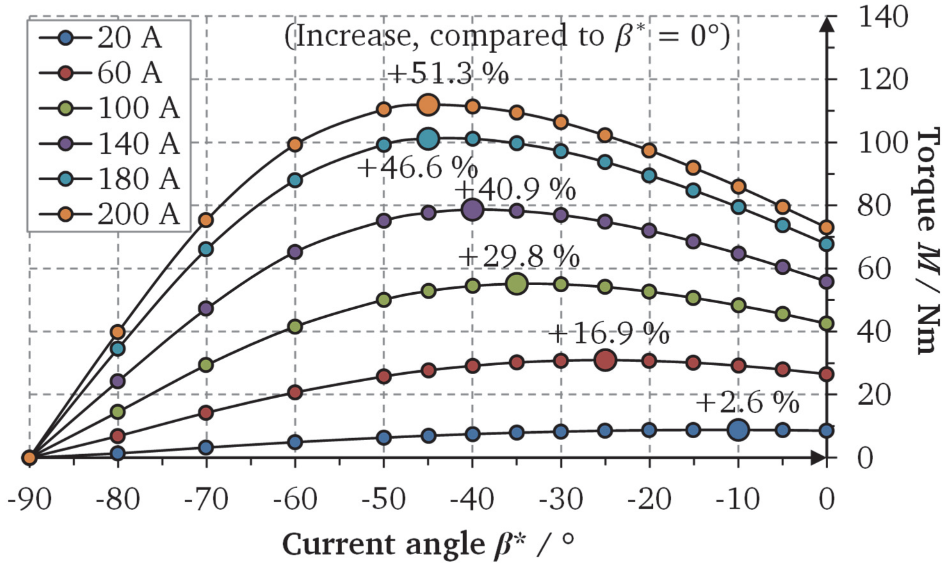

Fig. 5.9: Prototype machine: Measured motor torque by varying the current angle β^* with different current values I_s (RMS) up to 200 % rated current at rated speed $n_N = 4167\ \mathrm{min}^{-1}$

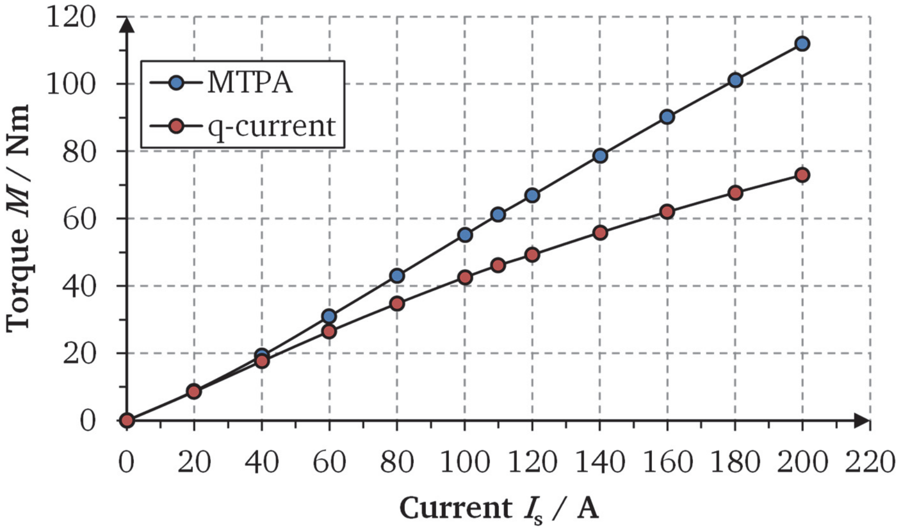

Fig. 5.10: Prototype machine: Measured torque M - current I_s - curves with a) a motor control algorithm of maximum torque per ampere and b) with pure q-current operation $I_s = I_{sq}$, $I_{sd} = 0$ at rated speed $n_N = 4167\ \mathrm{min}^{-1}$

5.3.1 Load operations with industrial inverter ServoOne

Initially, the prototype machine was powered by the industrial voltage source frequency inverter ServoOne from company *LTi-Motion* with a DC link voltage of $U_{DC} = 565$ V for the measurement of load operation. The measured electrical and mechanical parameters at the three operation points with this industrial inverter ServoOne are shown in Table 5.1. For these measurements, the prototype machine was heated, until the magnet temperature reached 100 °C, which is the steady-state temperature at rated load operation with an inverter switching frequency of $f_{sw} = 12$ kHz. During measurement, the magnet temperature changed only slightly: circa ± 2 K. The measured fundamental phase voltage $U_{s,1}$ and current $I_{s,1}$ (RMS) in Table 5.1 are average values of the three-phase voltages (U, V and W phase) and current fundamentals, measured by the power analyser Norma 5000. The electrical input power P_{el} includes also the current and voltage harmonics of higher harmonic order due to the inverter supply. The electrical input power fundamental $P_{el,1}$ is given by the fundamentals of voltage and current, and is smaller than the total electrical input power. The difference between these two power values $P_{d,PWM} = P_{el} - P_{el,1}$ represents the additional losses due to the high-order current harmonics $I_{s,k}$, caused by the PWM inverter supply. The total losses of the prototype machine were measured via the direct power measurement during the input-output test as $P_d = P_{el} - P_m$. The load dependent stray load losses $P_{d,ad}$ are measured with the subtraction from the measured total losses to the DC ohmic losses $P_{\mathrm{d,cu1,DC}}$ from the current fundamental $I_{\mathrm{s,1}}$ and the no-load losses P_{d0} from the no-load test ($P_{\mathrm{d,ad}} = P_{\mathrm{d}} - P_{\mathrm{d,cu1,DC}} - P_{\mathrm{d0}}$). The stray load losses $P_{\mathrm{d,ad}}$ include the increased iron losses at load operation due to the load dependent stator field $P_{\mathrm{d,Fe}} - P_{\mathrm{d,Fe0}}$, the additional losses in the stator windings due to the current displacement $P_{\mathrm{d,cu,AC}} - P_{\mathrm{d,cu1,DC}}$ and the additional eddy current losses $P_{\mathrm{d,PWM}}$ in the rotor's conductive parts (e.g., magnets and rotor iron sheets) and the stator iron sheets due to the current high-order harmonics $I_{\mathrm{s},k}$ (k: ordinal number of current spectrum).

The average winding temperature $\vartheta_{\mathrm{cu,av}}$ was determined from the measured winding temperature in the stator slot and in both winding overhangs with the help of the winding length ratios of the stator slot and of both winding overhangs (5.5).

$$\vartheta_{\mathrm{cu,av}} = \frac{2l_{\mathrm{Fe}} \cdot \vartheta_{\mathrm{slot}} + l_{\mathrm{b}} \cdot \vartheta_{\mathrm{WO,NDE}} + l_{\mathrm{b}} \cdot \vartheta_{\mathrm{WO,DE}}}{2l_{\mathrm{Fe}} + 2l_{\mathrm{b}}} \tag{5.5}$$

The differences between the calculated total motor losses $P_{\mathrm{d,calc}}$ and the measured total motor losses P_{d} come from the additional losses due to the PWM inverter supply due to current spectrum $I_{\mathrm{s},k}$ and the uncertainty of the correction factor for the iron losses, with $k_{\mathrm{v}} = 1.5$ used for the loss calculations. With these considerations, the numerically calculated losses show good accordance with the measured values.

5.3.2 Temperature rise with load operations with the industrial inverter

The temperature rises at the stator winding and the magnets in the rotor of the prototype machine were measured during load operations. Three PT100 temperature sensors were installed in the stator winding (one in the stator copper winding in the slot $\vartheta_{\mathrm{slot}}$, two on each winding overhang $\vartheta_{\mathrm{WO,DE}}$, $\vartheta_{\mathrm{WO,NDE}}$). For magnet temperature measurement, a PT100 sensor was mounted under one magnet in the rotor, and the temperature signal ϑ_{M} was measured via rotor slip rings for this sensor's leads. The coolant inlet temperature $\vartheta_{\mathrm{coolant,in}}$, the coolant outlet temperature $\vartheta_{\mathrm{coolant,out}}$ and the ambient temperature ϑ_{amb} were measured using type-J thermocouples.

The temperature increases at the rated operating OP2 were measured until temperatures did not change more than 2 K in 1 hour. The prototype machine was cooled with a liquid cooling system with a flow rate of 7 l/min (Fig. 5.12). In 90 min, the winding temperatures reached steady state, while the magnet temperature took 180 min to reach steady state. At steady state, with average coolant temperature of $\vartheta_{\mathrm{coolant,av}} =$ 35 °C, the temperatures (and, in brackets, temperature rise over $\vartheta_{\mathrm{coolant,av}}$) of the winding overhang non-driving end (NDE), the winding overhang driving end (DE) and the stator slot reached $\vartheta_{\mathrm{WO,NDE}} = 76.4$ °C ($\Delta\vartheta_{\mathrm{WO,NDE}} = 41.4$ K), $\vartheta_{\mathrm{WO,DE}} = 75.9$ °C ($\Delta\vartheta_{\mathrm{WO,DE}}$ $= 40.9$ K) and $\vartheta_{\mathrm{slot}} = 67.0$ °C ($\Delta\vartheta_{\mathrm{slot}} = 32.0$ K), respectively, which is much lower than the limit of Thermal Class H (125 K). Due to the cast epoxy-based resin around the winding overhang, the temperature difference between the slot and the overhang is only 9.4 K. The steady-state temperature of the rotor magnets was $\vartheta_{\mathrm{M}} = 100.6$ °C ($\Delta\vartheta_{\mathrm{M}} =$ 65.6 K), which is much lower than the limiting operating temperature of the magnets $\vartheta_{\mathrm{M,lim}} = 170$ °C. This result shows that the hot spot of the prototype machine at rated operation is in the rotor.

To check the thermal boundary condition for the prototype machine, the temperature increases in 30 s at overload condition (OP1) and at field weakening range (OP3) were measured (Fig. 5.11). Before these measurements were done, the prototype machine was warmed up with the rated load until reaching steady-state temperature. Due to the short operating time of 30 s, the temperature rises of the magnet for both cases were negligibly small: $\Delta\vartheta_{\mathrm{M}} = 1.7$ K at overload condition and $\Delta\vartheta_{\mathrm{M}} = 0.9$ K at field weakening range. Due to high ohmic losses for both load conditions (OP1: $P_{\mathrm{d,cu1,DC}} = 2902$ W and OP3: $P_{\mathrm{d,cu1,DC}} = 1445$ W), the temperature rises in the stator winding in the stator slot and winding overhangs were $\Delta\vartheta_{\mathrm{slot}} = 16.6$ K, $\Delta\vartheta_{\mathrm{WO,DE}} = 11.3$ K, and $\Delta\vartheta_{\mathrm{WO,NDE}} = 15.0$ K for OP1 and $\Delta\vartheta_{\mathrm{slot}} = 9.6$ K, $\Delta\vartheta_{\mathrm{WO,DE}} = 5.5$ K, and $\Delta\vartheta_{\mathrm{WO,NDE}} = 6.4$ K for OP3. With consideration of the steady state temperature at the rated load operation (OP2) and the increased coolant temperature of 65 °C, the winding overhang on the NDE side after 30 s of overload condition (OP1) will be $\vartheta_{\mathrm{WO,NDE}} = 121.4$ °C, which gives a temperature reserve of 58.6 K with the used Thermal Class H ($\vartheta_{\mathrm{max}} = 180$ °C, IEC 60034) material of the winding insulation system. The corresponding rotor magnet temperature of $\vartheta_{\mathrm{M}} =$ 132.3 °C gives a safety margin of 37.7 K. Hence, the series motors can be equipped with the cheaper insulation of Thermal Class F ($\vartheta_{\mathrm{max}} = 155$ °C, IEC 60034) and with cheaper magnets with a temperature limit of only $\vartheta_{\mathrm{M,lim}} = 140$ °C. These magnets have a higher remanence and allow, therefore, a slight reduction of the stator currents.

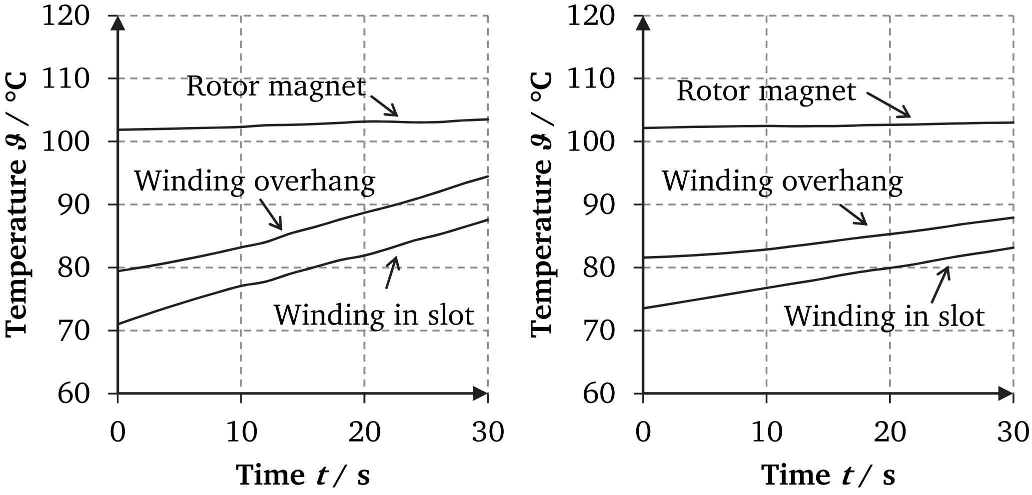

a)   b)

Fig. 5.11: Measured temperature of the prototype machine with the industrial inverter ServoOne for S2–30 s at a) overload (OP1: $M = 110\ \mathrm{Nm}, n_\mathrm{N} = 4167\ \mathrm{min}^{-1}$) with the temperature rise in 30 s: $\Delta\vartheta_\mathrm{slot} = 16.6\ \mathrm{K}$, $\Delta\vartheta_\mathrm{WO,DE} = 11.3\ \mathrm{K}$, $\Delta\vartheta_\mathrm{WO,NDE} = 15.0\ \mathrm{K}$, and $\Delta\vartheta_\mathrm{M} = 1.7\ \mathrm{K}$; b) field weakening (OP3: $M = 45.8\ \mathrm{Nm}, n = 10000\ \mathrm{min}^{-1}$) with the temperature rise in 30 s: $\Delta\vartheta_\mathrm{slot} = 9.6\ \mathrm{K}$, $\Delta\vartheta_\mathrm{WO,DE} = 5.5\ \mathrm{K}$, $\Delta\vartheta_\mathrm{WO,NDE} = 6.4\ \mathrm{K}$, and $\Delta\vartheta_\mathrm{M} = 0.9\ \mathrm{K}$

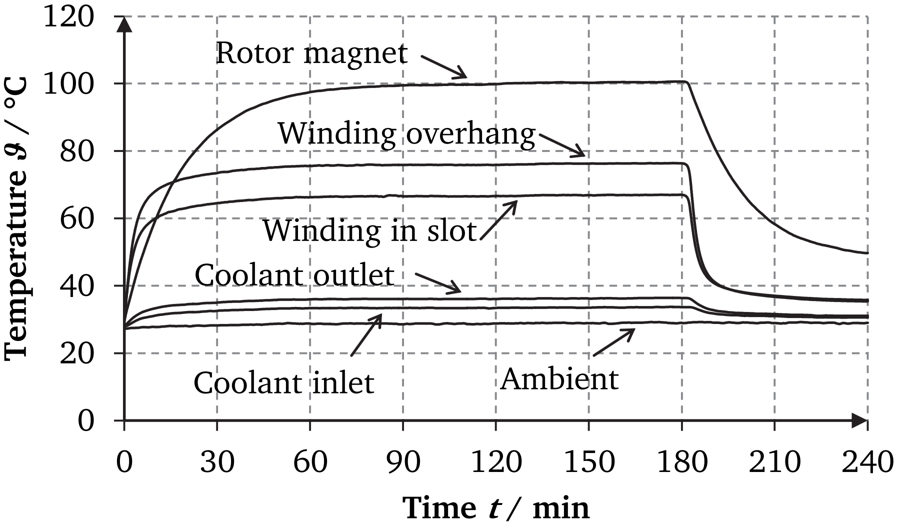

Fig. 5.12: Measured temperature rises of the prototype machine with the industrial inverter ServoOne at rated operation (OP2: $M_\mathrm{N} = 55\ \mathrm{Nm}, n_\mathrm{N} = 4167\ \mathrm{min}^{-1}$) with the steady-state temperatures at $t = 180\ \mathrm{min}$: $\vartheta_\mathrm{slot} = 67.0\ °\mathrm{C}$, $\vartheta_\mathrm{WO,DE} = 75.9\ °\mathrm{C}$, $\vartheta_\mathrm{WO,NDE} = 76.4\ °\mathrm{C}$, $\vartheta_\mathrm{M} = 100.6\ °\mathrm{C}$, $\vartheta_\mathrm{coolant,in} = 33.7\ °\mathrm{C}$, $\vartheta_\mathrm{coolant,out} = 36.4\ °\mathrm{C}$, and $\vartheta_\mathrm{amb} = 29.0\ °\mathrm{C}$

Table 5.1 Prototype machine: a) Measured motor electrical parameters and mechanical torque values at load operation with industrial inverter ServoOne ($U_{\mathrm{DC}} = 565$ V, $f_{\mathrm{sw}} = 12$ kHz and 8 kHz) and magnet temperature of $\vartheta_{\mathrm{M}} = 100$ °C, b) numerically calculated total losses at load operation with modified remanence of the magnet ($B_{\mathrm{R100,mod}} = 1.097$ T)

Measured:			**OP1**	**OP2**	**OP3**
Fundamental phase voltage (RMS)	$U_{\mathrm{s,1}}$	$\mathrm{V_{rms}}$	107.5	94.1	122.1
Fundamental phase current (RMS)	$I_{\mathrm{s,1}}$	$\mathrm{A_{rms}}$	194.1	99.0	138.0
Current angle	β^*	°	-42.5	-32.5	-75.3
Fundamental power factor	$\cos \varphi_{\mathrm{s,1}}$	-	0.818	0.894	0.999
Shaft torque	M_{m}	Nm	109.57	55.12	45.50
Speed	n	min^{-1}	4167.27	4167.33	10003.25
Mechanical output power	P_{m}	W	47816	24053	47668
Electrical input power fundamental	$P_{\mathrm{el,1}}$	W	51199	25000	50510
Electrical input power	P_{el}	W	51591	25269	50818
Efficiency	η	%	92.7	95.2	93.8
Winding temperature	$\vartheta_{\mathrm{cu,av}}$	°C	90.3	70.8	85.1
Stator resistance	$R_{\mathrm{s,hot}}$	mΩ	25.7	24.1	25.3
DC ohmic losses	$P_{\mathrm{d,cu1,DC}}$	W	2902	710	1445
No-load losses	P_{d0}	W	163	163	683
Total motor losses	P_{d}	W	3775	1216	3150
Stray load losses	$P_{\mathrm{d,ad}}$	W	710	343	1022
Additional motor losses due to PWM inverter supply	$P_{\mathrm{d,PWM}}$	W	392	269	308
Inverter switching frequency	f_{sw}	kHz	8	12	12
Inverter DC link voltage	U_{DC}	V	565	565	565
Calculated:					
Calculated total losses without $P_{\mathrm{d,PWM}}$	$P_{\mathrm{d,calc}}$	W	3230	1053	2726
Calculated total losses with $P_{\mathrm{d,PWM}}$ from measurements	$P_{\mathrm{d,calc}} + P_{\mathrm{d,PWM}}$	W	3622	1322	3034

5.3.3 Load operations with DMC524 inverter

For the automotive application with the DE-REX powertrain, the minimum DC voltage of the battery is defined at 300 V. Thus, the load measurement for the prototype machine was repeated with the DMC524 voltage source inverter from company *BRUSA*, with a DC link voltage of only $U_{\mathrm{DC}} = 325$ V. Table 5.2 shows the measured electrical and mechanical parameters at the three operation points with the DMC524 inverter. Due to the much higher switching frequency $f_{\mathrm{sw}} = 24$ kHz (doubled) and lower DC link voltage (nearly halved), yielding a higher inverter voltage modulation index and a lower current ripple, the steady-state magnet temperature at the rated load operation was reduced from $\vartheta_{\mathrm{M}} = 100$ °C to $\vartheta_{\mathrm{M}} = 60$ °C.

The measured additional losses that due to the current high-order harmonics $I_{\mathrm{s},k}$ of the PWM inverter supply $P_{\mathrm{d,PWM}}$ were reduced significantly with the use of the fast-switching DMC524 inverter. At overload operation (OP1), the prototype machine with the industrial inverter (Table 5.1) showed additional losses due to the PWM inverter supply $P_{\mathrm{d,PWM}}$, that were 5.7 times greater than those measured when the DMC524 inverter was used. In the case of the field weakening region (OP3), the machine with the industrial inverter produced additional losses $P_{\mathrm{d,PWM}}$ that were 8.8 times greater than when the DMC524 inverter was used. There are two reasons for these differences: higher switching frequencies and higher modulation indices due to the lower DC link voltage. Compared with the DMC524 inverter switching frequency of $f_{\mathrm{sw}} = 24$ kHz for the entire operating range, the industrial inverter was operated with a lower switching frequency of $f_{\mathrm{sw}} = 12$ kHz for the rated operation (OP2) and the field weakening operation (OP3), and with a reduced switching frequency of $f_{\mathrm{sw}} = 8$ kHz for the overload operation (OP1) to keep inverter losses at measured current constant. The lower modulation index leads to larger stator current ripples. These current ripples caused the bigger additional ohmic losses in the stator winding, the bigger additional iron losses and the additional eddy current losses in the rotor's conductive parts [42]. Even though the prototype machine operates at the same fundamental motor voltage level, the modulation indices are different: For example, see at the field weakening operation (OP3) with the stator phase voltage fundamental $U_{\mathrm{s1}} = 122.1$ V / 120.1 V a modulation index $m = 0.61/1.05$ (industrial inverter / DMC524 inverter). With the higher modulation index m, the stator phase voltage spectrum shows significantly higher amplitude for the fundamental component than the amplitudes of the higher-order harmonics. On the other hand, when the machine operates with a low modulation index m, the relative contribution of the higher-order harmonics is increased, and they cause more iron losses in the stator and rotor iron sheets [43]. Due to the much smaller values $P_{\mathrm{d,PWM}}$, the calculated and measured total losses fit much better (Table 5.2).

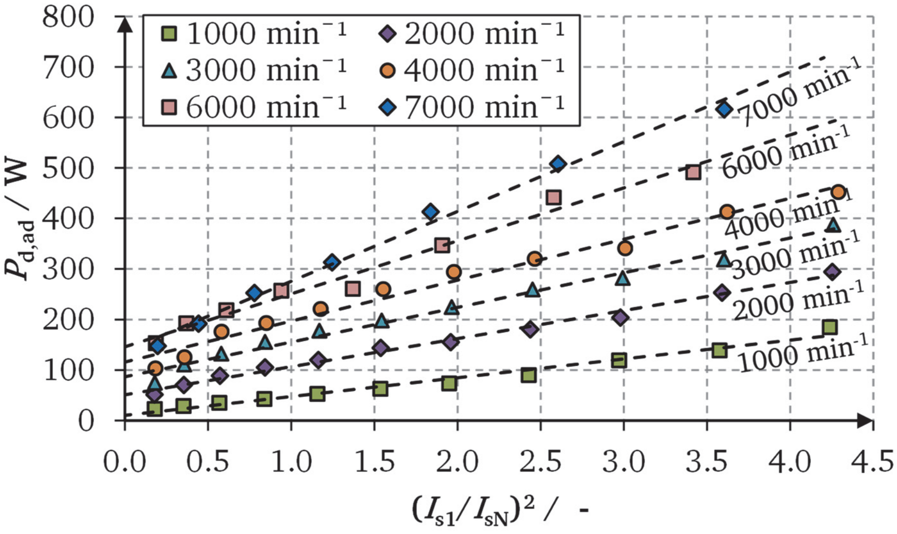

Fig. 5.13: Prototype machine: Measured stray load losses $P_{\mathrm{d,ad}}$ versus square of the RMS stator current per unit values $(I_{\mathrm{s1}}/I_{\mathrm{sN}})^2$ at different speed with DMC524 inverter ($U_{\mathrm{DC}} = 325\,\mathrm{V}, f_{\mathrm{sw}} = 24\,\mathrm{kHz}$) and their linear trend lines

In order to understand better the dependence of the stray load losses $P_{\mathrm{d,ad}}$ on the rotation speed n and the stator current $I_{\mathrm{s,1}}$, a few sets of measurements were taken at different loads. The measured stray load losses $P_{\mathrm{d,ad}}$ at different load conditions are presented in Fig. 5.13. The results show that the stray load losses are in a close to linear relationship with the square of the stator current $P_{\mathrm{d,ad}} \sim I_{\mathrm{s1}}^2$. The measured stray load losses graphed against the rotation speed at constant output torque are shown in Fig. 5.14. At low rotation speeds (up to rated speed of $4167\,\mathrm{min}^{-1}$), the losses rise almost linear with the rotation speed at constant torque. However, when the rotation speed is increased, the losses suddenly increased significantly, even at the same mechanical output torque. At high rotation speeds, the machine needs more negative d-current component to suppress the high induced voltage, thus the required current for the given torque increases. The measured stray load losses have an almost linear dependence on the product of the square of stator current and rotation speed $P_{\mathrm{d,ad}} \sim I_{\mathrm{s1}}^2 \cdot n$ (Fig. 5.15).

Table 5.2 Prototype machine: a) Measured motor electrical parameters and mechanical torque values at load operation with DMC524 inverter ($U_{\mathrm{DC}} = 325$ V, $f_{\mathrm{sw}} = 24$ kHz) and magnet temperature of $\vartheta_{\mathrm{M}} = 60$ °C and b) numerically calculated total losses at load operation with modified remanence of the magnet ($B_{\mathrm{R60,mod}} = 1.16$ T)

Measured:			**OP1**	**OP2**	**OP3**
Fundamental phase voltage	$U_{\mathrm{s,1}}$	$\mathrm{V_{rms}}$	101.9	95.3	120.1
Fundamental phase current	$I_{\mathrm{s,1}}$	$\mathrm{A_{rms}}$	194.9	98.1	140.2
Fundamental power factor	$\cos\varphi_{\mathrm{s,1}}$	-	0.864	0.894	1.000
Shaft torque	M_{m}	Nm	110.48	55.23	45.63
Speed	n	min^{-1}	4166.93	4166.60	10000.00
Mechanical output power	P_{m}	W	48210	24100	47780
Electrical input power fundamental	$P_{\mathrm{el,1}}$	W	51471	25052	50498
Electrical input power	P_{el}	W	51540	25126	50533
Efficiency	η	%	93.5	95.9	94.6
Winding temperature	$\vartheta_{\mathrm{cu,av}}$	°C	65.6	61.8	61.4
Stator resistance	$R_{\mathrm{s,hot}}$	mΩ	23.73	23.43	23.40
DC ohmic losses	$P_{\mathrm{d,cu1,DC}}$	W	2703	676	1380
No-load losses	P_{d0}	W	173	173	759
Total motor losses	P_{d}	W	3330	1026	2753
Stray load losses	$P_{\mathrm{d,ad}}$	W	454	177	614
Additional motor losses due to PWM inverter supply	$P_{\mathrm{d,PWM}}$	W	69	74	35
Inverter switching frequency	f_{sw}	kHz	24	24	24
Inverter DC link voltage	U_{DC}	V	325	325	325
Calculated:					
Calculated total losses without $P_{\mathrm{d,PWM}}$	$P_{\mathrm{d,calc}}$	W	3116	1009	2683
Calculated total losses with $P_{\mathrm{d,PWM}}$ from measurements	$P_{\mathrm{d,calc}} +$ $P_{\mathrm{d,PWM}}$	W	3185	1083	2718

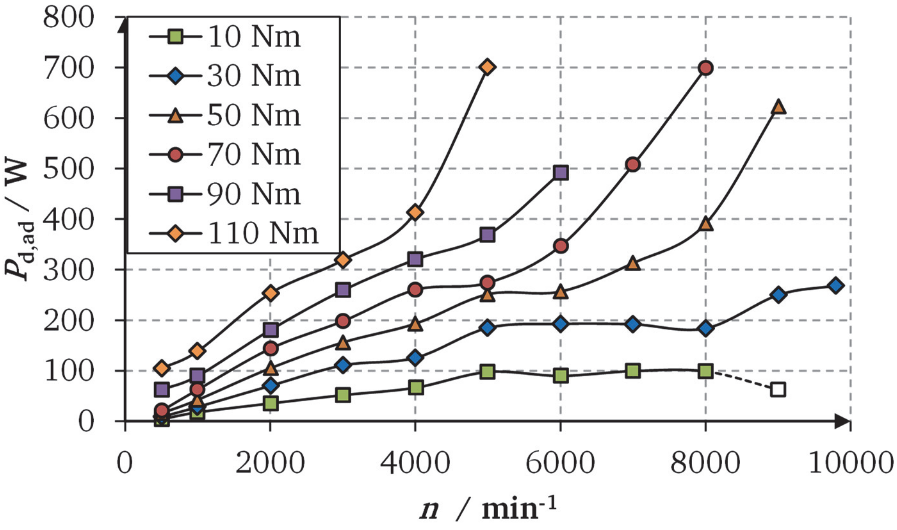

Fig. 5.14: Prototype machine: Measured stray load losses $P_{\mathrm{d,ad}}$ versus the rotation speed n at different loads of the prototype machine with DMC524 inverter ($U_{\mathrm{DC}} = 325$ V, $f_{\mathrm{sw}} = 24$ kHz)

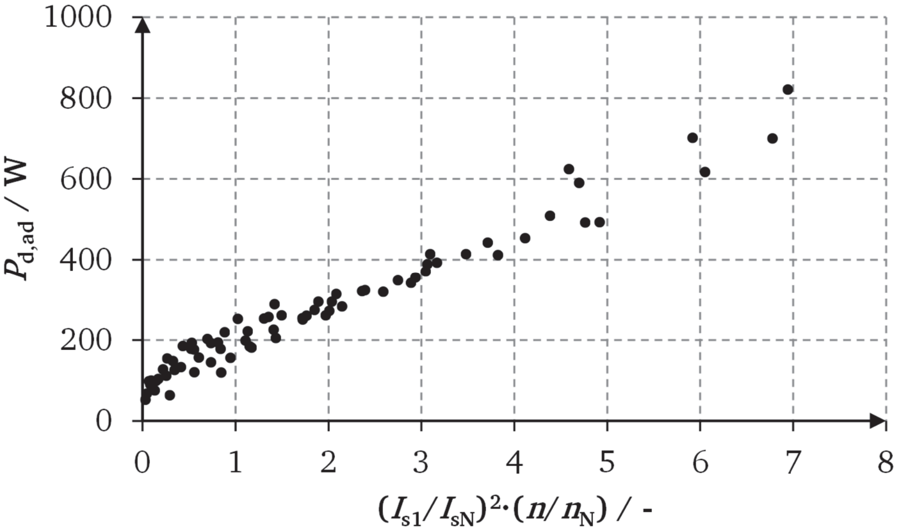

Fig. 5.15: Prototype machine: Measured stray load losses $P_{\mathrm{d,ad}}$ versus the product of rotation speed and the square of stator current per unit values $(I_{\mathrm{s1}}/I_{\mathrm{sN}})^2 \cdot (n/n_{\mathrm{N}})$ with DMC524 inverter ($U_{\mathrm{DC}} = 325$ V, $f_{\mathrm{sw}} = 24$ kHz)

5.3.4 Temperature rise with load operation with the DMC524 inverter

With the DMC524 inverter, which has double switching frequency of $f_{\mathrm{sw}} = 24$ kHz and a lower, battery-fitting DC link voltage of $U_{\mathrm{DC}} = 325$ V, the prototype machine produced less stray load losses $P_{\mathrm{d,ad}}$. Hence, the heat in the rotor due to the additional eddy current losses in the rotor's conductive parts (e.g., magnets and rotor iron sheets) was reduced. When the temperature rise at rated operation (OP2) with the DMC524 inverter was measured until it reached steady-state, as expected, this measured steady-state temperature of the magnet at the rated load (OP2) was reduced to $\vartheta_{\mathrm{M}} = 64.5$ °C. With the steady-state average coolant temperature of $\vartheta_{\mathrm{coolant,av}} = 32.6$ °C, the temperature rise of the magnet temperature over the average coolant temperature was $\Delta\vartheta_{\mathrm{M}} = 31.9$ K. Compared to load operation with the industrial inverter ServoOne, load operation with the DMC524 inverter resulted in rotor magnets that were 34 K cooler. Due to the lower total motor losses P_{d}, the measured temperatures (and, in brackets, temperature rise over $\vartheta_{\mathrm{coolant,av}}$) of the winding overhang NDE, the winding overhang DE and the stator slot also reached lower steady-state temperatures of $\vartheta_{\mathrm{WO,NDE}} = 70.5$ °C ($\Delta\vartheta_{\mathrm{WO,NDE}} = 37.9$ K), $\vartheta_{\mathrm{WO,DE}} = 67.1$ °C ($\Delta\vartheta_{\mathrm{WO,DE}} = 34.5$ K) and $\vartheta_{\mathrm{slot}} = 59.9$ °C ($\Delta\vartheta_{\mathrm{slot}} = 27.3$ K), respectively, compared with previous measurements in Chapter 5.3.2.

The temperature increases of the prototype machine with DMC524 inverter at overload

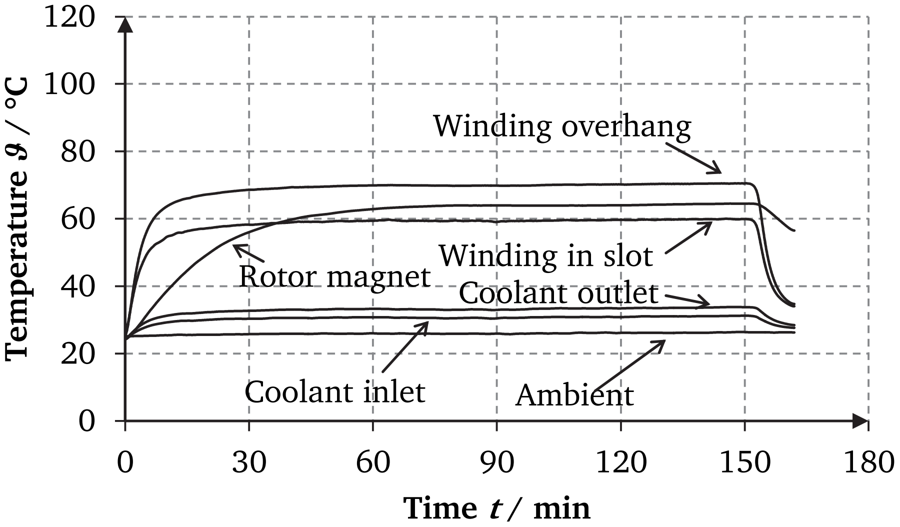

Fig. 5.16: Prototype machine: Measured temperature increases with the DMC524 inverter at rated operation (OP2: $M_{\mathrm{N}} = 55$ Nm, $n_{\mathrm{N}} = 4167$ min^{-1}) with the steady-state temperatures at $t = 150$ min: $\vartheta_{\mathrm{slot}} = 59.9$ °C, $\vartheta_{\mathrm{WO,DE}} = 67.1$ °C, $\vartheta_{\mathrm{WO,NDE}} = 70.5$ °C, $\vartheta_{\mathrm{M}} = 64.5$ °C, $\vartheta_{\mathrm{coolant,in}} = 31.3$ °C, $\vartheta_{\mathrm{coolant,out}} = 33.8$ °C, and $\vartheta_{\mathrm{amb}} = 26.4$ °C

condition (OP1) and at field weakening range (OP3) were measured with short-term duty of S2 – 30 s. Before this measurement, the prototype machine had been run at rated operation (OP2) until the steady-state temperature was reached, as discussed previously. The temperature increase of the winding parts in the stator slot and in the winding overhangs was $\Delta\vartheta_{\mathrm{slot}} = 12.1\ \mathrm{K}$, $\Delta\vartheta_{\mathrm{WO,DE}} = 7.1\ \mathrm{K}$, and $\Delta\vartheta_{\mathrm{WO,NDE}} = 12.1\ \mathrm{K}$ for overload condition (OP1) and $\Delta\vartheta_{\mathrm{slot}} = 10.4\ \mathrm{K}$, $\Delta\vartheta_{\mathrm{WO,DE}} = 6.3\ \mathrm{K}$, and $\Delta\vartheta_{\mathrm{WO,NDE}} = 6.6\ \mathrm{K}$ for field weakening operation (OP3). The temperature increase of the rotor magnets was nearly not increased due to the short measuring time of 30 s, as it was discussed with previous short duty measurements.

Given the large thermal reserve for Thermal Class H ($\vartheta_{max} = 180\ °\mathrm{C}$, IEC 60034) material used, the prototype machine could produce more power due to the high thermal reserve, so an increase of thermal utilization of the prototype machine was possible. The prototype machine was driven with a new load condition with increased rated torque ($M = 75.5\ \mathrm{Nm}$, $n_{\mathrm{N}} = 4167\ \mathrm{min}^{-1}$, $P = 33\ \mathrm{kW}$) with the DMC524 inverter until the steady-state temperature was reached (104 min). The machine was then operated with a newly defined increased overload condition ($M = 150\ \mathrm{Nm}$, $n_{\mathrm{N}} = 4167\ \mathrm{min}^{-1}$, $P = 65\ \mathrm{kW}$) for 30 s, after which operation was returned to the previous load of $M = 75.5\ \mathrm{Nm}$, $n_{\mathrm{N}} = 4167\ \mathrm{min}^{-1}$, $P = 33\ \mathrm{kW}$. Fig. 5.18 shows the measured temperature rises with the average coolant temperature of $\vartheta_{\mathrm{coolant,av}} = 35.2\ °\mathrm{C}$. The steady-state

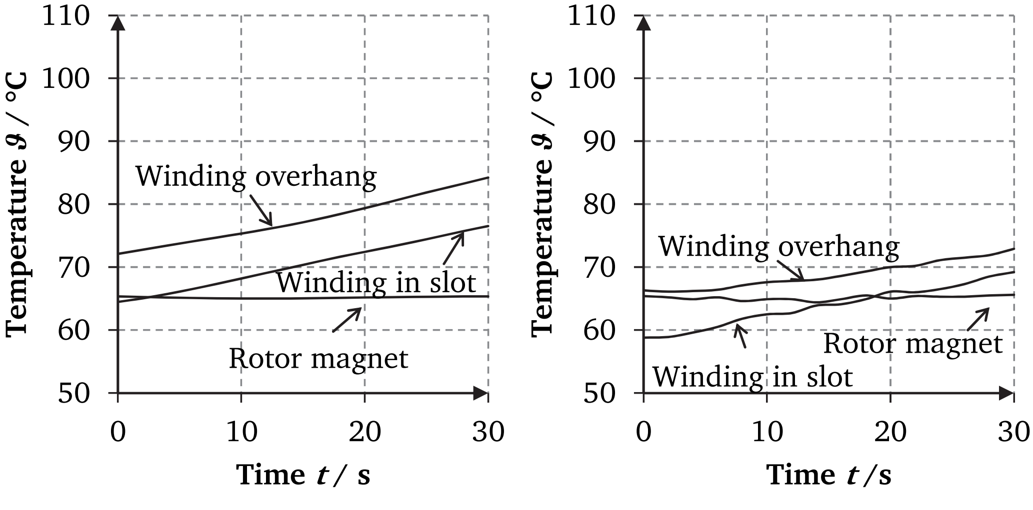

a) b)

Fig. 5.17: Prototype machine: Measured temperature with the DMC524 inverter for S2–30 s a) at overload (OP1: $M = 110\ \mathrm{Nm}, n_{\mathrm{N}} = 4167\ \mathrm{min}^{-1}$) with the temperature rise over 30 s: $\Delta\vartheta_{\mathrm{slot}} = 12.1\ \mathrm{K}$, $\Delta\vartheta_{\mathrm{WO,DE}} = 7.1\mathrm{K}$, $\Delta\vartheta_{\mathrm{WO,NDE}} = 12.1\ \mathrm{K}$, and $\Delta\vartheta_{\mathrm{M}} = 0.0\ \mathrm{K}$, b) at field weakening (OP3: $M = 45.8\ \mathrm{Nm}, n = 10000\ \mathrm{min}^{-1}$) with the temperature rise over 30 s: $\Delta\vartheta_{\mathrm{slot}} = 10.4\ \mathrm{K}$, $\Delta\vartheta_{\mathrm{WO,DE}} = 6.3\ \mathrm{K}$, $\Delta\vartheta_{\mathrm{WO,NDE}} = 6.6\ \mathrm{K}$, and $\Delta\vartheta_{\mathrm{M}} = 0.2\ \mathrm{K}$

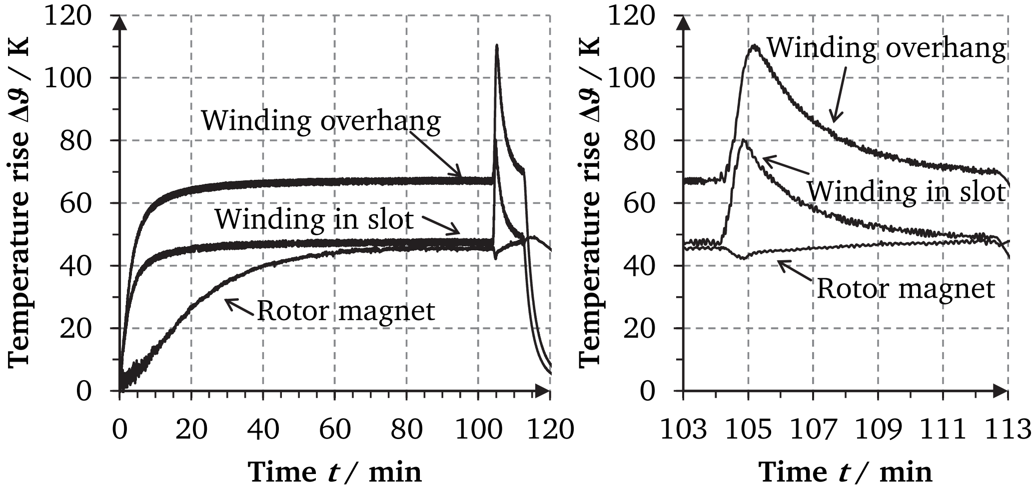

a) b)

Fig. 5.18: Prototype machine: Measured temperature rises with the DMC524 inverter at new operation point ($M = 75.5$ Nm, $n_\mathrm{N} = 4167\ \mathrm{min}^{-1}, P = 33$ kW) up to 104 min with the steady-state temperature increase at $t = 104$ min: $\Delta\vartheta_\mathrm{slot} = 46.9$ K, $\Delta\vartheta_\mathrm{WO,DE} = 61.3$ K, $\Delta\vartheta_\mathrm{WO,NDE} = 67.3$ K, and $\Delta\vartheta_\mathrm{M} = 45.0$ K with the average coolant temperature of $\vartheta_\mathrm{coolant,av} = 35.2$ °C followed by new overload condition ($M = 150$ Nm, $n_\mathrm{N} = 4167\ \mathrm{min}^{-1}$, $P = 65$ kW) for 30 s: maximum temperature of winding in slot $\Delta\vartheta_\mathrm{slot} = 80.3$ K, and winding overhang NDE side $\Delta\vartheta_\mathrm{WO,NDE} = 110.6$ K, a) whole measuring period (0 to 120 min), b) close-up period (103 to 113 min)

temperature rise of the winding parts in the stator slot, in the winding overhang NDE side, in the winding overhang DE side and the temperature rise in the rotor magnets at steady-state, e.g. $t = 104$ min, were $\Delta\vartheta_\mathrm{slot} = 46.9$ K, $\Delta\vartheta_\mathrm{WO,DE} = 61.3$ K, $\Delta\vartheta_\mathrm{WO,NDE} = 67.3$ K and $\Delta\vartheta_\mathrm{M} = 45.0$ K, respectively. After the 30 s overload condition, the temperature increased in the winding in the stator slot to $\Delta\vartheta_\mathrm{slot} = 80.3$ K and in the winding overhang on the NDE side to $\Delta\vartheta_\mathrm{WO,NDE} = 110.6$ K. Due to the short duration of the overload condition, the rotor magnet temperature remained at almost the same temperature. The hot spot of the machine was at the winding overhang on the NDE side $\vartheta_\mathrm{WO,NDE} = 175.6$ °C with an increased coolant temperature of 65 °C. It had still a slight temperature reserve of 4.4 K for Thermal Class H (IEC 60034).

5.4 Measured efficiency map of the electric machine

For the vehicle simulation model with MATLAB/Simulink, the efficiency map of the prototype machine was measured. The measurements were performed over the entire speed-torque range with 14 different speed values (1000 min^{-1} increments up to 10000

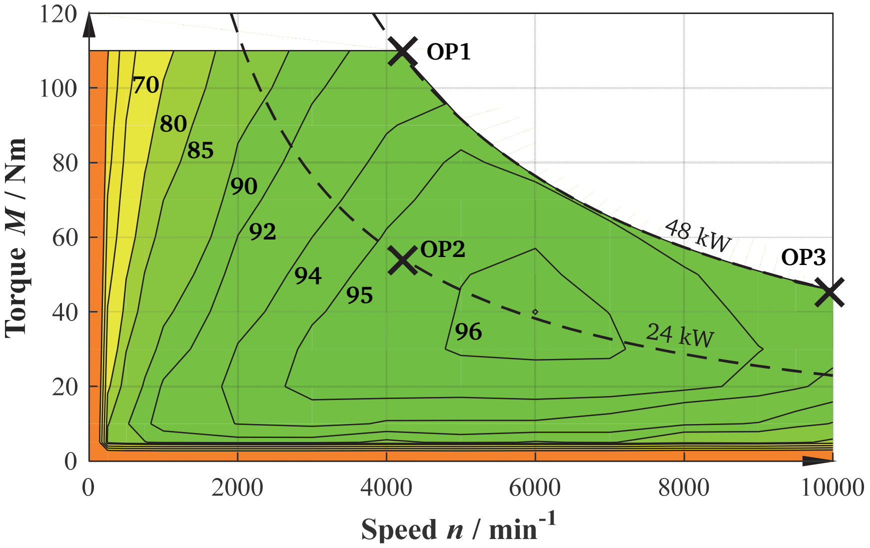

Fig. 5.19: Measured efficiency map of the prototype machine with a stator winding temperature of $\vartheta_{\mathrm{cu}} \approx 100$ °C and a rotor magnet temperature of $\vartheta_{\mathrm{M}} \approx 60$ °C

min^{-1} and additionally 250, 500, 750 and 9500 min^{-1}) and 12 different load torque values (10 Nm increments up to 110 Nm and 5Nm) to derive an accurate efficiency map. The prototype machine was first operated at rated load until the steady state of the magnet temperature of $\vartheta_{\mathrm{M}} = 60$ °C was reached. To minimize the magnet temperature fluctuation during the measurement, the measurements were taken alternately between high-load operations (with high ohmic losses) and low-load operations (with low ohmic losses). The electrical power P_{el} and mechanical power P_{m} were measured with the power analyser and torque transducer, respectively. With these measured values, the efficiency was determined with (5.6). Fig. 5.19 shows the measured efficiency map of the prototype machine at a winding temperature of $\vartheta_{\mathrm{cu}} \approx 100$ °C and at a rotor magnet temperature of $\vartheta_{\mathrm{M}} \approx 60$ °C. As expected, the region at low rotation speed with high-load torque shows low efficiency due to high ohmic losses. With constant load torque, the measured efficiency increased with increasing rotation speed. After it reached a maximum efficiency value, it decreased again due to the high ohmic losses at high speed, caused by the additional negative d-current component for field weakening operation, and due to the high iron losses at high rotation speed. The maximum measured efficiency was 96.3 % at $M = 40$ Nm and $n = 6000\ \mathrm{min}^{-1}$.

$$\eta_{\mathrm{mot}} = \frac{P_{\mathrm{m}}}{P_{\mathrm{el}}} = \frac{P_{\mathrm{m}}}{P_{\mathrm{m}} + P_{\mathrm{d}}} \tag{5.6}$$

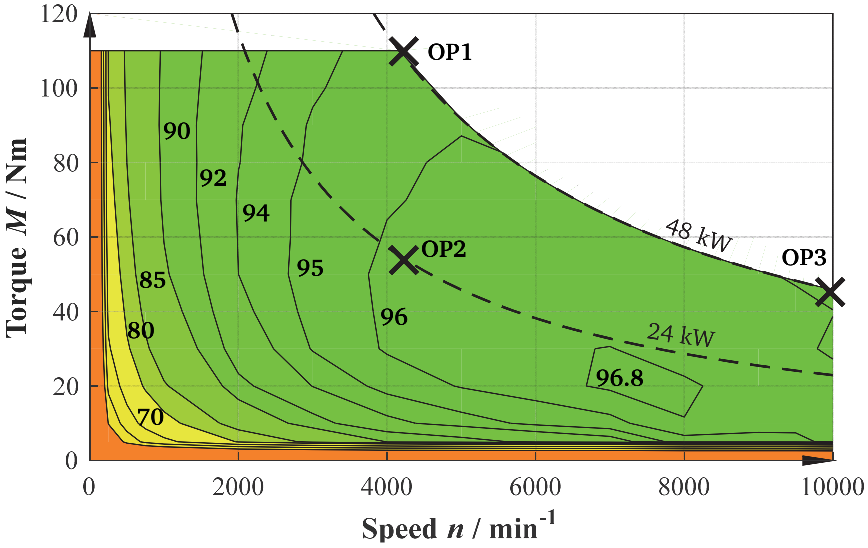

Fig. 5.20: Measured efficiency map of the DMC524 inverter with a rotor magnet temperature of $\vartheta_\mathrm{M} \approx 60$ °C and DC link voltage of $U_\mathrm{DC} \approx 325$ V

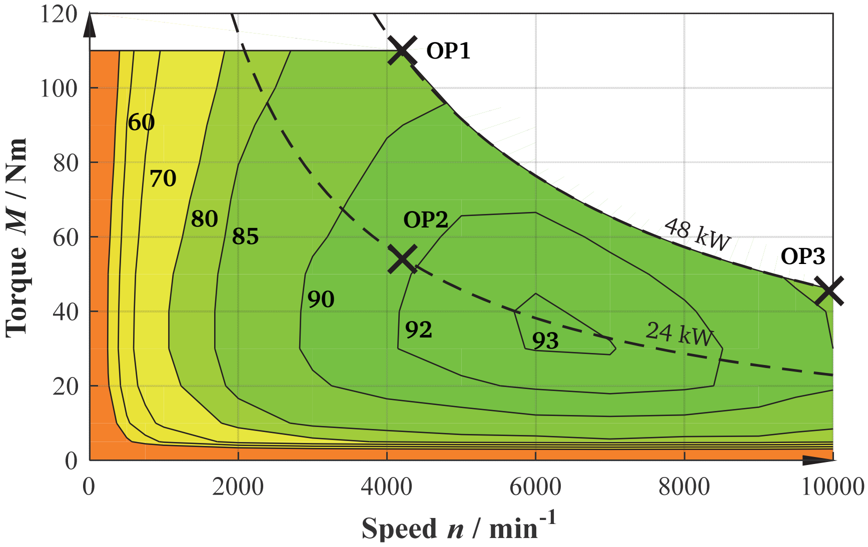

Fig. 5.21: Measured efficiency map of the electric propulsion system, constituted by the prototype machine and the DMC524 inverter, with an average winding temperature of $\vartheta_\mathrm{cu} \approx 100$ °C and a rotor magnet temperature of $\vartheta_\mathrm{M} \approx 60$ °C

The efficiency of the DMC524 inverter was measured with the DC input current I_DC and DC link voltage U_DC of the inverter and the input electrical power of the prototype machine P_el (5.7). As shown in Fig. 5.20, the inverter had lower efficiency at low speed and low load torque regions due to the high input DC link voltage. In addition, at low speed and high-load torque regions, the inverter efficiency showed lower values because of the high current, which incurs high conducting losses in the IGBTs and diodes. The maximum measured efficiency of the inverter was about 97 % at $M = 30$ Nm and $n =$

$7000\ \mathrm{min}^{-1}$. This value shows good agreement with the given efficiency data from company *BRUSA* [44].

$$\eta_{\mathrm{inv}} = \frac{P_{\mathrm{el}}}{P_{\mathrm{DC}}} = \frac{P_{\mathrm{el}}}{U_{\mathrm{DC}} \cdot I_{\mathrm{DC}}} \tag{5.7}$$

Fig. 5.21 presents the efficiency map of the resulting electric propulsion system, constituted by the prototype machine and the DMC524 inverter. The efficiency of the electric propulsion system was determined with the electrical input power of the inverter P_{DC} and the mechanical output power of the prototype machine P_{m} in motor operation. The maximum measured efficiency of the electric propulsion system was about 93.1 % at $M = 40$ Nm and $n = 6000\ \mathrm{min}^{-1}$. This efficiency map is later used for the driving simulation model.

$$\eta_{\mathrm{tot}} = \frac{P_{\mathrm{m}}}{P_{\mathrm{DC}}} = \frac{P_{\mathrm{m}}}{U_{\mathrm{DC}} \cdot I_{\mathrm{DC}}} \tag{5.8}$$

5.5 Demagnetization test at sudden short circuit after generator no-load

The prototype machine was designed to be safe from the risk of irreversible demagnetization at a high magnet operating temperature of $\vartheta_{\mathrm{M}} = 150$ °C and at a high stator current loading, even during a sudden short circuit. In order to verify that, a sudden short circuit test at no-load generator condition was conducted. The inverter for the prototype machine, however, was not designed to withstand a sudden short-circuit condition during load operation. Hence, the sudden short-circuit test at load condition could not be performed.

For the no-load test, the rotor magnets first had to be heated up to 150 °C. For that, similar as with the generator short circuit test in Chapter 5.2, the terminals of all three-phase windings of the prototype machine were short circuited, and the machine was driven by the load machine. In the meantime, the cooling system of the prototype machine was shut down. Thus, the heat produced in the stator winding by the high short-circuit current I_{sc} transferred not only to the cooling channel but also to the rotor. When the magnet temperature reached the desired level of 150 °C, the machine was stopped, and the three phase terminals were opened. To keep the rotor magnet temperature high, this process was done fast. The prototype machine was then driven at rated speed of $4167\,\mathrm{min}^{-1}$, and the three-phase winding was now suddenly short circuited with a switch. During this test, the phase currents and the torque variation over time were measured. The sudden short-circuit test was repeated several times to make any potential rotor magnet demagnetization more noticeable. The measured sudden short-circuit current and torque variation on the shaft are shown in Fig. 5.22 a) and b). They show good agreement with the analytical calculation results for a magnet temperature of

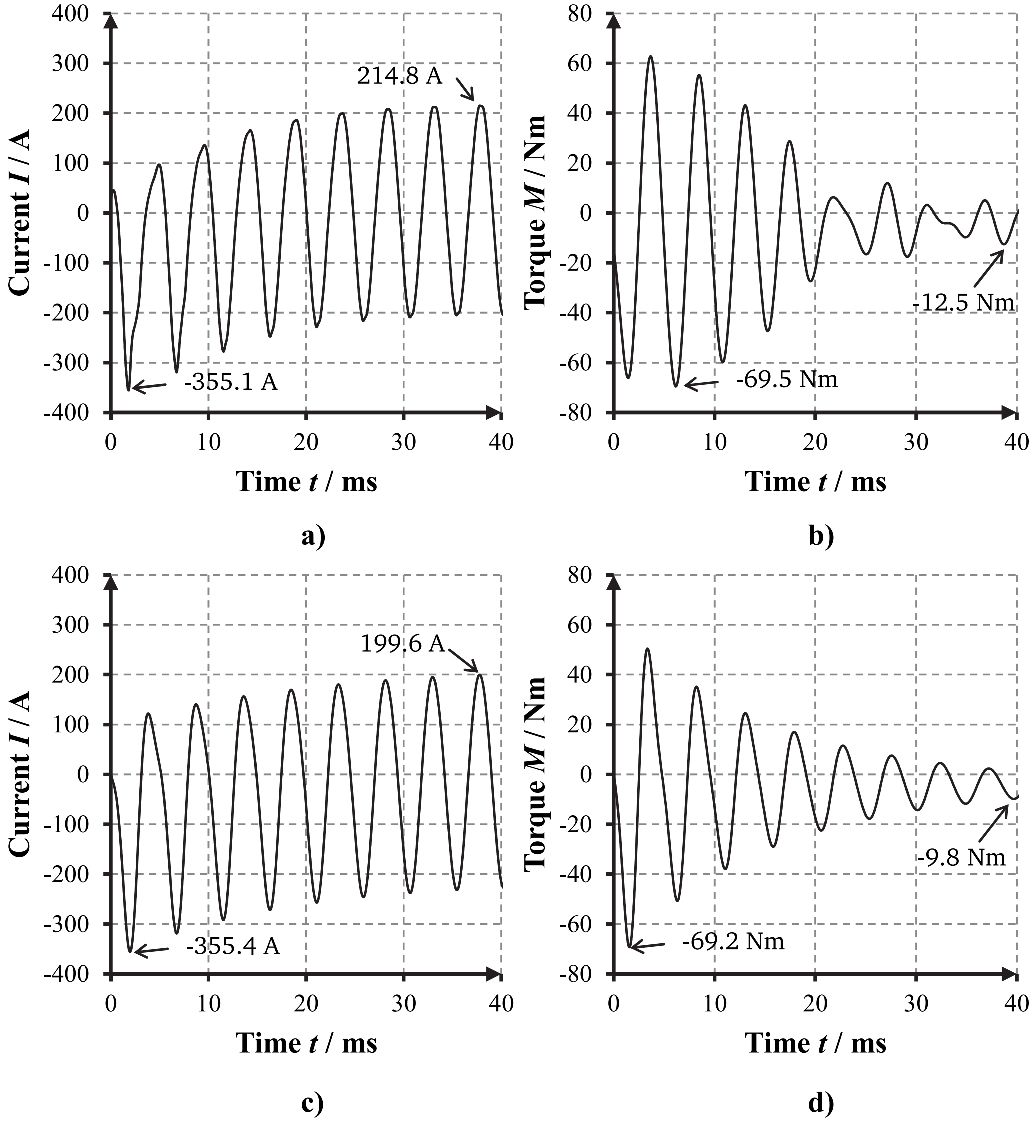

Fig. 5.22: Prototype machine: a) measured sudden short-circuit current, b) measured sudden short-circuit torque, c) analytically calculated sudden short-circuit current and d) analytically calculated sudden short-circuit torque at generator no-load condition with the speed of $n_{\mathrm{N}} = 4167\ \mathrm{min}^{-1}$ and rotor magnet temperature of $\vartheta_{\mathrm{M}} = 150\ ^{\circ}\mathrm{C}$

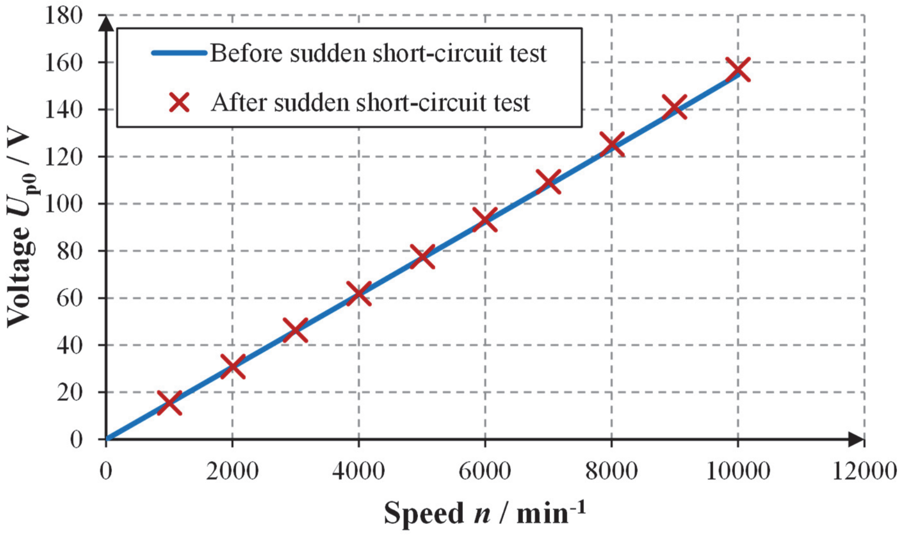

Fig. 5.23: Prototype machine: Measured induced no-load voltage (at $\vartheta_M = 100$ °C) before sudden short-circuit test (blue line) and after the test (red cross)

$\vartheta_M = 150$ °C in Fig. 5.22 c) and d). The peak of the short-circuit torque at $\vartheta_M = 150$ °C magnet temperature (Fig. 5.22) is 15.9 % lower than at $\vartheta_M = 100$ °C (Fig. 2.19) due to the by 8.3 % lower PM flux linkage Ψ_M.

To check whether the rotor magnets were demagnetized, the induced voltage was measured again at different speed up to 10000 min^{-1}. As shown in Fig. 5.23, no difference between the measured induced voltages U_{p0} before and after the sudden short-circuit and overload tests can be seen. Hence the magnets were not demagnetized during the sudden short-circuit test even with a high magnet temperature $\vartheta_M = 150$ °C.

5.6 Measurement of DE-REX powertrain with driving cycles at test bench for individual measurement of electric machines

The functionality of the DE-REX powertrain was tested at the test bench for the individual measurement of the electric machine (Fig. 4.10). On the test bench, one electric machine can be controlled and measured. For that the required torque and speed were calculated in advance with the driving simulation model from Chapter 6.1. For determining the DE-REX powertrain operation modes, the thermal conditions of the two electric machines were not considered. For measurement of the DE-REX powertrain at the test bench for the single-machine measurements, driving simulations with MATLAB Simulink were carried out with two driving cycles: the NEDC and the worldwide harmonized light vehicles test cycle (WLTC).

5.6.1 Test results with the NEDC

Fig. 5.24 shows the measurement results of the DE-REX powertrain at the test bench for the individual measurement of the electric machines EM1 and EM2 during the NEDC. The NEDC needs low driving power during the entire cycle. Thus, the first electric machine (EM1) was operated alone. The maximum temperature rise at the stator winding in the stator slot and at the winding overhang on the NDE side were 16.7 K and 19.5 K, respectively, while the second electric machine remained nearly at ambient temperature. By selecting this second electric machine (EM2) for driving the vehicle, the two electric machines can be evenly utilized and unwanted early derating of both electric machines can be avoided. This is discussed in Chapter 6.6. The estimated energy consumption for the NEDC is listed in Table 5.3. On the test bench, no battery was used. Thus, a constant internal resistance of the battery of 0.14 Ω was chosen to estimate the battery losses.

Table 5.3 Measured results of the DE-REX powertrain at the test bench for the individual measurement of the electric machine with the NEDC: EMs = both electric machines (EM1+EM2), Inv = inverter losses, Bat = battery losses with an assumed constant internal resistance 0.14 Ω, Add200 = 200 W auxiliary losses, Add500 = 500 W auxiliary losses

Electric machine		Unit	EM1	EM2
$\vartheta_{\text{coolant,end,av}}$		°C	32.7	-
$\Delta\vartheta_{\text{slot,max}}$		K	16.7	0
$\Delta\vartheta_{\text{slot,end}}$		K	14.9	0
$\Delta\vartheta_{\text{WO,NDE,max}}$		K	19.5	0
$\Delta\vartheta_{\text{WO,NDE,end}}$		K	19.5	0
Energy consumption	EMs+Inv	kWh/100km	12.85	
	EMs+Inv+Bat		13.30	
	EMs+Inv+Bat+Add200		14.05	
	EMs+Inv+Bat+Add500		14.79	

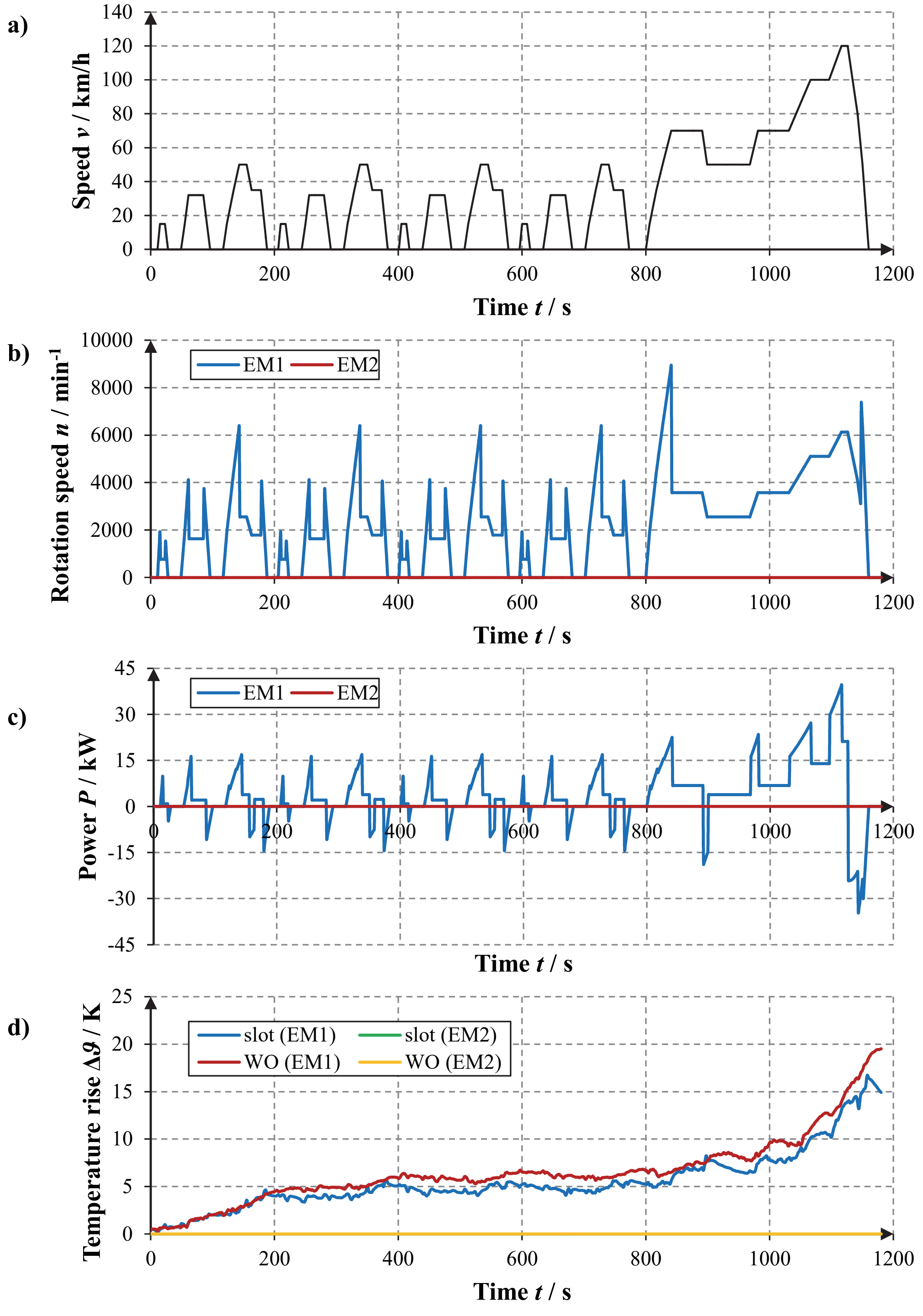

Fig. 5.24: a) Driving profile of the NEDC, b) required rotation speeds for both electric machines (EM1, EM2), c) required mechanical power for both electric machines (EM1, EM2), d) measured temperature rise in stator winding parts in the stator slot $\Delta\vartheta_{\mathrm{slot}}(t)$ and in the winding overhang NDE side $\Delta\vartheta_{\mathrm{WO,NDE}}(t)$ of both electric machines (EM1, EM2)

5.6.2 Test results with the WLTC

The measured results of the DE-REX powertrain during the WLTC are shown in Fig. 5.25. Due to the empirical driving data, which define the WLTC, the propulsion system needs much more dynamic driving performance than during the NEDC. Thus, the powertrain required also the second electric machine (EM2) to recover electricity at t = 576 s and to propel the vehicle at t = 1185 s and 1550 s. The maximum temperature increase at the winding overhang on the NDE side was 21.9 K for EM1 and 4.1 K for EM2. Table 5.4 shows the calculated energy consumptions during the WLTC. In comparison with the measured results from the NEDC, the vehicle needs roughly 20 % more electric energy to complete the WLTC.

Table 5.4 Measured results of the DE-REX powertrain at the test bench for the individual measurement of the electric machines with the WLTC: EMs = both electric machines (EM1+EM2), Inv = inverter losses, Bat = battery losses with an assumed constant internal resistance 0.14 Ω, Add200 = 200 W auxiliary losses, Add500 = 500 W auxiliary losses

Electric machine		**Unit**	**EM1**	**EM2**
$\vartheta_{\mathrm{coolant,end,av}}$		°C	34.4	31.2
$\Delta\vartheta_{\mathrm{slot,max}}$		K	18.5	4.5
$\Delta\vartheta_{\mathrm{slot,end}}$		K	16.1	2.7
$\Delta\vartheta_{\mathrm{WO,NDE,max}}$		K	21.9	4.1
$\Delta\vartheta_{\mathrm{WO,NDE,end}}$		K	20.5	2.6
Energy consumption	EMs+Inv	kWh/100km	15.52	
	EMs+Inv+Bat		16.23	
	EMs+Inv+Bat+Add200		16.77	
	EMs+Inv+Bat+Add500		17.31	

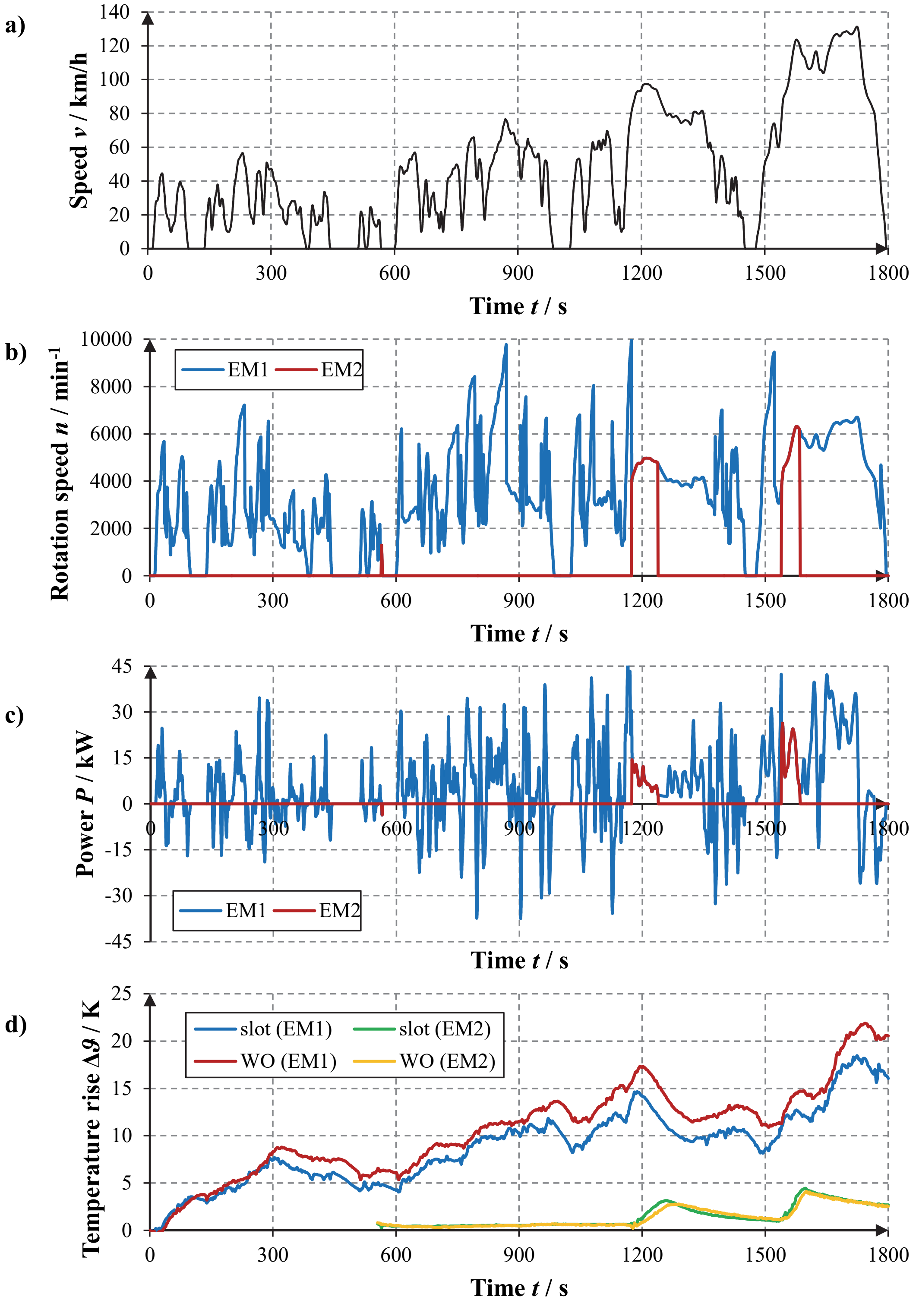

Fig. 5.25: a) Driving profile of the WLTC, b) required rotation speed profile for both electric machines (EM1, EM2), c) required torque profile for both electric machines (EM1, EM2), d) measured temperature increase in the stator winding parts in the stator slot $\Delta\vartheta_{\mathrm{slot}}(t)$ and in the winding overhang NDE side $\Delta\vartheta_{\mathrm{WO,NDE}}(t)$ of both electric machines (EM1, EM2)

6. Vehicle simulation model

The aim of a vehicle driving simulation is to investigate a) the functionality of the proposed powertrain concept and b) the energy flow in the powertrain, including the losses in each component. By comparing simulation results with various powertrain concepts, an optimised powertrain concept for given demands can be selected. The results of the simulation are a prediction of driving performance and driving range for given battery capacity as well as the energy consumption by the propulsion system. Additionally, possible flaws in the powertrain can be detected with the simulation model. Thus, the powertrain can be modified before its prototype production. Consequently, the simulation helps to reduce development time and cost.

There are two main modelling methods which are used to simulate the specific vehicles: a forward method and a backward method.

In a forward method, also called cause–effect method, a driver model controls the demanded torque (cause) of the ICE or of the electrical motors by changing the angle of the acceleration pedal or of the brake pedal to chase the velocity profile (effect) of the driving cycle. In this case, the direction of calculation is identical to the direction of the power flow from energy stores, such as a fuel tank or a battery, to the drive axles, as in real life. As a drawback of this method, the driver model needs a fine-tuned controller (e.g. a PID speed controller) to meet the desired velocity profile, or else it will bring a speed difference and exert an adverse influence on driving performance. Due to the complex control loops and control algorithms, forward driving simulations need rather small time steps, which result as long simulation times. Therefore, forward simulation methods are more suitable for evaluating the vehicle dynamic performance or for developing control strategies.

In a backward method, also called effect–cause method, unlike as a forward method, a demanded velocity profile of a driving cycle is imposed onto a vehicle simulation model to calculate forces acting on vehicle tyres. Required power and losses of each component are computed in backward fashion up to an energy storage system (e.g. battery or fuel tank). In this way, the necessary energy for the vehicle for moving along the given driving cycle can be estimated. In general, the backward simulation model uses efficiency maps of electric machines to predict the energy consumption. These efficiency maps are analytically calculated or measured in thermal steady-state conditions. Therefore, the backward simulation model is also called 'quasi-static' model. Because of such features, this method does not fit for estimating the dynamic performance of the DE-REX powertrain. On the other hand, there is no drive controller needed in this simulation model. So, the calculation time for this simulation model is shorter than for the forward method due to the relatively larger time steps. Therefore, a backward simulation model is suitable to predict the energy consumption of the proposed powertrain.

For this reason, simple backward vehicle simulation models for pure electric driving are constructed to calculate the energy consumption of the powertrain hereafter.

6.1 Structure of vehicle simulation model

Fig. 6.1 shows a diagram of the backward driving simulation model for pure electric driving mode. In the driving cycle module, the demanded velocity profile $v_{\mathrm{veh}}(t)$ and road incline $\alpha_{\mathrm{slope}}(t)$ as functions of time for the simulation are imposed onto the driving simulation model. The next step is calculating the demanded driving force to match against the driving resistances, which consist of aerodynamic, rolling, acceleration and grade resistances in the driving resistance module [45]. With the calculated driving force and speed, which correspond to the angular velocity n_{wheel} and torque M_{wheel} at the wheels, the proper driving mode with optimum energy consumption is selected in the module 'determine driving mode'. Typically, the pre-calculated efficiency maps of the electric machine and the transmission are used to select the energy-optimal driving mode. Finally, the total required power of the powertrain is estimated with the calculated required power of the two electric machines, the additionally demanded power from auxiliary equipment and the losses in the battery unit.

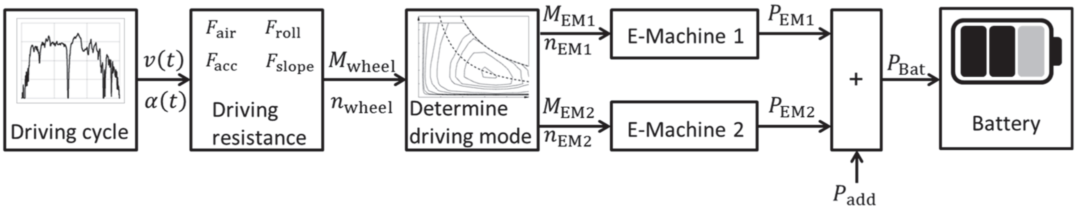

Fig. 6.1: Structure of a backward driving simulation model
for pure electric driving mode

6.2 Transmission for the DE-REX powertrain

A transmission in a vehicle adjusts the rotational speed and torque of electric machines to the lower speed and higher torque of tyres of the vehicle. In general, electric machines for automobiles are operated with a high rotation speed to reduce the volume of the electric machines. The transmission reduces the high rotation speed of the electric machine n_{EM} to the low wheel speed n_{wheel} and increases the wheel torque M_{wheel} at the same time. Most commercial electric vehicles have a single fixed gear ratio. However, for the DE-REX powertrain, two parallel sub-transmissions with two fixed gear ratios were designed by the *Institute for Mechatronic Systems in Mechanical Engineering* (IMS) at *TU Darmstadt* to increase the propulsive efficiency of the vehicle by shifting operating points. For reasons of efficiency and simplicity, an automated manual transmission (AMT) technology was used for the sub-transmissions with a BLDC motor for executing gear shifts [75]. The sub-transmissions use dog clutches instead of frictional clutches to couple the gears to the rotating shafts. In addition, an integrated parking lock function is possible with the coaxial layout of the powertrain [75]. The gear ratios of the sub-transmission have been determined by a multi-objective optimization with the maximum power of the traction machines [46]. As a result, two gear ratios were selected $i_1 = 14.8$ and $i_2 = 5.9$ to satisfy the required starting torque and the maximum speed of the vehicle, as listed in Table 1.3.

For calculating the transmission losses in the driving simulation model, efficiency maps of the sub-transmissions were generated with the transmission design software ROMAX Designer [75]. The calculated efficiency maps for both gear ratios are shown in Fig. 6.2. The efficiency calculation results show that the efficiency of both gear ratios is between 95 % and 97 % in a wide range of operating region. The transmission with the first gear ratio i_1 has a higher efficiency than with the second gear ratio i_2. Only at high rotation speeds and low loads, the efficiency drops significantly below 90 %, due to the high rotation speed dependent splash losses from the transmission oil.

The transmission losses increase the required power of the propulsion system to overcome driving resistances. On the other hand, the losses reduce the regenerated power, which is recovered by the vehicle. Power required for the electrical motors and input power from an electrical generator from recuperation $P_{\mathrm{m,EM}}$ with consideration of the transmission efficiency η_{tr} are shown in (6.1) with the required power or the recovered power of the vehicle P_{veh}.

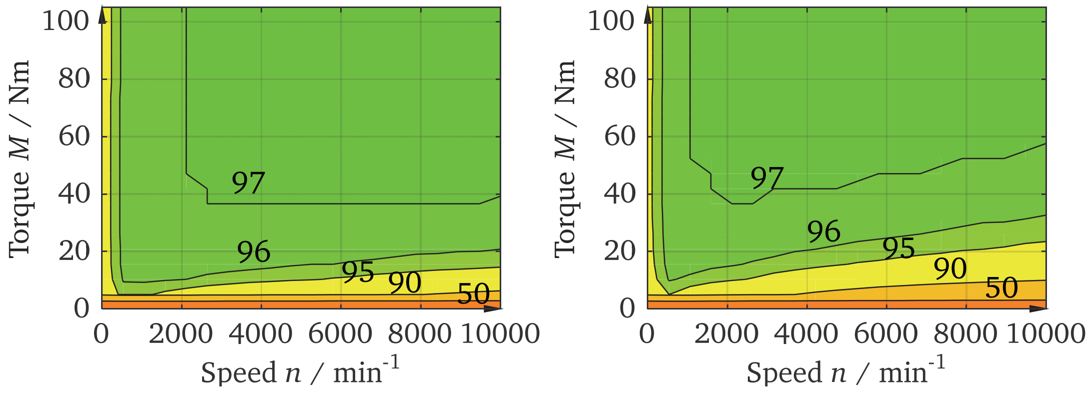

a) b)

Fig. 6.2: Calculated efficiency map of the transmission with transmission oil temperature of 70 °C (SAE75w) [75]. a) Efficiency map of the transmission with the first gear ratio i_1=14.8, b) Efficiency map of the transmission with the second gear ratio i_1=5.9 (x-axis: rotational speed of electric machine, y-axis: mechanical torque of electric machine, values: efficiency in percentage)

$$\begin{aligned} P_{\mathrm{m,EM}} &= \frac{P_{\mathrm{veh}}}{\eta_{\mathrm{tr}}} && \text{(Driving)} \\ &= P_{\mathrm{veh}} \cdot \eta_{\mathrm{tr}} && \text{(Recuperation)} \end{aligned} \tag{6.1}$$

6.3 Driving cycles module

A driving cycle is a standardized vehicle driving pattern for estimating emissions of air pollutants, measuring energy consumption or verifying driving performances of the vehicle. With a standardized driving cycle, different vehicles can be compared to each other. Typically, driving cycles are represented in terms of vehicle speed v in km/h as a function of time t in s. Driving cycles can be roughly divided into ‘steady-state’ driving cycles and ‘transient’ driving cycles. Steady-state driving cycles have a fixed operating condition with a constant rotation speed and a constant load on a powertrain. Thus, they are usually used for measurement of heavy-duty diesel engines. On the other hand, with transient driving cycles, operating points of a powertrain change continuously over time [47]. Thus, transient driving cycles are suitable for the driving simulation model for the DE-REX powertrain. Three transient driving cycles were used for the driving simulation model for the DE-REX in the driving cycle module.

6.3.1 New European Driving Cycle (NEDC)

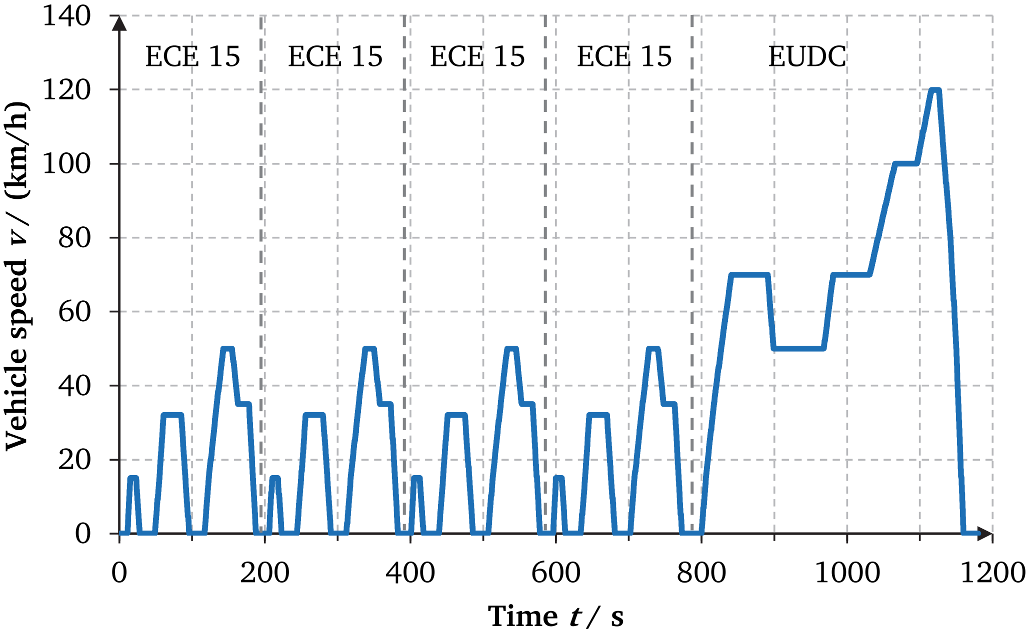

Fig. 6.3: Velocity profile of the New European Driving Cycle (NEDC) [47]

The New European Driving Cycle (NEDC) is a standard test procedure in the European Union (EU) to assess the emissions level and energy consumption of a light-duty vehicle. As shown in Fig. 6.3, the NEDC is a stylized driving cycle, which means that it consists of periods of constant acceleration, constant speed, and constant deceleration. Thus, it does not represent a real driving pattern [47]. In the NEDC, an urban driving cycle (ECE 15) is repeated four times without interruption. Afterwards one Extra-Urban Driving Cycle (EUDC) follows. The NEDC covers a total distance of 11.02 km within a total test time of 1180 s. The maximum vehicle speed of the NEDC is 120.1 km/h at the end of the EUDC. During this NEDC procedure, the vehicle stops 14 times, and the total standing time is 241 s, which is 20.4 % of the total time. Due to many standing events, long constant speed periods and low acceleration and deceleration values, some experts determined that the standard test procedure with the NEDC shows large differences from real driving conditions, which means that the NEDC does not adequately represent real-life driving patterns [48]. For these reasons, other transient driving cycles with more frequent acceleration and deceleration and less vehicle idle time are required.

6.3.2 HYbrid technology approaching efficient Zero Emission Mobility (HYZEM) highway cycle

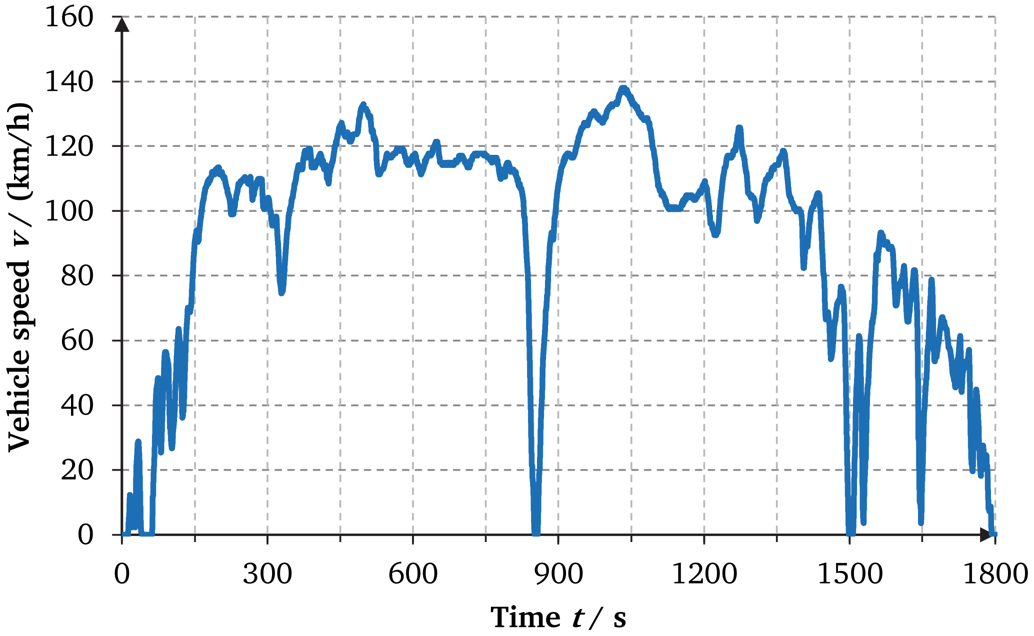

Fig. 6.4: Velocity profile of the HYbrid technology approaching efficient Zero Emission Mobility (HYZEM) highway driving cycle [49]

The 'hybrid technology approaching efficient zero emission mobility' (HYZEM) driving cycle was developed for evaluating hybrid vehicles. It was derived from the research projects Drive-Modem and BRITE/EURAM-HYZEM [49]. In contrast to the NEDC, the HYZEM driving cycles show dramatic changes of the vehicle speed over time. The HZYEM represents better real-life driving patterns than the NEDC. There are three types of cycles in the HYZEM driving cycles: an urban driving cycle, an extra-urban driving cycle and a highway driving cycle. Fig. 6.4 shows the velocity profile of the HYZEM highway driving cycle. It covers a 46.2 km driving distance with a total test time of 1804 s. It has a relatively long driving time of 1760 s, corresponding to 97.6 % of the total time. The HYZEM highway driving cycle has, as the name indicates, a high average driving speed of 94.5 km/h and a maximum speed of 137.7 km/h.

6.3.3 Worldwide harmonized Light vehicles Test Cycle (WLTC) for a class 3 vehicle

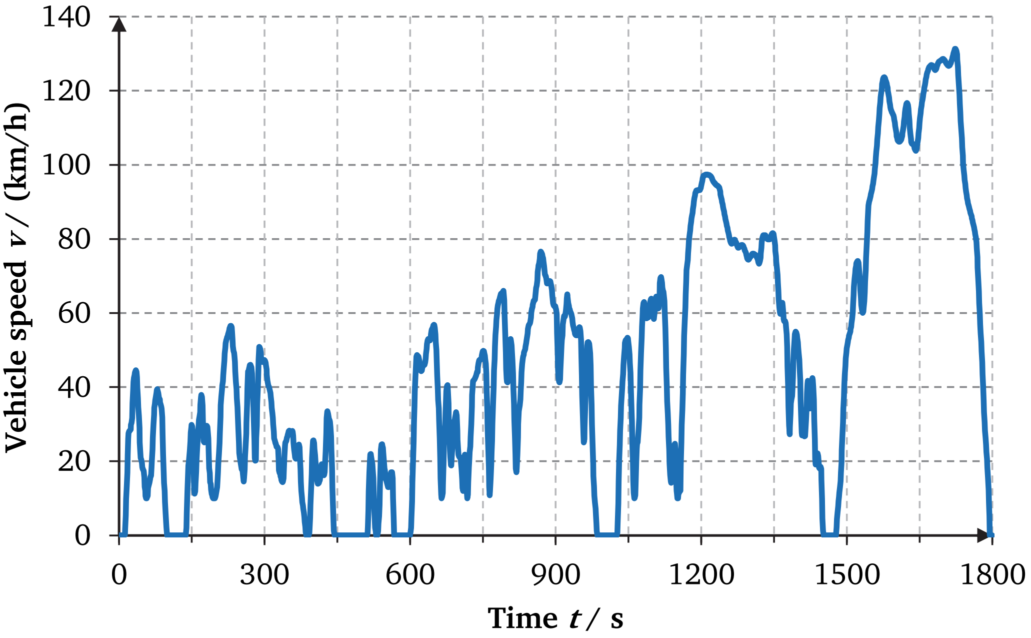

Fig. 6.5: Velocity profile of the 'Worldwide harmonized Light vehicles Test Cycle' (WLTC) for a class 3 vehicle [50]

Based on real driving patterns from 12 countries on three different continents (Asia, Europe and USA), a new test procedure, the Worldwide harmonized Light vehicle Test Protocol (WLTP) was developed on behalf of the United Nations [50]. This protocol includes the new driving cycle, Worldwide harmonized Light vehicle Test cycle (WLTC). Because of the empirical driving data behind it, the WLTC represents better real driving conditions than the NEDC.

Depending on the power and curb weight ratio, there are three different test cycles in the WLTP based on vehicle class. The prototype vehicle for the DE-REX powertrain has a high power to weight ratio of 45 kW/t with a total rated power of 81 kW. Thus, the prototype vehicle belongs to class 3 [50]. Fig. 6.5 shows the WLTC for a class 3 vehicle. The WLTC for a class 3 vehicle divided into four sections: urban driving, suburban driving, extra-urban driving, and highway driving. The WLTC for a class 3 vehicle has a test duration 1800 s and a total driving range of 23.3 km. And the amount of vehicle idle time has been reduced to 235 s, corresponding to 13.4 % of the total test time, which means that the WLTC shows much more dynamic driving performance than the NEDC.

Also, the WLTC has a higher average velocity of 46.5 km/h and a higher maximum speed of 131.3 km/h compared to the average velocity of the NEDC of 33.6 km/h and the maximum speed of 120.1 km/h. Therefore, higher energy consumption will be expected with the WLTC.

6.4 Driving resistances module

In general, the braking force from aerodynamic drag F_{air}, the braking force from rolling resistance between the tyres and the road F_{roll}, the braking or accelerating force due to the slope of the road F_{slope} and the accelerating or decelerating force F_{acc} of the propulsion system should be considered in the driving resistance module to calculate the movement of the vehicle. The resulting driving or braking force F_{res}, corresponding to the sum of the driving resistances and F_{acc}, is transferred to the next module for determining a driving mode.

$$F_{\mathrm{res}} = F_{\mathrm{air}} + F_{\mathrm{roll}} + F_{\mathrm{slope}} + F_{\mathrm{acc}} \tag{6.2}$$

The aerodynamic drag of the vehicle F_{air} depends proportionally on the air mass density ρ_{air}, the drag coefficient c_{w}, and the facing surface of the vehicle A_{f} and to the square of the vehicle speed v_{veh}. Due to the variation of the air mass density in temperature and humidity, an average constant air density value of 1.204 kg/m^3 (20 °C, the standard atmosphere and dry air) was used.

$$F_{\mathrm{air}}(v_{\mathrm{veh}}) = \frac{1}{2} \cdot \rho_{\mathrm{air}} \cdot c_{\mathrm{w}} A_{\mathrm{f}} \cdot v_{\mathrm{veh}}^2 \tag{6.3}$$

There is an almost linear relation between the tangential rolling resistance force F_{roll} and the vertical force F_{N} on the tyres, which is expressed by the rolling resistance coefficient f_{roll}. Due to the deformation of the tyre, the rolling resistance coefficient varies with the vehicle speed. Its dependence on the speed can be approximated by (6.5). For a typical SR-tyre with rated air pressure, the coefficients $f_{\mathrm{roll,0}} = 0.009$, $f_{\mathrm{roll,1}} = 0.0015$, and $f_{\mathrm{roll,4}} = 0.0012$ were used from [51].

$$F_{\mathrm{roll}}(v_{\mathrm{veh}}, \alpha_{\mathrm{slope}}) = f_{\mathrm{roll}}(v_{\mathrm{veh}}) \cdot F_{\mathrm{N}} = f_{\mathrm{roll}}(v_{\mathrm{veh}}) \cdot m_{\mathrm{veh}} \cdot g \cdot \cos(\alpha_{\mathrm{slope}}) \tag{6.4}$$

$$f_{\mathrm{roll}}(v_{\mathrm{veh}}) = f_{\mathrm{roll,0}} + f_{\mathrm{roll,1}} \cdot \left(\frac{v_{\mathrm{veh}}(\text{in km/h})}{100\ \text{km/h}}\right) + f_{\mathrm{roll,4}} \cdot \left(\frac{v_{\mathrm{veh}}(\text{in km/h})}{100\ \text{km/h}}\right)^4 \tag{6.5}$$

When the vehicle is driven on a road with a slope α_{slope}, gravity pulls the vehicle. It can be opposed to the driving force (positive slope) or it can help to recover electric energy (negative slope). The slope resistance force F_{slope} is calculated with (6.6).

$$F_{\mathrm{slope}} = m_{\mathrm{veh}} \cdot g \cdot \sin(\alpha_{\mathrm{slope}}) \tag{6.6}$$

The acceleration resistance F_{acc} is calculated as the product of the acceleration of the vehicle a_{veh} and the sum of the translational acceleration of the vehicle mass m_{veh} and the rotational acceleration of the equivalent rotating mass m_{rot}. All rotating parts, depending on vehicle speed, are included in the equivalent rotating mass. The rotational inertia constant λ expresses the ratio of the equivalent rotating mass to the vehicle mass. The rotational inertia constants for the powertrain for DE-REX vary between $\lambda = 1.06$ and $\lambda = 1.14$, depending on the driving mode with a selected gear ratio. For calculation convenience, a constant average value of $\lambda = 1.1$ was used.

$$F_{\mathrm{acc}} = (m_{\mathrm{veh}} + m_{\mathrm{rot}}) \cdot a_{\mathrm{veh}} = \lambda \cdot m_{\mathrm{veh}} \cdot a_{\mathrm{veh}} \tag{6.7}$$

$$m_{\mathrm{rot}} = \sum \frac{J_{\mathrm{k}} \cdot i_{\mathrm{k}}^2}{r_{\mathrm{dyn}}^2} \tag{6.8}$$

J_{k} and i_{k} are moments of inertia and gear ratios of rotating parts.

6.5 Determine driving mode module

In pure electric driving mode, the ‘Determine driving mode’ module decides the combination of the two electric machines (EM1, EM2) and the corresponding gear ratios i_1 and i_2. The possible states of the driving modes are listed in Table 6.1. At partial load, only one electric machine (EM1) is operated to propel the vehicle at low speed with the first gear ratio $i_1 = 14.8$ (driving mode #1) and at high speed with the second gear ratio $i_2 = 5.9$ (driving mode #2). At full load, especially at starting or going uphill, both electric machines are needed to produce thrust to accelerate the vehicle with the first gear ratio (driving mode #3). When the driver wants to overtake a vehicle at high speed,

Table 6.1 Possible driving modes for DE-REX powertrain with a driving strategy without considering the thermal condition of both electric machines

Driving modes			EM1		EM2	
#	Electric motor	Gear ratio	$M_{\mathrm{EM1}}/\mathrm{Nm}$	$n_{\mathrm{EM1}}/\mathrm{min}^{-1}$	$M_{\mathrm{EM2}}/\mathrm{Nm}$	$n_{\mathrm{EM2}}/\mathrm{min}^{-1}$
1	EM1	i_1	$\frac{M_{\mathrm{Wheel}}}{(i_1 \cdot \eta_{\mathrm{G1}})}$	$n_{\mathrm{Wheel}} \cdot i_1$	0	0
2	EM1	i_2	$\frac{M_{\mathrm{Wheel}}}{(i_2 \cdot \eta_{\mathrm{G2}})}$	$n_{\mathrm{Wheel}} \cdot i_2$	0	0
3	EM1+2	i_1	$\frac{1}{2} \cdot \frac{M_{\mathrm{Wheel}}}{(i_1 \cdot \eta_{\mathrm{G1}})}$	$n_{\mathrm{Wheel}} \cdot i_1$	$\frac{1}{2} \cdot \frac{M_{\mathrm{Wheel}}}{(i_1 \cdot \eta_{\mathrm{G1}})}$	$n_{\mathrm{Wheel}} \cdot i_1$
4	EM1+2	i_2	$\frac{1}{2} \cdot \frac{M_{\mathrm{Wheel}}}{(i_2 \cdot \eta_{\mathrm{G2}})}$	$n_{\mathrm{Wheel}} \cdot i_2$	$\frac{1}{2} \cdot \frac{M_{\mathrm{Wheel}}}{(i_2 \cdot \eta_{\mathrm{G2}})}$	$n_{\mathrm{Wheel}} \cdot i_2$

the driving mode #4 can be chosen, which uses both electric machines with the second gear ratio. The controller can decide to change the driving mode at each load condition. In order to select the energy-optimal driving mode depending on the load condition, the controller compares the total losses in the powertrain for each driving mode and determines the driving mode with the minimum power consumption. For calculating the losses, the pre-calculated efficiency maps of the electric machine and the inverter with the constant winding temperature of 100 °C from Fig. 3.8 and of the transmission from Fig. 6.2 were used.

In this case, the actual temperatures of the windings of both electric machines were not considered for determining the driving mode. Hence, this is a driving strategy without thermal management of both electric machines. Therefore, at partial load, only the first electric machine (EM1) is selected, which leads to a higher thermal burden on this electric machine, especially in the stator copper winding. Here is an example. The vehicle has been driven by an electric machine (EM1) for a long time in partial load range such as city driving. Meanwhile, the other electric machine (EM2) is switched off, (driving mode #1 or #2). Suddenly, the driver enters the highway. Thus, the vehicle needs high torque to accelerate (changing the driving mode to #3 or #4). In this case, the already heated first electric machine (EM1) has no chance to cool down. Hence, the first machine (EM1) can suffer from high temperature. This can cause an accelerated ageing and an unwanted derating of this electric machine, if the thermal limit of the winding is reached. High temperature in the stator winding means an increase of ohmic losses, as the stator winding resistance increases. By having the benefit of two operating electric machines for driving the vehicle at partial load, with the proper selection of the electric machines, electrical energy can be saved by reducing the ohmic losses, and the vehicle can avoid an undesired derating of one of the electric machines [79].

6.6 Driving strategy with thermal management of both electric machines

When the actual winding temperatures of both electric machines are considered in selecting the driving mode, the controller can select the ‘cooler’ electric machine to drive the vehicle, when changing the driving mode. Fig. 6.6 shows the developed driving simulation model for the driving strategy with thermal management of both electric machines [79, 80]. In the ‘Determine driving mode’ module, the actual winding temperatures of both electric machines are considered to determine the energy-optimal driving mode. In order to select the driving mode with minimum total losses, the losses in the electrical system, which includes the electric machines and the corresponding inverters, are calculated. The total losses of the electrical system include the ohmic losses $P_{\mathrm{d,cu}}$, the iron losses in the stator and rotor iron stacks $P_{\mathrm{d,Fe}}$, the mechanical friction losses $P_{\mathrm{d,fr}}$ and the inverter losses $P_{\mathrm{d,inv}}$. The ohmic losses $P_{\mathrm{d,cu}}$ of each electric machine were calculated with the re-calculated stator resistances with the actual winding temperatures of each electric machine $R_{\mathrm{DC}}(\vartheta_{\mathrm{cu}})$ from (3.3) and the required stator currents I_{s}.

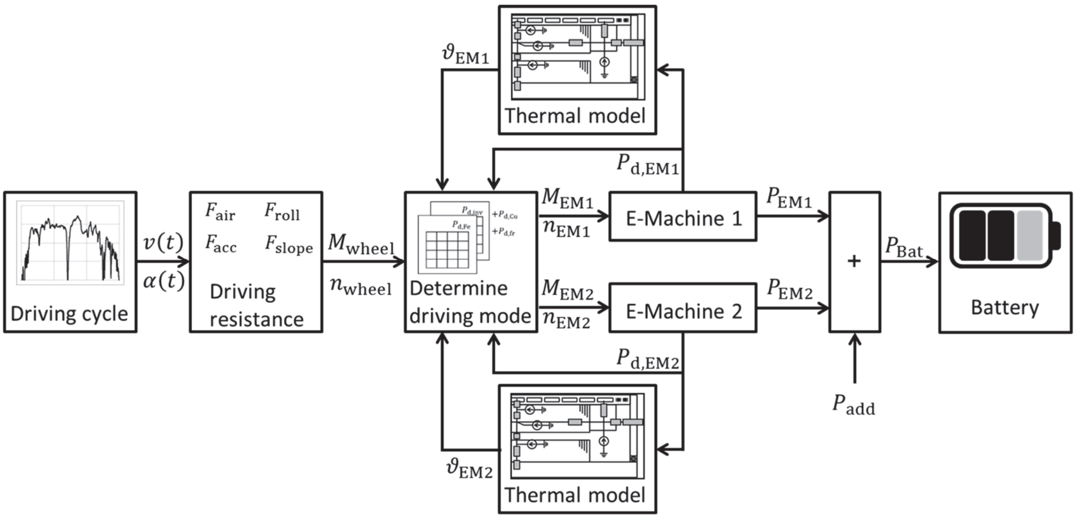

Fig. 6.6: Structure of a backward driving simulation model for pure electric driving mode with thermal network models of both electric machines

The iron losses $P_{\mathrm{d,Fe}}$ and the losses in the inverter $P_{\mathrm{d,inv}}$ were taken from the pre-calculated losses tables for all speed and torque ranges. The friction losses $P_{\mathrm{d,fr}}$ were calculated as a function of the rotational speeds of the electric machines from Chapter 3.4. The actual winding temperatures of both electric machines can be monitored via a Controller Area Network (CAN bus) during the entire operating time by the controller of the DE-REX powertrain. Thus, the measured electric machine temperatures are applied to determine the energy-optimal driving mode. For the simulation model, the thermal network model from Chapter 2.6.3 was introduced into the driving simulation model (Fig. 6.6) to predict the actual temperatures of both electric machines, EM1 and EM2. The actual winding temperatures of the electric machines were calculated with the previously calculated losses of the electrical system. The possible driving modes for the driving strategy with thermal management are listed in Table 6.2. In contrast to the original driving strategy of Table 6.1, two further driving modes, #1' and #2', are presented in Table 6.2, in which the second electric machine (EM2) participates in driving the vehicle in partial load regions. This will help to reduce the thermal burden of the first electric machine (EM1) and to minimize total ohmic losses. Since switching between electric machines also cause losses in the transmission, which was not simulated

Table 6.2 Possible driving modes for DE-REX powertrain with a driving strategy with considering the thermal condition of both electric machines

Driving modes			**EM1**		**EM2**	
#	Electric motor	Gear ratio	$M_{\mathrm{EM1}}/\mathrm{Nm}$	$n_{\mathrm{EM1}}/\mathrm{min}^{-1}$	$M_{\mathrm{EM2}}/\mathrm{Nm}$	$n_{\mathrm{EM2}}/\mathrm{min}^{-1}$
1	EM1	i_1	$\frac{M_{\mathrm{Wheel}}}{(i_1 \cdot \eta_{\mathrm{G1}})}$	$n_{\mathrm{Wheel}} \cdot i_1$	0	0
2	EM1	i_2	$\frac{M_{\mathrm{Wheel}}}{(i_2 \cdot \eta_{\mathrm{G2}})}$	$n_{\mathrm{Wheel}} \cdot i_2$	0	0
1'	EM2	i_1	0	0	$\frac{M_{\mathrm{Wheel}}}{(i_1 \cdot \eta_{\mathrm{G1}})}$	$n_{\mathrm{Wheel}} \cdot i_1$
2'	EM2	i_2	0	0	$\frac{M_{\mathrm{Wheel}}}{(i_2 \cdot \eta_{\mathrm{G2}})}$	$n_{\mathrm{Wheel}} \cdot i_2$
3	EM1+2	i_1	$\frac{1}{2} \cdot \frac{M_{\mathrm{Wheel}}}{(i_1 \cdot \eta_{\mathrm{G1}})}$	$n_{\mathrm{Wheel}} \cdot i_1$	$\frac{1}{2} \cdot \frac{M_{\mathrm{Wheel}}}{(i_1 \cdot \eta_{\mathrm{G1}})}$	$n_{\mathrm{Wheel}} \cdot i_1$
4	EM1+2	i_2	$\frac{1}{2} \cdot \frac{M_{\mathrm{Wheel}}}{(i_2 \cdot \eta_{\mathrm{G2}})}$	$n_{\mathrm{Wheel}} \cdot i_2$	$\frac{1}{2} \cdot \frac{M_{\mathrm{Wheel}}}{(i_2 \cdot \eta_{\mathrm{G2}})}$	$n_{\mathrm{Wheel}} \cdot i_2$

in the driving simulation model, the switching is triggered only if there is a temperature difference of at least 10 K between the two electric machines or if the saved power with the new driving mode is higher than 3 % of the required power with the previous driving mode.

6.7 Simulation results with both driving strategies

With the driving strategy considering the thermal condition of both electric machines (hereinafter known as Operation Strategy 2), the powertrain can select the ‘cooler’ electric machine to propel the vehicle to avoid unwanted thermal derating of the electric machine and to reduce ohmic losses. To verify this Operation Strategy 2, driving simulations with MATLAB Simulink were carried out with three driving cycles: the NEDC, WLTC and HYZEM-highway driving cycles. The results were compared with the first driving strategy without considering the thermal condition of the electric machines (hereinafter termed Operation Strategy 1). For estimating the temperature rise of the windings of the electric machines, a constant coolant temperature and ambient temperature were set to 65 °C and 25 °C, respectively. The initial temperatures of both electric machines were defined as 65 °C for all driving simulations. The vehicle parameters from Table 1.3 were used for the driving simulation.

6.7.1 Simulation results with NEDC

Fig. 6.7 and Fig. 6.8 show the driving simulation results with the NEDC with Operation Strategy 1 and Operation Strategy 2, respectively. Due to low demand for driving power, the first electric machine (EM1) was operated alone for 893.7 s with Operation Strategy 1. The final temperature of EM1 was 77.7 °C, while EM2 showed a final temperature of 63.2 °C, which was reduced due to the ambient temperature of 25 °C. Also, the maximum temperature difference between the electric machines was 15.9 K at t = 1160 s.

By using Operation Strategy 2, on the other hand, both electric machines operated more evenly. The operation time of EM1 and EM2 were 498.6 s and 416.0 s, which were 42.3 % and 35.3 % utilization rate. The end temperature difference of both electric machines was only 4.6 K. The temperature difference between the windings of both electric machines exceeded 10 K at t = 1115 s. Thus, EM2 took over the operation to propel the vehicle. Due to the high winding temperature of EM1 with Operation Strategy 1, the

Table 6.3 Comparison of simulation results of both Operation Strategies 1 and 2 with the NEDC

Operation Strategy	**Strategy 1**		**Strategy 2**	
Electric machine	**EM1**	**EM2**	**EM1**	**EM2**
ϑ_0 / °C	65	65	65	65
$\Delta\vartheta_{\mathrm{WO,NDE,max}}$ / K	14.1	0	9.3	3.0
$\Delta\vartheta_{\mathrm{WO,NDE,end}}$ / K	12.7	-1.8	7.2	2.6
Operation time / s	893.7	0	498.6	416.0
Utilization rate*)	75.7 %	0 %	42.3 %	35.3 %
Accumulated ohmic losses of both electric machines $\int P_{\mathrm{d,cu,EM12}}\mathrm{d}t$ / Wh	53.6		48.8 (−9.0%)	
Accumulated total losses of both electric machines $\int P_{\mathrm{d,EM12}}\mathrm{d}t$ / Wh	95.8		93.0 (−3.0 %)	
Energy consumption**) in kWh / 100 km	12.40		12.38	

*) Utilization rate: operation time over total test time of NEDC 1180 s

**) Energy consumption with auxiliary losses of 200 W and battery losses

accumulated ohmic losses and the accumulated total losses of the electric machines with Operation Strategy 2 were 9.0 % and 3.0 % less. Although Operation Strategy 2 reduced the ohmic losses during the test, there was no significant reduction of the energy consumption (Table 6.3). In general, typical downtown driving cycles do not require high power and high torque over a long duration. It means that only small ohmic losses occur. Therefore, the absolute saving of losses by Operation Strategy 2 was negligibly small. However, there are some real applications, where Operation Strategy 2 saves considerable energy consumption such as overtaking at steep slopes on the roads or driving with high speed on highway. These applications were discussed in [80].

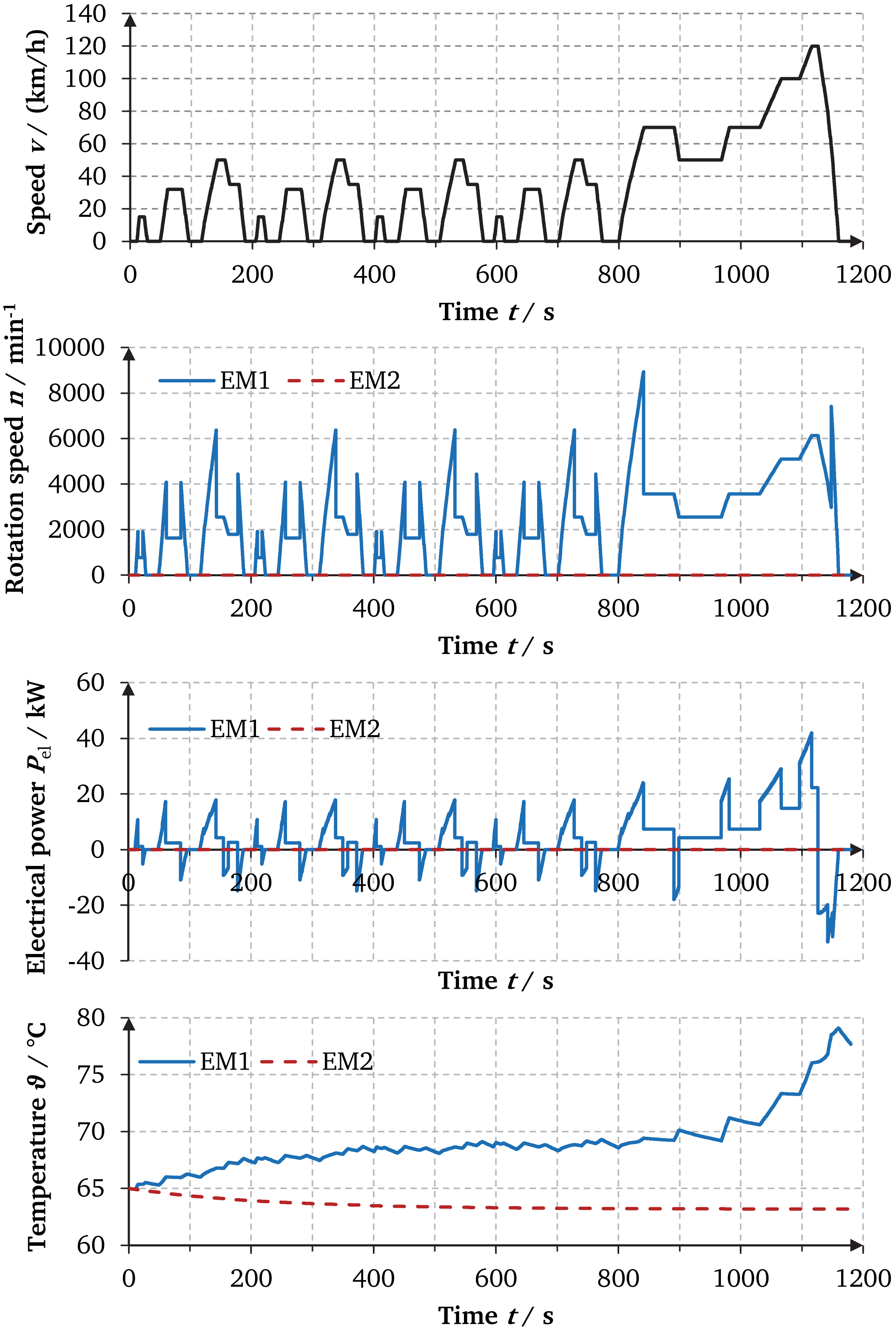

Fig. 6.7: Simulation results with Operation Strategy 1: Velocity profile of the NEDC, required rotation speeds for both electric machines, required electrical power for both electric machines, and calculated temperature rise in the winding overhang NDE side $\Delta\vartheta_{\mathrm{WO,NDE}}(t)$ of both electric machines EM1 and EM2

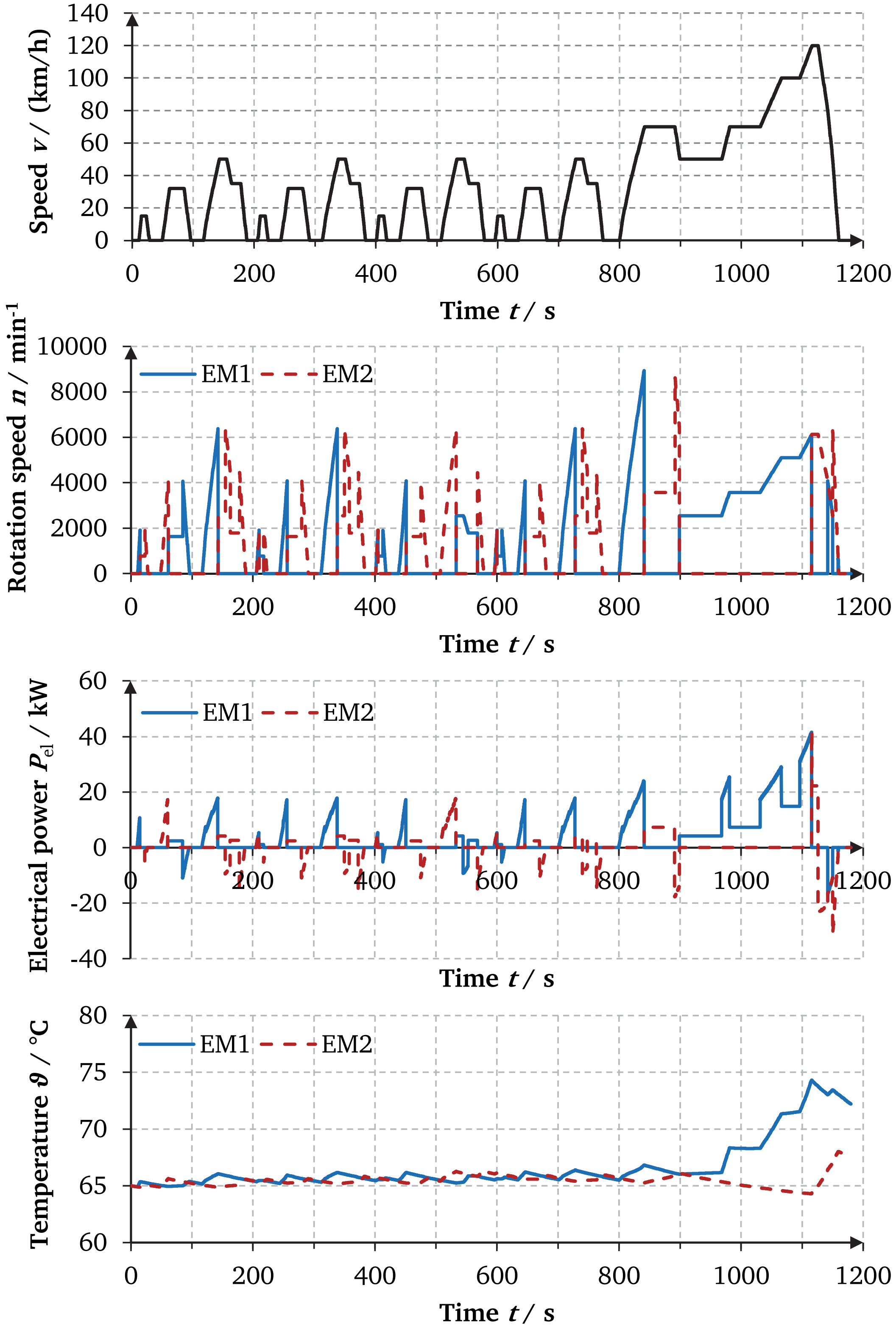

Fig. 6.8: Simulation results with Operation Strategy 2: Velocity profile of the NEDC, required rotation speeds for both electric machines, required electrical power for both electric machines, and calculated temperature rise in the winding overhang NDE side $\Delta\vartheta_{\mathrm{WO,NDE}}(t)$ of both electric machines EM1 and EM2

6.7.2 Simulation results with WLTC

The driving simulation results with the WLTC with Operation Strategy 1 and Operation Strategy 2 are presented in Fig. 6.9 and Fig. 6.10, respectively. Similar to the simulation results with the NEDC, the electric machines were unevenly utilized with the Operation Strategy 1. During the WLTC test, EM2 was operated only for 59 s, while EM1 drove the vehicle for 1544 s. Thus, the maximum temperature of EM1 reached 80.3 °C, whereas EM2 showed a maximum temperature of 65.6 °C. Because of the high temperature of EM1, the accumulated ohmic losses of both electric machines with the Operation Strategy 1 were 10 % higher than with the Operation Strategy 2. The energy consumptions with auxiliary losses of 200 W and battery losses with an internal resistance 0.14 Ω were 14.75 kWh / 100 km and 14.73 kWh / 100 km with Operation Strategy 1 and Operation Strategy 2, respectively. As previously mentioned, energy consumption with the WLTC was about 19 % higher than with the NEDC. Reduction of energy consumption with Operation Strategy 2, like previous simulation results, was negligibly small. The simulation results comparison between Operation Strategy 1 and 2 with the WLTC is presented in Table 6.4.

Table 6.4 Comparison of simulation results of both Operation Strategies 1 and 2 with the WLTC

Operation Strategy	**Strategy 1**		**Strategy 2**	
Electric machine	**EM1**	**EM2**	**EM1**	**EM2**
ϑ_0 / °C	65	65	65	65
$\Delta\vartheta_{\mathrm{WO,NDE,max}}$ / K	15.3	0.6	11.1	5.4
$\Delta\vartheta_{\mathrm{WO,NDE,end}}$ / K	13.6	−1.0	9.7	2.1
Operation time / s	1544	59	829	843
Utilization rate*)	85.8 %	3.3 %	46.1 %	46.8 %
Accumulated ohmic losses of both electric machines $\int P_{\mathrm{d,cu,EM12}}\mathrm{d}t$ / Wh	109.5		99.6 (−9.0 %)	
Accumulated total losses of both electric machines $\int P_{\mathrm{d,EM12}}\mathrm{d}t$ / Wh	218.1		212.3 (−2.7 %)	
Energy consumption**) in kWh / 100 km	14.75		14.73	

*) Utilization rate: operation time over total test time of WLTC 1800 s

**) Energy consumption with auxiliary losses of 200 W and battery losses

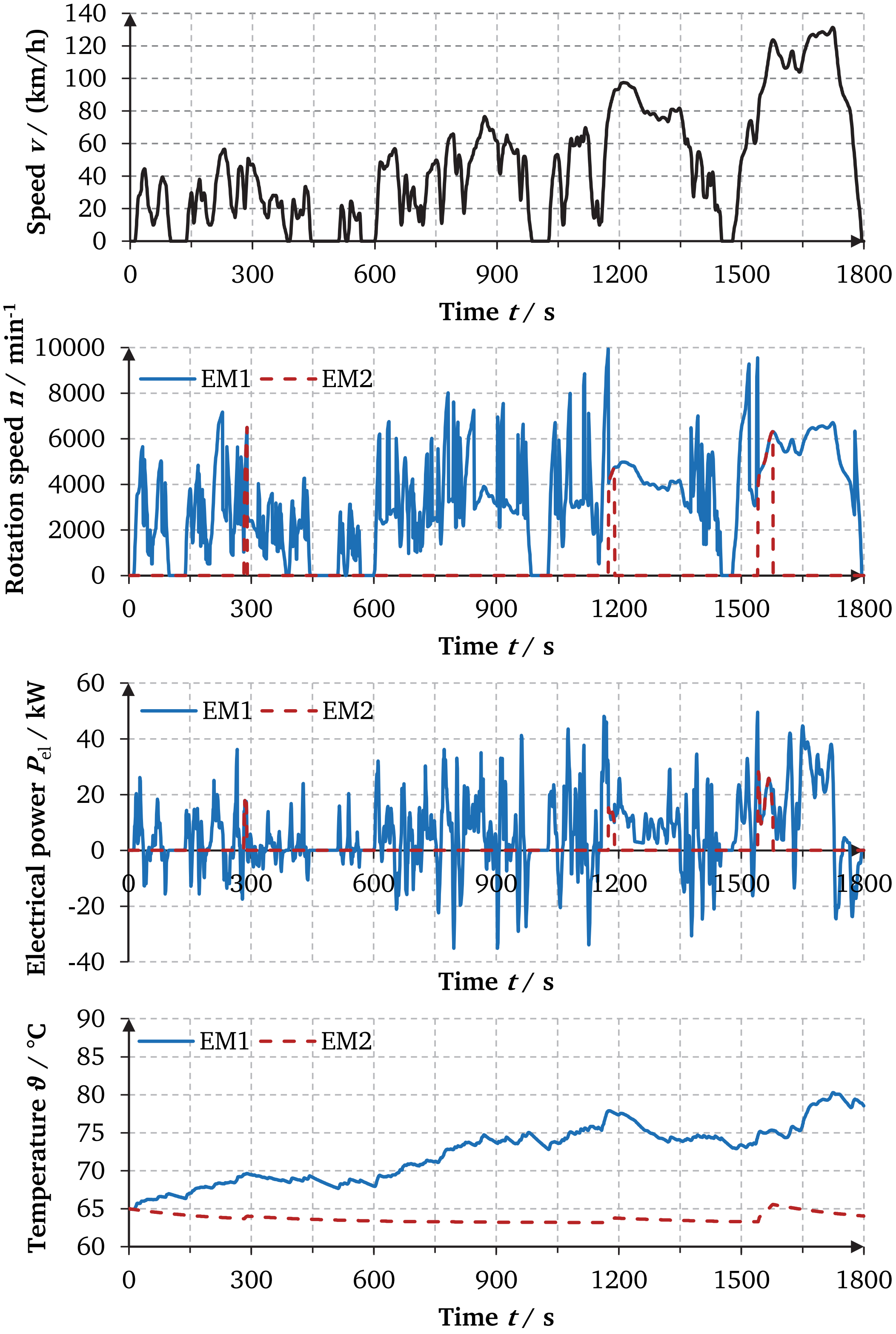

Fig. 6.9: Simulation results with Operation Strategy 1: Velocity profile of the WLTC, required rotation speeds for both electric machines, required electrical power for both electric machines, and calculated temperature rise in the winding overhang NDE side $\Delta\vartheta_{\mathrm{WO,NDE}}(t)$ of both electric machines EM1 and EM2

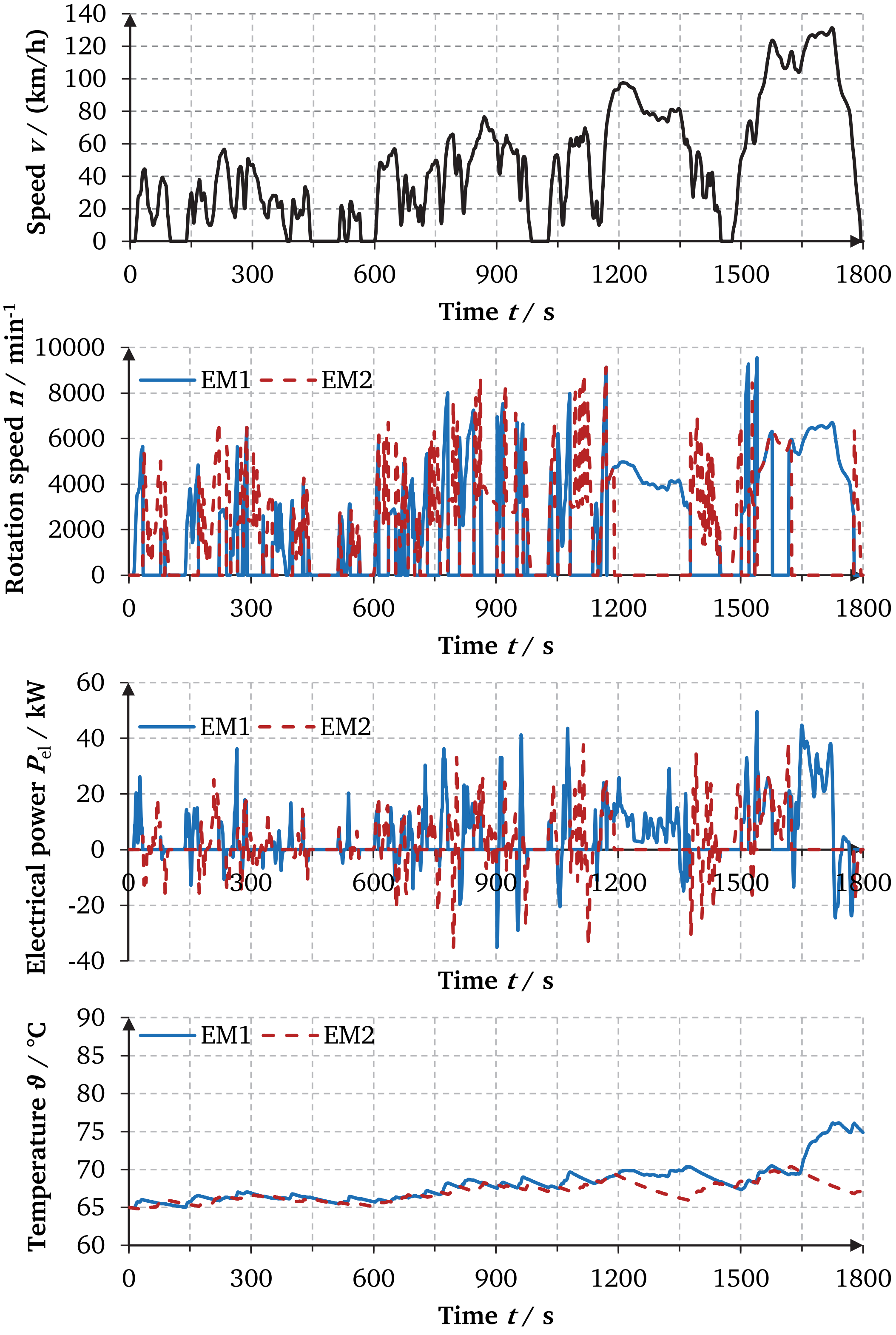

Fig. 6.10: Simulation results with Operation Strategy 2: Velocity profile of the WLTC, required rotation speeds for both electric machines, required electrical power for both electric machines, and calculated temperature rise in the winding overhang NDE side $\Delta\vartheta_{\mathrm{WO,NDE}}(t)$ of both electric machines EM1 and EM2

6.7.3 Simulation results with HYZEM-highway driving cycle

In order to increase driving loads, the driving simulation was carried out with the HYZEM-highway driving cycle with a constant inclination of the road of 1.7 %. The driving simulation results are listed in Table 6.5. Fig. 6.11 presents the calculated temperature rise at the winding overhang on the NDE side for both electric machines EM1 and EM2 with Operation Strategy 1 as dashed lines and with Operation Strategy 2 as solid lines. From the driving simulation results with Operation Strategy 1, the maximum temperature of EM1 was 91.1 °C, while EM2 reached only 72.0 °C. In the case of the driving simulation with Operation Strategy 2, the maximum temperatures of EM1 and EM2 were 81.9 °C and 78.0 °C, respectively. This shows that both electric machines were evenly utilized with Operation Strategy 2. In addition, due to the lower temperature of both electric machines, they had a bigger thermal reserve keeping them from a thermal derating. Hence, Operating Strategy 2 can be a solution for avoiding an early derating of the electric machines.

Table 6.5 Comparison of simulation results of both Operation Strategies 1 and 2 with the HYZEM-highway-driving cycle at 1.7 % incline

Operation Strategy	**Strategy 1**		**Strategy 2**	
Electric machine	**EM1**	**EM2**	**EM1**	**EM2**
ϑ_0 / °C	65	65	65	65
$\Delta\vartheta_{\mathrm{WO,NDE,max}}$ / K	26.1	7.0	16.9	12.9
$\Delta\vartheta_{\mathrm{WO,NDE,end}}$ / K	19.0	1.6	9.4	9.2
Operation time / s	1733.5	484.8	1169.1	1305.1
Utilization rate*)	96.2 %	26.9 %	64.8 %	72.4 %
Accumulated ohmic losses of both electric machines $\int P_{\mathrm{d,cu,EM12}}\mathrm{d}t$ / Wh	273.5		241.9 (−11.6 %)	
Accumulated total losses of both electric machines $\int P_{\mathrm{d,EM12}}\mathrm{d}t$ / Wh	535.2		526.6 (−1.6 %)	

*) Utilization rate: operation time over total test time of HYZEM-highway driving cycle 1803 s

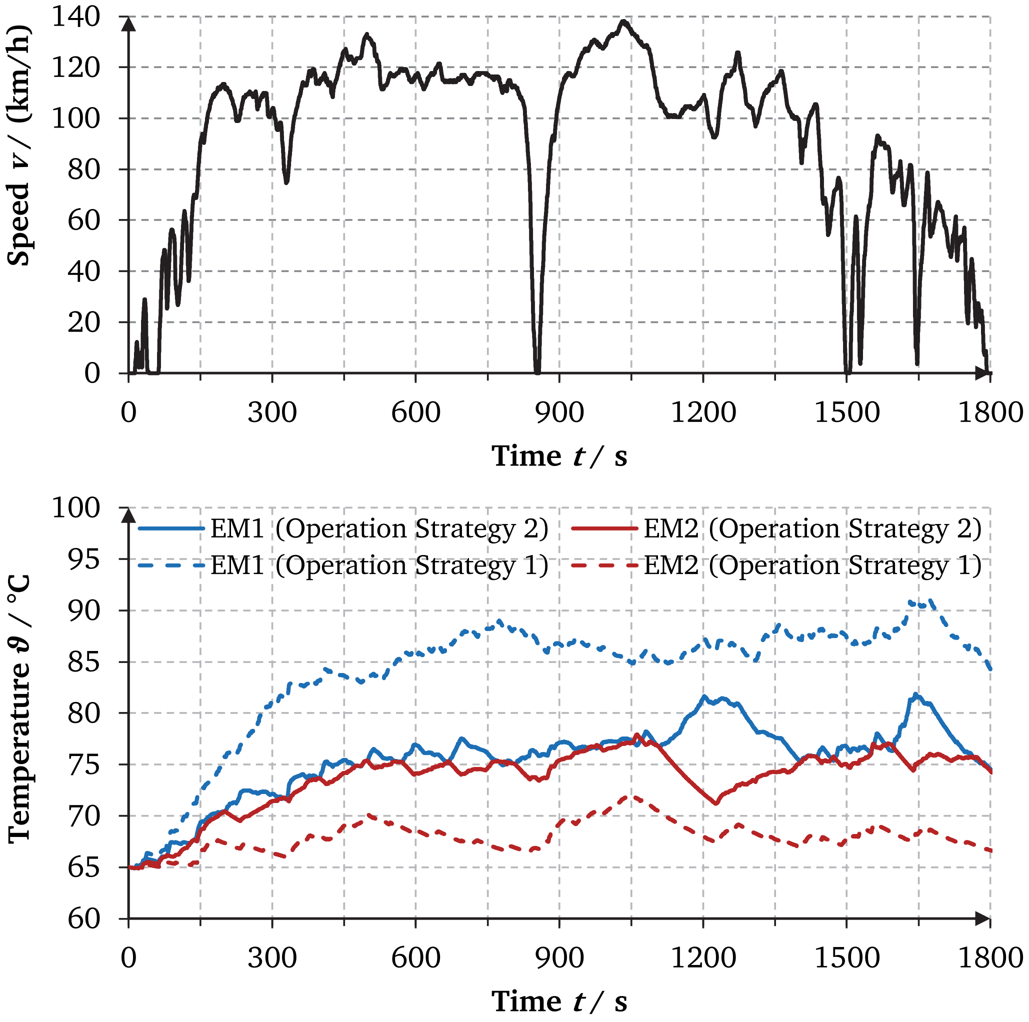

Fig. 6.11: Simulation results with Operation Strategy 1 and 2: Velocity profile of the HYZEM-highway driving cycle, calculated temperature rise in the winding overhang NDE side $\Delta\vartheta_{\mathrm{WO,NDE}}(t)$ of both electric machines EM1 and EM2

7. Downsizing possibilities for the prototype machine

For the hybrid operation of the powertrain, the winding temperature of the electric motor should not exceed the thermal limit of the insulation 180 °C (Thermal Class H, IEC 60034) at the following predefined thermal boundary condition, which was set for operation conditions with driving 30 min at rated operation (OP2) and then for 30 seconds at maximum overload operation (OP1). Considering the maximum allowed coolant temperature of 65 °C and the calculated temperature rise during 30 s at OP1 $\Delta\vartheta_{\mathrm{WO,OP1}}(30\ \mathrm{s}) = 37\ \mathrm{K}$, the maximum temperature at the winding overhang on the NDE side is $\vartheta_{\mathrm{WO,NDE,max}} = 65\ \mathrm{°C} + 38.1\ \mathrm{K} + 37\ \mathrm{K} = 140.1\ \mathrm{°C}$, which gives a temperature reserve of 40 K for Thermal Class H (IEC 60034). The corresponding rotor magnet temperature of $\vartheta_{\mathrm{M,max}} = 97.1\ \mathrm{°C}$ gives a 73 K safety margin, with the limiting operating temperature of the magnet $\vartheta_{\mathrm{M,lim}} = 170\ \mathrm{°C}$ (VACODYM 863 TP, company *Vacuumschmelze* GmbH, Hanau). To thermally utilize the machine, the electric motor either can be equipped with a cheaper insulation system of a lower Thermal Class, such as Thermal Class F (155 °C, IEC 60034), or can be redesigned with higher thermal utilization by downsizing of the machine. In this chapter, the second method is discussed.

There are two possibilities for downsizing the electric motors. In the next section 7.1, the electric motor is redesigned to increase electromagnetic and thermal utilization to avoid any thermal reserve by decreasing the active volume of the machine. Chapter 7.2 describes the second approach to downsizing by using a stator wave hairpin winding, which has a higher slot fill factor than the round wire winding. Finally, the results from the original electric motor performance and from the redesigned motors are compared [83].

7.1 Machine downsizing by increasing thermal utilization via decreasing active volume of electric machine

7.1.1 Shortening of active iron length of the machine

The active iron length of the machine l_{Fe} can be shortened to thermally utilize the electric machine by increasing the electromagnetic utilization C, while the stator geometry and stator winding type are unmodified. In order to produce the same rated torque with the shortened active iron length l'_{Fe}, the stator current must be increased $I'_{\mathrm{s}} = I_{\mathrm{s}} \cdot (l_{\mathrm{Fe}}/l'_{\mathrm{Fe}})$, thereby causing the electric machine to produce more heat via ohmic losses. Thus, the temperature rise in the machine, especially the winding temperature, must be considered to find the proper active iron length l'_{Fe} with the thermal boundary condition. To simplify the calculation of the temperature rise, the machine was considered as a homogeneous body model. In addition, iron losses and friction losses were small compared to the ohmic losses. Thus, they were neglected, and only the ohmic losses were considered as a heat source $P_{\mathrm{d}} \approx P_{\mathrm{d,cu}}$. Therefore, the losses are square proportional to the stator current $P_{\mathrm{d}} \sim I_{\mathrm{s}}^2$. The heat in the machine is transferred from the surface area A_{mot} of the machine to the flowing coolant in the cooling channel with a heat transfer coefficient α. Heat is also stored in the stator winding with an equivalent specific thermal capacity with $m_{\mathrm{cu}} \cdot c$. We used the copper mass m_{cu} of the stator winding and the specific heat capacity of copper c. The homogeneous body temperature rise is calculated with the initial winding temperature $\Delta\vartheta_0$:

$$\Delta\vartheta(t) = \Delta\vartheta_\infty \cdot (1 - e^{-t/T_\vartheta}) + \Delta\vartheta_0 \cdot e^{-t/T_\vartheta} \;, \tag{7.1}$$

where the steady-state temperature rise is $\Delta\vartheta_\infty = P_{\mathrm{d}}/(\alpha \cdot A_{\mathrm{mot}})$, and the thermal constant is $T_\vartheta = (m_{\mathrm{cu}} \cdot c)/(\alpha \cdot A_{\mathrm{mot}})$. This can be simplified when the considered time is much shorter than the thermal constant $t \ll T_\vartheta$.

$$\Delta\vartheta(t) \approx \Delta\vartheta_\infty \cdot \frac{t}{T_\vartheta} + \Delta\vartheta_0 \cdot \left(1 - \frac{t}{T_\vartheta}\right) \text{ (when } t \ll T_\vartheta\text{)} \tag{7.2}$$

These parameters are dependent on the iron length l_{Fe}. Thus, they are changed with a reduced active iron length l'_{Fe} (Table 7.1). The stator winding resistance R_{s} and the mass of the stator winding m_{cu} are proportional to the sum of the active iron length and the winding overhang length $l_{\mathrm{Fe}} + l_{\mathrm{b}}$. The machine cooling surface A_{mot} is decreased with the reduced active length of the machine l'_{Fe}. Due to the short-term operating duration at OP1 of 30 s, which is much shorter than the thermal time constant T'_{ϑ}, the temperature rise at overload condition (OP1) is calculated linear with the initial temperature of the steady-state temperature at rated load (OP2) with T'_{ϑ} in [s]

$$\begin{aligned}&\Delta\vartheta'_{\infty,\mathrm{OP2}} + \Delta\vartheta'_{\mathrm{OP1}}(30\ \mathrm{s}) \approx \\ &\approx \Delta\vartheta'_{\infty,\mathrm{OP1}} \cdot \frac{30}{T'_{\vartheta}} + \Delta\vartheta'_{\infty,\mathrm{OP2}} \cdot \left(1 - \frac{30}{T'_{\vartheta}}\right) = \frac{P'_{\mathrm{d,OP1}}}{\alpha \cdot A'_{\mathrm{mot}}} \cdot \frac{30}{T'_{\vartheta}} + \frac{P'_{\mathrm{d,OP2}}}{\alpha \cdot A'_{\mathrm{mot}}} \cdot \left(1 - \frac{30}{T'_{\vartheta}}\right),\end{aligned} \tag{7.3}$$

where the ohmic losses in the winding with a reduced active iron length l'_{Fe} at the overload condition (OP1) and rated load (OP2) are denoted as $P'_{\mathrm{d,OP1}}$ and $P'_{\mathrm{d,OP2}}$, respectively. By substituting the changed parameters with a reduced active iron length l'_{Fe} from Table 7.1 into (7.3), we get (7.4) with T_{ϑ} in [s].

$$\begin{aligned}&\Delta\vartheta'_{\infty,\mathrm{OP2}} + \Delta\vartheta'_{\mathrm{OP1}}(30\ \mathrm{s}) \approx \\ &\approx \Delta\vartheta_{\infty,\mathrm{OP1}} \cdot \frac{30}{T_{\vartheta}} \cdot \left(\frac{l_{\mathrm{Fe}}}{l'_{\mathrm{Fe}}}\right)^2 + \Delta\vartheta_{\infty,\mathrm{OP2}} \cdot \left(\frac{l'_{\mathrm{Fe}}+l_{\mathrm{b}}}{l_{\mathrm{Fe}}+l_{\mathrm{b}}}\right) \cdot \left(\frac{l_{\mathrm{Fe}}}{l'_{\mathrm{Fe}}}\right)^3 \cdot \left(1 - \frac{30}{T_{\vartheta}} \cdot \left(\frac{l_{\mathrm{Fe}}+l_{\mathrm{b}}}{l'_{\mathrm{Fe}}+l_{\mathrm{b}}}\right) \cdot \left(\frac{l'_{\mathrm{Fe}}}{l_{\mathrm{Fe}}}\right)\right)\end{aligned} \tag{7.4}$$

Table 7.1 Changed parameters with a reduced active iron length l'_{Fe}

Stator current	$I'_{\mathrm{s}} = I_s \cdot \left(\frac{l_{\mathrm{Fe}}}{l'_{\mathrm{Fe}}}\right)$
Stator winding resistance per phase	$R'_{\mathrm{s}} = R_{\mathrm{s}} \cdot \left(\frac{l'_{\mathrm{Fe}} + l_{\mathrm{b}}}{l_{\mathrm{Fe}} + l_{\mathrm{b}}}\right)$
Copper winding mass	$m'_{\mathrm{cu}} = m_{\mathrm{cu}} \cdot \left(\frac{l'_{\mathrm{Fe}} + l_{\mathrm{b}}}{l_{\mathrm{Fe}} + l_{\mathrm{b}}}\right)$
Stator cooling surface	$A'_{\mathrm{mot}} = A_{\mathrm{mot}} \cdot \left(\frac{l'_{\mathrm{Fe}}}{l_{\mathrm{Fe}}}\right)$
Thermal time constant	$T'_{\vartheta} = T_{\vartheta} \cdot \left(\frac{l'_{\mathrm{Fe}} + l_{\mathrm{b}}}{l_{\mathrm{Fe}} + l_{\mathrm{b}}}\right) \cdot \left(\frac{l_{\mathrm{Fe}}}{l'_{\mathrm{Fe}}}\right)$
Ohmic losses	$P'_{\mathrm{d}} = P_{\mathrm{d}} \cdot \left(\frac{l'_{\mathrm{Fe}} + l_{\mathrm{b}}}{l_{\mathrm{Fe}} + l_{\mathrm{b}}}\right) \cdot \left(\frac{l_{\mathrm{Fe}}}{l'_{\mathrm{Fe}}}\right)^2$

With the maximum admissible temperature of Thermal Class H and the coolant temperature of 65 °C, the winding temperature rise should be $\Delta\vartheta'_{\infty,\mathrm{OP2}} + \Delta\vartheta'_{\mathrm{OP1}}(30\ \mathrm{s}) = 115\ \mathrm{K}$. Using the previously calculated temperature rise from the FEM calculation, the steady-state temperatures at both load cases are $\Delta\vartheta_{\infty,\mathrm{OP1}} = 132\ \mathrm{K}$ and $\Delta\vartheta_{\infty,\mathrm{OP2}} = 35\ \mathrm{K}$. By solving the cubic polynomial, the shortened active iron length is calculated $l'_{\mathrm{Fe}} = 110\ \mathrm{mm}$. Due to the low temperature rise of the magnet (Fig. 5.16), a different magnet material can be used which has a lower admissible temperature limit, such as VACODYM 956 TP. It has a higher remanence of $B_{\mathrm{R}} = 1.21\ \mathrm{T}$ at 100 °C, which results in 5.8 % higher remanence than the original magnet material of VACODYM 863 TP. This leads to a further reduction of the active iron length $l'_{\mathrm{Fe}} = 107\ \mathrm{mm}$. In that way, the electromagnetic utilization and the corresponding thermal utilization were increased to

$$C' = \frac{S_\delta}{d_{\mathrm{si}}^2 \cdot l'_{\mathrm{Fe}} \cdot n_{\mathrm{N}}} = 7.12\ \mathrm{kVA} \cdot \mathrm{min/m^3}, \tag{7.5}$$

$$A' = \frac{2m_{\mathrm{s}} \cdot N_{\mathrm{s}} \cdot I'_{\mathrm{N}}}{d_{si} \cdot \pi} = 578\ \mathrm{A/cm}, \tag{7.6}$$

$$J' = \frac{I'_N}{\alpha \cdot A_{\mathrm{cu}}} = 11.4\ \mathrm{A/mm^2}\ . \tag{7.7}$$

The increased current loading A' leads to a higher hot-spot temperature of nearly 180 °C in the winding overhang, fitting with the temperature limit of Thermal Class H.

7.1.2 Redesign of electric machine with increased electromagnetic utilization and thermal utilization

With the increased electromagnetic utilization $C' = 7.12\ \mathrm{kVA} \cdot \mathrm{min/m^3}$ (7.5) and the increased thermal utilization $A' \cdot J' = 6590\ \mathrm{A/cm} \cdot \mathrm{A/mm^2}$ (7.6), (7.7), the electric machine is redesigned for the given requirements in Table 1.4. As with the prototype machine, the redesigned machine also has 6 poles and 36 semi-closed slots with constant tooth width. In order to reduce the deviations of the air-gap flux radial component distribution from the ideal sine wave shape along the rotor circumference, a two-layer 5/6-short pitched three-phase lap winding is used. The stator bore diameter is reduced from $d_{\mathrm{si}} = 92.8\ \mathrm{mm}$ to 85 mm, and the active iron length is $l_{\mathrm{Fe}} = 125\ \mathrm{mm}$. Due to the reduced flux, the number of turns per phase was increased from $N_{\mathrm{s}} = 24$ to 28 to get the same flux linkage in the stator winding. As stated previously, high energy NdFeB permanent magnets of type VACODYM 956 TP were used to avoid permanent

Table 7.2 Main data of the redesigned electric machine with the increased electromagnetic utilization C' and the increased thermal utilization $A' \cdot J'$

Parameter		Value	Parameter		Value
Outer diameter of stator iron stack	d_{so}	142 mm	Inner diameter of stator iron stack	d_{si}	85 mm
Axial iron length of stator iron stack	l_{Fe}	120 mm	Length of stator winding overhang	l_{b}	94.5 mm
Magnet segment height	h_{M}	3.6 mm	Magnet segment width	b_{M}	7.4 mm
Number of turns per phase	N_{s}	28	Number of turns per phase and slots	N_{c}	14
Air gap width	δ	0.6 mm	Number of parallel winding branches	a	6
Cross section of conductor per turn 2 × ∅0.6mm, 2 × ∅0.75mm	A_{cu}	1.45 mm²	Stator winding resistance per phase (20 °C)	$R_{\text{s,20}}$	24.2 mΩ

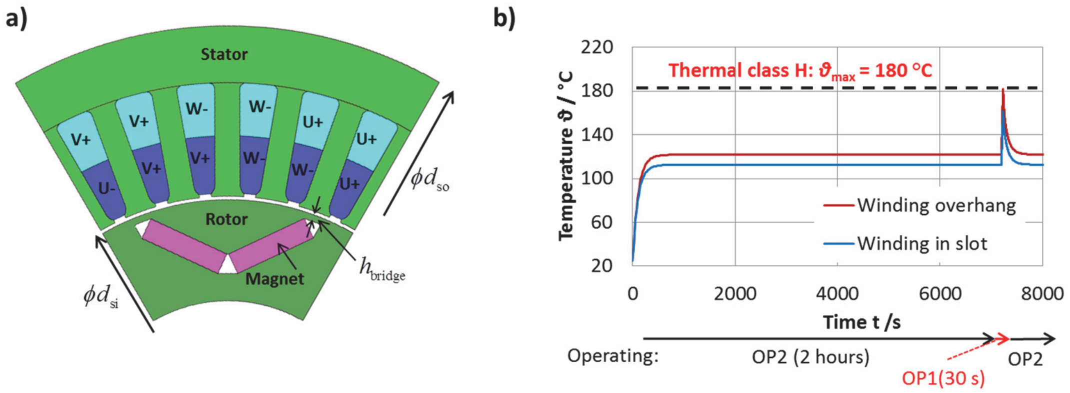

Fig. 7.1 a) Axial cross section of the redesigned electric machine for FEM simulation, b) Calculated temperature rise for 2 hours, until steady state is reached at OP2. Then follows short-term (30 s) maximum overload OP1 at a coolant temperature of $\vartheta_{\text{coolant}} = 65$ °C.

demagnetization of the magnet at high temperatures up to 160 °C. Due to the reduced rotor diameter, the height of the rotor side bridges was reduced by 25 % from $h_{\text{bridge}} =$ 2 mm to 1.5 mm. This is still sufficient to withstand the centrifugal force at 120 % of the maximum speed. The smaller iron bridge allows for less magnet material in the rotor, because the magnetic flux leakage via the iron bridges is decreased with a smaller iron

Table 7.3 Calculated redesign steps of the electric machine with distributed round wire lap winding (d_{so}: stator outer diameter, l_{Fe}: active iron length, ϑ_{H}: highest temperature in the winding, V : active volume, m_{act} : active mass, m_{M} : magnet mass, η_{OP2} : motor efficiency at OP2)

	Prototype electric machine	**1st Redesign**	**2nd Redesign**	**Redesigned electric machine**
	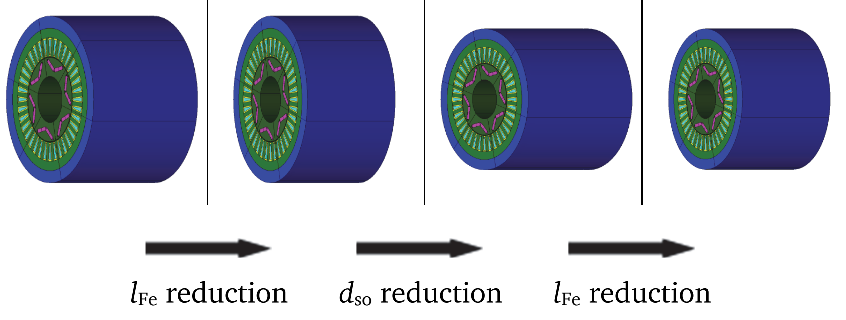			
d_{so} / mm	150	150	142	142
d_{si} / mm	92.8	92.8	85	85
l_{Fe} / mm	140	107	128	120
ϑ_{H} / °C	136	180	165	181
C / (kVA·min/m^3)	5.41	7.12 (+32 %)	7.12 (+32 %)	7.35 (+36 %)
$A{\cdot}J$ / (A/cm·A/mm^2)	4345	6590 (+52 %)	6254 (+44 %)	7088 (+63 %)
η_{OP2} / %	95.76	-	-	94.60
V / cm^3	2474	1891 (−24 %)	2027 (−18 %)	1900 (−23 %)
m_{act} / kg	16.0	12.2 (−24 %)	13.4 (−16 %)	12.6 (−21 %)
m_{M} / kg	1.06	0.81 (−23 %)	0.63 (−41 %)	0.59 (−44 %)

bridge height. Thus, the electric machine has an increased magnetic flux density of $B_{\delta 1} = 0.9$ T.

The temperature rise of the redesigned machine was simulated via 3D FEM software JMAG with the same thermal boundary conditions as for the prototype motor in Chapter 2.6.4. The calculated maximum temperature of the winding was 166 °C after 30 s overload condition (OP1) with the initial temperature at the steady-state temperature for the rated operation (OP2), which still has a 14 K safety margin. Thus, the electric machine was shortened again according to (7.4). The reduced active iron length of the redesigned motor was $l_{\mathrm{Fe}} = 120$ mm. The main data of the redesigned electric machine is presented in Table 7.2. The axial cross section of the machine and the calculated temperature rise of the winding are shown in Fig. 7.1. A further reduction of active iron length to 120 mm resulted in a hotspot temperature of 180 °C at the winding overhang and in a 23% reduction of active volume V and a 44 % reduction of magnet mass m_{M} in comparison with the prototype electric machine. Table 7.3 shows the redesigned steps of the prototype machine with a distributed round wire lap winding.

$$V = \frac{\pi}{4} \cdot d_{\mathrm{so}}^2 \cdot l_{\mathrm{Fe}} = 1900\ \mathrm{cm}^3 \tag{7.8}$$

$$m_{\mathrm{M}} = \rho_{\mathrm{M}} \cdot V_{\mathrm{M}} = 0.59\ \mathrm{kg} \tag{7.9}$$

7.2 Machine downsizing by increasing the slot fill factor with a hairpin winding

7.2.1 Hairpin winding

The benefits of hairpin wave windings with rectangular wire cross-section are a higher fill factor k_{f} in the stator slots, a shorter axial winding overhang and a better cooling of the winding overhang due to the larger cooling surface, compared with the conventional round wire lap windings [52]. Usually, two-layer wave windings with form-wound coils of one turn per coil with profiled rectangular conductor cross-section are used in large high voltage electric machines, having a highly complex manufacturing process and accordingly high manufacturing costs [15]. Recently, several manufacturers have also produced smaller electric machines for use in cars with profiled wire windings such as hairpin four-layer windings, typically in the lower to medium power range 20 … 100 kW for battery electric vehicles [53, 54, 55, 56] and hybrid vehicles [57, 58, 59].

The half coils are inserted in slots, and by many welding spots, these ‘hairpin’ half coils are completed as full coils with one turn per coil and are serially connected as wave windings in two or four or more layers to increase the number of turns per phase. Compared to the slot fill factor of conventional round wire lap windings of up to 45 %, a hairpin winding can reach up to approximately 70 % slot fill factor, when designed for low rated voltage $U < 1$ kV. With the same conductor cross-section area in the stator slot, the electric machine requires less stator slot height h_{Q}. Thus, we can reduce the overall size and mass of the electric machine [56, 58].

The wave winding leads to series connection of all coils per phase ($a = 1$), thus requiring a small number of turns per coil N_c. This fits to the hairpin winding topology with one turn per coil. This may lead to an increased cross-section area A_cu of conductor per turn, if a low voltage at a rather big power is used. This bigger area of A_cu causes a high current displacement effect, especially at high electric stator frequency, constituted as skin and proximity effects. In order to limit these unwanted AC effects, the height of the rectangular wire h_TL should be selected to be as small as possible. But also, the wire width b_TL is limited by the width limit of the stator teeth, otherwise the stator teeth are too narrow, which can cause high magnetic saturation. Therefore, a compromise is needed in selecting the rectangular wire dimensions h_TL and b_TL.

7.2.2 Increase of slot fill factor with hairpin winding for reduction of active mass of electric machine

For hairpin windings, the half-coil profiled wires are bent into a U shape as so-called hairpins. These hairpins are axially inserted into the semi-closed stator slots with each of the two hairpin legs located in different stator slots, separated by roughly one pole pitch according to the chosen coil span W. The half-coil ends are bent outwards for the wave-winding layout. So, each leg end can be connected to a different leg end of the next series coil, depending on the winding scheme. Finally, the contacted ends are welded to build the electrical connections [53, 60]. Fig. 7.2 shows an example of a four-layer wave winding scheme with 3 phases, 6 poles and 36 stator slots, which acts electrically as a two-layer three-phase wave winding with $N_\mathrm{c} = 2$ turns per coil layer and slot.

The electric machine for the DE-REX powertrain was redesigned with such a two-layer three-phase hairpin wave winding. First, the electric machine was designed with the same pole count $2p = 6$, the same stator bore diameter $d_\mathrm{si} = 92.8\,\mathrm{mm}$, the same active length of iron stack $l_\mathrm{Fe} = 140\,\mathrm{mm}$ and the same 36 stator slots as the prototype electric machine. The winding of the redesigned machine has four rectangular bars per slot, as shown in Fig. 7.3 b), with a conductor height, width and cross-section area of $h_\mathrm{TL} = 2.5\,\mathrm{mm}$, $b_\mathrm{TL} = 4.5\,\mathrm{mm}$ and $A_\mathrm{cu} = 10.70\,\mathrm{mm}^2$, respectively, as two turns per coil $N_\mathrm{c} = 2$ in a two-layer winding. The wire dimensions were selected from the standards for rectangular wire [61], yielding a slot fill factor of 60 % with respect to manufacturing considerations [62, 63]. For a fair comparison, the height of the yoke $h_\mathrm{yoke} = 10\,\mathrm{mm}$ and the slot opening height $h_\mathrm{so} = 0.6\,\mathrm{mm}$ and the slot opening width

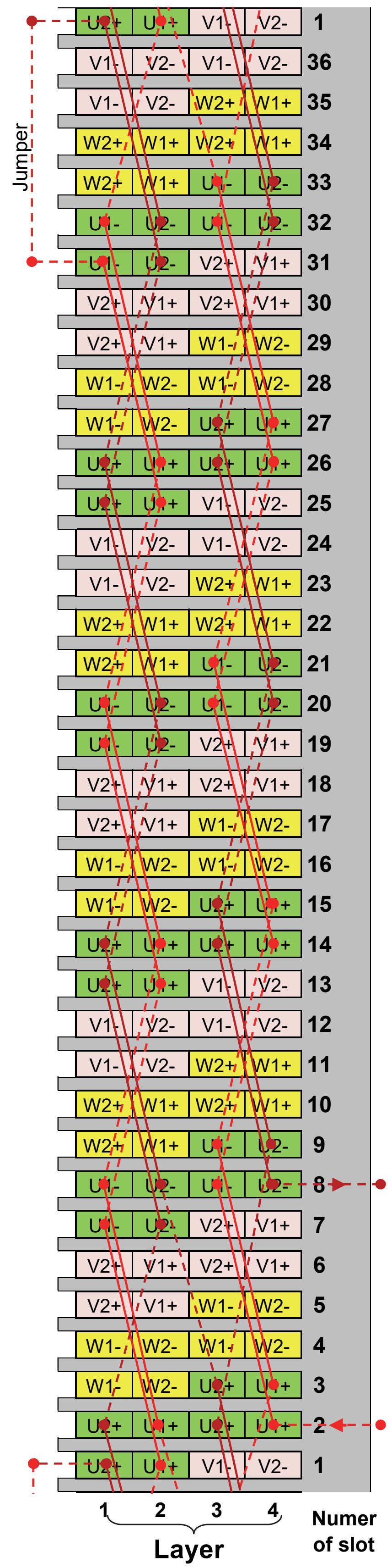

Fig. 7.2 Hairpin wave four-layer winding scheme: Phase U in green with coil connections, solid line: winding overhang DE side, dashed line: winding overhang NDE side

$b_{so} = 2$ mm were kept constant as with the round-wire machine. The hairpin winding has a smaller degree of freedom in electromagnetic design due to the small even numbers of possible conductor arrangements per slot. Here, the redesigned machine has the number of turns per coil $N_c = 2$ with a series connection $a = 1$ of all coils per phase, resulting in a number of turns per phase $N_s = 24$. In order to utilize a similar thermal utilization $A \cdot J$, the total conductor cross-section area A_{tot} was kept similar to the round-wire machine. Hence the outer diameter of the stator d_{so} could be reduced (Fig. 7.3). The increased AC resistance $R_{s,AC}(\vartheta_{cu})$, due to the current displacement effect in the wire depending on the stator fundamental frequency, was calculated analytically using equations of [64] (Table 7.5).

For the thermal calculation of the machine with a hairpin winding, the winding overhang was modelled as a 3D model with JMAG (Fig. 7.4). Due to the large contact area of the rectangular wire surface with the slot insulation and due to the shorter length of the winding overhang, the calculated hotspot temperature in the winding overhang was reduced to 131.7 °C at a coolant inlet temperature of 65 °C. This allows an increase of the power density by reducing the active volume V and an increase of the thermal utilization $A \cdot J$. Hence, as a second step, the stator bore diameter d_{si} and the active iron length l_{Fe} were reduced with respect to Chapter 7.1.2. Due to the reduced stator inner diameter, the size of the rectangular wires had to be modified to $h_{TL} = 2.8$ mm, $b_{TL} = 4.0$ mm and $A_{cu} = 10.65$ mm^2 to increase the tooth width in order to avoid too high iron saturation. The other hairpin winding parameters remained constant. This new model

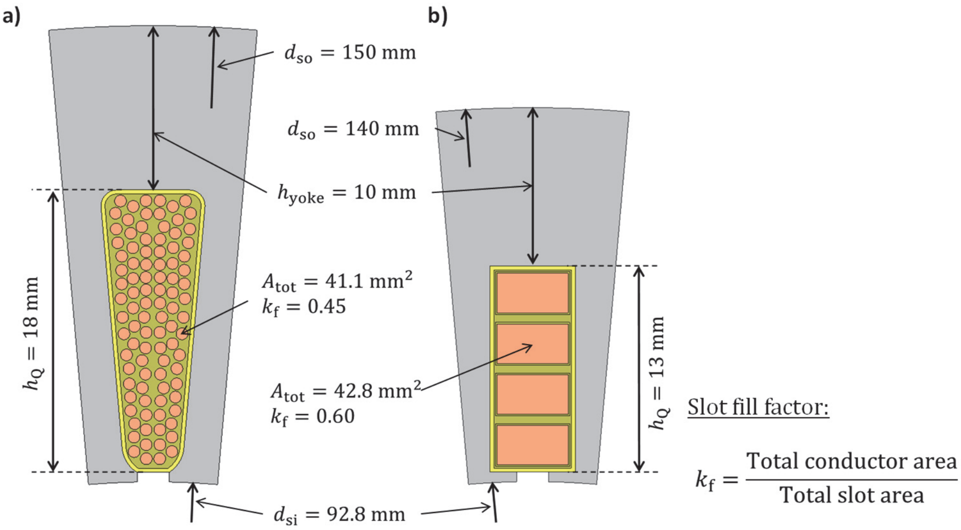

Fig. 7.3 Cross section of a stator slot of the electric machine with a) round wire winding and b) hairpin winding, A_{tot} : total cross section area of conductors in a slot, k_f: slot fill factor, h_Q: stator slot height and h_{yoke}: stator yoke height.

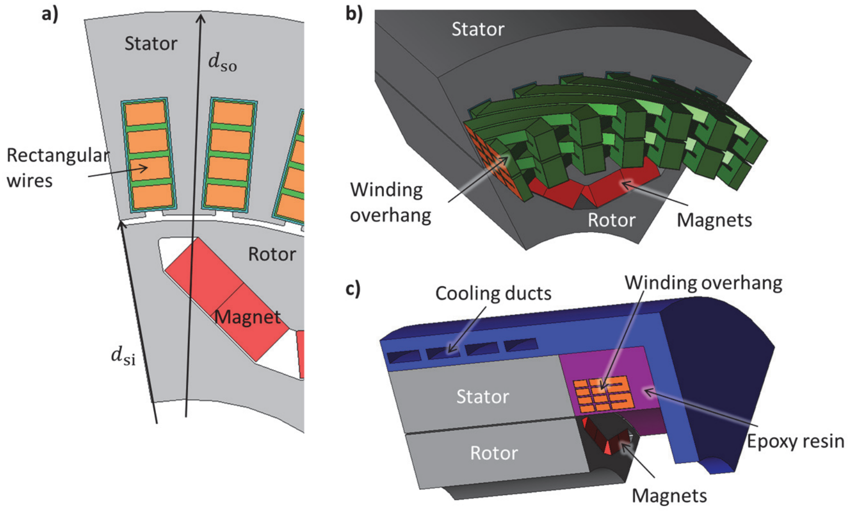

Fig. 7.4 Geometry model in JMAG of the electric machine with hairpin winding: a) Cross section as 2D Finite Element Method (FEM) model for electromagnetic calculation, b) 3D model of hairpin winding overhang, c) one twelfth of machine as 3D model with winding overhang, stator and rotor iron stack, stator housing and end shield for thermal calculation

yields an increased maximum calculated winding overhang temperature of 177 °C (< 180 °C, Thermal Class H, IEC 60034) for the previously defined drive cycle with consecutive OP2 and OP1 operation, as explained in Chapter 7.1.

Finally, this redesigned electric motor with hairpin winding is compared with the redesigned motor with round wire winding from Chapter 7.1 and with the original machine of Chapter 2 in Table 7.4. Both the redesigned electric motors with round wire winding and with hairpin winding allow a reduction of the magnet mass m_{M} by 44 %, leading to a corresponding cost reduction. The active volume V_{act} can be reduced by 32 % for the machine with hairpin winding. Based on the smaller volume, the reduction of active mass is also higher for the machine with hairpin winding, which offers an active mass reduction by 27.5 %. The redesigned electric machine with hairpin winding shows 38 % higher maximum power density, with a maximum power of 48 kW.

Table 7.5 shows the comparison of the calculated results for the original machine of Chapter 2 and the both redesigned electric machine with round wire winding from Chapter 7.1 and with hairpin winding. Due to the reduced volume for the same required rated power of both redesigned machines, the calculated average winding temperature at thermal steady-state of rated operation (OP2) for both redesigned machines are $\vartheta_{\mathrm{cu}} = 120$ °C with consideration of the average coolant temperature of $\vartheta_{\mathrm{coolant}} = 65$ °C. At rated operation (OP2), the redesigned machine with hairpin winding needs a 30 % higher RMS electric current per phase to produce rated torque $M_{\mathrm{N}} = 55$ Nm. However, the smaller stator resistance and the smaller iron losses, due to the reduced active iron volume, allow this machine to have only a slightly lower efficiency at OP2 than the original motor. However, at overload operation (OP1), 43 % higher RMS electric current per phase is needed for the redesigned machine with hairpin winding to produce maximum power, due to high iron saturation. Therefore, the machine has low efficiency of 90.5 %. At maximum speed (OP3), the hairpin winding produces high additional ohmic losses, due to the current displacement effect in the wire. However, the redesigned machine with hairpin winding needs less negative d-current to suppress high induced voltage, due to the reduced flux linkage from the reduced size of the machine.

Table 7.4 Comparison of the prototype electric machine for the DE-REX powertrain (chapter 2), the redesigned machine with round wire lap winding (chapter 7.1) and with hairpin wave winding (chapter 7.2) (d_{so}: stator outer diameter, d_{si}: stator inner diameter, l_{Fe}: active iron length, ϑ_{H}: highest temperature in the winding, $R_{\mathrm{s20,DC}}$: DC stator resistance at 20 °C, V : active volume, m_{act} : active mass, m_{M} : magnet mass, p_{max}: maximum power density)

	Prototype electric machine	**Redesigned electric machine**	
		with round wire winding	**with hairpin winding**
d_{so}	150 mm	142 mm	133.6 mm
d_{si}	92.8 mm	85 mm	85 mm
l_{Fe}	140 mm	120 mm	120 mm
ϑ_{H}	136.2 °C	181.3 °C	176.8 °C
C	5.41 kVA·min/m^3	7.35 kVA·min/m^3	7.62 kVA·min/m^3
$A \cdot J$	4345 A/cm·A/mm^2	7088 A/cm·A/mm^2	7760 A/cm·A/mm^2
Winding	2 x ∅ 0.67 mm 2 x ∅ 0.8 mm	2 x ∅ 0.6 mm 2 x ∅ 0.75 mm	h_{TL} = 2.8 mm b_{TL} = 4.0 mm
$R_{\mathrm{s,20,DC}}$	19.6 mΩ	24.2 mΩ (+23 %)	15.7 mΩ (-20 %)
N_{s} / N_{c}	24 / 12	28 / 14	24 / 2
a	6	6	1
V	2474 cm^3	1900 cm^3 (−23 %)	1682 cm^3 (−32 %)
m_{act}	16.0 kg	12.6 kg (−21 %)	11.6 kg (−27.5 %)
m_{M}	1.06 kg	0.59 kg (−44 %)	0.59 kg (−44 %)
p_{max}	3.00 kW/kg	3.81 kW/kg (+27 %)	4.14 kW/kg (+38 %)

Therefore, even considering of high ohmic loss increase factor $k_\mathrm{R} = 1.223$, the redesigned machine with hairpin winding produces less ohmic losses. With lower iron losses from the reduced stator volume, the redesigned machine with hairpin winding shows high efficiency of 95.5 % at OP3.

Table 7.5 Calculated comparison of the prototype electric machine for the DE-REX powertrain (chapter 2), the redesigned machine with round wire lap winding (chapter 7.1) and with hairpin wave winding (chapter 7.2) (ϑ_cu: winding temperature at thermal steady-state for OP2 with $\vartheta_\mathrm{coolant} = 65$ °C, $R_\mathrm{s,DC}(\vartheta_\mathrm{cu})$: DC stator resistance at ϑ_cu, k_R: ohmic loss increase factor due to current displacement with stator fundamental frequency, $P_\mathrm{d,cu,AC}$: ohmic losses with AC resistance, $P_\mathrm{d,Fe}$: iron losses, calculated with k_v=1.5, η: motor efficiency)

		Prototype electric machine	**Redesigned electric machine**	
			with round wire winding	**with hairpin winding**
ϑ_cu		100 °C	120 °C	120 °C
$R_\mathrm{s,DC}(\vartheta_\mathrm{cu})$		25.7 mΩ	33.7 mΩ (+31 %)	21.8 mΩ (-15 %)
OP2	k_R	1.010	1.008	1.039
	I_s	95 A	99 A (+4 %)	123.8 A (+30 %)
	$P_\mathrm{d,cu,AC}$	704 W	1005 W (+43 %)	1042 W (+48 %)
	$P_\mathrm{d,Fe}$	352 W	317 W (-10 %)	215 W (-39 %)
	η	95.8 %	94.8 %	95.0 %
OP1	k_R	1.010	1.008	1.039
	I_s	184 A	207 A (+13 %)	263 A (+43 %)
	$P_\mathrm{d,cu,AC}$	2635 W	4360 W (+65 %)	4691 W (+78 %)
	$P_\mathrm{d,Fe}$	455 W	424 W (-7 %)	319 W (-30 %)
	η	93.9 %	90.8 %	90.5 %
OP3	k_R	1.058	1.048	1.223
	I_s	138 A	145 A (+5 %)	137 (-1 %)
	$P_\mathrm{d,cu,AC}$	1548 W	2244 W (+45 %)	1508 W (-3 %)
	$P_\mathrm{d,Fe}$	1148 W	1193 W (+4 %)	729 W (-36 %)
	η	94.6 %	93.2 %	95.5 %

8. Summary and conclusions

The ‘twin-drive transmission with a range extender (DE-REX)’ is an innovative powertrain concept for electric and hybrid vehicles. Due to the lack of space in the engine compartment, the powertrain needs electric machines with a high-power density. Thus, this thesis presents the design of an interior permanent magnet synchronous machine (IPMSM) with embedded rotor magnets in a V-shaped arrangement for the DE-REX powertrain.

The DE-REX powertrain concept, which consists of two electric machines, a two-speed transmission and an ICE as a range extender, is introduced. It is suitable for both pure electric-drive and hybrid-drive operation and can be operated in several operating modes in combination with the two-speed transmission. Roughly, the powertrain can be operated in any of five driving modes: two in pure electric drive and three in hybrid driving mode. In addition, at partial load, it is possible to achieve increased powertrain efficiency by operating only one electric machine, while the other machine is switched off. Due to this special layout of the powertrain, DE-REX offers potential for increased driving range and reduced energy consumption. In comparison with a conventional powertrain concept, which has only one central electric machine with a single fixed gear ratio, the DE-REX powertrain could save about 16 % of energy consumption in the NEDC and about 14 % in the WLTC.

To achieve high power density in an electric machine, an IPMSM with a buried V-shaped rotor magnet arrangement was designed which can produce additional reluctance torque from rotor saliency. Using this rotor saliency properly required special control strategies, MTPA and MTPV, which are discussed in the thesis. In addition, two methods to reduce cogging torque and torque ripple in the electric machine are presented: adopting a 5-step-skewed rotor and using a fractional number of stator slots per pole and phase. By using a 5-step-skewed rotor, the designed electric machine almost eliminated the cogging torque (a 99 % reduction), and it reduced the torque ripple at rated load by 82 %. In comparison, through use of a fractional number of stator slots per pole and phase $q_s=1.5$, the machine diminished cogging torque and torque ripple by 72 % and 75 %, respectively.

To verify the electric machine’s magnet stability, when subject to a three-phase sudden short circuit, the thesis presents an analytical method of calculating the sudden short circuit current and torque at both no-load and load condition. Results of these calculations compared favourably to FEM simulation results. Testing with a high magnet temperature of 150 °C confirmed that the prototype machine's rotor magnets were not irreversibly demagnetized even after several no-load sudden short circuit tests. Due to the compact size of the electric machine, it needs a water jacket cooling system. To estimate temperature rises in parts of the stator winding, a lumped parameter thermal network model was used. It was verified with 3D FEM simulation by JMAG software. Embedded magnets in the electric machine's rotor are fixed by the rotor laminations. Thus, the machine did not require any additional fixation method, such as a bandage. To verify the mechanical stability of the rotor iron bridges, mechanical stress on the bridges was calculated using both a rough analytical method and a more accurate 2D numerical method. These methods confirmed that the rotor configuration will not be deformed by high centrifugal force at 120 % of the maximum speed.

The chapter 'Loss components and efficiency calculation' presents all losses at the electric machine (ohmic losses, eddy current losses in the stator winding, iron losses, mechanical losses, additional eddy current losses in magnets) and losses in the inverter. These losses were calculated across the complete torque–speed range of the electric machine. Calculated losses distribution maps and efficiency maps of the electric machine were created. The electric machine had a maximum calculated efficiency of 96.3 % at 45 Nm and 6000 min^{-1}. With consideration of losses in the inverter, the maximum efficiency of the electric system was 94.5 %. Those efficiencies were calculated with a constant winding temperature of 100 °C and a constant magnet temperature of 100 °C.

In the subsequent chapter, all steps to construct a prototype electric machine and four further electric machines for use in the DE-REX powertrain (two for the powertrain Hardware in the Loop (HiL) test bench and two for the prototype vehicle) are described. In addition, the test bench for the individual measurement of the prototype machine and the measurement devices are presented.

In the chapter 'Measurement of the prototype electric machine', all measurement results are presented. Basic measurements and generator no-load and short-circuit tests were performed to validate the electromagnetic design of the prototype machine. Furthermore, measurements of the operating points OP1, OP2 and OP3 were performed. The measured results are discussed in the chapter. In addition, measured efficiency maps of the prototype machine, the inverter, and the electric system, which includes both electric machine and corresponding inverter, were created over the entire torque–speed range. The measured maximum efficiency of the prototype machine was 96.3 % at

6000 min^{-1} and 40 Nm, which is nearly same result, as given by the calculated efficiency. The measured temperature with the given thermal condition showed that the machine has a large thermal reserve for the used Thermal Class H insulation material. Thus, the prototype machine could produce higher power to avoid this high thermal reserve and to increase the thermal utilization of the machine. Thus, the temperature increase was measured with a new increased continuous power of 33 kW and a new increased maximum power of 65 kW for 30 s. As a result, the temperature of the winding overhang on the NDE side reached 175.6 °C with consideration of the maximum coolant temperature 65 °C. The prototype machine had still a small temperature reserve of 4.4 K for the used Thermal Class H insulation material. Additionally, the functionality of the DE-REX powertrain was tested at the individual electric machine test bench. Before measurements were done, demanded torque and speed profiles for both electric machines were calculated with a driving simulation model. The measurements were carried out with the NEDC and the WLTC. Due to the more dynamic driving performance in the WLTC, the powertrain consumed about 20 % more energy to drive during the WLTC (15.52 kWh/100 km) than the measured energy consumption during the NEDC (12.85 kWh/100 km).

In order to investigate functionalities and energy flows of the DE-REX powertrain, driving simulation models were designed and are presented in the chapter 'Vehicle simulation model'. Due to special features of the powertrain, which has two electric machines, the vehicle is able to choose, which electric machine should be used to drive. Two possible operation strategies are presented: with and without consideration of the electric machines' winding temperatures to determine the driving mode for energy-optimal driving. Both driving strategies were verified with the driving simulation models in three driving cycles: the NEDC, the WLTC, and the HYZEM-highway cycle. Results showed that by taking the winding temperatures of both electric machines into account in selecting the operating mode, both electric machines were uniformly utilized in all three driving simulations. Hence the thermal burden on the first electric machine was reduced. Due to the lower winding temperature of both electric machines, a larger thermal reserve was available for driving with demanded high power, such as overtaking at high speed. Further an unwanted thermal derating, when reaching the thermal limit of the electric machines, could be avoided.

Given the large thermal reserve of the prototype electric machine, two possible methods for downsizing the machine are presented in the chapter 'Downsizing possibilities for the prototype machine'. Minimizing the thermal reserve leads to an increased electromagnetic utilization C and thermal utilization $A \cdot J$ by reducing the active size of the electric machine. A further increase of power density was achieved with a higher slot fill factor by adopting a hairpin winding instead of a round wire winding. The redesigned electric machine with round wire winding reduced the active mass by 21 % and the active volume by 23 %. A redesigned machine using a hairpin winding had its active mass reduced by 27.5 % and its magnet mass reduced by 44 %, corresponding to a reduction of its active volume by 32%. Obviously, the increased electromagnetic utilization and thermal utilization led to a higher loss density. Thus, the redesigned machines showed a slightly lower motor efficiency for the rated operation compared to the prototype machine.

Appendix A. Drawings of electric machine components

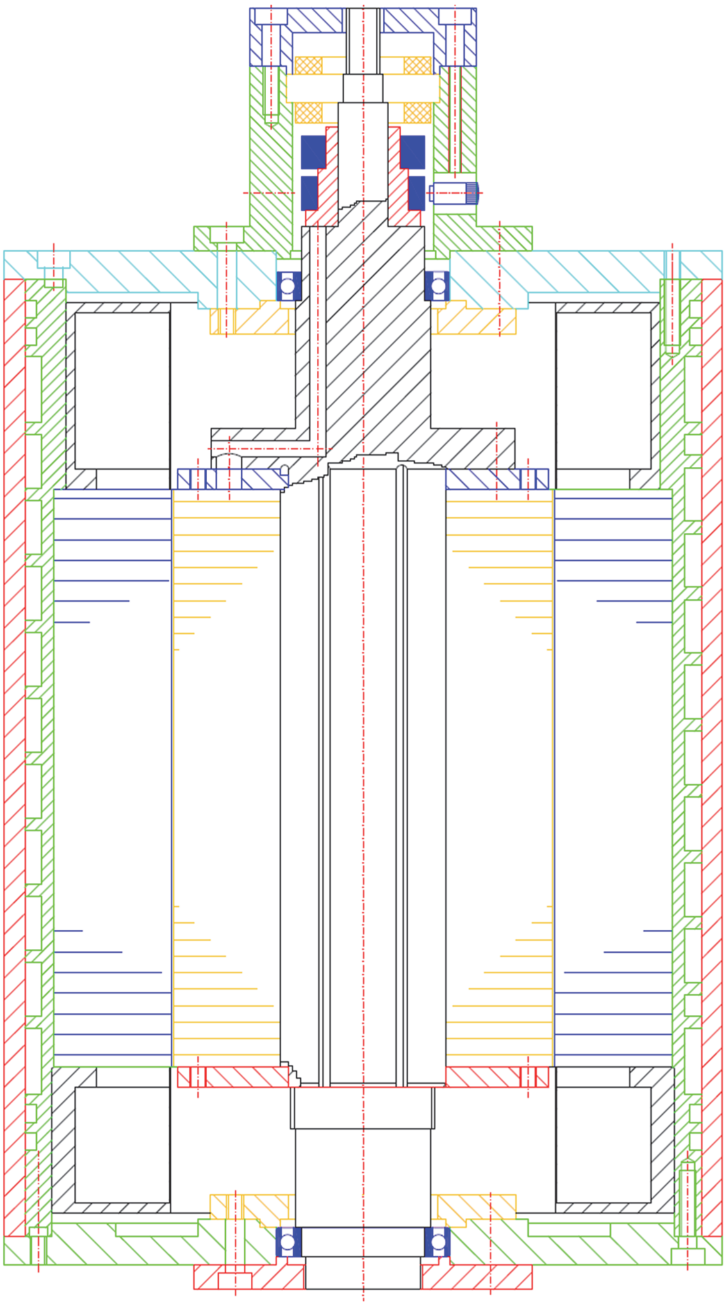

Fig. A.1 Assembly drawing of the prototype machine

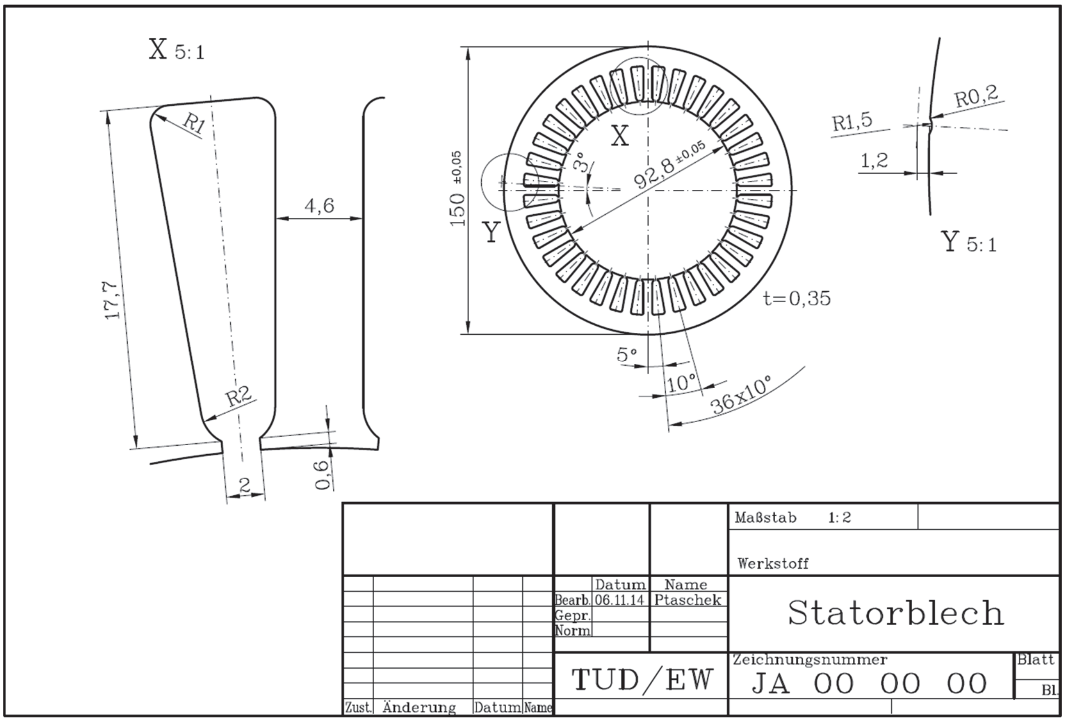

Fig. A.2 Drawing of the stator iron sheet

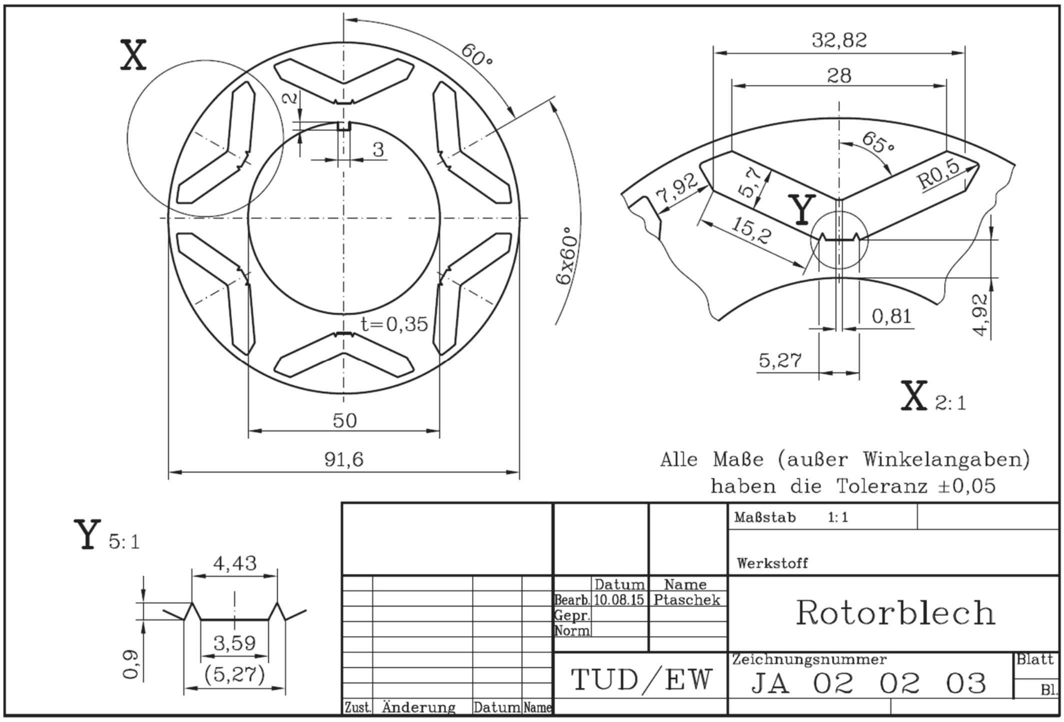

Fig. A.3 Drawing of the rotor iron sheet

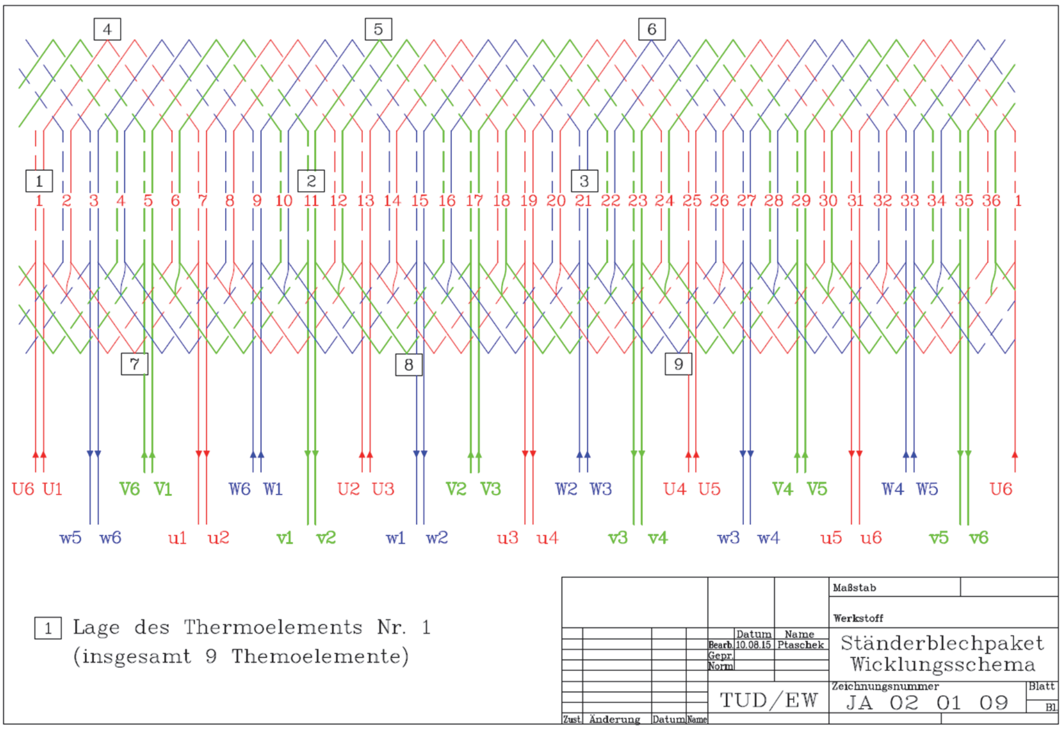

Fig. A.4 Stator winding diagram

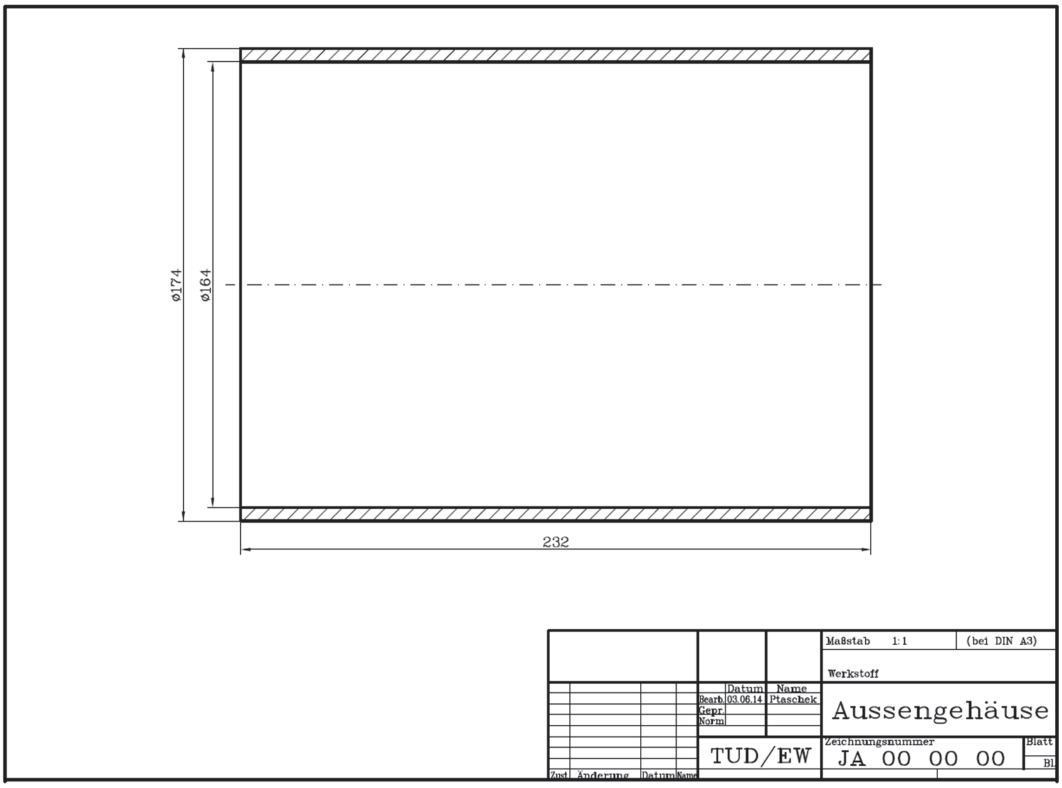

Fig. A.5 Drawing of housing outer component for the prototype machine

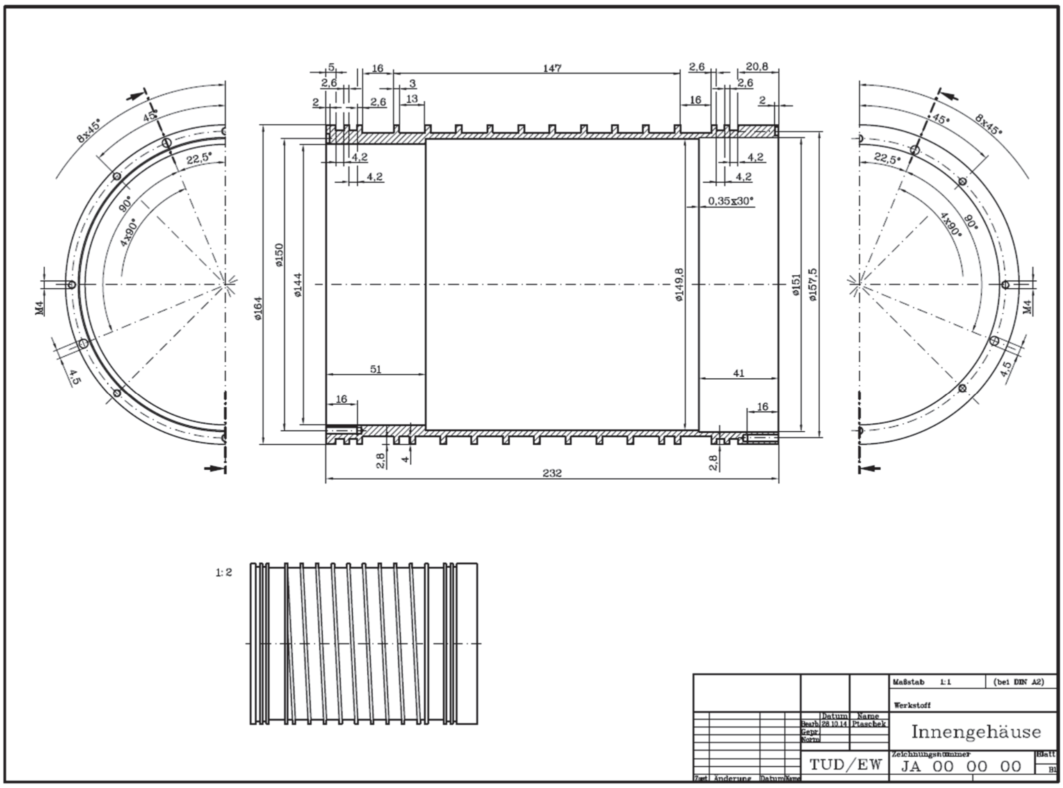

Fig. A.6 Drawing of housing inner component for the prototype machine

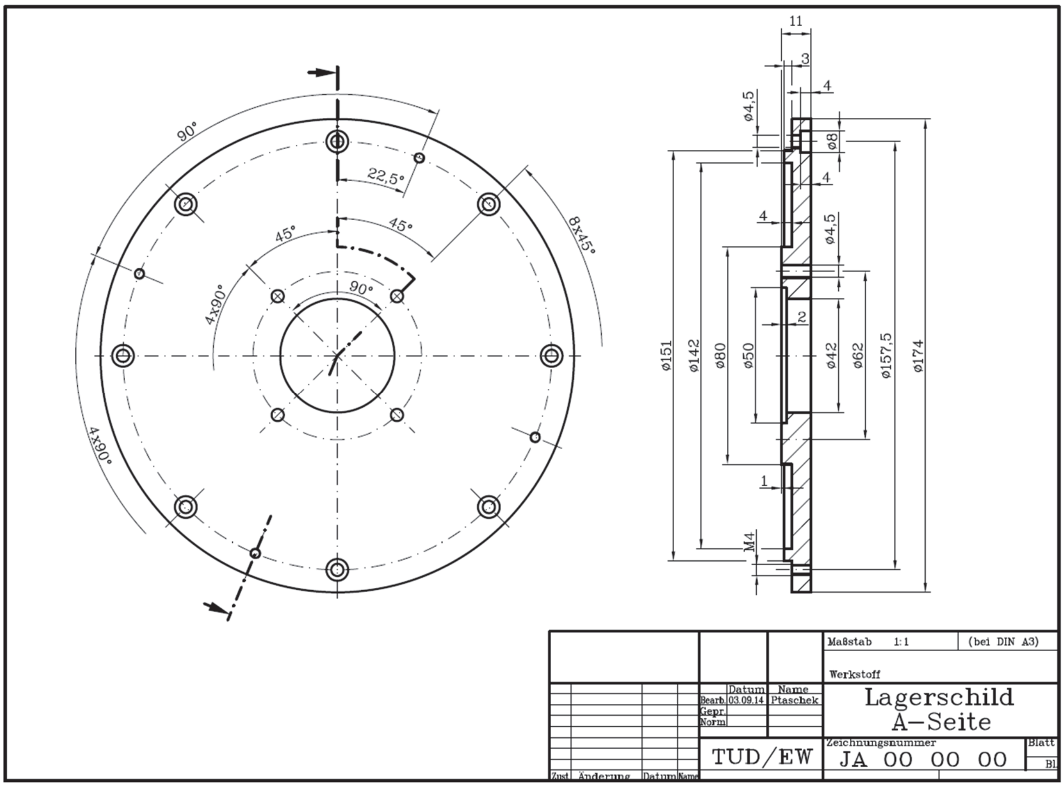

Fig. A.7 Drawing of the end shield DE-side for the prototype machine

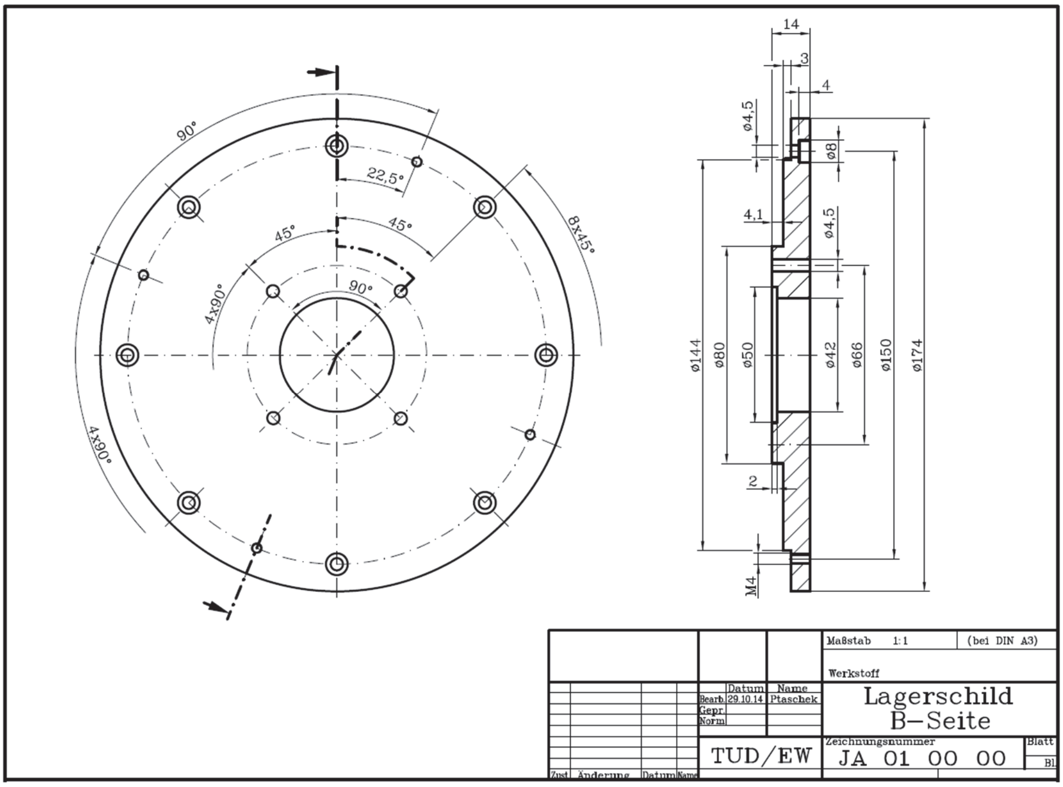

Fig. A.8 Drawing of end shield NDE-side for the prototype machine

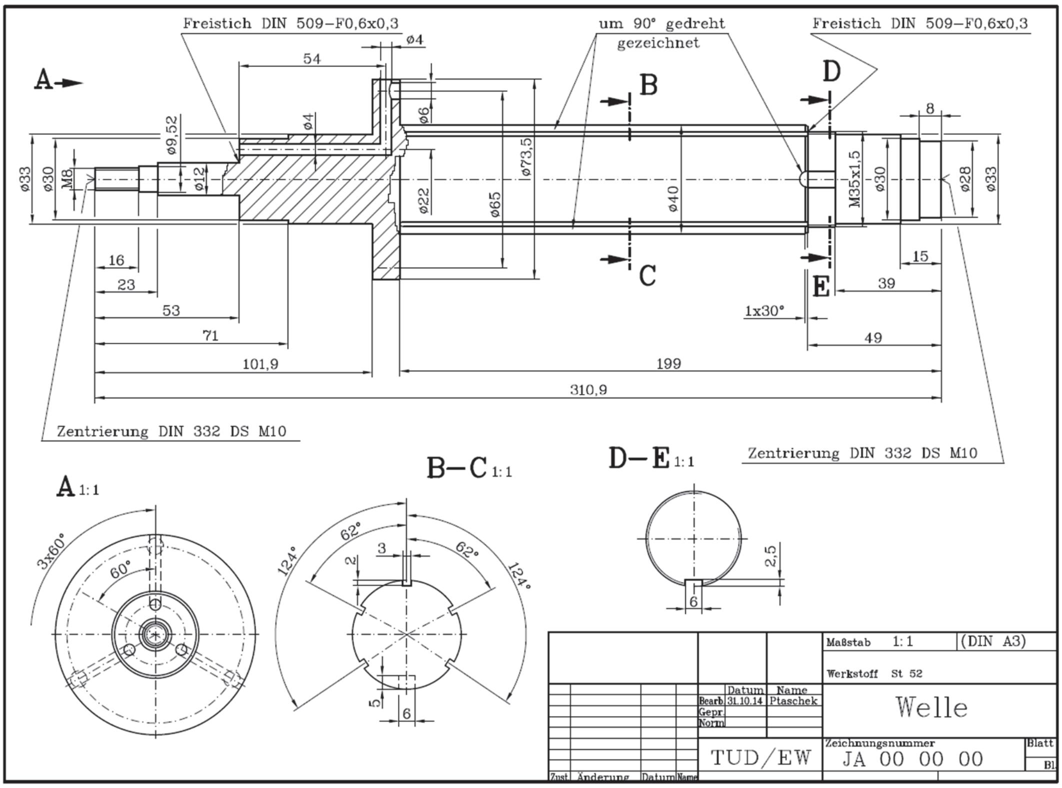

Fig. A.9 Drawing of rotor shaft for the prototype machine

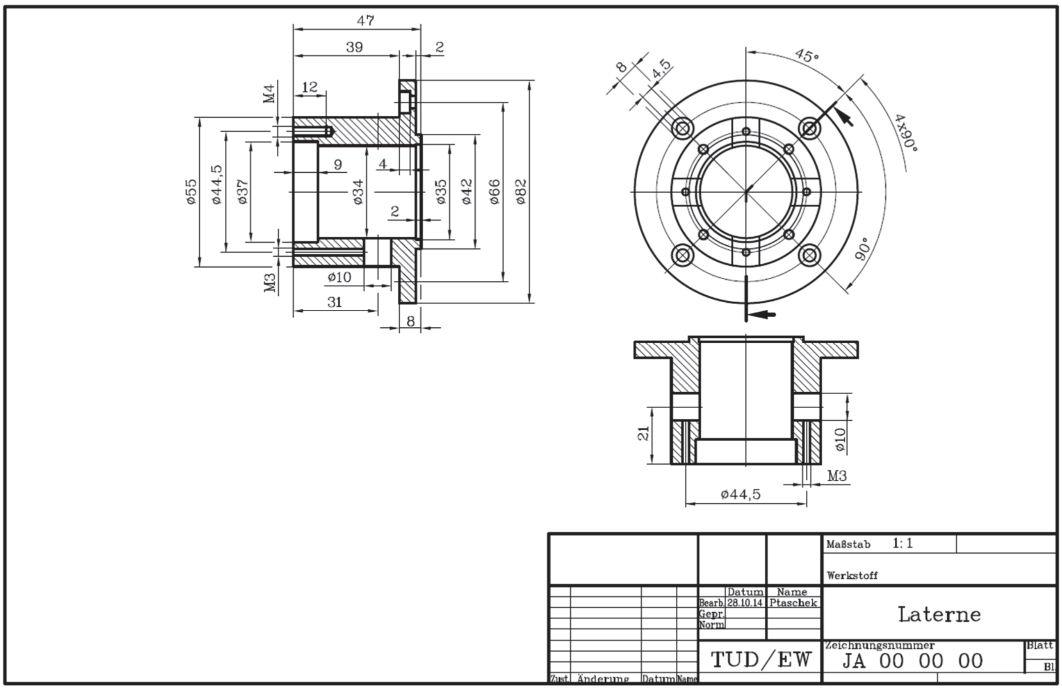

Fig. A.10 Drawing of brush holder for the prototype machine

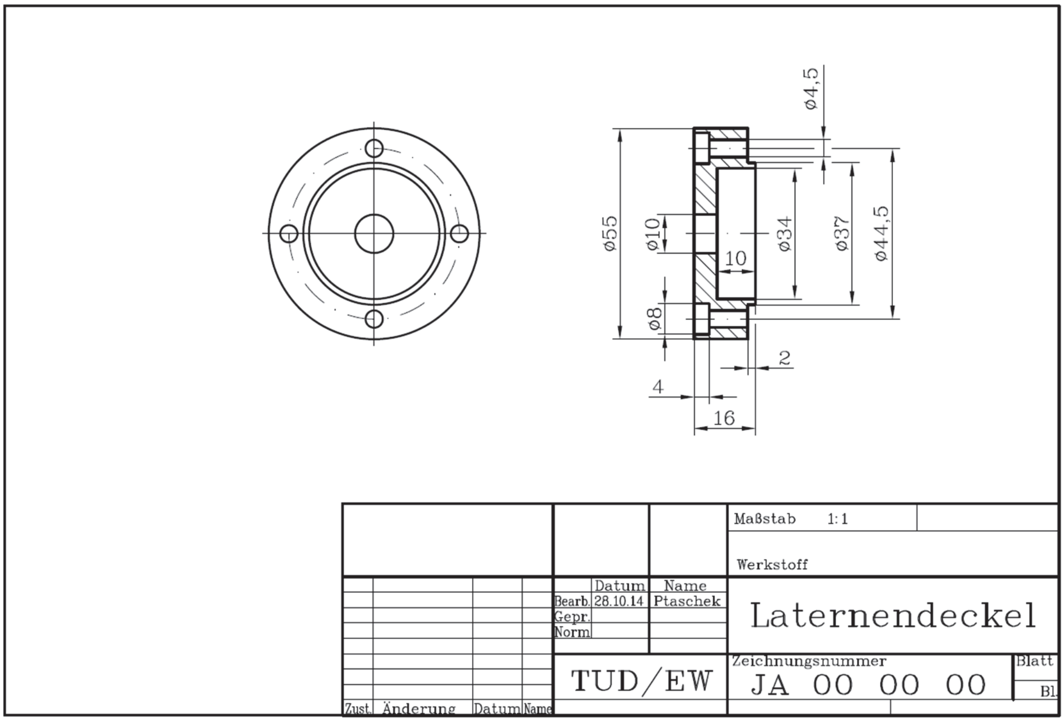

Fig. A.11 Drawing of brush holder cover for the prototype machine

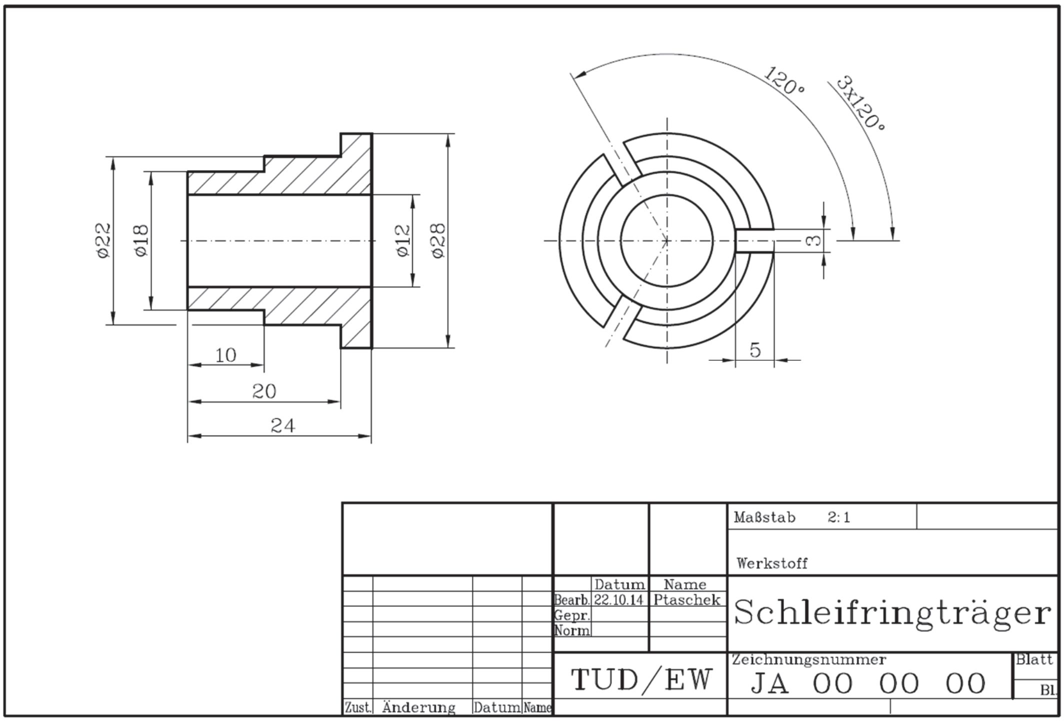

Fig. A.12 Drawing of slip ring body for the prototype machine

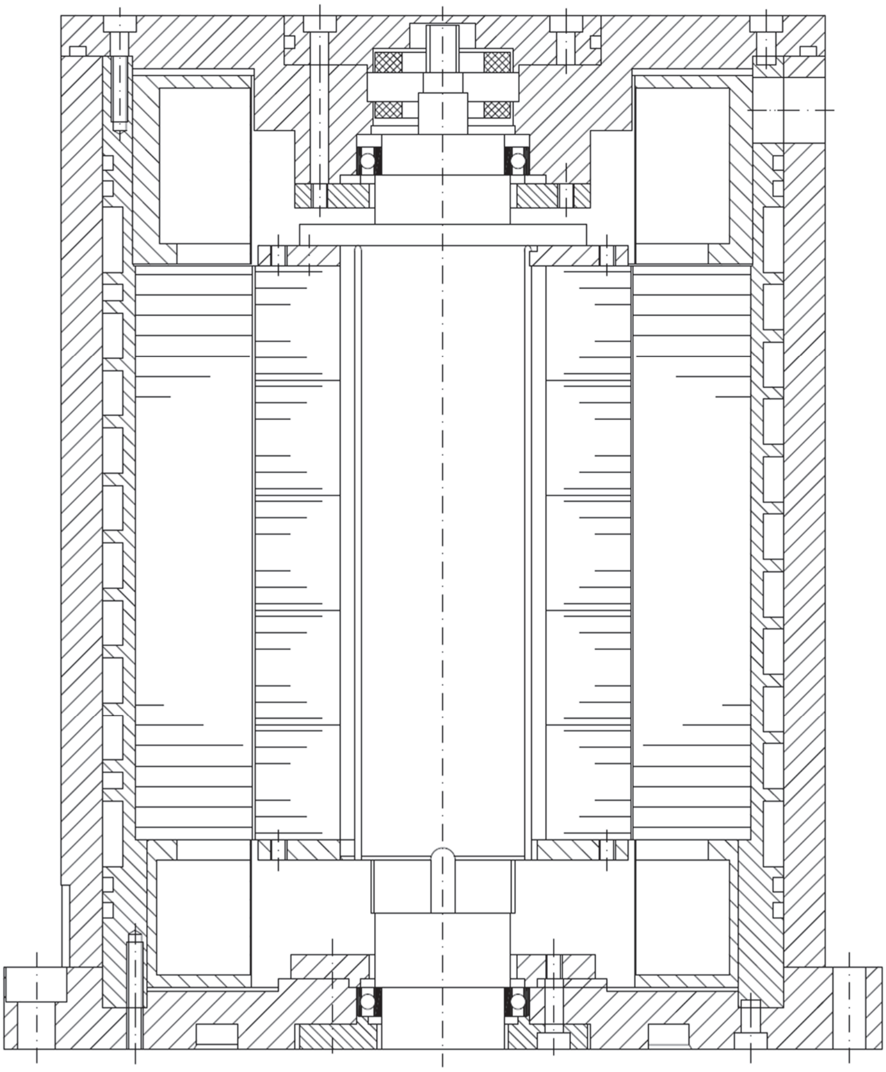

Fig. A.13 Assembly drawing of the electric machine for the DE-REX powertrain (EM1, EM2, EM3, EM4)

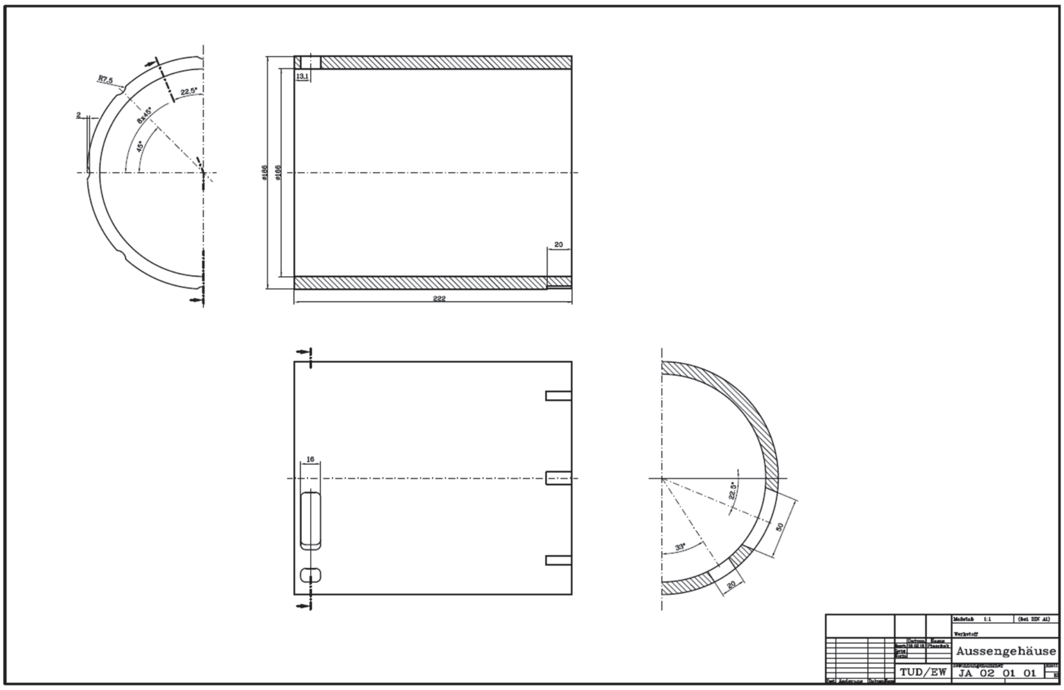

Fig. A.14 Drawing of housing outer component of the electric machine for the DE-REX powertrain (EM1, EM2, EM3, EM4)

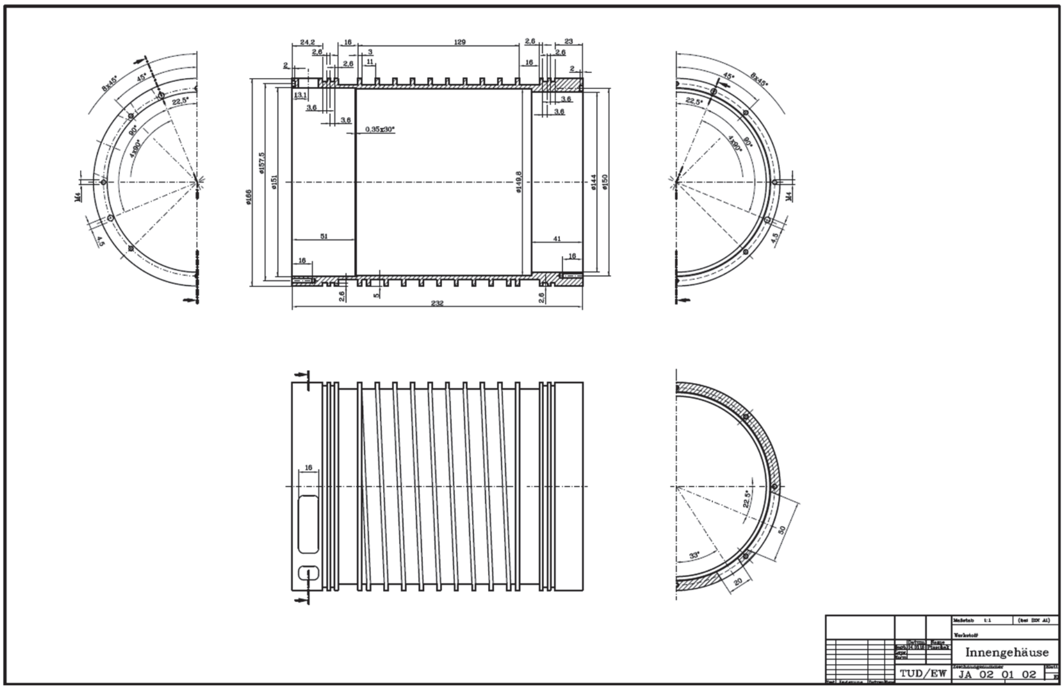

Fig. A.15 Drawing of housing inner component of the electric machine for the DE-REX powertrain (EM1, EM2, EM3, EM4)

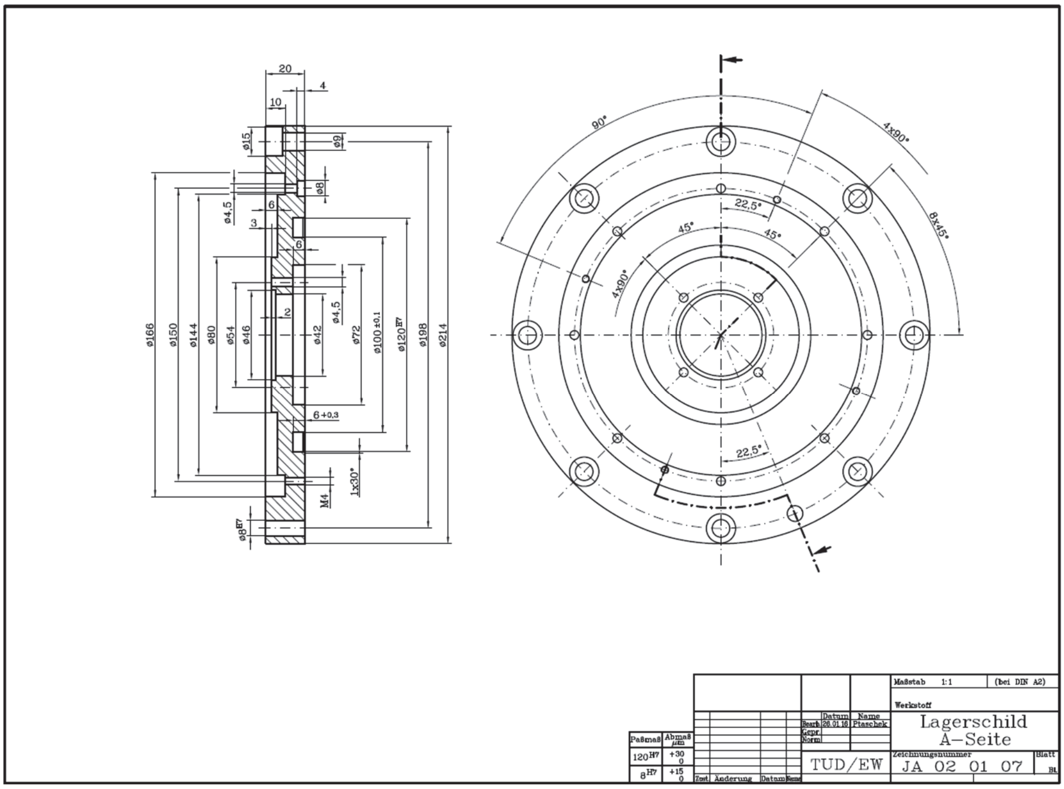

Fig. A.16 Drawing of end shield DE-side of the electric machine for the DE-REX powertrain (EM1, EM2, EM3, EM4)

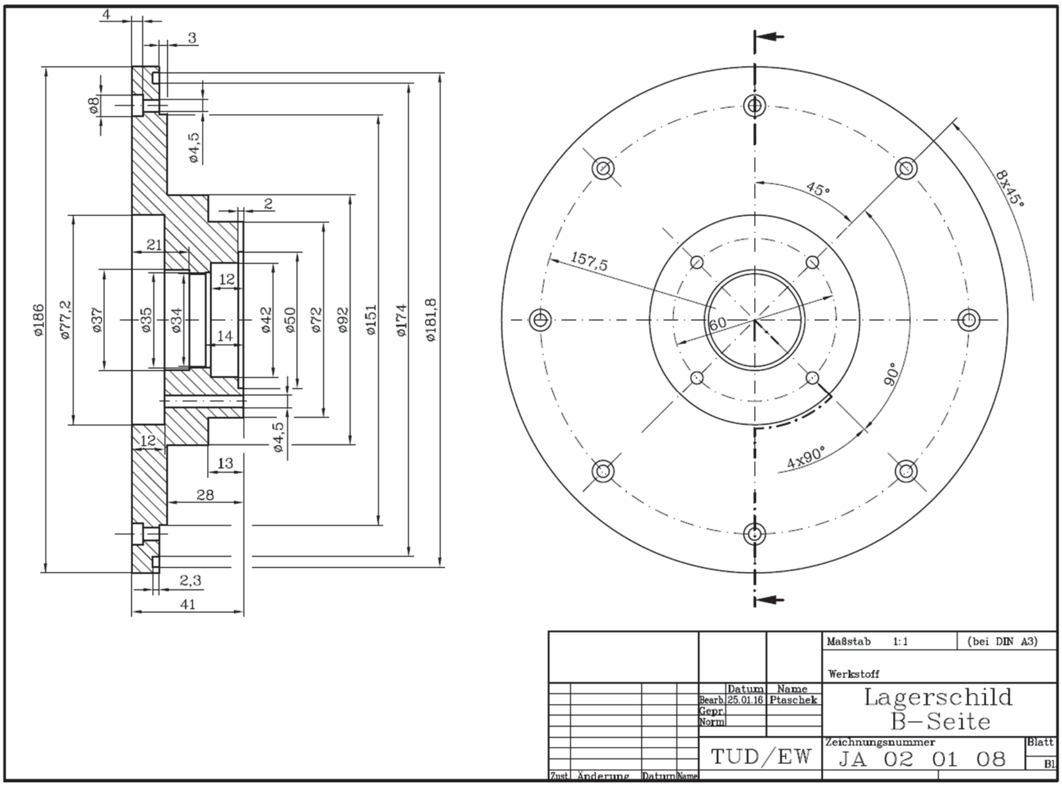

Fig. A.17 Drawing of end shield NDE-side of the electric machine for the DE-REX powertrain (EM1, EM2, EM3, EM4)

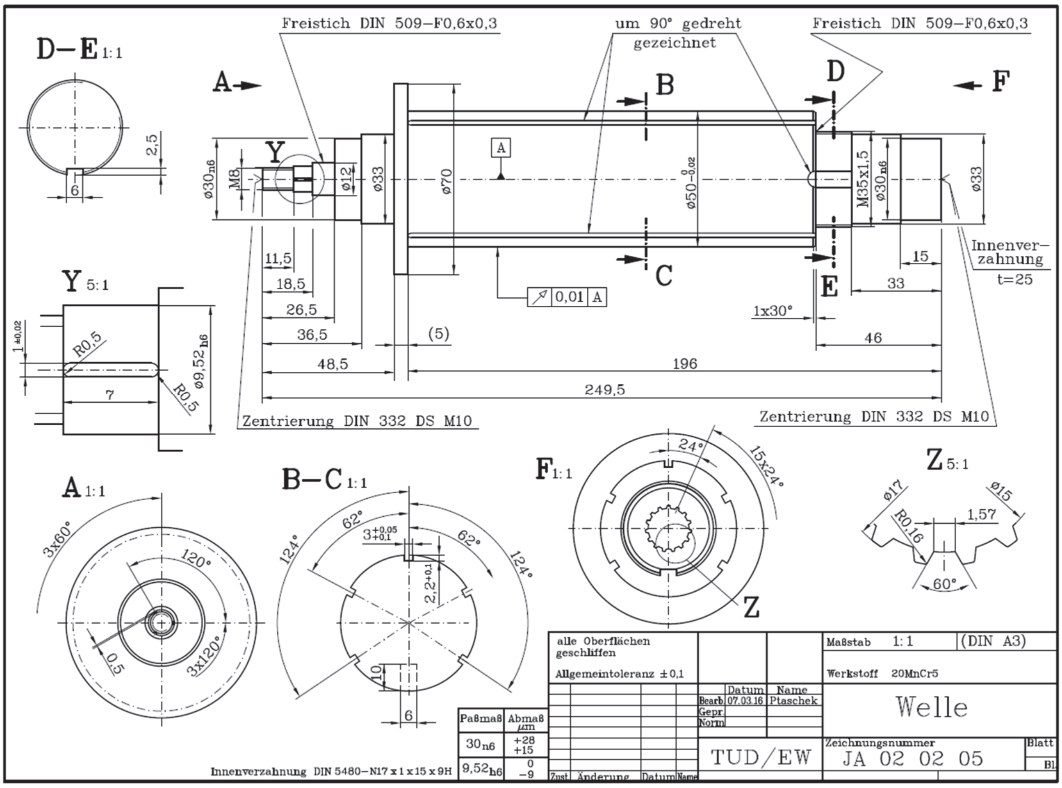

Fig. A.18 Drawing of rotor shaft of the electric machine for the DE-REX powertrain (EM1, EM2, EM3, EM4)

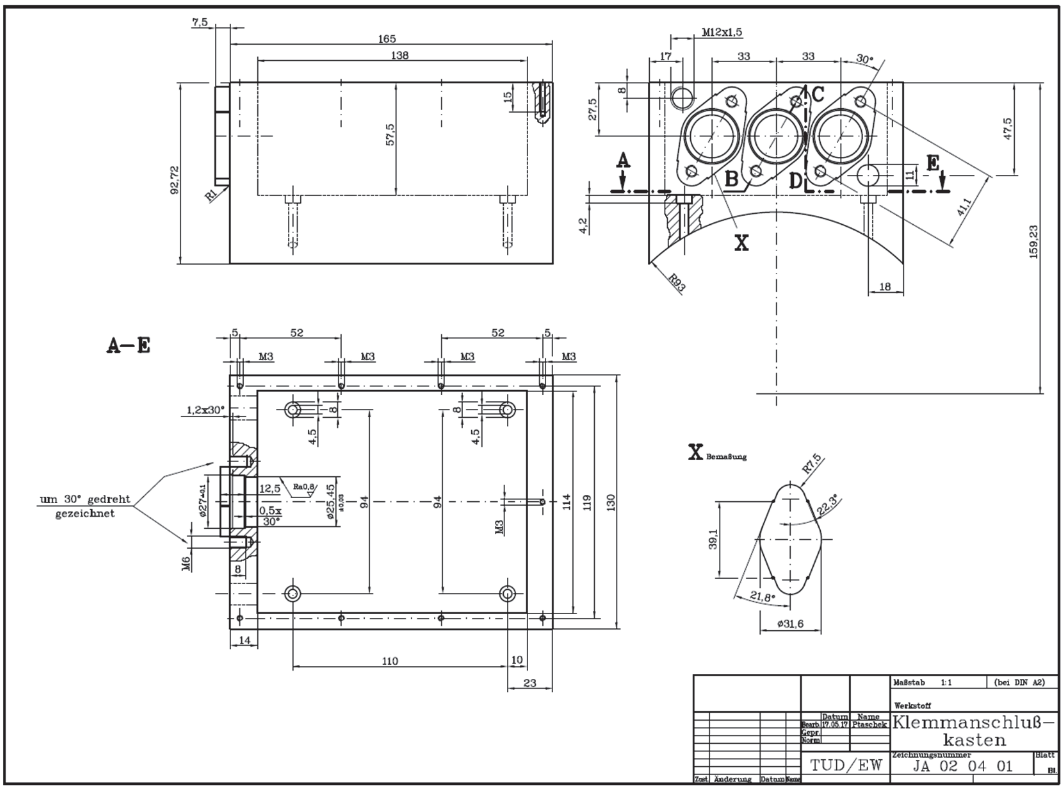

Fig. A.19 Drawing of terminal box of the electric machine for the DE-REX powertrain (EM1, EM2, EM3, EM4)

Appendix B. Material properties

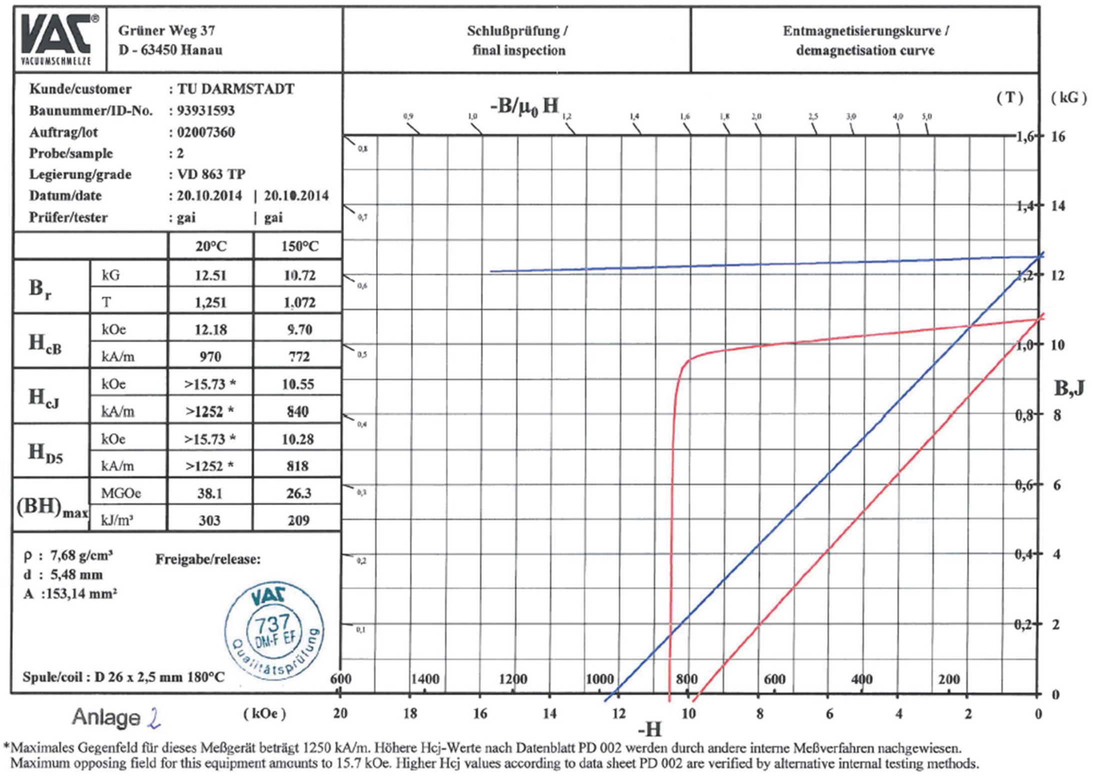

Grüner Weg 37
D - 63450 Hanau

Schlußprüfung /
final inspection

Entmagnetisierungskurve /
demagnetisation curve

Kunde/customer : TU DARMSTADT
Baunummer/ID-No. : 93931593
Auftrag/lot : 02007360
Probe/sample : 2
Legierung/grade : VD 863 TP
Datum/date : 20.10.2014 | 20.10.2014
Prüfer/tester : gai | gai

		20°C	150°C
B_r	kG	12.51	10.72
	T	1,251	1,072
H_{cB}	kOe	12.18	9.70
	kA/m	970	772
H_{cJ}	kOe	>15.73 *	10.55
	kA/m	>1252 *	840
H_{D5}	kOe	>15.73 *	10.28
	kA/m	>1252 *	818
$(BH)_{max}$	MGOe	38.1	26.3
	kJ/m³	303	209

ρ : 7,68 g/cm³
d : 5,48 mm
A :153,14 mm²

Freigabe/release:

VAC 737 DM-F EF Qualitätsprüfung

Spule/coil : D 26 x 2,5 mm 180°C

Anlage 2

*Maximales Gegenfeld für dieses Meßgerät beträgt 1250 kA/m. Höhere Hcj-Werte nach Datenblatt PD 002 werden durch andere interne Meßverfahren nachgewiesen.
Maximum opposing field for this equipment amounts to 15.7 kOe. Higher Hcj values according to data sheet PD 002 are verified by alternative internal testing methods.

Fig. B.1 Measured demagnetisation curve of permanent magnet material of type VACODYM 863 TP from company *VACUUMSCHMELZE* GmbH, Hanau, Germany

Table B.1 Magnetic properties of VACODYM 863 TP by magnet temperature 20 °C

Parameter	**Symbol**	**Unit**	**Value**
Remanence flux density	B_{R}	T	1.251
Coercive field strength	H_{cB}	kA/m	970
Relative magnetic permeability	μ_{M}	-	1.026
Electrical conductivity	κ_{M}	S/m	754072
Mass density	ρ_{M}	kg/m³	7680

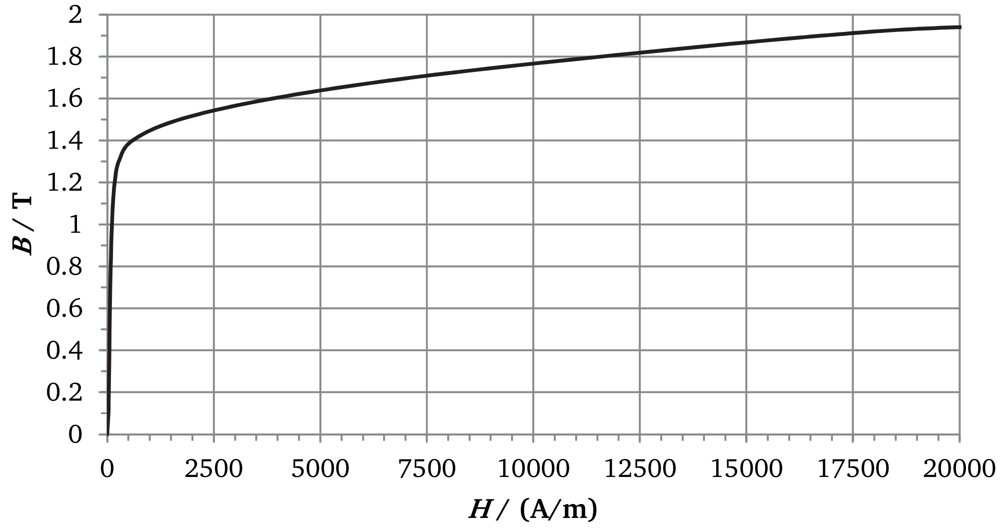

Fig. B.2 Magnetization curve $B(H)$ of iron sheet M270-35A [68]

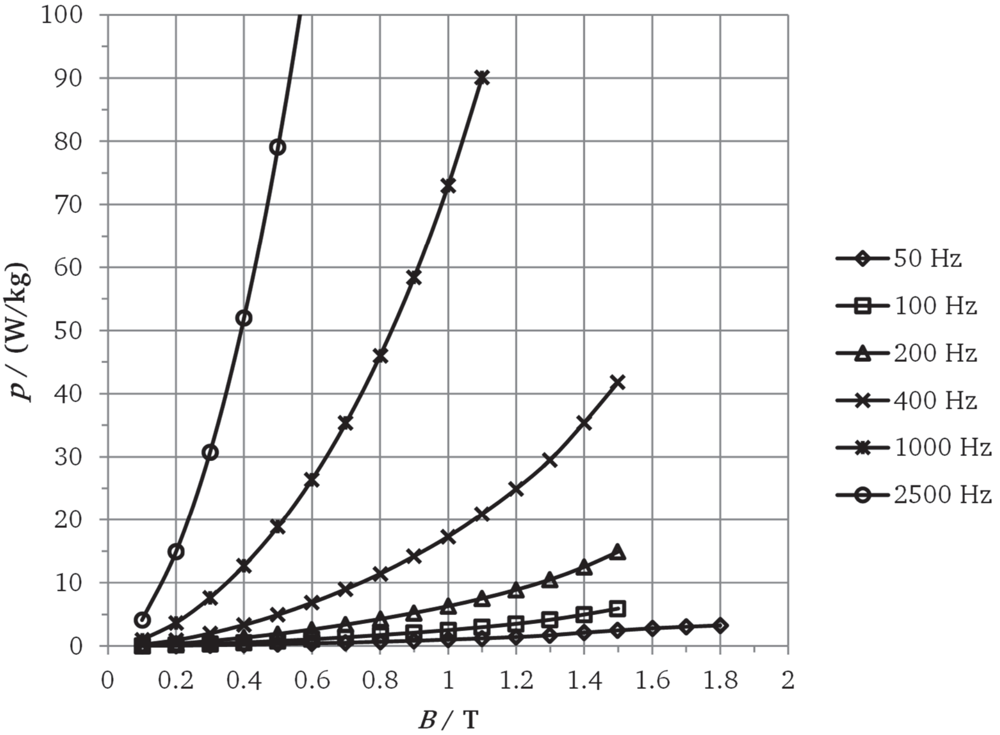

Fig. B.3 Iron loss density curve of iron sheet M270-35A [68]

Appendix C. Thermal network model

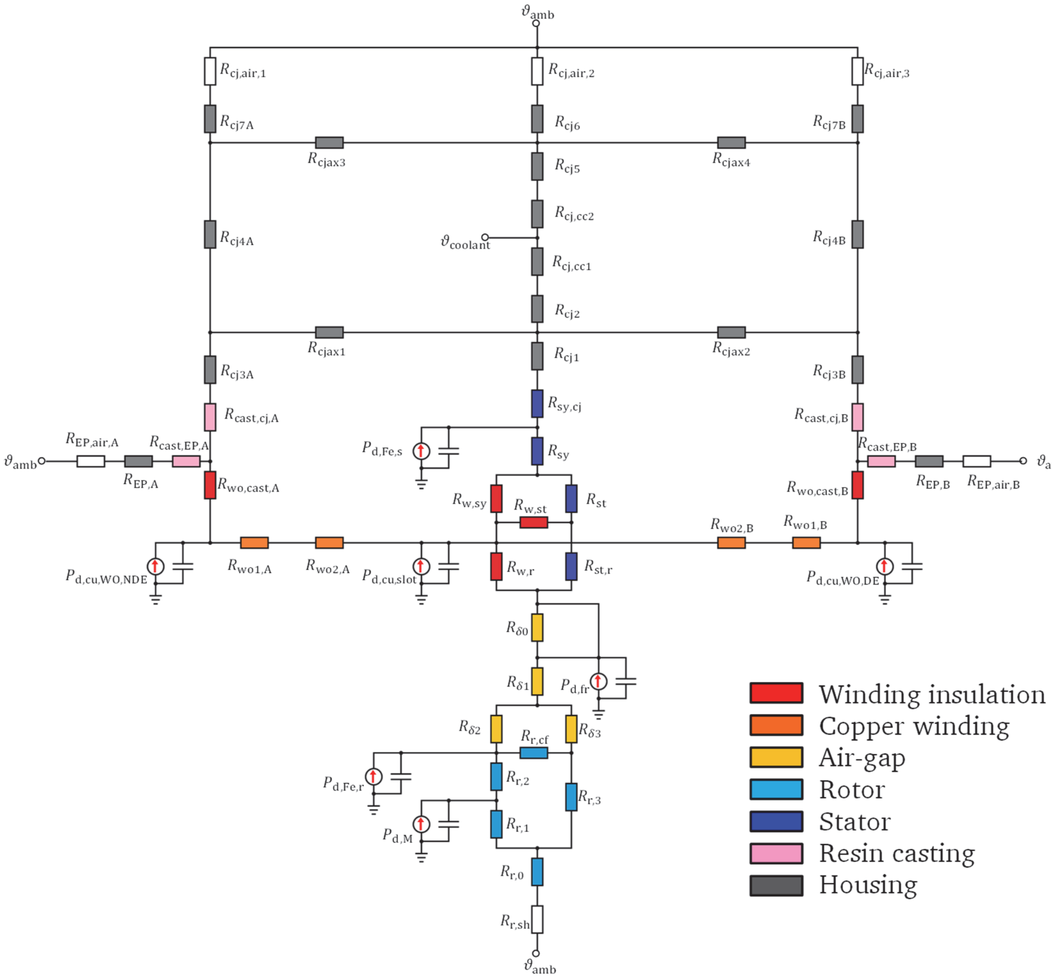

Fig. C.1 Thermal network model of the electric machine for the DE-REX powertrain

Thermal resistances in the stator	
$R_{\mathrm{st}} = \frac{h_{\mathrm{Qs}}/2}{A_{\mathrm{st}} \cdot \lambda_{\mathrm{Fe}} \cdot Q_{\mathrm{s}}} = 0.0153\ \mathrm{K/W}$	The stator teeth
$R_{\mathrm{sy}} = \frac{\ln\left(d_{\mathrm{so}}/\left(d_{\mathrm{so}}-2h_{\mathrm{sy}}\right)\right)}{2\pi \cdot l_{\mathrm{Fe}} \cdot \lambda_{\mathrm{Fe}}} = 0.0067\ \mathrm{K/W}$	The stator yoke
$R_{\mathrm{sy,cj}} = \frac{1}{\alpha_{\mathrm{sp1}} \cdot A_{\mathrm{sy,cj}}} = 0.0022\ \mathrm{K/W}$	Between the stator yoke and the housing
Thermal resistances in the copper winding	
$R_{\mathrm{wo1,A,B}} = \frac{l_{\mathrm{b}}/2}{A_{\mathrm{cu}} \cdot \lambda_{\mathrm{cu}} \cdot Q_{\mathrm{s}}} = 0.0906\ \mathrm{K/W}$	Between the middle of stator winding overhang and the beginning of stator winding overhang
$R_{\mathrm{wo2,A,B}} = \frac{l_{\mathrm{Fe}}/2}{A_{\mathrm{cu}} \cdot \lambda_{\mathrm{cu}} \cdot Q_{\mathrm{s}}} = 0.1200\ \mathrm{K/W}$	Between the middle of stator winding in the stator iron stack and the beginning of stator winding overhang
Thermal resistances in the winding insulation	
$R_{\mathrm{w,st}} = \frac{\mathrm{b_{SF}} \cdot \ln(x_{\mathrm{o1}}/x_{\mathrm{i1}})}{2\lambda_{\mathrm{SF}} \cdot l_{\mathrm{Fe}} \cdot (x_{\mathrm{o1}}-x_{\mathrm{i1}}) \cdot Q_{\mathrm{s}}} = 0.0204\ \mathrm{K/W}$	The winding insulation and the slot filling in tangential direction
$R_{\mathrm{w,r}} = R_{\mathrm{w,sy}} = \frac{\mathrm{b_{SF}} \cdot \ln(x_{\mathrm{o2}}/x_{\mathrm{i2}})}{\lambda_{\mathrm{SF}} \cdot l_{\mathrm{Fe}} \cdot (x_{\mathrm{o2}}-x_{\mathrm{i2}}) \cdot Q_{\mathrm{s}}} = 0.1795\ \mathrm{K/W}$	The winding insulation and the slot filling in radial direction
$R_{\mathrm{wo,cast,A,B}} = \frac{1}{(2/R_{\mathrm{SF,wo,t1}}+2/R_{\mathrm{SF,wo,r1}}) \cdot Q_{\mathrm{s}}} = 0.0235\ \mathrm{K/W}$	The winding insulation at the winding overhang
$R_{\mathrm{SF,wo,t1}} = \frac{b_{\mathrm{SF}} \cdot \ln(x_{\mathrm{o1}}/x_{\mathrm{i1}})}{l_{\mathrm{b}}/2 \cdot (x_{\mathrm{o1}}-x_{\mathrm{i1}}) \cdot \lambda_{\mathrm{Resin}}} = 2.0722\ \mathrm{K/W}$	The winding insulation at the winding overhang in tangential direction
$R_{\mathrm{SF,wo,r1}} = \frac{b_{\mathrm{SF}} \cdot \ln(x_{\mathrm{o2}}/x_{\mathrm{i2}})}{l_{\mathrm{b}}/2 \cdot (x_{\mathrm{o2}}-x_{\mathrm{i2}}) \cdot \lambda_{\mathrm{Resin}}} = 9.1197\ \mathrm{K/W}$	The winding insulation at the winding overhang in radial direction
Thermal resistances in the resin casting	
$R_{\mathrm{cast,cj,A}} = \frac{\ln(d_{\mathrm{so}}/d_{\mathrm{woA}})}{2\pi \cdot l_{\mathrm{woA}} \cdot \lambda_{\mathrm{cast}}} = 0.3535\ \mathrm{K/W}$	The resin casting at DE side in radial direction
$R_{\mathrm{cast,cj,B}} = \frac{\ln(d_{\mathrm{so}}/d_{\mathrm{woB}})}{2\pi \cdot l_{\mathrm{woB}} \cdot \lambda_{\mathrm{cast}}} = 0.3086\ \mathrm{K/W}$	The resin casting at NDE side in radial direction
$R_{\mathrm{cast,EP,A,B}} = \frac{l_{\mathrm{wo,EP}}}{A_{\mathrm{wo,EP,A,B}} \cdot \lambda_{\mathrm{cast}}} = 0.2795\ \mathrm{K/W}$	The resin casting in axial direction
Thermal resistances in the air-gap	
$R_{\delta 0} = \frac{1}{\alpha_{\delta} \cdot d_{\mathrm{si}} \cdot \pi \cdot l_{\mathrm{Fe}}} = 0.3660\ \mathrm{K/W}$	Between the stator inner surface and the air-gap
$R_{\delta 1} = \frac{0.9}{\alpha_{\delta} \cdot d_{\mathrm{ro}} \cdot \pi \cdot l_{\mathrm{Fe}}} = 0.3337\ \mathrm{K/W}$	Between the air-gap and the rotor surface

$R_{\delta 2} = \frac{0.1}{\alpha_\delta \cdot d_{\mathrm{ro}} \cdot \pi \cdot l_{\mathrm{Fe}}} \cdot \frac{\varphi_{\mathrm{syn}}}{\varphi_{\mathrm{m,out}}} = 0.0494\,\mathrm{K/W}$	Between the air-gap and the rotor surface
$R_{\delta 3} = \frac{0.1}{\alpha_\delta \cdot d_{\mathrm{ro}} \cdot \pi \cdot l_{\mathrm{Fe}}} \cdot \frac{\varphi_{\mathrm{syn}}}{\varphi_{\mathrm{syn}} - \varphi_{\mathrm{m,out}}} = 0.1489\,\mathrm{K/W}$	Between the air-gap and the rotor surface
Thermal resistances in the rotor	
$R_{\mathrm{r0}} = \frac{\ln(2 \cdot r_{\mathrm{node}}/d_{\mathrm{ri}})}{2\pi \cdot l_{\mathrm{Fe}} \cdot \lambda_{\mathrm{Fe}}} = 0.0093\,\mathrm{K/W}$	Between the middle of the rotor and the inner rotor
$R_{\mathrm{r1}} = \frac{R_{\mathrm{rc1}} + R_{\mathrm{M,air}} + R_{\mathrm{rc2}}}{2 \cdot 2 \cdot p} = 0.2771\,\mathrm{K/W}$	Sum of R_{rc1}, $R_{\mathrm{M,air}}$ and R_{rc2}
$R_{\mathrm{r2}} = \frac{R_{\mathrm{rc2}} + R_{\mathrm{M,air}} + R_{\mathrm{rc3}}}{2 \cdot 2 \cdot p} = 0.2797\,\mathrm{K/W}$	Sum of R_{rc2}, $R_{\mathrm{M,air}}$ and R_{rc3}
$R_{\mathrm{r3}} = \frac{(R_{\mathrm{rc4}} + R_{\mathrm{rc5}})/2}{2 \cdot 2 \cdot p} = 0.0447\,\mathrm{K/W}$	Sum of R_{rc4} and R_{rc4}
$R_{\mathrm{r,cf}} = \frac{(R_{\mathrm{rc3,cf}} + 2 \cdot R_{\mathrm{rc6,cf}})/4}{2 \cdot 2 \cdot p} = 0.0452\,\mathrm{K/W}$	The rotor iron bridge in tangential direction
$R_{\mathrm{rc1}} = \frac{\ln(r_{\mathrm{Mi}}/r_{\mathrm{node}})}{2\pi \cdot l_{\mathrm{Fe}} \cdot \lambda_{\mathrm{Fe}}} = 0.0093\,\mathrm{K/W}$	Between the magnet pocket and middle of the rotor
$R_{\mathrm{rc2}} = \frac{h_{\mathrm{M}}/2}{\lambda_{\mathrm{M}} \cdot b_{\mathrm{M}} \cdot l_{\mathrm{Fe}}} = 0.1310\,\mathrm{K/W}$	The magnet
$R_{\mathrm{rc3}} = \frac{\ln(r_{\mathrm{ro}}/r_{\mathrm{mo}})}{2\pi \cdot l_{\mathrm{Fe}} \cdot \lambda_{\mathrm{Fe}}} \cdot \frac{2\pi}{\varphi_{\mathrm{M,air}}} = 0.0406\,\mathrm{K/W}$	Between the upper the magnet pocket and the outer rotor
$R_{\mathrm{rc4}} = \frac{\ln(r_{\mathrm{mi}}/r_{\mathrm{node}})}{2\pi \cdot l_{\mathrm{Fe}} \cdot \lambda_{\mathrm{Fe}}} = 0.0093\,\mathrm{K/W}$	Between the middle of the rotor and upper part of the rotor
$R_{\mathrm{rc5}} = \frac{\ln(r_{\mathrm{ro}}/r_{\mathrm{mi}})}{2\pi \cdot l_{\mathrm{Fe}} \cdot \lambda_{\mathrm{Fe}}} \cdot \frac{2\pi}{(\varphi_{\mathrm{syn}} - \varphi_{\mathrm{M,air}})/2} = 1.0642\,\mathrm{K/W}$	The rotor iron between two magnet poles in radial direction
$R_{\mathrm{M,air}} = \frac{h_{\mathrm{M,air}}}{\lambda_{\mathrm{M,air}} \cdot b_{\mathrm{M}} \cdot l_{\mathrm{Fe}}} = 3.1852\,\mathrm{K/W}$	Air-gap between the magnet and the rotor iron
$R_{\mathrm{rc3,cf}} = \frac{\varphi_{\mathrm{M,air}}}{2 \cdot \lambda_{\mathrm{Fe}} \cdot l_{\mathrm{Fe}}} \cdot \frac{r_{\mathrm{ro}} + r_{\mathrm{mo}}}{r_{\mathrm{ro}} - r_{\mathrm{mo}}} = 2.0088\,\mathrm{K/W}$	The Rotor iron upper the magnet pocket in tangential direction
$R_{\mathrm{rc6,cf}} = \frac{(\varphi_{\mathrm{M,air}} - \varphi_{\mathrm{M,out}})/2}{2 \cdot \lambda_{\mathrm{Fe}} \cdot l_{\mathrm{Fe}}} \cdot \frac{2 \cdot r_{\mathrm{ro}} - h_{\mathrm{bridge}}}{h_{\mathrm{bridge}}} = 0.0806\,\mathrm{K/W}$	The rotor iron bridge in tangential direction
Thermal resistances in the shaft	
$R_{\mathrm{r,sh}} = \frac{1}{(1/R_{\mathrm{t,A}} + 1/R_{\mathrm{t,B}})} = 2.9952\,\mathrm{K/W}$	Total thermal resistance of the shaft
$R_{\mathrm{t,A}} = R_{\mathrm{t,sh1}} + R_{\mathrm{t,sh3}} + R_{\mathrm{t,b}} + R_{\mathrm{t,EP1}} + R_{\mathrm{t,EP,\delta 1}} = 5.8189\,\mathrm{K/W}$	Between the middle of the shaft and the ambient in DE side
$R_{\mathrm{t,B}} = R_{\mathrm{t,sh2}} + R_{\mathrm{t,sh4}} + R_{\mathrm{t,b}} + R_{\mathrm{t,EP2}} + R_{\mathrm{t,EP,\delta 2}} = 6.1725\,\mathrm{K/W}$	Between the middle of the shaft and the ambient in NDE side

$R_{\mathrm{t,sh}k} = \frac{l_{\mathrm{sh},k}}{\lambda_{\mathrm{sh}} \cdot A_{\mathrm{sh},k}}\ (k = 1, 2, 3, 4) =$ $0.8913, 0.8913, 1.8038, 2.1574\ \mathrm{K/W}$	Partial thermal resistances in the shaft in axial direction
$R_{\mathrm{t,b}} = \frac{2 \cdot h_{\mathrm{film}}}{\lambda_{\mathrm{film}} \cdot 4 \cdot A_{\mathrm{HZ}}} = 0.0484\ \mathrm{K/W}$	The bearing
$R_{\mathrm{t,EP1,2}} = \frac{\ln(d_{\mathrm{cool,out}}/d_{\mathrm{in}})}{\lambda_{\mathrm{sh}} \cdot 2\pi \cdot l_{\mathrm{EP}}} = 0.0984\ \mathrm{K/W}$	The end plates in radial direction
$R_{\mathrm{t,EP,\delta 1,2}} = \frac{1}{\alpha_{\mathrm{air3}} \cdot A_{\mathrm{EP}}} = 4.2441\ \mathrm{K/W}$	Between the end plates and the ambient
Thermal resistances in the housing	
$R_{\mathrm{cjax1}} = \frac{(l_{\mathrm{Fe}}/2 + l_{\mathrm{cj,Fe1}}/2)}{A_{\mathrm{cjax1}} \cdot \lambda_{\mathrm{al}}} = 0.2683\ \mathrm{K/W}$	The cooling jacket under the cooling channel in axial direction (DE side)
$R_{\mathrm{cjax2}} = \frac{(l_{\mathrm{Fe}}/2 + l_{\mathrm{cj,Fe2}}/2)}{A_{\mathrm{cjax1}} \cdot \lambda_{\mathrm{al}}} = 0.2834\ \mathrm{K/W}$	The cooling jacket under the cooling channel in axial direction (NDE side)
$R_{\mathrm{cjax3}} = \frac{(l_{\mathrm{Fe}}/2 + l_{\mathrm{cj,Fe1}}/2)}{A_{\mathrm{cjax2}} \cdot \lambda_{\mathrm{al}}} = 0.1458\ \mathrm{K/W}$	The cooling jacket upper the cooling channel in axial direction (DE side)
$R_{\mathrm{cjax4}} = \frac{(l_{\mathrm{Fe}}/2 + l_{\mathrm{cj,Fe2}}/2)}{A_{\mathrm{cjax2}} \cdot \lambda_{\mathrm{al}}} = 0.1540\ \mathrm{K/W}$	The cooling jacket upper the cooling channel in axial direction (NDE side)
$R_{\mathrm{cj1}} = \frac{\ln((d_{\mathrm{sa}} + 3\mathrm{e}^{-3})/d_{\mathrm{sa}})}{2\pi \cdot l_{\mathrm{Fe}} \cdot \lambda_{\mathrm{al}}} = 0.0979\ \mathrm{mK/W}$	At the middle of the cooling jacket under the cooling channel in radial direction
$R_{\mathrm{cj2}} = \frac{\ln((d_{\mathrm{sa}} + 6\mathrm{e}^{-3})/(d_{\mathrm{sa}} + 3\mathrm{e}^{-3}))}{2\pi \cdot l_{\mathrm{Fe}} \cdot \lambda_{\mathrm{al}}} = 0.0960\ \mathrm{mK/W}$	At the middle of the cooling jacket under the cooling channel in radial direction
$R_{\mathrm{cj5}} = \frac{\ln((d_{\mathrm{cool,out}} - 5\mathrm{e}^{-3})/(d_{\mathrm{cool,out}} - 10\mathrm{e}^{-3}))}{2\pi \cdot l_{\mathrm{Fe}} \cdot \lambda_{\mathrm{al}}} =$ $0.1484\ \mathrm{mK/W}$	At the middle of the cooling jacket upper the cooling channel in radial direction
$R_{\mathrm{cj6}} = \frac{\ln(d_{\mathrm{cool,out}}/(d_{\mathrm{cool,out}} - 5\mathrm{e}^{-3}))}{2\pi \cdot l_{\mathrm{Fe}} \cdot \lambda_{\mathrm{al}}} = 0.1441\ \mathrm{mK/W}$	At the middle of the cooling jacket upper the cooling channel in radial direction
$R_{\mathrm{cj3A}} = \frac{\ln((d_{\mathrm{sa}} + 3\mathrm{e}^{-3})/d_{\mathrm{sa}})}{2\pi \cdot l_{\mathrm{cjFe1}} \cdot \lambda_{\mathrm{al}}} = 0.3606\ \mathrm{mK/W}$	At the cooling jacket under the cooling channel in radial direction (DE side)
$R_{\mathrm{cj3B}} = \frac{\ln((d_{\mathrm{sa}} + 3\mathrm{e}^{-3})/d_{\mathrm{sa}})}{2\pi \cdot l_{\mathrm{cjFe2}} \cdot \lambda_{\mathrm{al}}} = 0.2855\ \mathrm{mK/W}$	At the cooling jacket under the cooling channel in radial direction (NDE side)
$R_{\mathrm{cj4A}} = \frac{\ln((d_{\mathrm{cool,out}} - 5\mathrm{e}^{-3})/(d_{\mathrm{sa}} + 3\mathrm{e}^{-3}))}{2\pi \cdot l_{\mathrm{cjFe1}} \cdot \lambda_{\mathrm{al}}} = 0.0018\ \mathrm{K/W}$	At the cooling jacket upper the cooling channel in radial direction (DE side)
$R_{\mathrm{cj4B}} = \frac{\ln((d_{\mathrm{cool,out}} - 5\mathrm{e}^{-3})/(d_{\mathrm{sa}} + 3\mathrm{e}^{-3}))}{2\pi \cdot l_{\mathrm{cjFe2}} \cdot \lambda_{\mathrm{al}}} = 0.0014\ \mathrm{K/W}$	At the cooling jacket upper the cooling channel in radial direction (NDE side)
$R_{\mathrm{cj7A}} = \frac{\ln(d_{\mathrm{cool,out}}/(d_{\mathrm{cool,out}} - 5\mathrm{e}^{-3}))}{2\pi \cdot l_{\mathrm{cjFe1}} \cdot \lambda_{\mathrm{al}}} = 0.5309\ \mathrm{K/W}$	At the cooling jacket upper the cooling channel in radial direction (DE side)
$R_{\mathrm{cj7A}} = \frac{\ln(d_{\mathrm{cool,out}}/(d_{\mathrm{cool,out}} - 5\mathrm{e}^{-3}))}{2\pi \cdot l_{\mathrm{cjFe2}} \cdot \lambda_{\mathrm{al}}} = 0.4203\ \mathrm{K/W}$	At the cooling jacket upper the cooling channel in radial direction (NDE side)

$R_{\mathrm{cj,cc,1,2}} = \frac{1}{\alpha_{\mathrm{channel}} \cdot A_{\mathrm{channel}}} = 0.8259\,\mathrm{K/W}$	Between the cooling channel and the coolant
Others thermal resistances	
$R_{\mathrm{EP,A,B}} = \frac{l_{\mathrm{EP}}}{A_{\mathrm{EP}} \cdot \lambda_{\mathrm{al}}} = 0.0028\,\mathrm{K/W}$	The end plates
$R_{\mathrm{EP,air,A,B}} = \frac{1}{\alpha_{\mathrm{air3}} \cdot A_{\mathrm{EP}}} = 4.2441\,\mathrm{K/W}$	Between the end plates and the ambient
$R_{\mathrm{cj,air},k} = \frac{1}{\alpha_{\mathrm{air3}} \cdot A_{\mathrm{housing},k}}\ (k = 1, 2, 3) = 0.8711, 3.2094, 2.5408\,\mathrm{K/W}$	Between the housing and the ambient

Appendix D. Analytical calculation of short-circuit current and torque

- Dynamic equation set of PMSM in d-q rotor reference frame

$$u_{\mathrm{d}}(t) = R_{\mathrm{s}} \cdot i_{\mathrm{d}}(t) + \frac{d\psi_{\mathrm{d}}(t)}{dt} - \omega_{\mathrm{m}} \cdot p \cdot \psi_{\mathrm{q}}(t) \tag{D.1}$$

$$u_{\mathrm{q}}(t) = R_{\mathrm{s}} \cdot i_{\mathrm{q}}(t) + \frac{d\psi_{\mathrm{q}}(t)}{dt} + \omega_{\mathrm{m}} \cdot p \cdot \psi_{\mathrm{d}}(t) \tag{D.2}$$

$$\psi_{\mathrm{d}}(t) = L_{\mathrm{d}} \cdot i_{\mathrm{d}}(t) + \Psi_{\mathrm{M}} \tag{D.3}$$

$$\psi_{\mathrm{q}}(t) = L_{\mathrm{q}} \cdot i_{\mathrm{q}}(t) \tag{D.4}$$

$u_{\mathrm{d}}, u_{\mathrm{q}}$: Stator voltage components in d- and q-axis

$i_{\mathrm{d}}, i_{\mathrm{q}}$: Stator currents components in d- and q-axis

$L_{\mathrm{d}}, L_{\mathrm{q}}$: Stator self-inductances per phase in d- and q-axis

$\psi_{\mathrm{d}}, \psi_{\mathrm{q}}$: Stator flux linkages per phase in d- and q-axis

ω_{m}: Angular rotational frequency

$\omega_{\mathrm{m}} \cdot p$: Stator angular frequency (ω_{s})

R_{s}: Stator winding resistance per phase

Ψ_{M}: Stator flux linkage per phase from rotor permanent magnets

- Laplace transformed equations of (D.1)−(D.4)

$$U_{\mathrm{d}}(s) = R_{\mathrm{s}} \cdot I_{\mathrm{d}}(s) + s \cdot \Psi_{\mathrm{d}}(s) - \psi_{\mathrm{d0}} - \omega_{\mathrm{s}} \cdot \Psi_{\mathrm{q}}(s) \tag{D.5}$$

$$U_{\mathrm{q}}(s) = R_{\mathrm{s}} \cdot I_{\mathrm{q}}(s) + s \cdot \Psi_{\mathrm{q}}(s) - \psi_{\mathrm{q0}} + \omega_{\mathrm{s}} \cdot \Psi_{\mathrm{d}}(s) \tag{D.6}$$

$$\Psi_{\mathrm{d}}(s) = L_{\mathrm{d}} \cdot I_{\mathrm{d}}(s) + \Psi_{\mathrm{M}}/s \tag{D.7}$$

$$\Psi_{\mathrm{q}}(s) = L_{\mathrm{q}} \cdot I_{\mathrm{q}}(s) \tag{D.8}$$

with initial conditions of

Currents: $i_{\mathrm{d}}(0^-) = i_{\mathrm{d0}}$, $i_{\mathrm{q}}(0^-) = i_{\mathrm{q0}}$

Flux linkages: $\psi_{\mathrm{d}}(0^-) = \psi_{\mathrm{d0}} = L_{\mathrm{d}} \cdot i_{\mathrm{d0}} + \Psi_{\mathrm{M}}$, $\psi_{\mathrm{q}}(0^-) = \psi_{\mathrm{q0}} = L_{\mathrm{q}} \cdot i_{\mathrm{q0}}$

Voltages: $u_{\mathrm{d}}(0^-) = u_{\mathrm{d0}} = R_s \cdot i_{\mathrm{d0}} - \omega_{\mathrm{m}} \cdot p \cdot \psi_{\mathrm{q0}}$, $u_{\mathrm{q}}(0^-) = u_{\mathrm{q0}} = R_s \cdot i_{\mathrm{q0}} + \omega_{\mathrm{m}} \cdot p \cdot \psi_{\mathrm{d0}}$

- Stator voltage is zero $u_\mathrm{d} = 0$, $u_\mathrm{q} = 0$ at a three-phase sudden short circuit at $t = 0$,:

$$\begin{pmatrix} L_\mathrm{d} \cdot i_\mathrm{d0} \\ L_\mathrm{q} \cdot i_\mathrm{q0} - \omega_\mathrm{m} \cdot \Psi_\mathrm{M}/s \end{pmatrix} = \begin{pmatrix} R_\mathrm{s} + s \cdot L_\mathrm{d} & -\omega_\mathrm{m} \cdot L_\mathrm{q} \\ \omega_\mathrm{m} \cdot L_\mathrm{d} & R_\mathrm{s} + s \cdot L_\mathrm{q} \end{pmatrix} \cdot \begin{pmatrix} I_\mathrm{d}(s) \\ I_\mathrm{q}(s) \end{pmatrix} \tag{D.9}$$

$$\begin{pmatrix} I_\mathrm{d}(s) \\ I_\mathrm{q}(s) \end{pmatrix} = \frac{1}{Det} \cdot \begin{pmatrix} R_\mathrm{s} + s \cdot L_\mathrm{q} & \omega_\mathrm{s} \cdot L_\mathrm{q} \\ -\omega_\mathrm{s} \cdot L_\mathrm{d} & R_\mathrm{s} + s \cdot L_\mathrm{d} \end{pmatrix} \cdot \begin{pmatrix} L_\mathrm{d} \cdot i_\mathrm{d0} \\ L_\mathrm{q} \cdot i_\mathrm{q0} - \omega_\mathrm{s} \cdot \Psi_\mathrm{M}/s \end{pmatrix} \tag{D.10}$$

Determinant of the impedance matrix in (D.9):

$$Det = (R_\mathrm{s} + s \cdot L_\mathrm{d}) \cdot (R_\mathrm{s} + s \cdot L_\mathrm{q}) + \omega_\mathrm{s}^2 \cdot L_\mathrm{d} \cdot L_\mathrm{q} = (s - \underline{s}_1) \cdot (s - \underline{s}_2), \qquad \underline{s}_{1,2} = -a \pm j \cdot b$$

with the coefficients: $a = \frac{1}{2}\left(\frac{1}{\tau_\mathrm{d}} + \frac{1}{\tau_\mathrm{q}}\right)$, $b = \frac{1}{2} \cdot \sqrt{4\omega_\mathrm{s}^2 - \left(\frac{1}{\tau_\mathrm{d}} - \frac{1}{\tau_\mathrm{q}}\right)^2}$, the electric time constants in d- and q-axis are $\tau_\mathrm{d} = \frac{L_\mathrm{d}}{R_\mathrm{s}}$, $\tau_\mathrm{q} = \frac{L_\mathrm{q}}{R_\mathrm{s}}$

- Inverse Laplace transform of (D.10):

$$i_\mathrm{d}(t) = -i_\mathrm{pd} + e^{-a \cdot t} \cdot (K_\mathrm{d} \cdot \cos(b \cdot t) + M_\mathrm{d} \cdot \sin(b \cdot t)), \tag{D.11}$$

$$i_\mathrm{q}(t) = -i_\mathrm{pq} + e^{-a \cdot t} \cdot \left(K_\mathrm{q} \cdot \cos(b \cdot t) + M_\mathrm{q} \cdot \sin(b \cdot t)\right), \tag{D.12}$$

$$\underline{i}_{\mathrm{s(dq)}}(t) = i_\mathrm{d}(t) + j \cdot i_\mathrm{q}(t), \tag{D.13}$$

with the coefficients:

$i_\mathrm{pd} = \frac{\omega_\mathrm{s}^2 L_\mathrm{q} \Psi_\mathrm{M}}{L_\mathrm{d} L_\mathrm{q} (a^2 + b^2)}$,

$i_\mathrm{pq} = \frac{\omega_\mathrm{s} R_\mathrm{s} \Psi_\mathrm{M}}{L_\mathrm{d} L_\mathrm{q} (a^2 + b^2)} = i_\mathrm{pd} \cdot \frac{1}{\omega_\mathrm{s} \cdot \tau_\mathrm{q}}$,

$K_\mathrm{d} = i_\mathrm{d0} + i_\mathrm{pd}$,

$M_\mathrm{d} = -\left(i_\mathrm{d0} - i_\mathrm{pd}\right) \cdot \frac{a}{b} + \frac{R_\mathrm{s} L_\mathrm{d} i_\mathrm{d0} + \omega_\mathrm{s} L_\mathrm{q}^2 i_\mathrm{q0}}{L_\mathrm{d} L_\mathrm{q} b}$,

$K_\mathrm{q} = i_\mathrm{q0} + i_\mathrm{pq}$,

$M_\mathrm{q} = -\left(i_\mathrm{q0} - i_\mathrm{pq}\right) \cdot \frac{a}{b} + \frac{-\omega_\mathrm{s} L_\mathrm{d}^2 i_\mathrm{d0} + R_\mathrm{s} L_\mathrm{q} i_\mathrm{q0} - L_\mathrm{d} \omega_\mathrm{s} \Psi_\mathrm{M}}{L_\mathrm{d} L_\mathrm{q} b}$.

- Transformation: from d-q-reference frame to α-β-reference frame

$$\underline{i}_{\mathrm{s}(\alpha\beta)}(t) = \underline{i}_{\mathrm{s}(\mathrm{dq})}(t) \cdot e^{j\gamma} \tag{D.14}$$

with the angle between both reference frames $\gamma = \omega_{\mathrm{s}} \cdot t + \gamma_0$, where γ_0 is the angle of d-q-reference frame corresponding to the real axis in α-β-reference frame at $t = 0$.
U-phase stator current $i_{\mathrm{u}}(t) = Re\{\underline{i}_{\mathrm{s}(\alpha\beta)}(t)\}$:

$$\begin{aligned} i_{\mathrm{u}}(t) = &-\left(i_{\mathrm{pd}} \cdot \cos(\omega_{\mathrm{s}} t + \gamma_0) - i_{\mathrm{pq}} \cdot \sin(\omega_{\mathrm{s}} t + \gamma_0)\right) \\ &+ \frac{1}{2} e^{-a \cdot t} \cdot \left[\left(K_{\mathrm{d}} + M_{\mathrm{q}}\right) \cdot \cos\left((\omega_{\mathrm{s}} + b)t + \gamma_0\right) + \left(K_{\mathrm{d}} - M_{\mathrm{q}}\right) \cdot \cos\left((\omega_{\mathrm{s}} - b)t + \gamma_0\right)\right. \\ &\left. -\left(K_{\mathrm{q}} - M_{\mathrm{d}}\right) \cdot \sin\left((\omega_{\mathrm{s}} + b)t + \gamma_0\right) - \left(K_{\mathrm{q}} + M_{\mathrm{d}}\right) \cdot \sin\left((\omega_{\mathrm{s}} - b)t + \gamma_0\right)\right] \end{aligned} \tag{D.15}$$

At high angular rotation speed the stator angular frequency has a much higher value than the inverse of both electric time constants $\omega_{\mathrm{s}} \gg \frac{1}{\tau_{\mathrm{d}}}, \frac{1}{\tau_{\mathrm{q}}}$, thus the equation can be simplified with $b \approx \omega_{\mathrm{s}}$ as

$$\begin{aligned} i_{\mathrm{U}}(t) \cong &-\sqrt{i_{\mathrm{pd}}^2 + i_{\mathrm{pq}}^2} \cdot \cos(\omega_{\mathrm{s}} t + \gamma_0 + \beta_1) \\ &+ \frac{1}{2} e^{-\frac{t}{\tau_{\mathrm{a}}}} \cdot \left[\sqrt{\left(K_{\mathrm{d}} + M_{\mathrm{q}}\right)^2 + \left(K_{\mathrm{q}} - M_{\mathrm{d}}\right)^2} \cdot \cos(2\omega_{\mathrm{s}} t + \gamma_0 + \beta_2)\right. \\ &\left. + \sqrt{\left(K_{\mathrm{d}} - M_{\mathrm{q}}\right)^2 + \left(K_{\mathrm{q}} + M_{\mathrm{d}}\right)^2} \cdot \cos(\gamma_0 + \beta_3)\right], \end{aligned} \tag{D.16}$$

with the stator armature time constant of $\tau_{\mathrm{a}} = \frac{1}{a} = \frac{\tau_{\mathrm{d}}\tau_{\mathrm{q}}}{2(\tau_{\mathrm{d}} + \tau_{\mathrm{q}})}$, $\beta_1 = \arctan\left(\frac{1}{\omega_{\mathrm{s}} \cdot \tau_{\mathrm{q}}}\right)$, $\beta_2 = \arctan\left(\frac{K_{\mathrm{q}} - M_{\mathrm{d}}}{K_{\mathrm{d}} + M_{\mathrm{q}}}\right)$ and $\beta_3 = \arctan\left(\frac{K_{\mathrm{q}} + M_{\mathrm{d}}}{K_{\mathrm{d}} - M_{\mathrm{q}}}\right)$

- General torque equation:

$$m_\mathrm{e}(t) = \frac{m}{2} \cdot p \cdot \left(\Psi_\mathrm{M} \cdot i_\mathrm{q}(t) + \left(L_\mathrm{d} - L_\mathrm{q}\right) \cdot i_\mathrm{d}(t) \cdot i_\mathrm{q}(t) \right) \tag{D.17}$$

Substituting the stator current components in d- and q-axis $i_\mathrm{d}(t)$, $i_\mathrm{q}(t)$ from (D.11) and (D.12) into (D.17), the torque equation is

$$\begin{aligned} m_\mathrm{e}(t) = \frac{m}{2} \cdot p \cdot \Bigg[& -\frac{i_\mathrm{pd}}{\omega_\mathrm{s} \cdot \tau_\mathrm{q}} \left(\Psi_\mathrm{M} - \left(L_\mathrm{d} - L_\mathrm{q}\right) \cdot i_\mathrm{pd} \right) + e^{-\frac{t}{\tau_\mathrm{a}}} \cdot A_1 \cdot \cos(bt - \alpha_1) \\ & + \frac{1}{2} \cdot \left(L_\mathrm{d} - L_\mathrm{q}\right) \cdot e^{-\frac{2t}{\tau_\mathrm{a}}} \cdot \left(K_\mathrm{d} K_\mathrm{q} + M_\mathrm{d} M_\mathrm{q} + A_2 \cdot \cos(2bt - \alpha_2) \right) \Bigg], \end{aligned} \tag{D.18}$$

with the coefficients

$$A_1 = \sqrt{\left(K_\mathrm{q}\Psi_\mathrm{M} - \left(L_\mathrm{d} - L_\mathrm{q}\right)\left(K_\mathrm{q} i_\mathrm{pd} + K_\mathrm{d} i_\mathrm{pq}\right)\right)^2 + \left(M_\mathrm{q}\Psi_\mathrm{M} - \left(L_\mathrm{d} - L_\mathrm{q}\right)\left(M_\mathrm{q} i_\mathrm{pd} + M_\mathrm{d} i_\mathrm{pq}\right)\right)^2},$$

$$A_2 = \sqrt{\left(K_\mathrm{d}K_\mathrm{q} - M_\mathrm{d}M_\mathrm{q}\right)^2 + \left(K_\mathrm{d}M_\mathrm{q} + M_\mathrm{d}K_\mathrm{q}\right)^2},$$

$$\alpha_1 = \arctan\left(\frac{M_q\Psi_M - (L_d - L_q)\cdot(M_q i_{pd} + M_d i_{pq})}{K_q\Psi_M - (L_d - L_q)\cdot(K_q i_{pd} + K_d i_{pq})}\right),$$

$$\alpha_2 = \arctan\left(\frac{K_\mathrm{d}M_\mathrm{q} + M_\mathrm{d}K_\mathrm{q}}{K_\mathrm{d}K_\mathrm{q} - M_\mathrm{d}M_\mathrm{q}}\right).$$

Bibliography

[1] "Climate Action in Figures (2017) – Facts, Trends and Incentives for German Climate Policy," Federal Ministry for the Environment, Nature Conservation, Building and Nuclear Safety (BMUB) Public Relations Division, 11055 Berlin, Germany, 2017.

[2] "A European Strategy for low-emission mobility," European Commission, [Online]. Available: https://ec.europa.eu/clima/policies/transport_en. [Accessed 08 May 2019].

[3] B. Parkin and W. Wilkes, "Millions of Electric Cars needed in Germany's War on Pollution," Bloomberg, 27 March 2019. [Online]. Available: https://www.bloomberg.com/news/articles/2019-03-27/millions-of-electric-cars-needed-in-germany-s-war-on-pollution. [Accessed 08 May 2019].

[4] C. C. Chan, "The State of the Art of Electric, Hybrid, and Fuel Cell Vehicles," *in Proceedings of the IEEE, vol. 95, no. 4,* pp. 704-718, April 2007.

[5] U. Knödel, A. Strube, U. C. Blessing and S. Klostermann, "Auslegung und Implementierung bedarfsgerechter elektrischer Antriebe," *ATZ - Automobiltechnische Zeitschrift,* pp. 462-466, June 2010.

[6] S. Roberts, "Multispeed-Getriebe für Elektrofahrzeuge," *ATZ - Automobiltechnische Zeitschrift,* pp. 298-303, April 2012.

[7] B. Stubbs and P. M. Fracchia, "eDCT: 4 speed seamless-shift technology for electric vehicles," in *in Proc. of the Hybrid and Electric Vehicles Conference 2013 (HEVC 2013) IET*, London, the United Kingdom, 2013.

[8] A. Viehmann, S. Fischer, R. König, S. Rinderknecht and C. Beidl, "Vergleich von Betriebsstrategien für das parallel-serielle Hybridantriebskonzept DE-REX [Comparison of operation strategies for the parallel-series hybrid powertrain concept DE-REX] (in German)," in *Conference Plug-In-Hybride und Range Extender, Haus der Technik*, Darmstadt, Germany, April 2016.

[9] S. Fischer, A. Viehmann, R. König, C. Beidl and S. Rinderknecht, "Potential of the hybrid operating modes of the plug-in hybrid powertrain concept 'Two-Drive

Transmission with Range Extender' (DE-REX)," *Der Antrieb von morgen 2017,* pp. 263-278, Proceedings. Springer Vieweg, Wiesbaden Germany.

[10] M. Eghtessad, M. Torben and S. Mirco, "Antriebsstrangkonfigurationen: Identifikation optimaler Antriebsstrangkonfigurationen für Elektrofahrzeuge," Abschlussbericht zum FVA- Projekt 641-I, Forschungsvereinigung Antriebstechnik, Frankfurt am Main, Germany, 2012.

[11] A. Binder, "CAD and System Dynamics of Electrical Machines," in *lecture notes*, TU Darmstadt, Institute of Electrical Energy Conversion, 2016.

[12] International Electrotechnical Commission, *IEC 60085: Electrical insulation - Thermal evaluation and designation,* 2007.

[13] International Electrotechnical Commission, *Rotating electric machines Part 1: Rating and performance,* Geneva, Switzerland, 2004.

[14] International Electrotechnical Commission, *IEC 60349-2: Electric traction-Rotating electrical machines for rail and road vehicles-, Part 2: Electronic converter-fed alternating current motors,* 2010.

[15] A. Binder, Elektrische Maschinen und Antriebe – Grundlagen, Betriebsverhalten, Heidelberg, Germany: Springer-Verlag, 2012.

[16] C. Z. Deak, Modular Permanent-Magnet Synchronous Motors with high Electromagnetic Utilization, Ph.D. Dissertation, TU Darmstadt: Shaker Verlag, 2012.

[17] N. Bianchi and S. Bolognani, "Design techniques for reducing the cogging torque in surface-mounted PM motors," *in IEEE Transactions on Industry Applications,* vol. 38, no. 5, pp. 1259-1265, 2002.

[18] G. Lee, S. Kim, J. Hong and J. Bahn, "Torque Ripple Reduction of Interior Permanent Magnet Synchronous Motor Using Harmonic Injected Current," *in IEEE Transactions on Magnetics,* vol. 44, no. 6, pp. 1582-1585, June 2008.

[19] H. Kleinrath, Stromrichtergespeiste Drehfeldmaschinen [Inverter-fed rotary field machines] (in German), Wien: Springer-Verlag, 1980.

[20] K. W. Klontz, T. J. E. Miller, M. I. McGilp, H. Karmaker and P. Zhong, "Short-Circuit Analysis of Permanent-Magnet Generators," *IEEE Transactions on Industry Applications,* vol. 47, no. 4, pp. 1670-1680, July-August 2011.

[21] G. Gotter, Erwärmung und Kühlung elektrischer Maschinen, Heidelberg: Springer-Verlag, 1954.

[22] D. A. Howey, P. R. N. Childs and A. S. Holmes, "Air-gap convection in rotating electrical machines," *in IEEE Transactions on Industrial Electronics,* vol. 59, no. 3, pp. 1367-1375, March 2012.

[23] C. Schätzer, Ein Verfahren zur Optimierung bei elektrischen Maschinen mit Hilfe der numerischen Feldberechnung, Ph.D. Dissertation, TU Darmstadt: Shaker Verlag, 2002.

[24] J. Pyrhönen, T. Jokinen and V. Hrabovcova, Design of Rotating Electrical Machines, 2nd Edition, Chichester, United Kingdom: John Wiley & Sons Ltd, 2013.

[25] K. Vogt, Berechnung rotierender elektrischer Maschinen, 3 ed., Berlin: VEB Verlag Technik, 1983.

[26] H. Jordan, "Die ferromagnetischen Konstanten für schwache Wechselfelder," *elektrische Nachrichtentechnik,* vol. 1, p. 8, 1924.

[27] DIN EN 10106, *Kaltgewalztes nicht kornorientiertes Elektroblech und -band im schlussgeglühten Zustand,* 2015.

[28] M. Reinlein, T. Hubert, A. Hoffmann and A. Kremser, "Optimization of analytical iron loss approaches for electrical machines," in *2013 3rd International Electric Drives Production Conference (EDPC)*, Nuremberg, Germany, 2013.

[29] J. Juergens, B. Ponick, O. Winter and A. Fricassè, "Influences of iron loss coefficients estimation on the prediction of iron losses for variable speed motors," in *2015 IEEE International Electric Machines & Drives Conference (IEMDC)*, Coeur d'Alene, USA, 2015.

[30] JMAG User's manual*, Iron Loss Formulas,* JSOL Corporation, issued: 12.2017.

[31] M. Mack, Luftreibungsverluste bei elektrischen Maschinen kleiner Baugröße (Air friction losses of electrical machines of small power ratings) in German, Stuttgart: Ph.D. Thesis, University of Stuttgart (TH), 1967.

[32] K. Atallah, D. Howe, P. H. Mellor and D. A. Stone, "Rotor loss in permanent-magnet brushless AC machines," *in IEEE Transactions on Industry Applications,* vol. 36, no. 6, pp. 1612-1618, 2000.

[33] D. Ishak, Z. Q. Zhu and D. Howe, "Eddy-current loss in the rotor magnets of permanent-magnet brushless machines having a fractional number of slots per pole," *in IEEE Transactions on Magnetics,* vol. 41, no. 9, pp. 2462-2469, September 2005.

[34] Z. Q. Zhu, K. Ng, N. Schofield and D. Howe, “Analytical prediction of rotor eddy current loss in brushless machines equipped with surface-mounted permanent magnets. I. Magnetostatic field model,” in *ICEMS'2001. Proceedings of the Fifth International Conference on Electrical Machines and Systems*, Shenyang, China, 2001.

[35] Z. Q. Zhu, K. Ng, N. Schofield and D. Howe, “Analytical prediction of rotor eddy current loss in brushless machines equipped with surface-mounted permanent magnets. II. Accounting for eddy current reaction field,” in *ICEMS'2001. Proceedings of the Fifth International Conference on Electrical Machines and Systems*, Shenyang, China, 2001.

[36] Z. Q. Zhu, K. Ng, N. Schofield and D. Howe, “Improved analytical modelling of rotor eddy current loss in brushless machines equipped with surface-mounted permanent magnets,” *in IEE Proceedings - Electric Power Applications,* vol. 151, no. 6, pp. 641-650, November 2004.

[37] T. Lu, Weiterentwicklung von hochtourigen permanenterregten Drehstromantrieben mit Hilfe von Finite-Elemente-Berechnungen und experimentellen Untersuchungen, Ph.D. Dissertation, TU Darmstadt: Shaker, 2004.

[38] R. L. Russell and K. H. Norsworthy, “Eddy currents and wall losses in screened-rotor induction motors,” *in Proceedings of the IEE - Part A: Power Engineering,* vol. 105, no. 20, pp. 163-175, April 1958.

[39] P. J. P. Perruchoud and P. J. Pinewski, “Power losses for space vector modulation techniques,” in *Power Electronics in Transportation*, Dearborn, USA, 1996, pp. 167-173.

[40] TAMAGAWA SEIKI Co, “Catalogue of VR type resolver Singlsyn,” February 2005. [Online]. Available: https://www.tamagawa-seiki.com/assets/img/downloads/pdf/resolver-synchro/1570N15EJ_shusei.pdf. [Accessed 18 January 2018].

[41] FLUKE, “NORMA 4000/5000 Power Analyzer Operators Manual,” June 2007. [Online]. Available: http://assets.fluke.com/manuals/norma___omeng0200.pdf. [Accessed 9 May 2019].

[42] A. Krings, J. Soulard and O. Wallmark, “Influence of PWM switching frequency and modulation index on the iron losses and performance of slot-less permanent

magnet motors," in *2013 International Conference on Electrical Machines and Systems (ICEMS)*, Busan, South Korea, 2013.

[43] Z. Gmyrek, A. Boglietti and A. Cavagnino, "Iron Loss Prediction With PWM Supply Using Low- and High-Frequency Measurements: Analysis and Results Comparison," *in IEEE Transactions on Industrial Electronics,* vol. 55, no. 4, pp. 1722-1728, April 2008.

[44] BRUSA, "Technical specifications of DMC524," [Online]. Available: http://www.brusa.biz/fileadmin/template/ Support-Center/Datenblätter/BRUSA_DB_EN_DMC5.pdf. [Accessed 27 April 2018].

[45] H. Neudorfer, Weiterentwicklung von elektrischen Antriebssystemen für Elektro- und Hybridstraßenfahrzeuge, volume 2 of OVE-Schriftenreihe für Habilitationen und Dissertationen, Wien: Österreichischer Verband für Elektrotechnik, 2010.

[46] R. König and S. Rinderknecht, "Multi-Objective Optimization of the Two-Drive-Transmission for a Hybrid Electric Vehicle," in *FISITA 2014 World Automotive Congress*, Maastricht, Netherlands, 2014.

[47] T. J. Barlow, S. Latham, I. S. McCrae and P. G. Boulter, "A reference book of driving cycles for use in the measurement of road vehicle emissions," Published Project Report PPR 354 Version 3, TRL Limited, November 2009.

[48] P. Kågeson, "Cycle beating and the EU test for cycle for cars," European Federation for Transport and Environment (T&E), Brussels, Belgium, November 1998.

[49] N. Burnete and B. O. Varga, Proceedings of the 4th International Congress of Automotive and Transport Engineering (AMMA 2018), Springer International Publishing, 2019.

[50] "Global WLTP roll-out for more realistic results in fuel consumption," German Association of the Automotive Industry (VDA), September 2017. [Online]. Available: https://www.vda.de/en/topics/environment-and-climate/Global-WLTP-roll-out-for-more-realistic-results-in-fuel-consumption/WLTP-Why-a-new-test-procedure.html . [Accessed 09 May 2019].

[51] M. Mitschke and H. Wallentowitz, Dynamik der Kraftfahrzeuge, Heidelberg: Springer-Verlag, 2004.

[52] S. Jurkovic, K. M. Rahman, J. C. Morgante and P. J. Savagian, "Induction Machine Design and Analysis for General Motors e-Assist Electrification Technology," *in*

IEEE Transactions on Industry Applications, vol. 51, no. 1, pp. 631-639, 2015.

[53] K. Rahman, S. Jurkovic, S. Hawkins, S. Tarnowsky and P. Savagian, "Propulsion System Design of a Battery Electric Vehicle," *in IEEE Electrification Magazine,* vol. 2, no. 2, pp. 14-24, June 2014.

[54] F. Momen, K. Rahman and Y. Son, "Electrical Propulsion System Design of Chevrolet Bolt Battery Electric Vehicle," *in IEEE Transactions on Industry Applications,* vol. 55, no. 1, pp. 376-384, 2019.

[55] R. Jäger, P. Ramminger, R. Matthé and M. Herrmann, "The Electric Propulsion System in the new Opel Ampera-e," in *38. Internationales Wiener Motorensymposium*, vol. 2, Vienna, Austria, VDI-Verlag, Düsseldorf, 2017, pp. 1-13.

[56] D. Jung, Y. Kim, U. Lee and H. Lee, "Optimum Design of the Electric Vehicle Traction Motor Using the Hairpin Winding," in *2012 IEEE 75th Vehicular Technology Conference (VTC Spring)*, Yokohama, Japan, 2012.

[57] K. M. Rahman, S. Jurkovic, C. Stancu, J. Morgante and P. J. Savagian, "Design and Performance of Electrical Propulsion System of Extended Range Electric Vehicle (EREV) Chevrolet Volt," *in IEEE Transactions on Industry Applications,* vol. 51, no. 3, pp. 2479-2488, 2015.

[58] Remy International Inc., "Inside the HVH Hybrid Motor: Technical Insights on Remy's Off-the-Shelf Hybrid Motor Solutions," October 2009. [Online]. Available: http://www.vaxosystems.com/store/images/file/pdf/inside-hvh-hybrid-motor.pdf. [Accessed 10 May 2019].

[59] T. Pfund, "Die Schaeffler eDrive Plattform, Modular und hochintegriert," in *11. Schaeffler Kolloquium*, Baden-Baden, Germany, 2018.

[60] Remy Inc., "Multi-set rectangular copper hairpin winding for electric machines". Anderson, USA Patent 6 894 417, 17 May 2005.

[61] International Electrotechnical Commission, *IEC 60317-0-2: Specifications for particular types of winding wires - Part 0-2: General requirements - Enamelled rectangular copper wire,* Geneva, Switzerland, 2013.

[62] D. Rey, "Tooth coils with Litz wire: Advantages for E-Drives," in *Coil Winding, Electric Motor & Transformer Manufacturing Exhibition, (CWIEME 2016)*, Berlin, Germany, May 2016.

[63] W. Hackmann, *Electrical Machines in Traction applications: Special requirements /*

Design / Measurements, Darmstadt, Germany: Invited lecture, Institute of Electrical Energy Conversion, TU Darmstadt, 12 January 2018.

[64] M. Klohr, Entwicklung und Konstruktion einer umrichtergespeisten magnetgelagerten Permanentmagnet-Synchronmaschine für 40 kW / 40000/min, Ph.D. Dissertation, TU Darmstadt: Shaker Verlag, 2008.

[65] MS Duroplast GmbH, "2-Component Casting System: a mixture EPIKOTE Resin 849 black and EPIKURE Curing Agent 849," MS Duroplast GmbH, July, 2013.

[66] VDI-Gesellschaft Verfahrenstechnik und Chemieingenieurwesen (GVC), VDI Heat Altas, Heidelberg: Springer-Verlag, 2010.

[67] Infineon, "Technical Information of IGBT-Module FF300R06KE3," 3 October 2013. [Online]. Available: https://www.infineon.com/dgdl/Infineon-FF300R06KE3-DS-v03_00-en_de.pdf?fileId=db3a304412b407950112b434a40a60d8. [Accessed 9 May 2019].

[68] Cogent Power Ltd., "Typical data for SURA M270-35A," Surahammars Bruks AB, June 2008.

[69] DuPont, "dupont™ nomex® paper type 410," August 2013. [Online]. Available: https://www.dupont.com/content/dam/assets/products-and-services/electronic-electrical-materials/assets/DPT16_21668_Nomex_410_Tech_Data_Sheet_me03_REFERENCE.pdf. [Accessed 2019 May 29].

[70] GLEICH Aluminiumwerk GmbH & CO. KG, "EN AW 7075: Technisches Datenblatt," 12 07 2016. [Online]. Available: https://gleich.de/de/wp-content/uploads/sites/2/2016/07/produktdatenblatt-en-aw-7075-aluminium-walzplatte.pdf. [Accessed 08 09 2019].

[71] H. Neudorfer, "Praxisorientierte Projektierung elektrischer Antriebe, Projekt-Seminar," in *lecture slides*, Darmstadt, TU Darmstadt, Institute of Electrical Energy Conversion, 2017.

Publications of the author in international conference proceedings and journals

[72] J. An, A. Binder and C. R. Sabirin, "Loss measurement of a 30 kW high speed permanent magnet synchronous machine with active magnetic bearings," 2013 International Conference on Electrical Machines and Systems (ICEMS), Busan, 2013, pp. 905-910.

[73] J. An, R. König and A. Binder, “Drive concept and motor design of a double-E-drive for hybrid electric vehicles,” *Advanced E-Motor Technology 2015*, Frankfurt, Germany, 24.-26. February 2015

[74] J. An and A. Binder, "Design of interior permanent magnet synchronous machine for two-drive-transmission," *2015 International Conference on Electrical Systems for Aircraft, Railway, Ship Propulsion and Road Vehicles (ESARS),* Aachen, 2015, pp. 1-6.

[75] R. König and J. An, “Entwicklung eines hocheffizienten Antriebsstrangs mit automatisiertem Mehrganggetriebe und Doppel-E-Antrieb zur unterbrechungsfreien Zugkraftübertragung,” Abschlussbericht zum FVA-Projekt 688, Forschungsvereinigung Antriebstechnik im VDMA, Frankfurt am Main, Germany, 2014.

[76] J. An and A. Binder, “Permanent magnet synchronous machine design for hybrid electric cars with double e-motor and range extender,” *e & i (Elektrotechnik und Informationstechnik),* vol. 133, no. 2, pp. 65-72, 2016.

[77] J. An and A. Binder, “Analysis of sudden short-circuit current of interior permanent magnet synchronous machines,” in *2016 International Symposium on Power Electronics, Electrical Drives, Automation and Motion (SPEEDAM)*, Anacapri, Italy, 2016, pp. 1324-1329.

[78] J. An, Y. Gemeinder and A. Binder, “Doppel-E-Antrieb mit Range-Extender (DE-REX),” in *8. Expert Forum E-MOTIVE*, Schweinfurt, Germany, 07.-08. September 2016.

[79] J. An, Y. Gemeinder, A. Viehmann, R. König, S. Fischer, A. Binder, S. Rinderknecht and C. Beidl, “Doppel-E-Antrieb mit Range-Extender (DE-REX)-System-Auslegung und Betriebsstrategien am Beispiel der eingesetzten Permanentmagnet-Synchronmaschinen [Twin-drive-transmission: System design and operation strategies with permanent magnet synchronous machine],” in *Proc. VDI-Conference Innovative Antriebe 2016*, Dresden, Germany, 23-24.11.2016.

[80] J. An and A. Binder, “Operation Strategy with Thermal Management of E-Machines in Pure Electric Driving Mode for Twin-Drive-Transmission (DE-REX),”

in *2017 IEEE Vehicle Power and Propulsion Conference (VPPC)*, Belfort, France, 2017.

[81] X. Li, N. Erd, J. An, G. Messager and A. Binder, "Design of a High-Speed Flywheel Energy Storage Demonstrator," in *Drive Systems 2017, 7th VDE/VDI Symposium*, Karlsruhe, Germany, 2017, pp. 1-6.

[82] Y. Gemeinder, J. An and A. Binder, "Concept study of the electrical machines for the twin-drive range-extender propulsion system (DE-REX)," *10. Expert Forum E-MOTIVE, International Conference on Electric Vehicle Drives*, Stuttgart, Germany, 12.-13. September 2018.

[83] J. An, Y. Gemeinder and A. Binder, "Downsizing possibilities of a PM synchronous motor for a hybrid vehicle," *e & i (Elektrotechnik und Informationstechnik)*, vol. 136, no. 2, pp. 143-152, 2019.

[84] A. Viehmann, R. König, Y. Gemeinder, J. An and S. Fischer, "DE-REX Doppel-E-Antrieb mit Range-Extender: Aufbau eines innovativen seriell-parallelen Doppel-E-Antriebskonzepts mit höchster Effizienz und zugkraftunterbrechungsfreiem Schaltgetriebe," Abschlussbericht zum FVA-Projekt 688-II, Forschungsvereinigung Antriebstechnik im VDMA, Frankfurt am Main, Germany , 2019 (unpublished).

Supervised student theses: *Masterarbeiten*

[85] A. Sharma, "Thermal analysis of interior permanent magnet synchronous machine (IPMSM) for electric vehicle applications," Masterarbeit Nr. 28, Institute of Electrical Energy Conversion, TU Darmstadt, Darmstadt, 2015.

[86] M. Tost Candel, "Cogging Torque Reduction for Interior Permanent Magnet Synchronous Motors," Masterarbeit Nr. 40, Institute of Electrical Energy Conversion, TU Darmstadt, Darmstadt, 2016.

[87] Y. Zhang, "Electromagnetic design of an interior permanent magnet synchronous machine for hybrid and electric vehicle applications," Masterarbeit Nr. 41, Institute of Electrical Energy Conversion, TU Darmstadt, Darmstadt, 2016.

Curriculum Vitae

Personal Data

Name: Jeongki An

Date of Birth: 04th of November 1983

Place of Birth: Busan / South Korea

Nationality: South Korean

Education / Professional Career

Since 07/2018	**Developing Engineer** Company Bosch Rexroth AG, Lohr am Main, Germany
04/2012 – 05/2018	**Scientific Assistant** Institute of Electrical Energy Conversion FB18, Electrical Engineering and Information Technology Darmstadt University of Technology, Germany
10/2009 – 02/2012	**Study for Master Degree** Master of Science in “Electrical Power Engineering” FB18, Electrical Engineering and Information Technology Darmstadt University of Technology, Germany
03/2002 – 02/2009	**Study for Bachelor Degree** Bachelor of Science in “Electronic and Electrical Engineering” Department of Electronic and Electrical Engineering Pohang University of Science and Technology (POSTECH), South-Korea
02/2002	**High School Degree** Yangjung High School, Busan, South Korea

Obertshausen,
September 2019

M.Sc. Jeongki An